Title

Direct numerical simulations, resolvent analysis, and flow control of laminar post-stall wakes around finite tapered swept wings

Author

Marques Ribeiro, Jean Helder

Publication Date

2023

Peer reviewed|Thesis/dissertation

UNIVERSITY OF CALIFORNIA
Los Angeles

Direct numerical simulations, resolvent analysis, and flow control of laminar post-stall wakes around finite tapered swept wings

A dissertation submitted in partial satisfaction
of the requirements for the degree
Doctor of Philosophy in Aerospace Engineering

by

Jean Hélder Marques Ribeiro

2023

ABSTRACT OF THE DISSERTATION

Direct numerical simulations, resolvent analysis, and flow control of laminar post-stall wakes around finite tapered swept wings

by

Jean Hélder Marques Ribeiro
Doctor of Philosophy in Aerospace Engineering
University of California, Los Angeles, 2023
Professor Kunihiko Taira, Chair

External flows over wings is a traditional flow of interest in aerodynamics. Over the last century, research efforts were dedicated to studying the wake patterns that form in the flows around finite wings. Among others, we can pinpoint the wing tip vortex, the separation region that develops under adverse pressure gradient, and the coherent vortical structures. Thanks to these past efforts, we were able to significantly extend our knowledge in aerodynamics, which paved the way for an impressive evolution of aircraft designs in the last century. Over the years, commercial flight became an ordinary asset in our society. More recently, small and micro air vehicles have also reached the market, being operated by individuals who hold no necessary knowledge of the complexity of the Navier–Stokes equations. The advanced knowledge currently held on flight physics has played a fundamental role in the development of aircraft designs, however, there is still room for improvement. In post-stall flow conditions, the aerodynamic performance of the wing decays considerably, making it challenging to sustain flight at high incidence angles. To enable flight in such flow conditions, it is important to develop physics-based flow control strategies capable of

improving the overall aerodynamic performance of the wing and its flight stability. The main implications are reduced fuel (and energy) consumption during flight, increased aircraft range, improvements in safety and productivity of air travel, attenuation of the acoustic signature, as well as enabled capability of aircraft to fly in challenging external environments.

Towards this goal, many studies have been performed to analyze and control flows over airfoils in spanwise periodic configurations. These may also be called infinite-span wings. These studies were fundamental to revealing important aspects of flow physics. However, in reality, the flows around wings are three-dimensional (3-D). In addition, modern aircraft wings are usually tapered and swept. The 3-D vortex dynamics of flows over wings has a significant influence on aircraft design, by reducing the overall lift, generating induced drag, and increasing flow unsteadiness. Thus, it is important to develop strategies to control the vortex dynamics that encompass the knowledge of the 3-D characteristics of the flow over finite, swept, and tapered wings. Especially for post-stall flow conditions, the wake dynamics around tapered swept wings is largely unexplored. It is still a challenge to understand how the wing geometry relates to the vortex formation for different aspect and taper ratios, as well as angles of attack and sweep. To design control strategies to improve aerodynamic performance for finite, swept, and tapered wings, we must go beyond the sole characterization of flow structures. In fact, the identification of perturbation dynamics is called for to modify the flow field.

Three-dimensional flow control is challenging due to the high-dimensional and nonlinear nature of the flow dynamics of the wakes. Thus, it is necessary to find an appropriate actuation setup for the problem that can alter the base flow behavior. This effort can be guided by modal analysis methods. In our work, we have used resolvent analysis, a method based on the singular value decomposition (SVD) of the resolvent, which is a linear operator constructed using the Navier–Stokes equations linearized with respect to the base flow. For

unsteady flows, the statistically converged time-averaged flow field is used as a base flow to construct the resolvent operator. The strength of the resolvent operator through this approach is the capability to find optimal forcing modes which amplify outputs in the flow field and give insights into the perturbed flow through the spatial response modes. The challenge within resolvent analysis is the SVD computation for large-scale resolvent operators that are generated for high-dimensional flow fields, such as three-dimensional and turbulent flows.

By taking advantage of low-rank approximation of the resolvent operator, recent developments using randomized numerical linear algebra have accelerated the computation of the dominant resolvent modes. With reduced computational costs, these efforts have enabled the use of resolvent analysis in turbulent flows over spanwise periodic airfoils and expanded its applicability to triglobal problems and higher Reynolds number flows. With the randomized algorithm, we can use resolvent analysis to uncover the dynamics of 3-D flows over finite, swept, and tapered wings, supporting flow control efforts to improve their overall aerodynamic performance.

The present study has shown how to develop a 3-D resolvent-based flow control over finite wings. We initiate by studying flows over finite wings and the effects of wing sweep and taper on the post-stall wake dynamics through direct numerical simulations (DNS). We consider laminar flows at chord-based Reynolds numbers of 400 and 600 with weak compressible effects at a freestream Mach number 0.1. The flows are studied around wings at angles of attack between 14° and 30° with semi aspect ratios ranging from 1 to 4, sweep angles up to 50°, and taper ratios from 0.27 to 1. Following a comprehensive characterization of the wake dynamics through DNS results, we extend our knowledge of the dynamics of flow perturbations by analyzing the triglobal resolvent modes. Through the identification of the optimal harmonic perturbations that can be amplified in the flow field, we develop 3-D active flow control that is shown to significantly modify the wake structures around the

wings. This comprehensive investigation provides novel and unique insights that reveal the flow structures that can be amplified in the wake and modify their dynamics in post-stall flow conditions.

The dissertation of Jean Hélder Marques Ribeiro is approved.

Jeffrey D. Eldredge

Ann R. Karagozian

Robert T. M'Closkey

Deanna M. Hunter

Kunihiko Taira, Committee Chair

University of California, Los Angeles

2023

To my wife Emille and all the people we love

TABLE OF CONTENTS

LIST OF FIGURES

LIST OF TABLES

ACKNOWLEDGMENTS

Obtaining a Ph.D. degree at one of the top universities in the world is a dream beyond any possibility I could ever imagine for my life. For this reason, I thank Prof. Kunihiko (Sam) Taira for having me in his group at UCLA. I also acknowledge the support from the US Air Force Office of Scientific Research (program manager: Dr. G. Abate, grant: FA9550-21-1-0174) and the US Army Research Office (program managers: Drs. M. J. Munson and R. Anthenien, grant: W911NF-21-1-0060). It is important to acknowledge the computational resources provided via these projects by the High Performance Computing Modernization Program at the US Department of Defense and the Texas Advanced Computing Center. I also acknowledge the support given by Mr. Kevin S. McAllister to our group in having access to these resources.

During this Ph.D. journey, some support was fundamental. I must acknowledge the crucial contribution of two past lab members, Calum S. Skene and Tulio R. Ricciardi, for all your help, discussions, and the many things you both have taught me over the years. It is no exaggeration to say that this dissertation would have never been completed the way it is without your help. In general, I can say that the lab atmosphere was very positive, in spite of some occasional tensions. The good work environment definitely helped me to move forward with my work and life in LA. I would like to thank the companionship of all current and past members of Prof. Taira's Lab: Muralikrishnan Gopalakrishnan Meena (I spelled your name without Google Search, man), Vedasri Godavarthi, Kai Fukami, Yonghong Zhong, Jonathan Tran, Luke Smith, Cheryl Lee, Anna Zhong, Vishal Anantharaman, Dylan House, Chi-An Yeh, Qiong Liu, Kai Zhang, Youngjae Kim, Hiroto Odaka, Laura-Victoria Rolandi, Alec Linot, and also Brener Ramos, whose help was fundamental when I moved to USA. I also want to thank the staff at UCLA, especially Amanda Gordillo that was always so nice and kind to me, and the CAPS resources. I have also many friends that helped me even if they were living almost 10,000 km away in Brazil. So I thank all my friends from Prof. William R. Wolf Lab that have helped in figuring out solutions for many technical problems I was

facing over the years.

I believe that coming from where I come from, not only in physical space but, most importantly, in social status, I've always felt a little bit out of place in LA (and USA, in general). Kind of like Will Smith in *The Fresh Prince of Bel-Air*, I felt that this place was not for me and often that I did not belong here. However, some people, really special ones, did not make me feel that way. Whenever I was around these people I always felt welcome and I always felt that I belong here. These people, I call my friends. And now that I am reaching the end of my time in LA, in some way I feel sad that this experience was so transient and maybe so short in my life, because I would love to keep them closer to me forever. Their friendship and support was extremely important to me all the way, so I would like to thank David Ren, Peter L. Wright, Diederik Beckers, Richard J. Abrantes, and also all my friends from the engineering Graduate Student Association: Vera Smirnova Kourtnik, Rajashree Bhattacharya, Swapnil Sayan Saha, Dona Jamie Leonard, Noor Nakhaei, Dylan Kupsh, Chris Yeung, Vikranth Jeyakumar, and many others. You were very supportive and cheerful all the time, I will always be missing you!

I would like to thank the love and support of all my friends and family from Brazil, but I apologize to the English-readers, as I will write to them in our mother language: *Agradeço a todos os meus amigos e a minha família por todo apoio que vocês me deram. Alguns bons amigos eu fiz aqui: Adriano Leão, Breno, Andréia Lírio, Dan Almeida, JP, Valéria, seus filhos e muitos outros. Espero vê-los em breve! Mas aos que estavam distantes, eu sinto a necessidade de pedir desculpas por ter estado tanto tempo longe. Foi um tempo muito difícil, especialmente com a COVID-19. Mas além disso, eu sei que perdi muitas coisas na vida de vocês durante esse tempo. Não pude ver seus filhos nascerem, crescerem, perdi seus casamentos, batizados, festas, aniversários. Não estive lá pra te dar um abraço quando seus entes queridos se foram. Eu senti saudades dos meus pais e da minha família a todo momento. Esse foi um custo emocional alto demais e eu não sei se teria forças para fazer isso de novo se soubesse o que me custou. Eu quero que saibam que o amor de vocês foi o que*

me deu forças para continuar, mesmo de tão longe. A gente sabe que é muito difícil vir de onde nós viemos e chegar aqui. Ainda mais numa época em que nossos governantes viravam as costas para a ciência. Mesmo assim, ainda era e é possível, não dava pra desistir. Com a fúria da beleza do Sol, essa conquista é por todos nós. A primavera vai chegar. Obrigado!

Lastly, I would like to thank my wife, Emille Andrade, for being a tremendous source of love and support over the years. No words are able to express all of my love, admiration, and how much I am thankful for having you with me. I don't know whether I would or not be able to do all this work without you, but I am 100% sure that, with you in my life, this whole thing was a much better experience. Thank you forever! I love you! Oh, and you, the reader, thank you very much for taking your time to read this dissertation! If you had to come here to search for something, it's probably because you are desperate about some details that you need to know. I wish you the best in solving your problems and I hope that this work helps you somehow.

VITA

2009–2010	Metrology Lab, Arcelor Mittal S. A., Contagem, MG, Brazil.
2010–2013	Formula SAE UFMG Student Team Member, Universidade Federal de Minas Gerais (UFMG), Belo Horizonte, MG, Brazil.
2011–2013	Lab Technician, Department of Physics and Aerospace, UFMG, Belo Horizonte, MG, Brazil.
2009–2014	B.Sc. in Mechanical Engineering, UFMG, Belo Horizonte, MG, Brazil.
2013–2015	Parts Department, Joy Global Inc., Belo Horizonte, MG, Brazil.
2015–2017	Graduate Researcher, Department of Energy, Universidade Estadual de Campinas (UNICAMP), Campinas, SP, Brazil.
2015–2017	M.Sc. in Mechanical Engineering, UNICAMP, Campinas, SP, Brazil.
2017–2018	Professor, Department of Engineering, UNA University Center, Belo Horizonte, MG, Brazil.
2018	Professor, Department of Mechanical and Aerospace Engineering, University FUMEC, Belo Horizonte, MG, Brazil.
Fall 2018	Graduate Researcher, Department of Mechanical Engineering, Florida State University, Tallahassee, FL, USA.
Fall 2020	Teaching Assistant, Department of Mechanical and Aerospace Engineering, University of California, Los Angeles, CA, USA.
2019–present	Graduate Researcher, Department of Mechanical and Aerospace Engineering, University of California, Los Angeles, CA, USA.

PUBLICATIONS

J. H. M. Ribeiro, C.-A. Yeh, and K. Taira, "Randomized resolvent analysis", Physical Review Fluids, 5(3), 033902, 2020.

J. H. M. Ribeiro, C.-A. Yeh, K. Zhang, and K. Taira, "Wing sweep effects on laminar separated flows", Journal of Fluid Mechanics, 950, A23.

J. H. M. Ribeiro, C.-A. Yeh, and K. Taira, "Triglobal resolvent analysis of swept-wing wakes", Journal of Fluid Mechanics, 954, A42.

J. H. M. Ribeiro, J. Neal, A. Burtsev, A. Amitay, V. Theofilis, and K. Taira, "Laminar post-stall wakes of tapered swept wings", *in review.*

J. H. M. Ribeiro and K. Taira, "Three-dimensional resolvent-based control of massively separated laminar flows around finite wings", *to be submitted*

CHAPTER 1

Introduction

We survey past studies on post-stall wakes and the effects of angle of attack, wing sweep, and taper at low Reynolds numbers. A brief description is also given for modal analysis methods with a detailed description of resolvent analysis and its application to guide flow control design. The motivation and outline of this thesis are provided.

1.1 A brief history of low-Reynolds-number flow separation

The post-stall wake dynamics around lifting devices has a critical importance to aircraft design [And10, And99, TC09]. Although the aeronautical engineering has traditionally focused on the study of turbulent and high-speed flows, over the last few decades, the study of low-speed and laminar flows has become increasingly attractive, especially in post-stall flow conditions. The first argument for the study of laminar separated flows is the characterization of the dynamics of flow separation in the absence of turbulence, enabling us to study the fundamental aspects of stalled flows. For turbulent flow regimes, even though the aerodynamic characterization of forces over the wing has been extensively explored, it remains a challenge to characterize post-stall flow structures in a global manner, as the stalled region exhibits highly complex nonlinear vortical interactions and spatiotemporal evolution [Van82]. For massively separated flows, however, although the Reynolds number, which is used to characterize a flow as turbulent or laminar, is important, it is not the most critical parameter. There are considerable similarities in the structure and organization of the large vortices observed in both laminar and turbulent separated flows over wings

[Wer56, WR56, Del01, Del13]. For this reason, insights obtained from water tunnel experiments in laminar (low-Reynolds-number) flow conditions were shown to be useful to study flow separation over commercial aircraft, helicopter rotor blades, and space launchers, which occur at turbulent flow regimes (high-Reynolds-number flows).

Another argument to study laminar flows over wings at high incidence is based on the recent engineering developments that have considerably expanded the range of possibilities in aircraft design. The evolution of computer science, electrical, manufacturing, and materials engineering, among others, have promoted a growing interest in low-Reynolds-number aerodynamics. Their main application is the development of micro aerial vehicles (MAV) and unmanned aerial vehicles (UAV). Those aircraft are designed to operate at a Reynolds number $\mathcal{O}(10^4)$, being remotely controlled, flying at high altitudes, and experiencing complex flow interactions between wake vortices, transition, and flow separation [PM00, Mue01, PB06]. An improvement in the aircraft design to operate at low-speed flow conditions can significantly impact many areas, such as environmental monitoring, rescue operations in complex environments, extraplanetary exploration missions, and many other critical problems.

Due to the scale effect, however, the design of MAVs and UAVs requires a distinct approach from that of high-speed aircraft [Lis83]. Even though the global flow structures may share similarities in both regimes, it is more challenging to generate lift in laminar flow conditions. Low-speed aeronautical design is often inspired by biological flight to operate in unsteady wing motion at high angles of attack [VSP04, LMS07]. However, early works on aeronautical engineering lack extensive results on low-Reynolds-number flows. Jacobs and Sherman [JS37], Schmitz [Sch41], and Marchman [Mar87] have attempted to study flows at Reynolds numbers at $\mathcal{O}(10^4)$ to provide insights on the mechanisms of flight used by birds and the design of model airplanes. Nonetheless, the sensitivity of wind tunnels and instruments available at that time harnessed the accuracy of the force measurements.

Accurate results published on research works prior to the 1970s were comprised of extensive wind tunnel experiments and analysis [Mil36, And36, SA40, Bla56, GC47, HM64,

MTS68]. These works focused in studying aerodynamic characteristics of wings that operate at high speeds, in post-stall angles of attack, exploring strategies to enhance lift-to-drag ratio, as well as the operation in transonic and supersonic flow conditions, among many others. Most of these works were released as technical reports from the National Advisory Committee for Aeronautics (NACA) and have provided many valuable insights that underpinned the development and design of early commercial and military aircraft.

In the 1970s and early 1980s, it became clear that engineers and scientists would need to study the organized flow motion that developed in the flow field in order to further improve aircraft design [BR74, WB80a, WBS80, Can81]. To this end, it was necessary to track the evolution and interaction of vortices in space and time, by reconstructing its overall structure in a 3-D manner [TP79, PT80, TP82]. Inspired by the singular points on differential equations [Poi82], theoretical approaches to 3-D flow separation were devised [Leg56, Lig63] based on the topology of skin friction lines and the idea of critical points that define flow separation. These approaches were further investigated in water tunnel experiments that demonstrated, through oil flow visualizations at the body surface, the formation of the separated flow region as predicted by theory [Wer56, WR56, Del01].

Initially, this was only possible using 2-D cut slices from water tunnel measurements experiments in a lower Reynolds number than that of the previous wind tunnel experiments [AL85, Wer71, HH85, HH86, Wer86]. By bringing the Reynolds numbers as low as $\mathcal{O}(10^3)$ and using novel methods for flow visualization it was possible to observe and study the 3-D formation of large vortices over wings [Fre85, Fre86, FFB86b, FFB86a, FFB87]. These efforts revealed that the key features of flow separation observed at higher Reynolds numbers were still present at such low-Reynolds-number flows and that it was possible to study them in the absence of the strong nonlinearities associated with turbulence.

This finding could, by itself, motivate the study of post-stall low-speed flows. This area become increasingly attractive as concurrent developments in other areas of engineering made it possible to design small- and micro-aerial vehicles [Mue01, PB06]. An example of

these devices is the mesicopter which is about the same size of a nickel. The design of such small-sized aircraft is aimed at autonomous flight applications, as well as operation at high angles of attack, high altitudes, and facing strong vortical interactions with the environment turbulence. Their unique design is distinct from traditional aircraft, enabling them to operate under such challenging flight conditions.

The technological boom in the 1990s expanded the range of possibilities for aerodynamics applications and promoted a surge of research works now focused not only on turbulent flows, but also on the laminar flow regime, as seen in figure 1.1. Aeronautics research was now aimed to study both low- and high-Reynolds number flows. Alongside experiments, numerical studies using computational fluid dynamics methods also became popular. Those took advantage of the improvements in computer engineering and numerical methods, deeply expanding our comprehension of the development, formation, and evolution of vortical structures. For turbulent flows, these works have explored flow separation [PMR90, LP96], noise generation and control [WM00, JSS10, WAL12, RWT22, DW22], dynamic stall, [RWY19, MWG22b, MWG22a, GV20, Vis12, VG19, HGV22], interaction with gust vortices [BVG15, GV15], among many other effects [MTP20, HTS22, LRW22]. There is further ongoing research dedicated to improving the current softwares and methods aiming to accurately capture the features associated with separation [GSK22, GBM22, TAT22].

In the past 30 years, experimental apparatus have also evolved, allowing studies with an in-depth characterization of wake dynamics [HWJ01, YSK09], tip vortices [GA91, DRL96, BLM04, Dur05, Giu13], as well as wings during unsteady maneuvers, such as surging [MMG15], rotation [LD09, JMS16], pitching [BS06, YR12], plunging and heaving [AB17], and flapping [BD01, DMN06]. Computational simulations of low-Reynolds number flows allowed us to understand how the aspect and taper ratios, angles of attack, and sweep can influence the wake characteristics [BFP01, HBV03, TC09, HVT15, RCO18, CCT10, ZHA20b, ZHA20a, ZT22, ZBH23, RYZ22b].

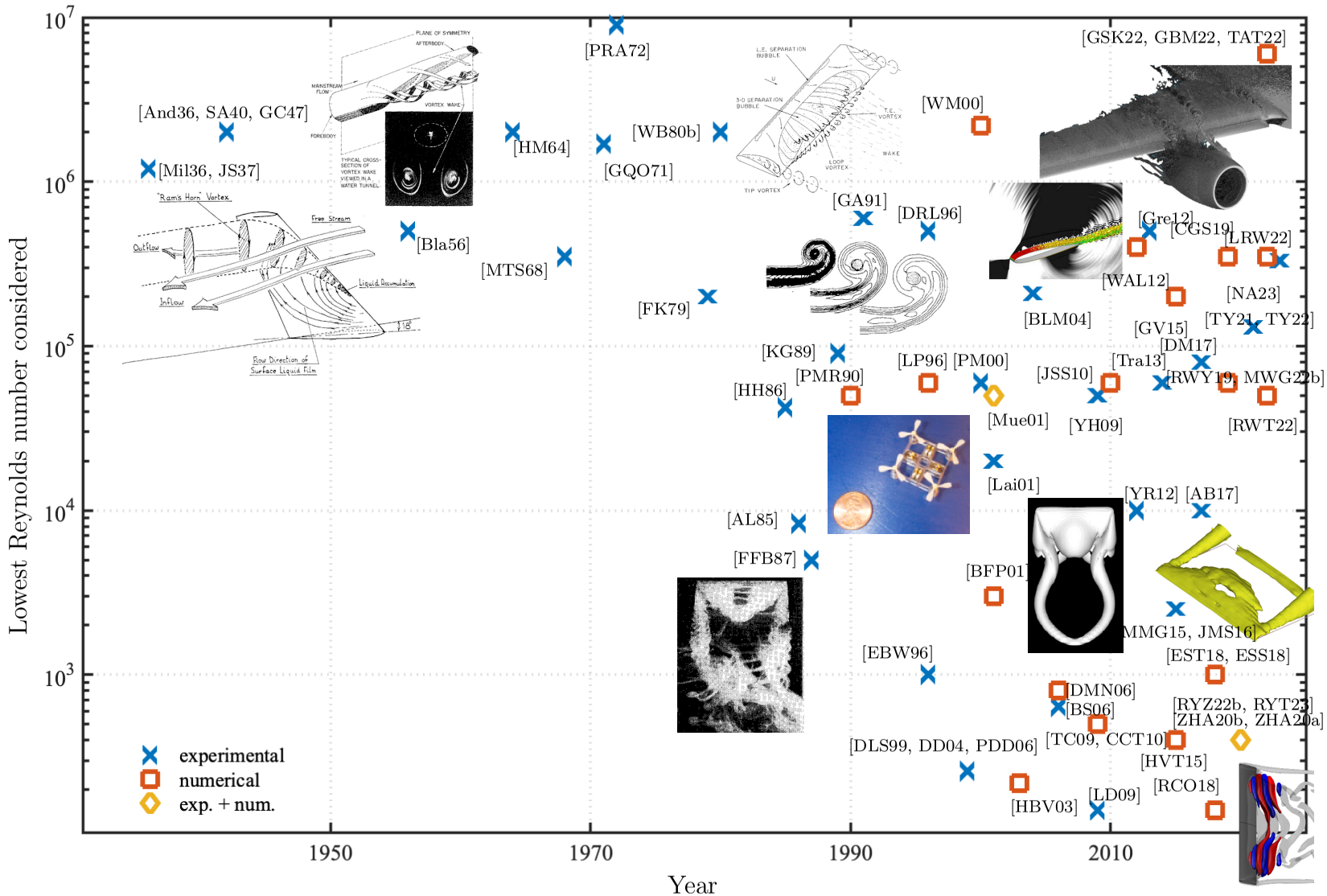

Figure 1.1: History of aeronautical research for flows over wings. Selected figures extracted from references.

These works have provided an abundance of high-quality well-resolved high-quality data in space and time which further called for proper post-processing methods to deepen our understanding of the flow field dynamics. Moreover, to design strategies to improve the aerodynamic performance of the wing, it became necessary to study the highly energetic oscillations, instabilities, and perturbations dynamics in the wake. We will discuss these methods in the next section, as we introduce modal analysis techniques [TBD17, THB20].

1.2 Modal analysis in a nutshell

One of the central questions in fluid dynamics is concerned with the evolution of perturbations. Gaining a detailed understanding of the perturbation dynamics from flow fields is a daunting task, due to the complex nonlinear dynamics that takes place over a range of spatial and temporal scales. To modify the global flow characteristics with a proper control strategy, it is necessary that the nonlinear interactions involving the actuation input (perturbation) become sufficiently large to alter the base flow. For flow control, we need not track all possible ways in which the actuation input can modify the flow, but instead, we can focus on the dominant directions in which the perturbation can be amplified in an efficient manner. This notion has led to the modal analysis-based approaches [HLB12, Sch10, TBD17, THB20], including the global stability analysis [The11] and the resolvent analysis [TTR93a].

1.2.1 Data-based methods

John L. Lumley was the first to introduce a data-based method to study coherent structures in fluid dynamics [Lum67, Lum70] with the proper orthogonal decomposition (POD), a second order statistics method to extract large energy-containing structures from turbulence. POD has since been widely applied in fluid dynamics as it can form an orthogonal basis for reduced-order modelling. Numerically, POD has been applied to study and model incompressible [AHL88] and compressible flows [Row02], being further extended to the basis

to adjoint solutions into the Balanced POD method [Row05]. Experimental data has also been studied using POD, applied to particle-image velocimetry data through the enstrophy norm [GLH06]. POD is based on the SVD of the data matrix, which can be expensive for large datasets of high-dimensional and turbulent flows. In general, a combination of block decomposition within the snapshot method allows POD to be employed to spot tonal noise related coherent structures in three-dimensional high-fidelity large-eddy simulations at high-Reynolds number flows and realistic aeronautical configurations of the turbulent flow over a landing gear [RW17, Rib17, RWS18]. In order to reduce uncoherent information in spatial modes and improve mode coupling, some authors employed the spectral POD method by Sieber, Paschereit, and Oberleithner [SPO16]. These efforts were further used to extend POD modes into machine learning models for turbulence [LW19].

Although similarities exist, POD does not describe the evolution of coherent structures extracted from data. To extract the dynamics, one must use the version of POD described by Towne, Schmidt, and Colonius [TSC18, STR18]. This method is also called Spectral POD and the modal decomposition is performed in a frequency domain correlation (instead of time). Another data-based method to evaluate coherent structures dynamics is the Dynamic Mode Decomposition (DMD) introduced by Peter J. Schmid [Sch10], which extracts modal structures from a low-dimensional evolution matrix, which can be derived from the second-order correlation matrix obtained from POD. The DMD modes can gather the less energetic but more unstable flow structures. There is a relation between the DMD modes as finite space representations of Koopman modes, used to investigate jets in crossflow [RMB09, TRL14]. Many extensions for DMD have been proposed such as DMD with control [PBK16] and multiresolution analysis [KFB16], among others. The overall cost of both data-based methods is dominated by the computation of the snapshot correlation matrix.

1.2.2 Operator-based methods

In fluid dynamics, we can take advantage of an *a priori* knowledge of the Navier–Stokes equations to model the flow dynamics. The Naviwe–Stokes equations are intrinsically nonlinear. We may, however, obtain important insights into the flow field via the linearized Navier–Stokes equations with respect to a predetermined base flow. The selection of the base flow is critical. For the linearized equations over a stable base flow solution, we may study the global linear stability of the flow, as shown in the works of Theofilis [The03, The11], which has been applied to investigate flows over wings in many configurations [HGP17, CGS19, NBJ19, PBD19, PDB21, BHH22, RJF22, NRL23].

In the presence of sustained perturbations or forcing inputs, the linear system response can be described by the transfer function from control theory. This linear analysis is greatly simplified when the input to the system is sinusoidal to reveal the gain and phase response of the system over a range of forcing frequencies. The transfer function that relates the system input to the output is called the resolvent and its analysis has been extended to fluid flows by Trefethen *et al.* [TTR93a]. The resolvent analysis is based on the pseudospectral analysis and has been used to study the transient energy growth [TTR93a] as well as the harmonic response of the system [JB05]. These initial studies of resolvent analysis were performed for stable laminar flows. In fact, linear stability and resolvent analyses are closely related [TTR93a, SH01].

An extension to resolvent analysis to study turbulent flows was proposed by Farrell and Ioannou [FI94] and McKeon and Sharma [MS10]. They considered the nonlinear advection term to be the self-sustained input to the linearized Navier–Stokes equations within the natural feedback loop of the fluid flow. This viewpoint has enabled the use of time-averaged base flows to reveal the input-output dynamics of turbulent flows. Moreover, discounting or finite-time horizon based extension of the resolvent analysis has enabled resolvent analysis to study flows with unstable base states [Jov04a, YT19]. As resolvent analysis can determine

the most amplified forcing and response directions, it serves as a powerful analytical tool to find effective active and passive flow control techniques [NFL17, YT19].

The resolvent analysis needs two key ingredients: (i) the base flow and (ii) the linearized Navier–Stokes operator. It is known that the accuracy of the base flow and the spatial discretization of the linear operators is critical for extracting response characteristics correctly [YT19]. The need for accurate discretization of the linearized Navier–Stokes operators calls for sufficient grid resolution and a suitable computational domain size. As such, the discrete resolvent operator becomes large with size $m \times m$. Here, m is essentially the number of variables times the size of the grid, which can easily be upward of $\mathcal{O}(10^6)$ for turbulent flows [KT17]. For resolvent analysis, the singular value decomposition (SVD) needs to be performed on the large resolvent operator requiring a taxing operation count of $\mathcal{O}(m^3)$. To use resolvent analysis for high Reynolds number flows, we must find a computational relief to perform SVD of the resolvent operator.

Although the resolvent analysis is performed on a very large matrix, only the leading forcing and response modes are generally sought. Based on the amount of necessary matrix data used to perform the analysis, the desired output is only a very small fraction of the input data size. For this reason, it would be natural to consider that all elements of the resolvent matrix are not necessary to determine the leading resolvent modes. Within the resolvent framework, the core of the computations lies with the SVD. In order to handle a large operator for SVD to find the leading modes, we can consider subsampling the matrix of interest and perform the SVD on the low-order representation of this large matrix. Randomized numerical linear algebra has recently emerged as an effective technique to reduce a large matrix to its low-order representation [HMT11a, DM16, TYU17], for applications including big data compression and data transfer. The key idea is to pass a randomly generated low-rank test matrix through the large matrix to obtain the so-called sketch of the full matrix. This sketch is low-rank but holds key information about the full matrix and can be used to derive appropriate bases to represent the full matrix in a low-dimensional manner

[CW09, WLR08, HMT11a, TYU17]. Randomized techniques can be incorporated into SVD to achieve tremendous computational and memory savings [WLR08, RST09, HMT11a].

In recent years, modal analyses are tackling flows over complex geometries and high-Reynolds number flows with increasingly large degrees of freedom [TBD17, THB20, JNJ16, STR18, DSN19, RW17, RWS18]. To further aid this endeavor, randomized SVD have been incorporated into data-based modal analysis techniques, including the proper orthogonal decomposition [RST09] and dynamic mode decomposition [EMK19]. For global operator-based analyses of high-Reynolds-number flows [JNJ16, STR18, DSN19], the leading singular values and modes can be determined with a significant reduction in computational costs with the aid of randomized techniques. The randomized technique presented in Chapter 2, Section 2.2, has shown tremendous potential to expand the applicability of the resolvent analysis to high-Reynolds number three-dimensional flows.

1.3 Motivation and contributions

Numerical simulations and experiments have extensively investigated flows over finite aspect ratio wings in laminar [EBW96, TC09, LD09, EJ19, ZHA20b] and turbulent flows [GV17, VG19]. When the analysis of finite wings incorporates the sweep angle to the wing design, the flow physics over the airfoil becomes increasingly more complex. Unique coherent structures can be formed over the wing and the additional spanwise flow advects LEVs over the span [EBW96, LD09, BRT12]. Under certain flow conditions, these coherent structures merge into the tip vortex leading to complex nonlinear interactions between vortical structures. Previous works have attempted to link wing geometry and flow parameters, such as angles of attack and sweep, as well as aspect and taper ratios, and the Reynolds number to aerodynamic forces and performance of the wing. However, many aspects on the dynamical behavior of the vortical structures in post-stall wake remain unexplored.

This work presents numerical experiments to obtain well-resolved spatiotemporal solu-

tions for the flow over finite swept and tapered wings. Once obtained, the well-resolved flow field data is analyzed to investigate the dynamics of the vortical structures, the interactions between vortices in the wake, and the growth of harmonic perturbations. With well-resolved spatiotemporal data, it is possible to obtain an accurate time-averaged flow solution. This solution is then used as a base flow to build the linear operator used within resolvent analysis. The modal behavior analyzed using these methods opens ways for the design of flow control strategies to enhance performance in aerodynamics and hydrodynamics [ESS18, SBH19, YT19, LSY21]. However, resolvent analysis is computationally expensive, particularly for high-dimensional flow fields. The onset of new methodologies, such as randomized resolvent by Ribeiro, Yeh and Taira [RYT20], has considerably reduced the computational costs for its application and allows us to pursue the analysis of three-dimensional global (triglobal) base flows. The main contributions of this work are listed as follows:

- We have developed the randomized resolvent analysis to large-scale problems. We have shown that the physics-based scaling of the random vectors considerably improves the accuracy of the resolvent modes computation.

- We have provided an extensive analysis of the wake characteristics of laminar separated flows over finite tapered and swept wings and revealed how wing taper and sweep influence the wake characteristics and aerodynamic performance of the wing.

- We have investigated the isolated effects of wing sweep on laminar separated flows and described how the strengthening of the swept-induced spanwise flow alters the perturbation dynamics and stabilizes wake oscillations.

- We performed a triglobal resolvent analysis on finite wings and reveal the dynamics of optimal perturbations and their relations to wing planform, angles of attack, and sweep. We have also revealed how the overlap of optimal inputs and outputs of the flow

field are associated with the self-sustained oscillations that appear over the separation bubble.

- Following the findings from triglobal resolvent analysis, we have developed a resolvent-based three-dimensional active flow control strategy that efficiently modifies the flow field. We have shown that the optimal forcing modes can be used as localized harmonic body forces. Moreover, this work describes the flow modifications that increase the overall lift and lift-to-drag ratio by reducing the volume of the laminar separation bubble. In addition, we have described the actuation modes that efficiently perturb the formation of the tip vortex and other characteristic structures around the wing.

The major outcome of the present thesis for the scientific community is the study of the dynamics of laminar separated flows over finite swept and tapered wings and the developments of the resolvent-based three-dimensional flow control over finite wings. Due to the vast usage of swept and tapered wing configurations in aeronautics and industrial applications, we believe that the outcome we provide herein is extremely valuable for future developments in aerodynamics and aircraft design.

1.4 Overview

The present work is organized as follows. We first present the methodology for the application of the randomized resolvent algorithm for the analysis of fluid flows in Chapter 2. In Chapter 3, present our comprehensive study of the fluid flows around finite wings, focusing on the effects of wing and taper in post-stall flow conditions. To isolate the effect of wing sweep, we conduct the analysis of flows over spanwise periodic swept wings, presented in Chapter 4, where we observe how sweep and the spanwise flow that forms within the stall region affect the wake structures and the evolution of flow perturbations. With a clear understanding of the effects of wing sweep on the separated wake dynamics, we move towards the global

study of flow perturbations using triglobal resolvent analysis in Chapter 5. Here, we will discuss the influence of wing geometry on wake perturbations and show how the overlap of forcing and response modes, named resolvent wavemaker, highlights the mechanisms that sustain wake shedding. The insights from triglobal resolvent analysis are then used to develop control strategies for finite wings, as shown in Chapter 6. We study how the control approach changes at different angles of attack, sweep, and taper ratios. The conclusions for the present work and a few suggestiong on future work are given in Chapter 7.

CHAPTER 2

Resolvent analysis

In this Chapter, we introduce the methodology to be used in the analysis of finite swept wings. In Section 1.2, we briefly introduced modal analysis methods, including the resolvent analysis. Here, we expand on the resolvent analysis, first introduced by Trefethen *et al.* [TTR93a] in the context of pseudospectra analysis for hydrodynamics. We define the model for resolvent analysis in Section 2.1 and later we cover the algorithm and methodology for the incorporation of randomized methods within the framework to obtain fast computation of resolvent modes in large and sparse operators. The randomized SVD algorithm described by Halko, Martinsson and Tropp [HMT11a] has been adopted in the one-dimensional resolvent analysis of turbulent channel flow by Moarref *et al.* [MST13b]. However, the details on the use and accuracy of the randomized techniques for large-scale resolvent analysis were omitted and the methodology for multi-dimensional turbulent base flows was not clear. The algorithm and examples were introduced by Ribeiro, Yeh and Taira [RYT20] and have enable the extension of the methodology into spanwise periodic flows over airfoils at much higher Reynolds numbers [YBT20] than it was possible with standard methods. Traditional methods to improve accuracy of randomized methods are discussed in 2.2.1. A physics-based technique to implement important sampling into the test matrix and take advantage of the gradients of the base flow to obtain randomized resolvent modes with higher accuracy is shown later in Section 2.3.3

2.1 Full resolvent analysis

Let us consider the flow state $\boldsymbol{q} \in \mathbb{R}^m$ as a sum of the time-invariant base state $\bar{\boldsymbol{q}}$ and the statistically stationary fluctuating component $\boldsymbol{q}'$. With this Reynolds decomposed flow variable and appropriate discretization, we can express the discrete Navier–Stokes equations as

$$\frac{\partial \boldsymbol{q}'}{\partial t} = \boldsymbol{L}_{\bar{\boldsymbol{q}}}\boldsymbol{q}' + \boldsymbol{f}', \tag{2.1}$$

where $\boldsymbol{L}_{\bar{\boldsymbol{q}}} \in \mathbb{R}^{m\times m}$ is the linearized Navier–Stokes operator about the base state $\bar{\boldsymbol{q}}$ and $\boldsymbol{f}'$ collects the nonlinear terms and the external forcing inputs. We gather the nonlinear terms as external forcing in the turbulent mean flow following the perspective of McKeon and Sharma [MS10], Farrel and Iouannou [FI94], and Schmid [Sch07]. For the traditional resolvent analysis, $\bar{\boldsymbol{q}}$ is chosen to be the stable laminar equilibrium state such that $\boldsymbol{f}'$ can be considered as the forcing input to the system with the nonlinear term neglected [JB05]. More recently, turbulent mean flows has been used for $\bar{\boldsymbol{q}}$ with $\boldsymbol{f}'$ representing the nonlinear terms as sustained forcing input within the natural feedback system [MS10].

We can consider the Fourier transform $[\boldsymbol{q}'(\boldsymbol{x},t), \boldsymbol{f}'(\boldsymbol{x},t)] = \int_{-\infty}^{\infty}[\hat{\boldsymbol{q}}_\omega(\boldsymbol{x}), \hat{\boldsymbol{f}}_\omega(\boldsymbol{x})]e^{-i\omega t}\mathrm{d}\omega$ and express the relationship between $\boldsymbol{q}'$ and $\boldsymbol{f}'$ in frequency space as

$$-i\omega\hat{\boldsymbol{q}}_\omega = \boldsymbol{L}_{\bar{\boldsymbol{q}}}\hat{\boldsymbol{q}}_\omega + \hat{\boldsymbol{f}}_\omega, \tag{2.2}$$

where ω is the frequency. Note that spatial Fourier transform can also be incorporated if directional homogeneity is present. For stable base flows, ω can be chosen to be real. To extend resolvent analysis to unstable base flows, we can consider the use of finite-time/discounted analysis [Jov04a, YT19] by choosing a complex frequency $\omega = \omega_r + i\beta$, where both ω_r and β are real and β discounts the modal growth rate of $\boldsymbol{L}_{\bar{\boldsymbol{q}}}$. The input-output relationship between $\hat{\boldsymbol{f}}$ and $\hat{\boldsymbol{q}}$ can be found from (2.2) as

$$\hat{\boldsymbol{q}}_\omega = \boldsymbol{A}\hat{\boldsymbol{f}}_\omega, \tag{2.3}$$

where

$$\boldsymbol{A} = [-i\omega \boldsymbol{I} - \boldsymbol{L}_{\bar{\boldsymbol{q}}}]^{-1} \in \mathbb{C}^{m \times m} \tag{2.4}$$

is referred to as the *r*esolvent operator [TTR93a, JB05, MS10]. It serves as a transfer function that amplifies (or attenuates) the harmonic forcing input $\hat{\boldsymbol{f}}_\omega$ and maps it to the response $\hat{\boldsymbol{q}}_\omega$. The goal of resolvent analysis is to identify the dominant directions along which $\hat{\boldsymbol{f}}_\omega$ can be most amplified through $\boldsymbol{A}$ to form the corresponding responses in $\hat{\boldsymbol{q}}_\omega$. This question is addressed by the SVD of

$$\boldsymbol{A} = \boldsymbol{U}\boldsymbol{\Sigma}\boldsymbol{V}^*, \tag{2.5}$$

where $\boldsymbol{V}^*$ denotes the Hermitian of $\boldsymbol{V}$. Resolvent analysis interprets left and right singular vectors $\boldsymbol{U} = [\hat{\boldsymbol{u}}_1, \hat{\boldsymbol{u}}_2, \ldots, \hat{\boldsymbol{u}}_m] \in \mathbb{C}^{m \times m}$ and $\boldsymbol{V} = [\hat{\boldsymbol{v}}_1, \hat{\boldsymbol{v}}_2, \ldots, \hat{\boldsymbol{v}}_m] \in \mathbb{C}^{m \times m}$ respectively as response modes and forcing modes, with the magnitude-ranked singular values $\boldsymbol{\Sigma} = \mathsf{diag}(\sigma_1, \sigma_2, \ldots, \sigma_m) \in \mathbb{R}^{m \times m}$ being the amplification (gain) for the corresponding forcing-response pair. For unstable base flows, it is important that a finite-time window is chosen with β larger than the highest growth rate such that the resolvent analysis reveals the input-output relationship on a shorter time scale than that of the base flow instability [Jov04a, YT19].

Performing the SVD of $\boldsymbol{A} \in \mathbb{C}^{m \times m}$ requires an theoretical operation count of $\mathcal{O}(m^3)$. In practice, some algorithms can reduce this operation count when only a few singular values are to be recovered, while still being computationally taxing for large m [MZ06]. Such cases are encountered in high-Reynolds number flows and bi/tri-global analysis settings. However, we note that many applications of resolvent analysis call only for the dominant forcing and response modes $[\hat{\boldsymbol{v}}_1, \hat{\boldsymbol{u}}_1]$ associated with the highest gain σ_1. This is appropriate when the first gain σ_1 is much larger than the rest of the gains $\sigma_{j>1}$ and shows a quick roll off. Such condition is related to non-normality of linear operator $\boldsymbol{L}_{\bar{\boldsymbol{q}}}$, which is encountered for flows with strong shear and separation [SH01].

When the contributions from the higher-order modes are neglected, it is referred to as the rank-1 assumption for which the flow response from forcing $\hat{\boldsymbol{f}}$ is approximated as

$\hat{\boldsymbol{q}} \approx \hat{\boldsymbol{u}}_1 \sigma_1 \langle \hat{\boldsymbol{v}}_1, \hat{\boldsymbol{f}} \rangle$, provided that $\sigma_1 \gg \sigma_2$ and $\hat{\boldsymbol{f}}$ has reasonable magnitude along $\hat{\boldsymbol{v}}_1$. For seeking only the dominant modal insights from resolvent analysis, we discuss a remedy for performing large-scale resolvent analysis [JNJ16, STR18] in a computationally tractable manner below.

2.2 Randomized resolvent analysis

For a flow that have dominant structures, we consider a low-rank representation of the resolvent operator $\boldsymbol{A}$. That is, instead of directly performing SVD of $\boldsymbol{A}$ and obtaining the leading-mode representation, we seek a low-rank representation of $\boldsymbol{A}$ and perform the SVD of the low-rank version of $\boldsymbol{A}$. We can consider finding an appropriate low-dimensional basis to project the large resolvent operator on a suitable subspace to derive the low-rank resolvent approximation.

The action of a full matrix on a vector should reveal some insights on which components are modified in the dominant directions. In the case of flow that can be described with the rank-1 approximation, there should be a low number of dominant directions. This very point can be taken advantage of through what is known as *s*ketching in numerical linear algebra. Sketching refers to a procedure in which a tall and skinny test matrix $\boldsymbol{\Omega} \in \mathbb{R}^{m \times k}$ (or $\mathbb{C}^{m \times k}$), where $k \ll m$, is passed through $\boldsymbol{A}$

$$\boldsymbol{Y} = \boldsymbol{A}\boldsymbol{\Omega}. \tag{2.6}$$

Here, matrix $\boldsymbol{Y} \in \mathbb{C}^{m \times k}$ is called the *s*ketch of the input matrix $\boldsymbol{A}$ [WLR08, HMT11a, TYU17]. The test matrix $\boldsymbol{\Omega}$ can be constructed using random values with Gaussian distribution [MRT11] and be weighted by any input matrix insight, as will be discussed in section 2.3.3 for a physics-inspired random test matrix. As the sketch holds the dominant influence of $\boldsymbol{A}$, we can consider orthonormalizing $\boldsymbol{Y}$ using a QR decomposition to form the orthonormal basis with $\boldsymbol{Q} \in \mathbb{C}^{m \times k}$ upon which we can project the full matrix $\boldsymbol{A}$ to derive its low-rank approximation. In this way, it is possible to approximate $\boldsymbol{A}$ for a rank $k \ll m$

as long as this approximation preserves the features of the leading modes.

Given this $\boldsymbol{Q}$, a low-rank approximation of $\boldsymbol{A}$ can be found as $\boldsymbol{A} \approx \boldsymbol{Q}\boldsymbol{Q}^*\boldsymbol{A}$ [HMT11a]. We can view this as a low-rank decomposition of $\boldsymbol{A} \approx \boldsymbol{Q}\boldsymbol{B}$, where $\boldsymbol{B} = \boldsymbol{Q}^*\boldsymbol{A} \in \mathbb{C}^{k\times m}$. It is this reduced matrix $\boldsymbol{B}$ upon which we can perform the SVD

$$\boldsymbol{B} = \tilde{\boldsymbol{U}}\boldsymbol{\Sigma}\boldsymbol{V}^* \tag{2.7}$$

Hence, as a low-rank approximation, we now have

$$\boldsymbol{A} \approx \boldsymbol{Q}\tilde{\boldsymbol{U}}\boldsymbol{\Sigma}\boldsymbol{V}^* \tag{2.8}$$

where we can consider $\boldsymbol{U} \approx \boldsymbol{Q}\tilde{\boldsymbol{U}}$. This process is the $r$andomized SVD [HMT11a], where the sketch $\boldsymbol{Y}$ was used to derive $\boldsymbol{Q}$. This approximation almost always satisfies $\|\boldsymbol{A} - \boldsymbol{Q}\boldsymbol{Q}^*\boldsymbol{A}\| \leq \left(1 + 9\sqrt{k+p}\sqrt{m}\right)\sigma_{k+1}$, where p is the oversampling parameter, which is applied to build an approximation of rank k while projecting the matrix $\boldsymbol{A}$ to the low-dimensional subspace with $(k+p)$ vectors. With this overall approach, the computational cost for SVD is reduced to $\mathcal{O}(mk^2)$ instead of $\mathcal{O}(m^3)$ for the full SVD. In our implementation, we use $\boldsymbol{v}_1$ from (2.8) and retrieve the leading singular value and left singular vector through

$$\boldsymbol{A}\hat{\boldsymbol{v}}_1 = \hat{\boldsymbol{u}}_1\sigma_1. \tag{2.9}$$

The singular value and vector can be separated by noticing that $\|\hat{\boldsymbol{u}}_1\| = 1$. For resolvent analysis, the last equation provides more accurate leading singular value σ_1 and left singular vector $\hat{\boldsymbol{u}}_1$ compared to the original randomized SVD algorithm by Halko *et al.* [HMT11a]. The same operation can be used to recover the higher-order modes, with better accuracy than using the original algorithm [HMT11a]. For applications where high-order modes and orthogonality are desired, we can solve for $\boldsymbol{U}\boldsymbol{\Sigma}$ and compute its SVD. In the present randomized resolvent analysis, we emphasize that only the discrete linear operator $\boldsymbol{L}_{\bar{\boldsymbol{q}}}$ is needed for sketching $\boldsymbol{Y}$ and to find the reduced matrix $\boldsymbol{B}$. Unlike the original resolvent method, matrix linear solvers are used to avoid calling for the inverse within the resolvent operator. The

resulting algorithm constitutes the *r*andomized resolvent analysis summarized in Algorithm 1.

To utilize the randomized SVD for resolvent analysis, we must be aware that the resolvent operator $\boldsymbol{A} = [-i\omega\boldsymbol{I} - \boldsymbol{L}_{\bar{\boldsymbol{q}}}]^{-1}$ contains an inverse operation in its definition, which need not be numerically performed. We do not intend to perform an inverse operation within $\boldsymbol{A}$ in the present work. In the full resolvent analysis, when the matrices become too large and the inverse can not be performed (which is likely the case for 2D and 3D problems), one can focus on modes corresponding to the smallest singular values of $\boldsymbol{A}^{-1}$ to find those for the largest singular values of $\boldsymbol{A}$. Similar approaches have avoided the inverse computation, including the work by Jeun, Nichols and Jovanović [JNJ16].

Both full resolvent and randomized resolvent analyses are shown schematically in figure 2.1. Notice that we are not interested in all singular values and vectors of $[-i\omega\boldsymbol{I} - \boldsymbol{L}_{\bar{\boldsymbol{q}}}]^{-1}$, but only in a few subset of the largest σ_j and their corresponding $\hat{\boldsymbol{u}}_j$ and $\hat{\boldsymbol{v}}_j$. In the randomized resolvent analysis, we can approximate a low-rank representation of it using $[-i\omega\boldsymbol{I} - \boldsymbol{L}_{\bar{\boldsymbol{q}}}]$. Figure 2.1 shows an adaptation of the procedure from Halko *et al.* [HMT11a] in order to compute the largest singular values of the resolvent without performing its inverse. In the randomized resolvent analysis, we solve a linear system with $[-i\omega\boldsymbol{I} - \boldsymbol{L}_{\bar{\boldsymbol{q}}}]$, the columns of the random matrix $\boldsymbol{\Omega}$ form the right-hand side and the sketch columns of $\boldsymbol{Y}$ are the unknowns. By doing so, we sketch $[-i\omega - \boldsymbol{L}_{\bar{\boldsymbol{q}}}]^{-1}$ without finding the actual inverse matrix. The same procedure is performed to project the matrix to the low-dimensional subspace. The matrices are re-arranged in a way that the projection is performed using $[-i\omega\boldsymbol{I} - \boldsymbol{L}_{\bar{\boldsymbol{q}}}]$, but results in the low-dimensional projection of $[-i\omega - \boldsymbol{L}_{\bar{\boldsymbol{q}}}]^{-1}$ instead. Figure 2.1 also illustrates the procedures for recovering the left singular vectors and the singular values from the original algorithm [HMT11a] and from the present implementation.

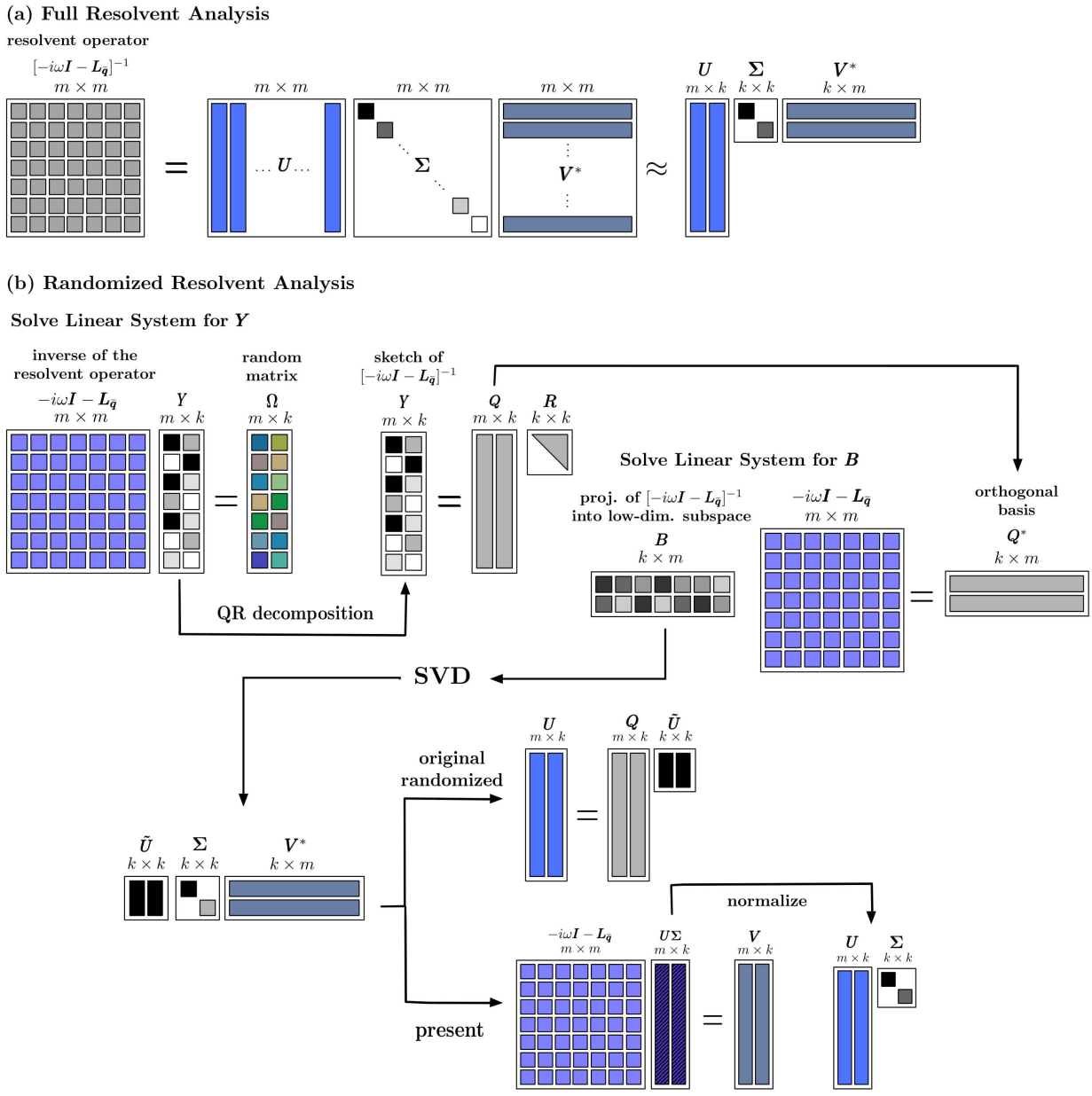

Figure 2.1: Schematics of the (a) full resolvent and (b) randomized resolvent analyses. For the full resolvent analysis, a direct SVD is applied. For the randomized resolvent analysis, the orthogonal basis $\boldsymbol{Q}$ is computed to project the operator into the low-dimensional subspace, where the SVD is performed on the reduced matrix $\boldsymbol{B}$. Two options to recover the left singular vectors and singular values are provided, using the original randomized approach [HMT11a] and the present implementation. Orthogonal vectors are represented by long bars.

Algorithm 1: Randomized Resolvent Analysis

Require: Discrete linear operator $\boldsymbol{L}_{\bar{\boldsymbol{q}}} \in \mathbb{C}^{m \times m}$

Function `randomized_resolvent(`ω`,`k`):`

$\boldsymbol{\Omega} \leftarrow$ `randn(`m`,`k`)` `// Random normal matrix generator. For scaling, see Section 2.3.3`

$\boldsymbol{Y} \leftarrow [-i\omega\boldsymbol{I} - \boldsymbol{L}_{\bar{\boldsymbol{q}}}] \backslash \boldsymbol{\Omega}$ `// Solve linear system for` $\boldsymbol{Y}$`,` $\mathcal{O}(m^2k)$

$(\boldsymbol{Q}, \sim) \leftarrow$ `qr(`$\boldsymbol{Y}$`,0)` `// Economy-sized QR decomposition,` $\mathcal{O}(mk^2)$

$\boldsymbol{B} \leftarrow \boldsymbol{Q}^* / [-i\omega\boldsymbol{I} - \boldsymbol{L}_{\bar{\boldsymbol{q}}}]$ `// Solve linear system for` $\boldsymbol{B}$`,` $\mathcal{O}(m^2k)$

$(\sim, \sim, \boldsymbol{V}) \leftarrow$ `svd(`$\boldsymbol{B}$`,'econ')` `// Reduced SVD decomposition,` $\mathcal{O}(mk^2)$

$\boldsymbol{U}^{\boldsymbol{\Sigma}} \leftarrow [-i\omega\boldsymbol{I} - \boldsymbol{L}_{\bar{\boldsymbol{q}}}] \backslash \boldsymbol{V}$ `// solve linear system to recover` $\boldsymbol{U\Sigma}$`,` $\mathcal{O}(m^2k)$

for $j \leftarrow 1$ *to* k **do**

  $\boldsymbol{\Sigma}_{j,j} \leftarrow$ `norm(`$\boldsymbol{U}^{\boldsymbol{\Sigma}}_{1:m,j}, 2$`)` `// Recover singular values` $\boldsymbol{\Sigma}$

  $\boldsymbol{U}_{1:m,j} \leftarrow \boldsymbol{U}^{\boldsymbol{\Sigma}}_{1:m,j} / \boldsymbol{\Sigma}_{j,j}$ `// Normalize` $\boldsymbol{U}$

end

$(\boldsymbol{U}, \boldsymbol{\Sigma}, \tilde{\boldsymbol{V}}) \leftarrow$ `svd(`$\boldsymbol{U}^{\boldsymbol{\Sigma}}$`,'econ')` `// (Optional) Recover` $\boldsymbol{U}$ `and` $\boldsymbol{\Sigma}$`,` $\mathcal{O}(mk^2)$

$\boldsymbol{V} \leftarrow \boldsymbol{V}\tilde{\boldsymbol{V}}$ `// (Optional) Recover improved` $\boldsymbol{V}$`,` $\mathcal{O}(mk)$

return $(\boldsymbol{U}, \boldsymbol{\Sigma}, \boldsymbol{V})$

2.2.1 Oversampling and power iteration schemes

Randomized algorithms can incorporate two additional procedures to improve performance and accuracy. Namely, they are oversampling [EVB19] and power or subspace iterations [RST09, HMT11a, Gu15]. Oversampling sketches the input matrix using $(k + p)$ vectors (with p extra vectors) and increases the low-dimensional subspace to accurately recover a smaller quantity of singular values k. For the randomized resolvent analysis, oversampling has the same outcome, in practice, of selecting a larger k and the influence of k will be discussed at the end of section 2.3.1. When k becomes large, it should be noticed that the memory consumption increases. Even for large sparse matrices, the sketch matrix and the subsequently reduced matrices that are formed are generally dense, which adds a computational burden.

The second procedure is the power or subspace iterations. These methods are a powerful tool when the singular values of the matrix decay slowly. For example, this type of spectral behavior appeared in the input-output analysis performed by Jeun *et al.* [JNJ16] for jet flows. The method consists of performing additional iterations after the sketch $\boldsymbol{Y}$ is evaluated. It should however be realized that such procedure calls for additional linear solvers, which is the most time consuming operation in Algorithm 1. For power iterations, one must compute the adjoint $\boldsymbol{A}\boldsymbol{A}^*$, where $\boldsymbol{A}^*$ is the Hermitian of $\boldsymbol{A}$, q times and solve the linear system k times. For subspace iterations, additional QR decompositions are necessary, and the number of additional linear systems to be solved will be q times k. In practice, small values of q improves the accuracy of the results substantially. More information on the general applicability of the subspace and power iterations are discussed by Halko *et al.* [HMT11a] and Erichson *et al.* [EVB19]. In section 2.3.3, we present another option for improving accuracy of the overall technique in a computationally inexpensive manner by constructing a physics-informed random test matrix $\boldsymbol{\Omega}$.

2.2.2 Test matrix $\mathbf{\Omega}$

The standard choice for the test matrix $\mathbf{\Omega}$ is the random matrix generated with a normal distributions. Such matrix is known to present excellent performance and accuracy [TYU17]. For some cases, especially for very large matrices or when the singular values present slow decay, larger values of k may be necessary to better approximate the matrix in the low-dimensional subspace. When large values of k are used, orthonormalization of the columns of the test matrix can be considered to improve numerical stability [DDH07, HMT11a]. The test matrix can also be generated using a Rademacher distribution [CW09]. It is also possible to build an ultrasparse matrix with Rademacher distribution in the non-sparse entries which allows for the control of cost, stability and reliability in the operations [TYU17, CW09].

When randomized SVD is applied, there is no a priori knowledge of the structure of the matrix. However, in the present application, we know how the resolvent operator is constructed. This theoretical insight can be used to build a random test matrix that outperforms the standard normal distribution matrix. We later propose a physics-informed test matrix $\mathbf{\Omega}$ that can focus our sketching operation for regions of physical importance. In our application, the dominant directions are related to regions with the presence of high shear. The results from this approach will be discussed in Chapter 2, Section 2.3.3. In this way, we have presented the method to be applied to analyze the physics of swept airfoil configurations. In the next section, we will clearly state the motivation and goals of the present project.

We demonstrate the use of randomized resolvent analysis on turbulent flow over a NACA 0012 airfoil. In this example, the randomized resolvent analysis will be applied a resolvent operator of size $m \times m$, where $m \simeq 7 \times 10^5$, to reveal the dominant gain and modal structures with a thin sketching matrix having as little as $k = 10$ columns. The convergence of the gain and resolvent modes will also be reported with respect to the size of the sketching matrix. Influence of the ratio between the first and the second singular values of the resolvent operator

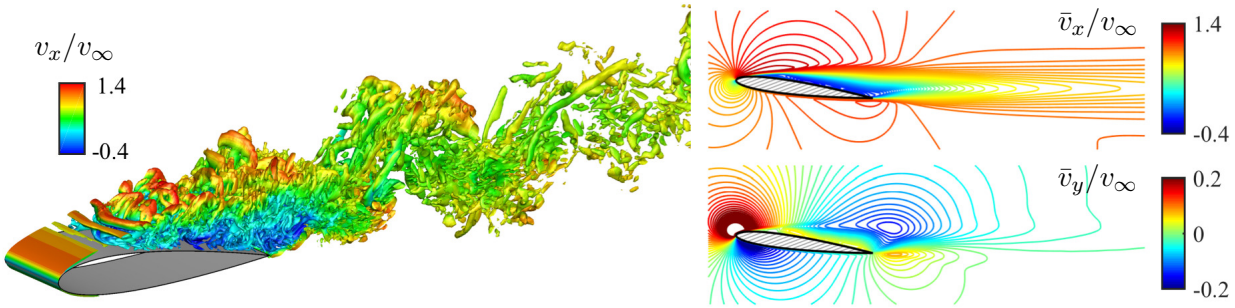

Figure 2.2: The instantaneous (left) and time/spanwise-averaged (right) flows over a NACA 0012 airfoil at $Re_{L_c} = 23,000$. The instantaneous flow visualization shows the isosurface of Q-Criterion ($QL_c^2/v_\infty^2 = 50$) colored by the instantaneous streamwise velocity.

will also be examined.

2.3 Example: Randomized resolvent of turbulent post-stall flows

We consider the spanwise-periodic turbulent flow over a NACA 0012 airfoil at an angle of attack of 9°, a chord-based Reynolds number of $Re_{L_c} \equiv v_\infty L_c/\nu_\infty = 23,000$ and a free stream Mach number of $M_\infty \equiv v_\infty/a_\infty = 0.3$. Here, v_∞ is the free-stream velocity, L_c is the chord length, a_∞ is the free-stream sonic speed, and ν_∞ is the kinematic viscosity. The time- and spanwise-averaged turbulent flow is considered as the base flow for the full and randomized resolvent analyses. For this 2D base flow, we adopt the bi-global setting that decomposes $\boldsymbol{q}'$ into spanwise Fourier modes with the wavenumber k_z.

To obtain the base flow, large-eddy simulation (LES) is performed using a finite-volume compressible flow solver *CharLES* [KHN11, BHN17a], which is second-order accurate in space and third-order accurate in time. Vremen's sub-grid scale model [Vre04] is utilized in the LES. The LES is performed on a C-shaped mesh with the domain extent of $x/L_c \in [-19, 26]$, $y/L_c \in [-20, 20]$ and $z/L_c \in [-0.1, 0.1]$ in the streamwise, transverse and spanwise

direction, respectively, with the airfoil leading edge at $x/L_c = y/L_c = 0$. Dirichlet boundary condition is specified at the far-field boundary as $(\rho, v_x, v_y, v_z, T) = (\rho_\infty, v_\infty, 0, 0, T_\infty)$, where ρ is the density, v_x, v_y and v_z are respectively the streamwise, transverse and spanwise velocity, and T is the temperature. Over the airfoil, the no-slip adiabatic boundary condition is prescribed. Along the outlet boundary, a sponge layer [Fre97] is applied with a running-averaged state being the target state. The simulation has been validated with respect to the time-averaged pressure, lift and drag over the airfoil. The turbulent separated flow over the airfoil is visualized in figure 2.2. The visualization of the instantaneous flow shows the laminar separation from the leading edge. We have found that the shear layer physics dominates the pseudospectral behavior of the linearized Navier–Stokes operator, as shear is the main source of nonnormality in the operator. Further details regarding the computational setup, flow physics, and resolvent analysis based flow control of this setup are reported in Yeh and Taira [YT19].

The full and randomized resolvent analyses are performed on a separate mesh from that used in the LES. This mesh has a 2D rectangular domain with the extent of $x/L_c \in [-15, 16]$ and $y/L_c \in [-12, 12]$, comprising approximately 0.15 million cells. Compared to the LES mesh, the mesh for resolvent analysis is coarser over the airfoil and in the wake, but is much finer in the upstream of the airfoil in order to resolve the forcing mode structures. The time- and spanwise-averaged flow $\bar{\boldsymbol{q}}$ obtained from LES is interpolated onto this mesh. At the far-field boundary and over the airfoil, Dirichlet conditions are set for density and velocities and Neumann condition is prescribed for pressure in $\boldsymbol{q}'$. At the outlet boundary, Neumann condition is set for all flow variables. With these boundary conditions for $\boldsymbol{q}'$ and the base flow $\bar{\boldsymbol{q}}$, we construct the linearized Navier–Stokes operator $\boldsymbol{L}_{\bar{\boldsymbol{q}}}(k_z)$ for a chosen k_z. The size of $\boldsymbol{L}_{\bar{\boldsymbol{q}}}$ and the resolvent operator is approximately 0.75 million $\times$ 0.75 million.

For this large operator, we summarize in Table 2.1 the computational costs of performing resolvent analysis using the Krylov-based Arnoldi-iteration method with a range of parameter setups (i.e., number of singular values (n_{ev}), Krylov subspace dimension ($\dim(\mathcal{S})$), and

tolerance) and compare them with those for the present randomized algorithm. The former was conducted by simply calling the svds command in MATLAB. It requires almost 80 gigabytes of memory and takes approximately 30 to 70 minutes (single-core) for each SVD. The high-memory demand necessitates the use of high performance computing resource to conduct the full resolvent analysis. In contrast, the randomized resolvent approach (Algorithm 1) achieves significant reductions in computational time and memory consumption. The present method only requires a third of the memory usage of the Arnoldi-iteration and cuts down the computational time by an order of magnitude. We also note that, in Algorithm 1, the linear systems solvers are the operations with higher computational cost. Since all the three linear systems solvers are conducted for the same operator, the LU decomposition of $[-i\omega \boldsymbol{I} - \boldsymbol{L}_{\bar{\boldsymbol{q}}}]$ is performed in the beginning of the algorithm and is passed through the three solvers. This decomposition becomes the main source of the memory consumption.

2.3.1 Results

We perform the full and randomized resolvent analyses for spanwise wavenumbers of $k_z L_c = 0$ and 20π. Since the base flow is found to be unstable [YT19], the finite-time approach is adopted with $v_\infty/\beta L_c = 3$ to ensure that the resolvent analysis is performed on a shorter time scale than that associated with the leading growth rate of the instability. Initially, for the randomized analysis, we consider $k = 10$ for the width of the test matrix $\boldsymbol{\Omega}$ with random Gaussian distribution. Later in Section 2.3.3, we show that this value of k can be further reduced without compromising accuracy.

The leading response and forcing modes obtained from both full and randomized analyses are compared in figure 2.3 for representative frequencies St and spanwise wavelength $k_z L_c$. Although $k/m = 1.3 \times 10^{-5}$, we observe excellent agreement between the modes from the full resolvent analysis and the randomized algorithm. We observe that randomized forcing and response modes are very similar to full resolvent ones. Only at $St = 1$ and $k_z L_c = 20\pi$ we observe the appearance of spatially distributed errors in the background, which we refer

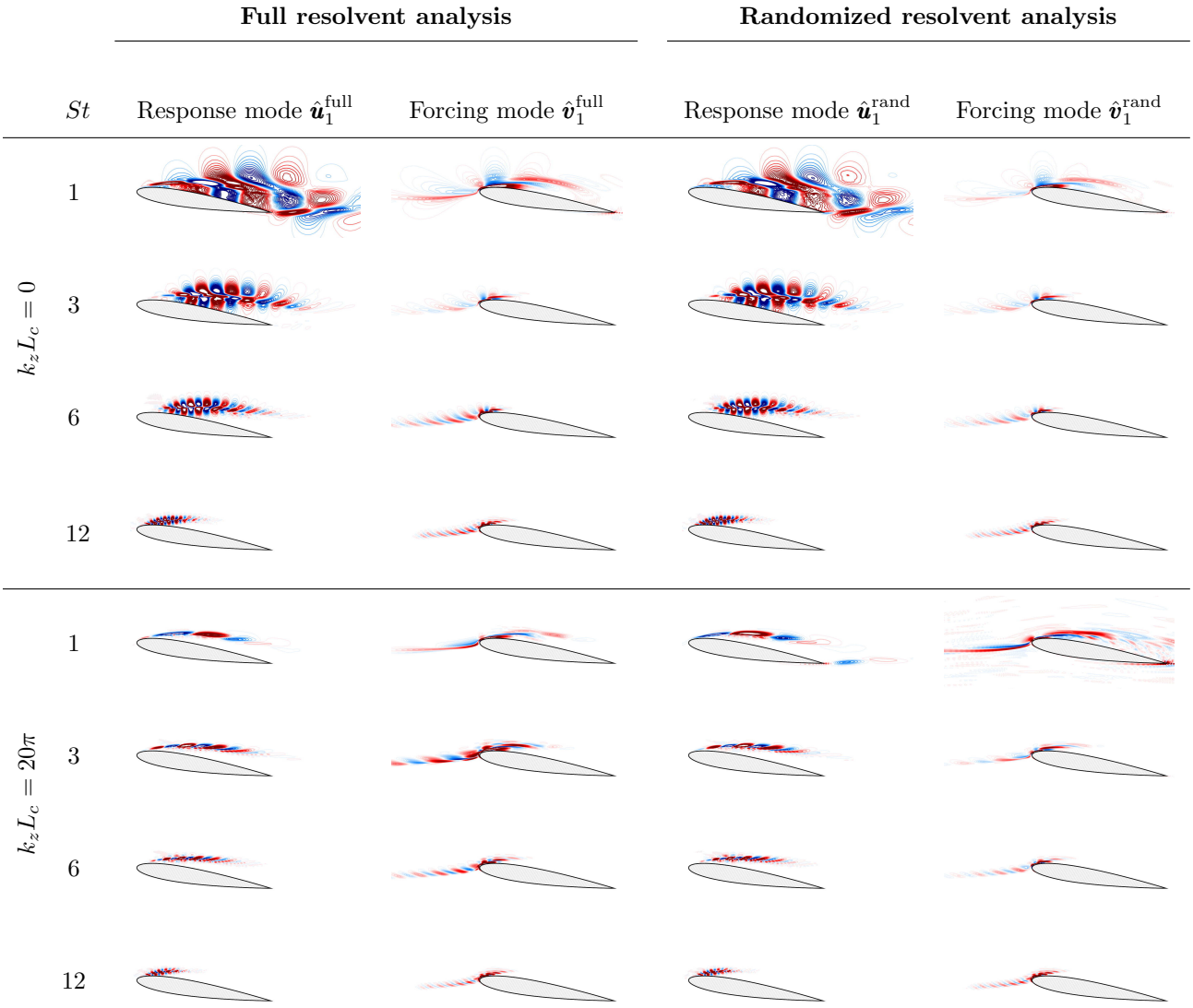

Figure 2.3: The leading response ($\hat{\boldsymbol{u}}_1$) and forcing ($\hat{\boldsymbol{v}}_1$) modes from the full and randomized resolvent analyses, using Algorithm 1, for $k_z L_c = 0$ and 20π at representative frequencies St. Modes are visualized with the streamwise velocity component with contour levels of $[-0.6, 0.6]$.

Iteratively restarted Arnoldi method (MATLAB svds)

n_{ev}	$\dim(\mathcal{S})$	tolerance	time (sec)	memory
10	30	1E-14	4185	78.6 GB
5	15	1E-14	2764	78.6 GB
2	6	1E-14	1486	78.6 GB
10	30	1E-05	2245	78.6 GB
10	15	1E-14	4194	78.6 GB

Randomized resolvent (present)

n_{ev}	k	time (sec)	memory
2	2	354	28.2 GB
5	5	462	28.4 GB
10	10	615	28.8 GB

Table 2.1: Comparison of the computational time and memory consumption for the implicitly restarted Arnoldi iteration (svds in MATLAB) with the present randomized approach for different parameter setups with the number of singular values (n_{ev}), Krylov subspace dimension ($\dim(\mathcal{S})$), and tolerance.

to as background noise.

The forcing modes are recovered directly from the SVD of the low-dimensional subspace projection. As they are used to recover the response modes using the linear operator, the accuracy of the forcing modes affect the results of the response ones. In the particular case of $St = 1$ and $k_z L_c = 20\pi$, when forcing mode is affected by noise, the randomized approach returns some structures emanating from the trailing edge in the response mode $\hat{\boldsymbol{u}}_1^{\text{rand}}$, which was not present from the full resolvent analysis. This behavior is related to leakage from high-order modes, as σ_1 and σ_2 are close in the energy spectrum. This remarkable level of agreement over all frequencies and spanwise wavenumbers ensures that the randomized

approach presented in Algorithm 1 can help extract insights into the spatial structures to identify regions of sensitivity and guide flow control efforts.

These results were obtained using the present implementation that extends the original randomized SVD algorithm. In figure 2.4, using the original randomized algorithm [HMT11a] within the resolvent analysis to recover the left singular vectors and singular values, the response modes contain background noise. Here, we use Algorithm 1 up to line 5, then SVD is performed as $\boldsymbol{B} = \tilde{\boldsymbol{U}}\boldsymbol{\Sigma}\boldsymbol{V}^*$ and $\boldsymbol{U}$ is recovered a posteriori using the original procedure for the randomized SVD with the resolvent analysis [HMT11a, MST13b], by $\boldsymbol{U} = \boldsymbol{Q}\tilde{\boldsymbol{U}}$. [YT19] showed that the present problem setup presents a peak in the singular values near $St = 6$ for both spanwise wavenumbers, influenced by the eigenmodes associated with the shear-layer structure over the separation bubble. These eigenmodes are highly nonnormal and induce high-energy amplification through pseudoresonance [TTR93a]. For the frequencies in a narrow region near $St = 6$, both implementations present similar results. Far from this band, the response modes obtained by the original procedure [HMT11a] are contaminated by random background noise or leakage from higher-order modes, as shown in figure 2.4 for $St = 0.5$ and 15 and $k_z L_c = 0$. In these critical cases, the original randomized approach may not provide meaningful insights into flow physics. The present implementation shown in Algorithm 1 improves solving for the response modes. Algorithm 1 does not enhance the forcing modes, as they are already accurate. When utilizing this technique to generate reduced-order models, one may perform steps 11 and 12 in Algorithm 1 to orthogonalize the left singular vectors. Considering the results obtained by our implementation, the modes are found very accurately for almost all frequencies and wavenumbers. To provide a concrete assessment, we quantitatively assess the accuracy of the randomized resolvent analysis.

The agreement between the full and randomized analyses with respect to the gain (leading singular value) and modes over a range of frequencies is presented in figure 2.5. When Algorithm 1 is applied to recover left singular vectors and singular values, the randomized analysis accurately captures the trend of gain distribution over $1 \lesssim St \lesssim 15$ in figure 2.5(a,b)

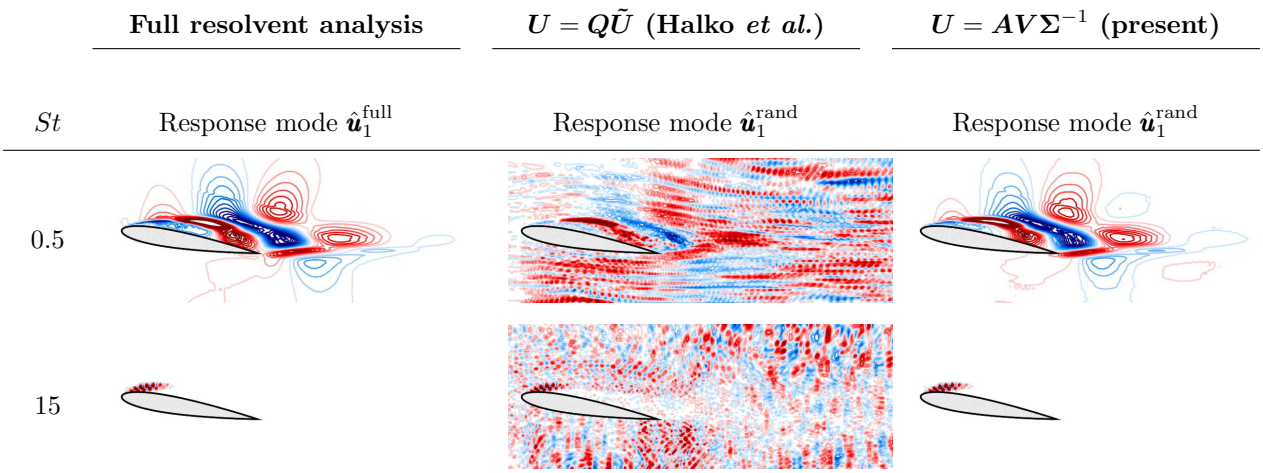

Figure 2.4: Comparison of the leading response modes ($\hat{\boldsymbol{u}}_1$) recovered from the randomized resolvent analyses using $\boldsymbol{U} = \boldsymbol{Q}\tilde{\boldsymbol{U}}$ (the original approach in [HMT11a]) and $\boldsymbol{U} = \boldsymbol{AV\Sigma}^{-1}$ (present, see equation (2.9)). The response modes from the full analysis are also shown for reference. Results are shown for $k_z L_c = 0$ at representative frequencies St. Modes are visualized with the streamwise velocity component with contour levels of $[-0.6, 0.6]$.

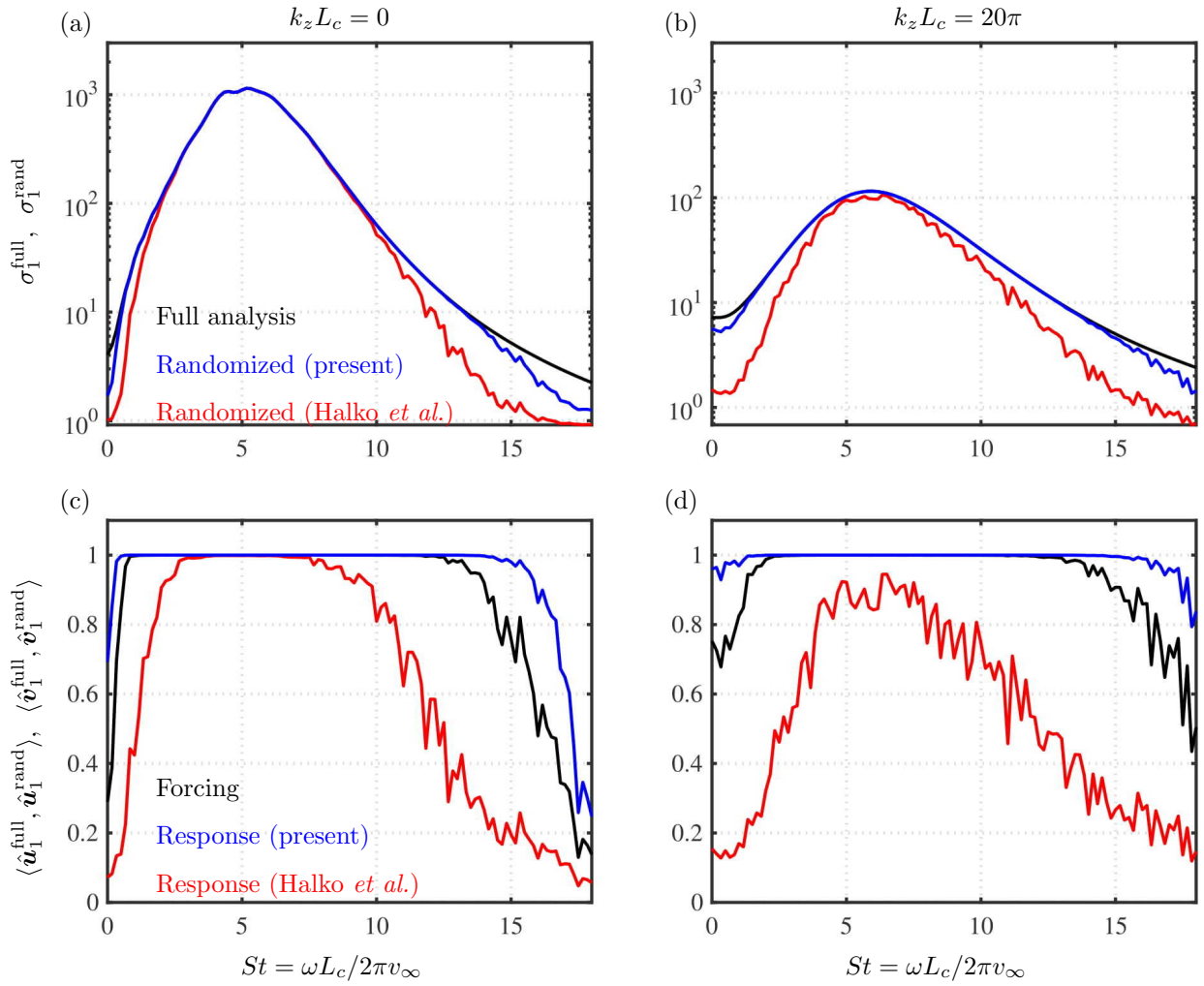

Figure 2.5: (a,b) The leading amplification for the full and randomized resolvent analyses. (c-d) Cosine similarities for the leading response $\langle \hat{\boldsymbol{u}}_1^{\text{full}}, \hat{\boldsymbol{u}}_1^{\text{rand}} \rangle$ and forcing $\langle \hat{\boldsymbol{v}}_1^{\text{full}}, \hat{\boldsymbol{v}}_1^{\text{rand}} \rangle$ modes. Improvements of accuracy in the present randomized analysis can be observed by comparing the σ_1^{rand} and $\hat{\boldsymbol{u}}_1^{\text{rand}}$ recovered from equation (2.9) to those from the original approach of [HMT11a] (note that forcing modes obtained from both approaches are identical). Results for spanwise wavenumber of $k_z L_c = 0$ and 20π are shown in the left and right columns, respectively.

for both wavenumbers. At the low and high-frequency ends, the gain shows deviations. The resemblance of the modal structure is quantified in figure 2.5(c,d) with the cosine similarities, i.e., the inner products, $\langle \hat{\boldsymbol{u}}_1^{\text{full}}, \hat{\boldsymbol{u}}_1^{\text{rand}} \rangle$ and $\langle \hat{\boldsymbol{v}}_1^{\text{full}}, \hat{\boldsymbol{v}}_1^{\text{rand}} \rangle$. As singular vectors are normalized, the cosine similarity of 1 suggests that perfect match is attained between the modes from full and randomized resolvent analyses. Since these modes are complex, the cosine similarity removes dependence on the phase difference. For almost the entire range of frequencies the cosine similarities are near unity, which means the agreement between full and randomized modes is excellent. When this value is reduced, the modes may be affected by noise, as seen for $\hat{\boldsymbol{v}}_1^{\text{rand}}$ at $St = 1$ and $k_z L_c = 0$ in figure 2.4. For the original approach, using the randomized SVD algorithm [HMT11a], the modes have good agreement for a narrow band of frequencies only. By comparing the results from figures 2.3 and 2.4 to the values in figure 2.5(c,d), we observe that the noise affects the modes when cosine similarity is below 0.5. For frequencies and wavenumbers with cosine similarity up to 0.8 or higher, there is no noise and the results for full and randomized resolvent agree well. For this reason, it is desirable to search for solutions that provide a reliable agreement up to this scale to a broad range of frequencies and both wavenumbers. With the high-gain frequency range well captured, randomized resolvent analysis has demonstrated its capability of predicting the dominant pathway for energy amplification over the spectral space with reduced computational cost.

As stated in Section 2.2, the use of low-rank approximation in the randomized approach is built upon the assumption of the low-rank nature of the resolvent operator. The randomized resolvent analysis shows its strength when the singular values exhibit fast decay, as evident from figure 2.6. The accuracy of the modal structured captured by randomized analysis is examined with respect to the ratio of the leading and second singular values, $(\sigma_1/\sigma_2)^{\text{full}}$ from the full resolvent analysis. The error in the modal structures exhibits a decreasing trend as this ratio increases. When this ratio is close to unity, the randomized technique may not accurately separate the first and second modes. In fact, the aforementioned trailing edge structure that appeared in the randomized response mode for $k_z L_c = 20\pi$ and $St = 1$

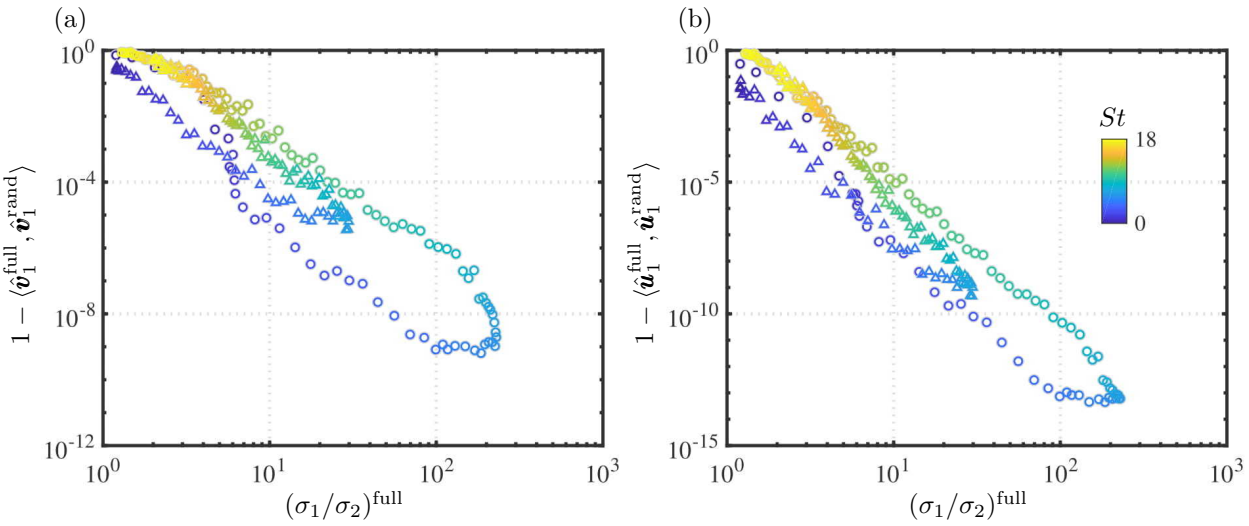

Figure 2.6: Error based on cosine similarity for the leading (a) forcing modes ($1-\langle\hat{\boldsymbol{v}}_1^{\text{full}},\hat{\boldsymbol{v}}_1^{\text{rand}}\rangle$) and (b) response modes ($1-\langle\hat{\boldsymbol{u}}_1^{\text{full}},\hat{\boldsymbol{u}}_1^{\text{rand}}\rangle$) over the leading gap from the full resolvent analysis. The symbols $\circ$ and $\triangle$ represent results from $k_z L_c = 0$ and 20π, respectively, colored by St.

is caused by the leakage of the structures from the second response mode (see figure 2.3). When the ratio $(\sigma_1/\sigma_2)^{\text{full}}$ is above 30, the error decreases to $\lesssim 10^{-5}$ for forcing modes and $\lesssim 10^{-8}$ for response modes.

Next, we study the influence of the width of the test matrix k on the error in the leading singular values and modes, as presented in figure 2.7. When the value of k is varied from 2 to 500, the error from the use of randomized analysis decreases. For three representative frequencies, we observe the same rate of convergence $\approx \mathcal{O}(k)$ for both the gain and cosine similarity. As stated in section 2.2, increasing k has the same practical effect of oversampling, in the present application. For this flow, we observe that $k = 10$ is sufficient to achieve sufficient accuracy with $\lesssim 1\%$ error, which is remarkably low when compared to the high dimensionality of the resolvent operator.

The computational cost of the randomized resolvent technique can be further reduced. For instance, the biconjugate gradient stabilized (BiCGStab) or the generalized minimum

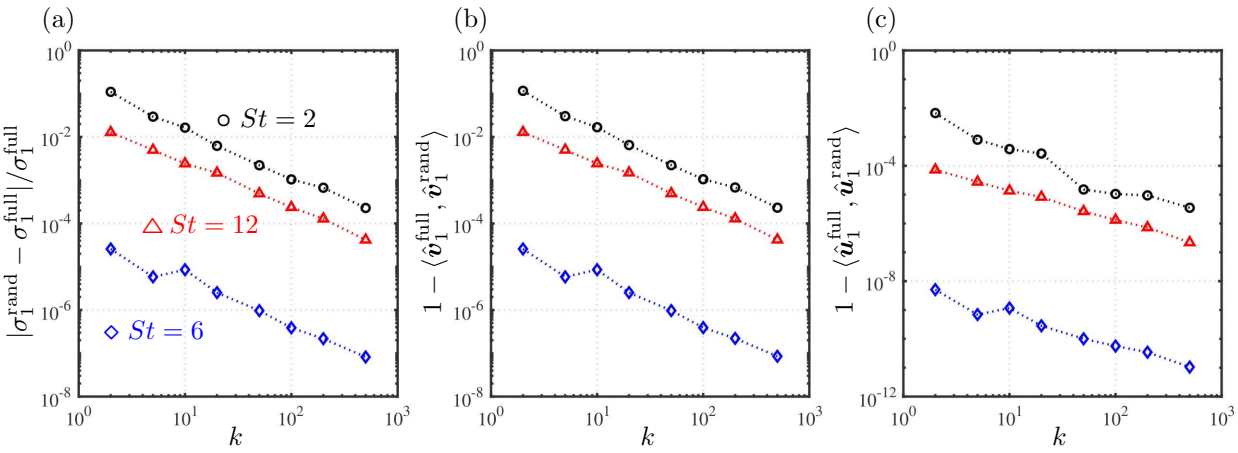

Figure 2.7: Influence of test matrix size k on the accuracy of (a) leading singular value, (b) forcing mode, and (c) response mode at $k_z L_c = 20\pi$. All exhibit $\mathcal{O}(k)$ convergence.

residual (GMRES) methods can be utilized to solve linear systems with appropriate preconditioners (e.g., incomplete LU and Jacobian).

2.3.2 Higher-order modes

Let us discuss the performance of the randomized technique with respect to the high-order modes. For some cases, the second largest singular value may also be spaced apart from the higher-order singular values and be determined accurately. In figure 2.8, we show for $k_z L_c = 0$ and $St = 4$ a case where both the leading and second singular values are spread from the rest of the singular values. In this case, the randomized algorithms accurately capture the second modes. The flow structures at the trailing edge are perceived in the response modes. The forcing modes appear over the pressure side near the trailing edge. For the results obtained from Algorithm 1, the modes are the same for randomized resolvent and for the full resolvent. However, for the resolvent analysis using the randomized SVD algorithm [HMT11a] within the resolvent analysis, the secondary singular values are poorly captured and the modes are polluted by background noise and leakage from other modes (not shown

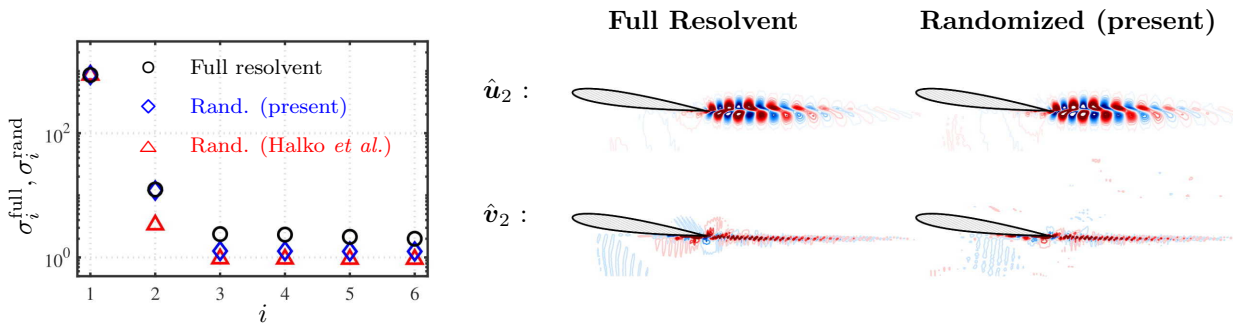

Figure 2.8: Recovery of the higher-order resolvent gains ($\sigma^{\text{rand}}_{i=1-6}$) and modes ($\hat{\boldsymbol{v}}_2$ and $\hat{\boldsymbol{u}}_2$) for $St = 4$ and $k_z L_c = 0$. The resolvent gains obtained from the present randomized analysis (◇, recovered by equation (2.9)) and those from the original approach of [HMT11a] (△) are compared to those from the full resolvent analysis (○).

here). For this reason, when applying randomized resolvent, the present implementation shown in Algorithm 1 must be considered as they can approximate the detached high-order modes accurately.

2.3.3 Choice of the test matrix $\boldsymbol{\Omega}$

For the randomized resolvent analysis with a test matrix size of $k = 10$, Gaussian, orthonormal, Rademacher and ultrasparse Rademacher test matrices provide similar results and no observable difference in computational savings. By using the implementation shown in Algorithm 1, all test matrices present similar accuracy as shown in figures 2.5 and 2.6. For very low and very high St numbers in the range of frequencies analyzed in this work, where the singular values decay slowly, one can increase the size k or apply subspace or power iterations. However, it is possible to obtain more accurate results by constructing a random test matrix $\boldsymbol{\Omega}$ that incorporates physical insights from the base flow.

While the random test matrix is effective in yielding accurate results, we can consider constructing a test matrix that can generate the entries in a smart manner by incorporating

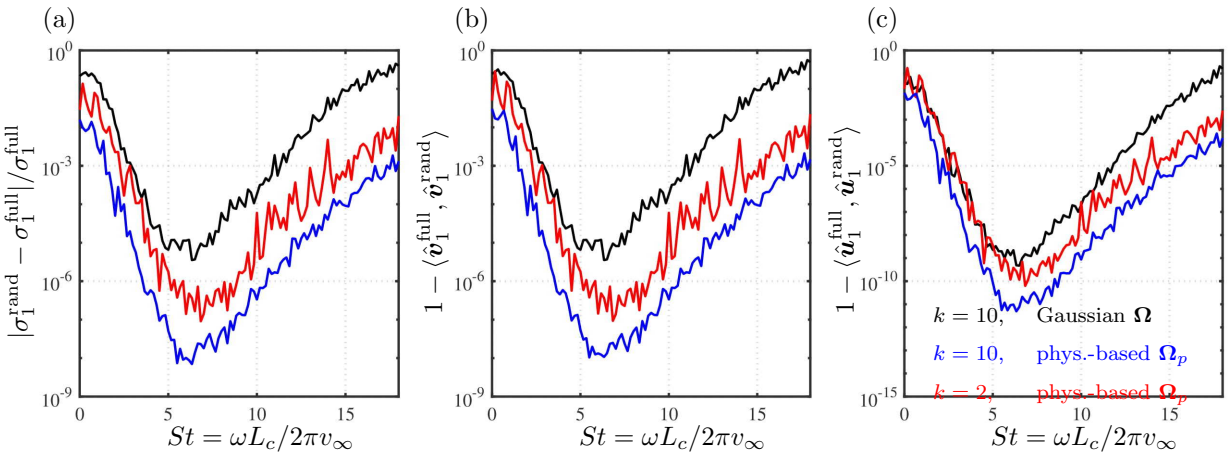

Figure 2.9: Influence of test matrices on the relative error for (a) gain distribution and cosine similarities for (b) forcing and (c) response modes, $\hat{\boldsymbol{v}}_1$ and $\hat{\boldsymbol{u}}_1$, at $k_z L_c = 20\pi$. Results are shown for Gaussian random normal distribution test matrix $\boldsymbol{\Omega}$ and physics-informed random test matrices $\boldsymbol{\Omega}_p = \mathsf{diag}(\boldsymbol{\Phi})\boldsymbol{\Omega}$ with sizes $k = 10$ and $k = 2$.

the knowledge of the base flow. We know that regions of strong shear are important in amplifying forcing inputs. Moreover, regions with minimal velocity gradients are not that important. For these reasons, the velocity gradient at each grid point can be used to scale the test matrix. Here, we propose a physics-informed test matrix, $\boldsymbol{\Omega}_p$, scaled by the 2-norm of the velocity gradient, $||\boldsymbol{\nabla v}||_2$, where $\boldsymbol{v}$ is the velocity vector. We construct a scaling factor $\boldsymbol{\Phi}_j = ||\boldsymbol{\nabla v}_j||_2$ at each grid point j. The scaling vector $\boldsymbol{\Phi}$ has to be stacked according to the number of variables to reach the size m of the linear operator. The physics-informed test matrix then becomes

$$\boldsymbol{\Omega}_p = \mathsf{diag}(\boldsymbol{\Phi})\boldsymbol{\Omega}. \tag{2.10}$$

The results based on the physics-informed test matrix are shown in figure 2.9. While the results obtained from the use of a normal distribution test matrix have shown excellent accuracy, the use of physics-informed test matrix further improves the accuracy by a few orders of magnitude for the considered frequencies and spanwise wavenumbers. More importantly, we achieve results with comparable or higher level of accuracy using a extremely low width

of the test matrix of $k = 2$. This results in a considerable reduction in computation time (see Table 2.1). Using $k = 10$, linear systems are solved at least 30 times. Now, using $k = 2$, only 6 linear solvers are needed to obtain the same accuracy, which is achieved only with a physics-informed scaling of the test matrix. By combining randomized numerical linear algebra and some physical insights, we are now empowered to perform the input-output analysis for ever more complex 2D and 3D turbulent base flows on a standard computer, or on a high-performance computing cluster to expand the envelope of resolvent analysis.

2.3.4 On the accuracy of linear systems solvers

For the randomized resolvent algorithm, direct and adjoint linear systems are solved in steps 2, 4, and 6 of Algorithm 1. For the present analysis, and all analyses used in the current thesis, linear systems are solved directly via LU decomposition. In some cases, it may be possible to avoid the need of a linear system solver, through the construction of an optimal basis [BGM22]. It remains a challenge, however, to obtain such a basis for complex geometries in 2-D or 3-D base flows.

For high-dimensional resolvent operators, the direct solution may not always be computationally feasible. In such cases, a reasonable approximation through iterative methods may be enough to yield insights into the perturbation dynamics. Such methods, as time-stepping, may increase the time costs, while significantly reducing the memory requirements [BBS08, MAB10, GBR16]. Recently, it was shown that even the computational time required by time-steppers can be reduced by incorporating streaming discrete Fourier transforms [MRT21, FTM21]. The use of iterative solvers has shown promising results to compute resolvent modes around a commercial aircraft model [HTS22, HTS23]. It is based on the usage of iterative solvers *in lieu* of the direct solvers that the analysis presented in this section is relevant.

In the present section, we add a Gaussian noise to the solutions of the linear systems obtained in steps 2, 4, and 6. These are, according to the Algorithm 1, the solutions obtained

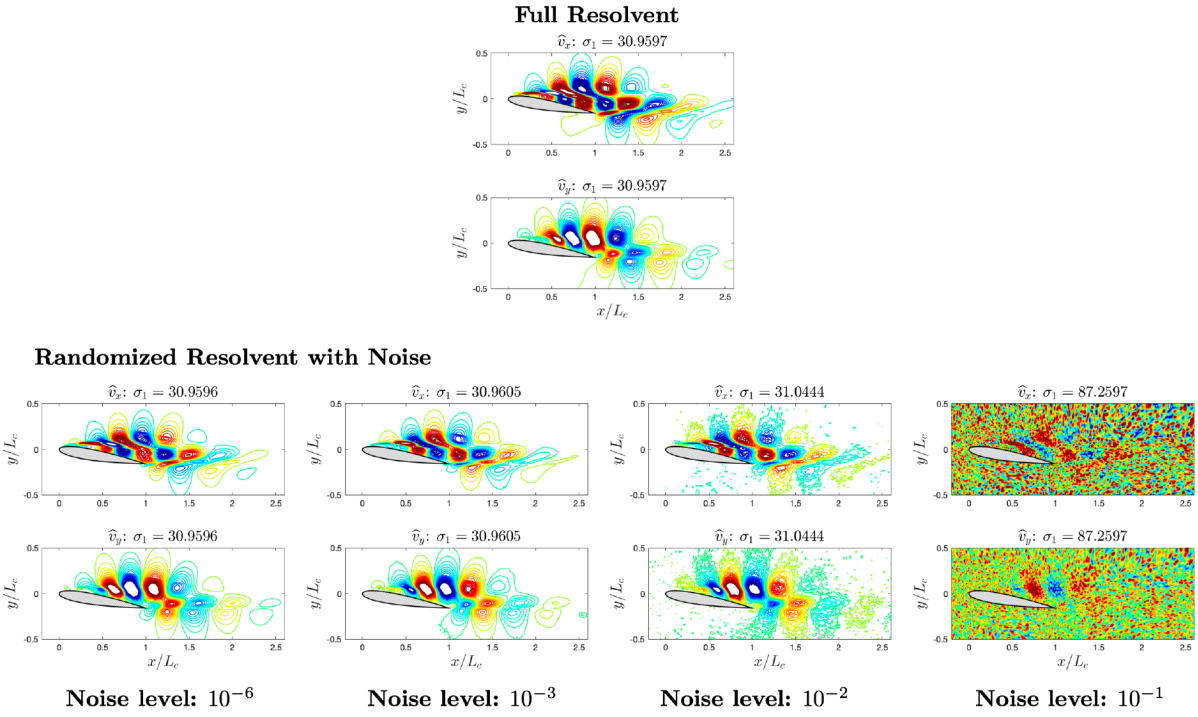

Figure 2.10: Leading amplification and response modes for $St = 1$ and $\beta = 0\pi$ computed with full resolvent approach [YT19] and randomized resolvent analysis with noisy linear system solutions with 4 different noise levels.

for sketch $\mathbf{Y}$, for the projection to the low-order basis $\mathbf{B}$, and the recovery of response modes $\mathbf{U\Sigma}$, respectively. The Gaussian noise is added as a $\epsilon\mathbf{\Omega}_{\text{noise}} \in \mathbb{C}^{m\times k}$, where norm $\|\mathbf{\Omega}_{\text{noise}}\|_2 = 1$, and ϵ is the noise level mentioned in figure 2.10 and 2.11. The objective is to mimic an inaccurate solution obtained by systems solvers, direct or iterative in case a convergence bound is set to a high value.

In figure 2.10, we add $\epsilon\mathbf{\Omega}_{\text{noise}}$ with the mentioned noise level to the 3 system solutions, $\mathbf{Y}$, $\mathbf{B}$, and $\mathbf{U\Sigma}$, in an equal manner. Up to $\epsilon = 10^{-3}$, the full resolvent results match the results obtained with inaccurate systems solutions, which suggests that we could relax the convergence limits of iterative solvers and still obtain the same resolvent modes as the ones achieved by direct solvers. For $\epsilon = 10^{-2}$ the amplification gain diverges, while the response modes remain similar to the full resolvent ones. For $\epsilon = 10^{-1}$ we cannot recover the spatial modes with any physical meaning.

The following question to be addressed is whether we need accurate solutions for all $\mathbf{Y}$, $\mathbf{B}$, and $\mathbf{U\Sigma}$ computations, or if we could relax one of these solutions. This question is addressed in figure 2.11. In the first row, we keep only one of the $\mathbf{Y}$, $\mathbf{B}$, and $\mathbf{U\Sigma}$ steps with high noise $\epsilon = 10^{-1}$, while the others are solved with good accuracy, or lower levels of noise $\epsilon = 10^{-6}$.

By keeping only $\mathbf{Y}$ with poor accuracy, the resolvent modes are still computed accurately. This result lies on the notion that a noisy or inaccurate solution to $\mathbf{Y}$ is only a solution to a different random matrix. In this way, the accuracy of the resolvent modes still lies within the accuracy bounds of the randomized SVD [HMT11b]. Having only an accurate $\mathbf{Y}$ results in poorly captured resolvent modes, which supports the idea that an accurate sketching is not the most crucial step to obtain accurate resolvent modes through the randomized resolvent analysis algorithm. The accuracy of the solutions to $\mathbf{B}$ and $\mathbf{U\Sigma}$ remains important. We observe in second and third columnds of figure 2.11, that whenever one of this solutions is inaccurate, at least one of the resolvent modes is not captured accurately and the resolvent gains diverge. This study serves as a cautionary note to the usage of iterative solvers to

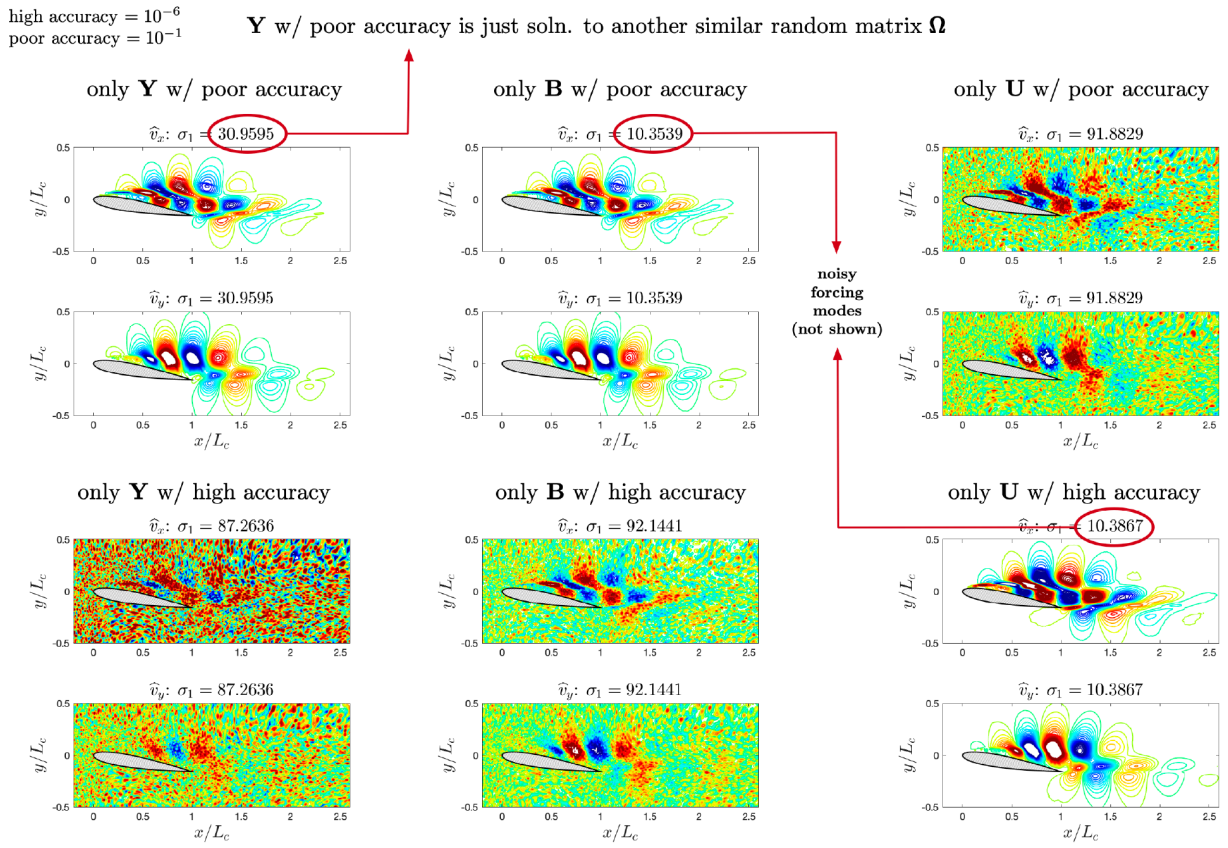

Figure 2.11: Leading amplification and response modes for $St = 1$ and $\beta = 0\pi$ computed with full resolvent approach [YT19] and randomized resolvent analysis with noisy linear system solutions on specific steps of the randomized resolvent algorithm.

compute resolvent modes and can be extended to any method, even though we have applied it to the randomized resolvent algorithm. In the context of randomized SVD applie to resolvent mode computations, the present results give insights on the convergence bounds that could be applied to each step of the randomized resolvent algorithm.

CHAPTER 3

Wake dynamics

Tapered and swept wings are widely used on aircraft, while the influence of their geometry parameters on their post-stall wake characteristics remains largely unexplored for low-Reynolds-number post-stall flows. To address this issue, we conduct an extensive study using direct numerical simulations to characterize the wing taper and sweep effects on laminar separated wakes. We analyze flows behind NACA 0015 cross-sectional profile wings at post-stall angles of attack $\alpha = 14°$–$22°$ with taper ratios $\lambda = 0.27$–1, leading edge sweep angles $0°$–$50°$, and semi aspect ratios $sAR = 1$, 2, and 4 at mean-chord-based Reynolds number of 400 and 600 and a freestream Mach number of 0.1. For untapered wings, we observe that the flow around unswept wings develops vortex shedding near the wing root with a quasi-steady tip vortex. For swept wings, vortex shedding is seen near the wing tip for low sweep angles, while the wakes are steady for wings with high sweep angles. For tapered wings, we report on the combined effects of leading and trailing edge sweep angles on the wakes. Wing taper reduces the tip chord length, weakening the tip vortex, and attenuates the inboard downwash over the wing. This results in unsteadiness to develop over a large portion of the wingspan at high angles of attack. Tapered wings with backward-swept leading edges develop unsteadiness near the wing tip, while wings with forward-swept trailing edges concentrate wake oscillations at the wing root. For highly swept untapered wings, the wake is steady, while tapered wings with high leading edge sweep angles exhibit wake shedding near the tip. Wake oscillations are larger towards the root for lower taper ratios. Moreover, the effects of taper on the aerodynamic forces over tapered wings are studied, revealing that the combined effect of taper and sweep can improve the aerodynamic performance of the wing.

The current findings shed light on the fundamental effects of wing taper and sweep on the post-stall wake dynamics.

3.1 Motivation

Understanding flow separation over finite swept wings is essential to the study of aircraft and biological flight [And10, VSP04, LMS07]. The aspect ratio, angle of attack, taper, and sweep play important roles in influencing stall and wake characteristics [ZHA20a, ZHA20b]. Although a number of studies have deepened our knowledge of laminar separated wakes around finite swept and unswept wings, coherent flow structures associated with the three-dimensional (3-D) flow separation have not been characterized their combined effects with taper in a comprehensive manner.

In aircraft design, tapered wings are used to achieve an approximation to the elliptic aerodynamic loading over the wingspan. Tapered wings are more feasible and less geometrically complex compared to elliptic wings [Pra20, McC95], from the point of view of manufacturing. The usage of tapered wings in aeronautics has called for initial studies to explore the wing taper effect, especially for high-Reynolds number flows [Mil36, And36, Irv37, SA40, Fal50]. For the laminar flow regime, the effect of wing taper on the wake dynamics is critical as the local Reynolds number flow at the wing tip is drastically reduced near the tip. For flows at a chord-based Reynolds number $Re_c = \mathcal{O}(10^4)$ wing, taper affects the aerodynamic loading with an increase in the pressure drag [Tra13, TBW15]. For $Re_c = \mathcal{O}(10^3)$, the aerodynamic characteristics are affected significantly by the viscous effects, and the influence of wing taper on the wakes remains elusive, especially for massively separated flows.

The wake dynamics of wings at post-stall flow conditions has attracted the attention of aeronautical researchers for many decades. The early efforts to understand post-stall flows over wings were performed over two-dimensional (2-D) wings [AV59, Gas67, TP82]. Valuable insights were obtained from 2-D analysis characterizing the behavior of the separated

laminar boundary layer [Hor68] and describing the relation between vortex shedding structures, adverse pressure gradient, and shear layer characteristics [PMR90]. Self-excitation mechanisms of laminar separation bubbles, in the absence of incoming disturbances exciting the shear layer instability were also studied [THD00], providing evidence for the appearance of the vortical patterns predicted by flow topological arguments [HP84, PH84]. Subsequent analyses of spanwise homogeneous three-dimensional (3-D) low-Reynolds number separated flow over 2-D wings [HGP17] corroborated the existence of 2-D traveling shear-layer and 3-D stationary spanwise-periodic linear instabilities and analyzed their modal and non-modal linear growth. The analysis of 2-D flows around canonical wings continues providing fundamental insights on the effect of angle of attack and Reynolds number on the wake shedding structures [LP96, HWJ01, YSK09, RCO18].

For separated flows, the increase in Reynolds number and the angle of attack can yield a 3-D flow field even around 2-D (or quasi-2-D) wings [BT80, WB80a, Sch01, HBV03, PM19]. In such cases, spanwise fluctuations emerge, producing 3-D vortical structures in the wake. Floquet analysis of the time-periodic wake flow ensuing linear growth of Kelvin-Helmholtz instability on the wing associated these 3-D vortical structures with secondary linear instability of the spanwise-homogeneous wake [HGP17].

For finite wings, the three-dimensionality of the vortical wake structures results from the tip effects. Around the wing tip, a strong streamwise vortex is formed, yielding 3-D wake formation with strong and complex nonlinear interactions [WB80a, FFB87, TC09, ZHA20b, NA23]. Tip vortices induce downwash inboard over the wing, which reduces the effective angle of attack near the tip, even suppressing stall formation [DCM20, TY21] and the wake shedding for low-aspect-ratio wings [TC09, ZHA20b]. Moreover, the tip vortex has been extensively studied to reveal its influence on the wake dynamics, aerodynamic forces, and pitch moments [FK79, GA91, DRL96, PM00, BLM04, TM04, BS06, YR12, ASS15, HTP17, TY21, TY22]. By understanding the tip vortex formation, evolution, and instability mechanisms, it is possible to develop control techniques to improve the aerodynamic performance

around finite wings [GW18, ESS18, NBJ19].

Separated wakes are also affected by wing sweep, which stabilizes flow oscillations and reduces wake three-dimensionality [ZHA20b, RYZ22b, RYT23]. The flow over swept wings induces a spanwise flow component within the stalled region, significantly impacting wake characteristics [HM64]. The stabilizing effect around laminar separated flows is related to the emergence of the sweep-induced spanwise flow in the stalled region [WTT14, RYZ22b]. For laminar flow regimes, a number of experimental and numerical efforts were carried out to examine the effects of backward and forward wing sweep in many different configurations [BL01, YH07, ZHA20a, ZT22, BHH22, RYT23].

Thus far, most studies have not considered wing taper effects on low-Reynolds number flows at high angles of attack. Only recently, a combined experimental, numerical, and theoretical effort has been initiated towards the understanding of the laminar flow over tapered wings in post-stall flow conditions [RTN23, NGA23, BTR23]. Effects of taper have been analyzed for planforms with tubercles to analyze swimming of whales [WNC18], for flows over tapered cylinders [PV93, THT98, VAJ02], and for separated wakes over tapered plates [NAP08]. For wing planforms with continuously variable chord length over the wingspan, the delta wings have also received substantial attention [Roc93, GGV05, TC09]. For laminar post-stall flows, wing taper was studied using trapezoidal plates [HVT15]. Nonetheless, there still is a lack of fundamental studies to understand the role of taper ratio, and how it interplays with leading edge (LE) and trailing edge (TE) sweep angle effects for massively separated laminar flows.

For laminar separated flows, the tip and sweep effects o the wake dynamics have been explored through experiments and numerical simulations [HGP17, ZHA20b, ZHA20a, HA21, HON22, ZT22]. The effect of wing taper remains elusive and its effects combined with sweep on post-stall flows remains unexplored for low-Reynolds number flows. The present chapter reveals the effects of taper and sweep in the laminar wake dynamics and the influence of LE and TE sweep angles on the vortical interactions through a comprehensive campaign of direct

numerical simulations of 3-D flows over finite NACA 0015 wings with different taper ratios and sweep angles. We characterize the stalled wakes of wings with backward-swept LE and forward-swept TE, identifying the combined effects of taper and sweep angle. This chapter is organized as follows. In section 3.2, we present our wing planform geometry definitions and the setup for direct numerical simulations. In section 3.3, we offer a detailed analysis and classification of the wake structures, highlighting the effects of taper and sweep.

3.2 Problem setup

We consider laminar flows over tapered and swept wings with a NACA 0015 cross-sectional profile. The spatial coordinates of streamwise, transverse, and spanwise directions are denoted by (x, y, z), respectively. The origin is placed at the LE of the wing root, as shown in figure 3.1. The NACA 0015 profile is defined on the (x, y) plane, which is extruded from the wing root in the spanwise direction to form the 3-D wing. Wing taper is defined by the taper ratio $\lambda = c_{\text{tip}}/c_{\text{root}}$, where c_{tip} and c_{root} are tip and root chord lengths, respectively, as shown in figure 3.1(a). For all wings considered herein, the chord length decreases linearly from root to tip. The non-dimensional mean chord length c at the spanwise location of $z = b/2$ is taken to be the characteristic length used to non-dimensionalize all spatial variables.

The semi-aspect ratio of the wings is set as $sAR = b/c = 1$ and 2, where b is the half-span length, as shown in figure 3.1(d). We consider half-span wing models with symmetry imposed at the root. The angles of attack, $14^\circ \leq \alpha \leq 30^\circ$, are defined between the airfoil chord line and the streamwise direction. The present wing geometries have sharp trailing edge and straight-cut wing tip. The mean-chord-based Reynolds number is set to $Re_c = 400$ and 600 and freestream Mach number $M_\infty = 0.1$ for the present study. For the flows shown in section 3.3.1, the mean-chord-based Reynolds number is set to $Re_c = 400$. Simulations of $Re_c = 400$ flows were performed over untapered wings only. For these cases, we have considered higher aspect ratio wings with $sAR = 4$ and higher angles of attack up to 30° as

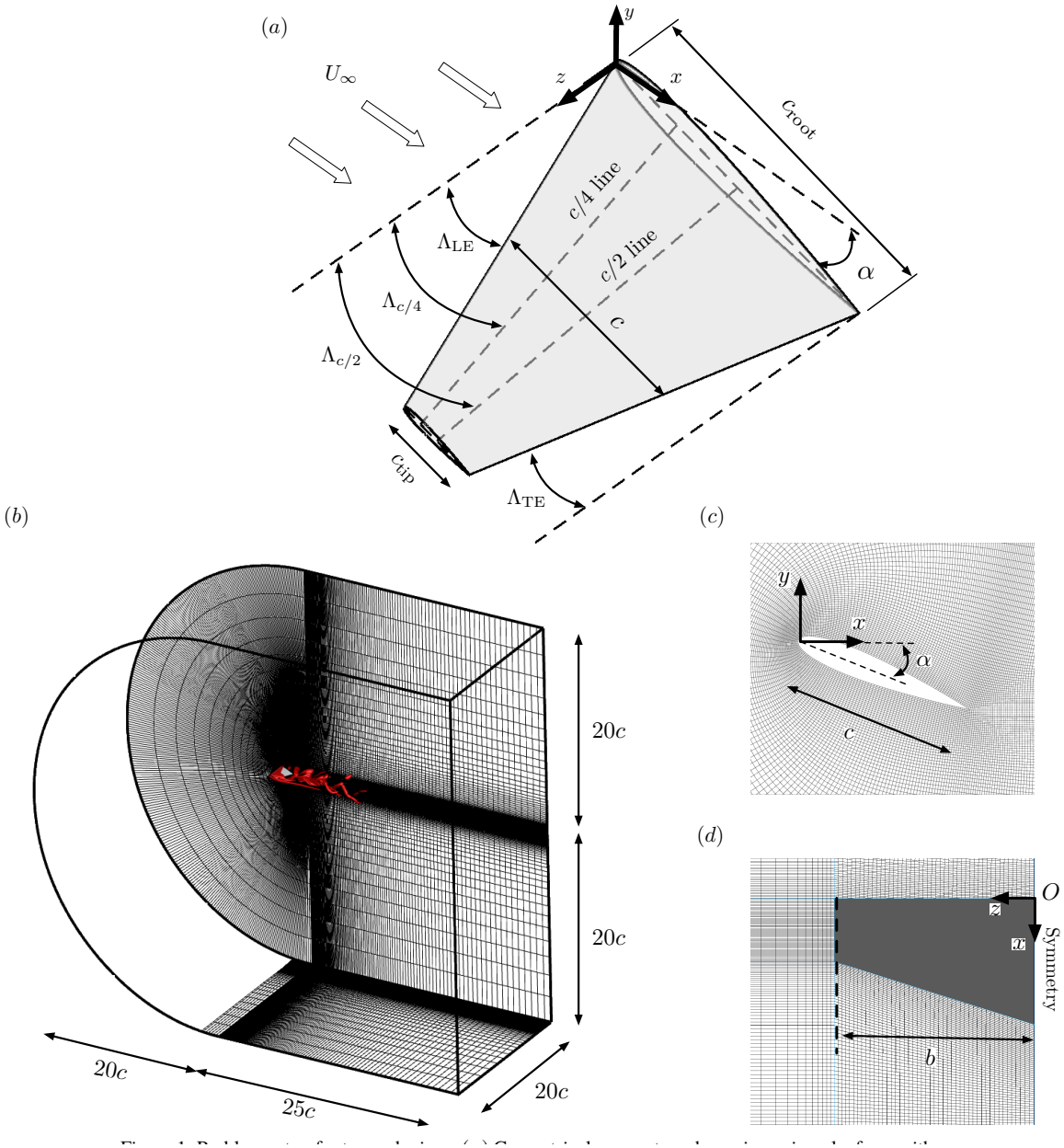

Figure 3.1: Problem setup for tapered wings. (a) Geometrical parameters shown in a wing planform with $sAR = b/c = 2$, $\alpha = 18°$, $\lambda = 0.27$, and $\Lambda_{LE} = 18.4°$. (b) Computational domain and (c, d) grids are shown with 2-D planes at $z/c = 1$ and $y/c = -0.5$, respectively.

well.

Further analysis considering lower aspect ratios and tapered wings was performed for flows with $Re_c = 600$. Throughout the text, we will explicitly mention the Reynolds number of the simulations to avoid any confusion throughout the discussion. However, the difference between $Re_c = 400$ and 600 flows is so mild that the overall structures are similar for both flow conditions. In fact, [ZHA20b] has already validated DNS simulations performed at $Re_c = 400$ with experiments performed at $Re_c = 600$, which enforces the notion that these flows are indeed similar to each other. We must also note that wing taper changes the local Reynolds number Re_{L_c}, defined as a function of the spanwise location [TBW15]. For the present study, the difference between c_{tip} and c_{root} accounts for a maximum variation of 60% on Re_{L_c} along the span, from $\min(Re_{L_c}) = 250$ and $\max(Re_{L_c}) = 950$ at the lowest taper ratio.

The wings considered in the present work have varied taper ratios and wing sweep. For tapered swept wings, the 3-D computational setup is sheared in the chordwise direction and Λ_{LE} is defined between the z-direction and the LE. Tapered wings have different Λ_{LE} and Λ_{TE} respectively, as shown in figure 3.1(a). In this chapter, we explore the combined effects of the LE and TE sweep angles on the wake dynamics, defining LE sweep angles between $0 \leq \Lambda_{\text{LE}} \leq 50^\circ$ and TE sweep angles between $-30^\circ \leq \Lambda_{\text{TE}} \leq 50^\circ$. Herein, negative sweep angles indicate a forward sweep, as shown in figure 3.1(a), while positive sweep angles represent a backward sweep. Through the aforementioned Λ_{LE} and Λ_{TE}, taper ratios are analyzed between $0.27 \leq \lambda \leq 1$.

Traditionally in aeronautics, tapered swept wings have wing sweep angle observed with respect to the quarter-chord line [And10, And36, Fal50] denoted by $\Lambda_{c/4}$, as shown in figure 3.1(a). [And99] considered the half-chord sweep angle $\Lambda_{c/2}$, such that aerodynamic load distribution becomes independent of the taper ratio. Straight tapered wings, those with $\Lambda_{c/4} = 0^\circ$ were studied by [TBW15]. On the other hand, [Irv37] considered the effect of the LE and TE sweep angles. For the present laminar separated flows, due to the crucial role

played by the LE vortex in defining the wake characteristics [VSP04, EJ19], we focus on Λ_{LE} and Λ_{TE} as the main independent parameters for our analysis and describe their influence on the wake dynamics. We note, however, that it is also possible to translate the findings reported herein with respect to the traditional quarter-chord and half-chord sweep angles, $\Lambda_{c/4}$ and $\Lambda_{c/2}$, respectively.

3.2.1 Direct numerical simulations

We conduct direct numerical simulations with a compressible flow solver *CharLES* [KHN11, BHN17b], which uses a second-order accurate finite-volume method in space with a third-order accurate total-variation diminishing Runge–Kutta scheme for time integration. The computational domain is discretized with a C-type grid with mesh refinement near the wing and in the wake. With the origin at the airfoil LE on the symmetry plane $(x/c,\ y/c, z/c) = (0, 0, 0)$, the computational domain extends over approximately $(x/c, y/c, z/c) \in [-20, 25] \times [-20, 20] \times [0, 20]$, which yields a maximum blockage ratio of 0.8% for the wing with $\lambda = 0.27$, $sAR = 2$, and $\alpha = 22^{\circ}$. The computational setup is shown in figure 3.1(*b-d*).

We have prescribed a Dirichlet boundary condition of $(\rho, u_z, u_y, u_z, p) = (\rho_\infty, U_\infty, 0, 0, p_\infty)$ at the inlet and farfield boundaries, where ρ is density, p is pressure, u_x, u_y, and u_z are velocity components in x, y, and z directions respectively. Symmetry boundary condition is prescribed along the root plane, $z/c = 0$. The subscript ∞ denotes the freestream values. A no-slip adiabatic boundary condition is set on the airfoil surface. For vortical structures to convect out of the domain, a sponge layer is applied over $x/L_c \in [15, 25]$ with the target state being the running time-averaged state over 5 convective time units [Fre97]. Simulations start from uniform flow and are performed with a constant acoustic Courant-Friedrichs-Lewy (CFL) number of 1 until transients are washed out of the computational domain. The time to flush out the transients varies depending on the wing planform and angle of attack, generally ranging from 50 to 300 convective time units. After the transients are washed out of the domain, we run the simulations with a constant time step defined such that CFL is smaller

	$\Lambda = 0°$		$\Lambda = 15°$		$\Lambda = 30°$		$\Lambda = 45°$	
	$\overline{C_L}$	$\overline{C_D}$	$\overline{C_L}$	$\overline{C_D}$	$\overline{C_L}$	$\overline{C_D}$	$\overline{C_L}$	$\overline{C_D}$
Present study	0.53	0.35	0.50	0.34	0.45	0.31	0.40	0.29
[ZHA20a]	0.53	0.35	0.51	0.33	0.44	0.30	0.40	0.29

Table 3.1: Time-averaged lift and drag coefficients ($\overline{C_L}$ and $\overline{C_D}$) compared to [ZHA20a] for laminar separated flow over NACA 0015 wings with $sAR = 4$, $\alpha = 20°$, and $\Lambda = 0°$, $15°$, $30°$, and $45°$.

than one. Flow statistics are collected for 100 to 300 convective time units, depending on the flow field characteristics and spectral content to ensure convergence. Close agreement for instantaneous and time-averaged velocity components was achieved with those from Zhang *et al.* [ZHA20a]. We have further validated our computations for time-averaged drag and lift coefficients,

$$C_D = \frac{F_x}{0.5\rho U_\infty^2 bc} \quad \text{and} \quad C_L = \frac{F_y}{0.5\rho U_\infty^2 bc} \,, \tag{3.1}$$

respectively, where F_x is the drag and F_y is the lift over the wing, as reported in table 3.1. These definitions abstain from considering changes in the reference area associated with the sweep and the angle of incidence and follow the definition of C_L and C_D from previous works [ZHA20a]. Lift and drag coefficients are defined herein for validation purposes only.

We verify the convergence of grid resolution for the numerical results using a wing with $(sAR, \alpha, \Lambda_{\text{LE}}, \lambda) = (2, 22°, 40°, 0.27)$. Herein, we report the aerodynamic forces through their lift coefficients defined as $C_L = F_y/(0.5\rho U_\infty^2 bc)$, where F_y is the y component of the viscous and pressure forces integrated over the wing surface. This planform combines a high leading-edge sweep angle and the lowest taper ratio considered in the present study. Two meshes are used for verification: a medium and a refined mesh. The medium mesh refinement is the one used throughout the present work. This mesh has 80 grid points on both pressure and suction sides of the wing and 48 grid points along the wingspan, with a total of approximately 3.1×10^6 control volumes. The refined mesh has 120 grid points on pressure and suction

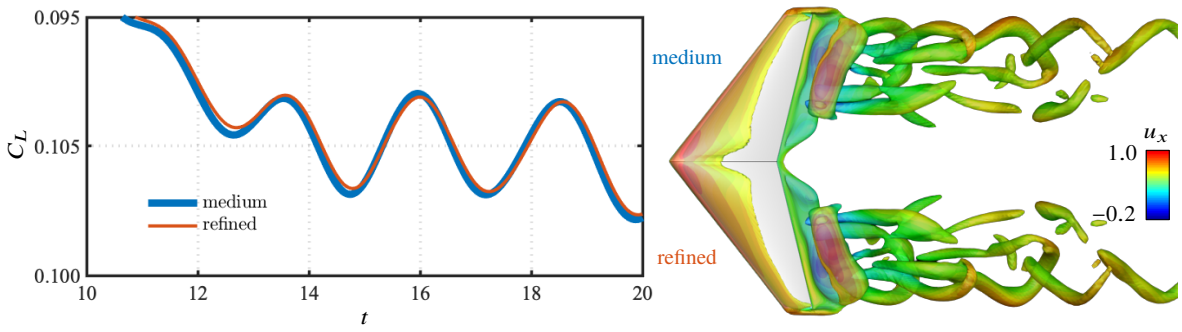

Figure 3.2: Lift coefficient over time and instantaneous flow field structures visualized using $Q = 1$ colored by instantaneous velocity component u_x at the lift peak for the two sets of meshes used for grid verification for the wing with $(sAR, \alpha, \Lambda_{\mathrm{LE}}, \lambda) = (2, 22°, 40°, 0.27)$.

sides, with 64 grid points along the wingspan, resulting in approximately 4.3×10^6 control volumes in total. For the refined mesh we have increased the temporal resolution by setting the CFL to 0.5. The quality of our medium mesh is assessed through the forces exerted over the wing and the instantaneous vortical elements as shown in figure 3.2.

3.3 Results overview

3.3.1 Flows over swept wings

A variety of wake patterns can be observed for different α, Λ, and sAR, as summarized in figure 3.3. For the present numerical results, the chord-based Reynolds number was set to $Re_c = 400$. In the bottom plot, the flow over the wing with $(sAR, \alpha, \Lambda) = (2, 30°, 0°)$ exhibits a quasi-steady streamwise oriented tip vortex. This structure is characteristic of flows over unswept wings and also appears around wings with different α and sAR. For such wings, unsteady spanwise vortices develop at the root plane. Between the root and the wing tip, there is an intermediate zone with braid-like vortices.

Wing sweep affects the wake structures. At low sweep angles, a spanwise flow devel-

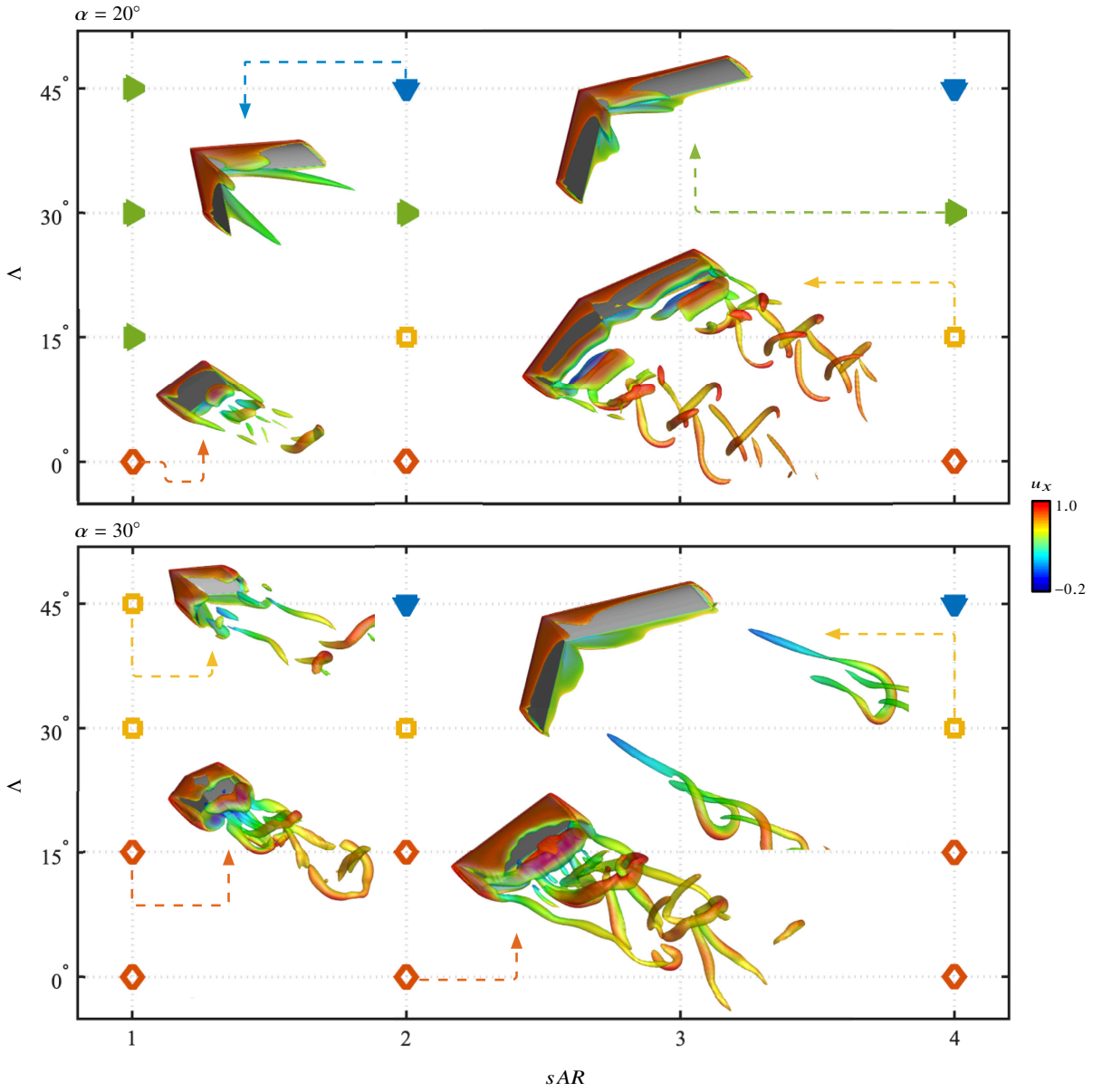

Figure 3.3: Instanteneous isosurfaces of $Q = 2$ colored by u_x for $Re_c = 400$ flows. Unsteady shedding near root (◇), unsteady shedding near wing tip (□), steady flow with root structures (▶), steady flow with streamwise vortices (▼).

ops over the wing and advects unsteady vortices towards the wing tip. For instance, for $(sAR, \alpha, \Lambda) = (4, 20°, 15°)$, spanwise vortices still appear. These structures are similar to the ones observed over unswept wings, although they form closer to the wing tip, and break into helical structures in the wake. For the flow around this wing, streamwise-oriented tip vortices are absent.

For higher Λ, wing sweep can stabilize wake oscillations. For $(sAR, \alpha, \Lambda) = (4, 30°, 30°)$ near-wake unsteadiness is reduced and unsteady vortices appear further downstream in the wake. We notice that these structures are absent when the angle of attack is lowered to 20°. Similarly, increasing the sweep angle to $\Lambda = 45°$ suppresses unsteady vortices on both angles of attack and the wake becomes steady. On such highly swept wings, ram-horn-shaped streamwise-oriented vortices develop from the root plane and extend into the wake.

For each (α, Λ) pair, the wake exhibits similar characteristics for wings with $sAR = 4$ and 2. Reducing the semi-aspect ratio to $sAR = 1$ has a strong influence on the wake dynamics, as shown in figure 3.3. For such wings, tip effects can suppress the formation of leading edge vortices at lower angles of attack. For instance, at $\alpha = 20°$, wake unsteadiness is reduced and swept wings exhibit steady flows with root structures.

Unsteady vortices are observed in flows over $sAR = 1$ wings at $\alpha = 30°$ for all considered sweep angles. The unsteadiness appears near the root for lower Λ. Further downstream, unsteady vortices appear over the entire wingspan. For higher Λ, vortices are generated near the wing tip and helical structures are observed in the wake. These observations agree with the characterizations by [ZHA20a]. To deepen our insights into swept-wing wake dynamics, we will call for the triglobal resolvent analysis of the present flow fields, which will be discussed in chapter 5. The triglobal resolvent analysis of these flows is a novel result and a contribution of the present work. The DNS results presented in this section are not, as incompressible flow simulations already covered the flow physics around these wings in previous studies [ZHA20b, ZHA20a, ZHA20a]. For this reason, we refrain from an extensive discussion of the present results and move on to the discussion of tapered wings wakes, which

consists of novel results that contribute to the present manuscript.

3.3.2 Tapered wing wakes

From now on, in the present chapter, we consider the effect of wing taper and sweep for $Re_c = 600$ flows around wings. Post-stall wakes around tapered wings exhibit a rich diversity of flow structures depending on the taper ratio, but they are also globally affected by aspect ratio, angles of attack and sweep, and, as shown in figure 3.4, through the combined effects of LE and TE sweep angles. Taper effects on laminar separated flows are entwined with the effects of LE and TE sweep angles. By studying straight taper, that is, wings with $\Lambda_{c/2}$ and $\Lambda_{c/4}$ approximately zero, we can separate the effects of taper from the sweep and other geometrical parameters.

For instance, let us explore the flows over wings with $(\lambda, \Lambda_{\mathrm{LE}}) = (1, 0^\circ)$ and compare them to the wake structures around $(\lambda, \Lambda_{\mathrm{LE}}) = (0.27, 10^\circ)$ wings; these flows have $\Lambda_{c/4} = 0^\circ$ and 1.8°, respectively. There is a strong reduction of the tip vortex length for tapered wings caused by the reduction in the tip chord length, but the downstream root shedding is similar, forming hairpin-like vortices in the wake. The near-wakes are different for these two flows. For the tapered wing, the root shedding presents spatial fluctuations over the spanwise vortex on the suction side. Such oscillations are absent in the vortical structure that forms over the untapered wing.

We can further explore the separate taper effects on the wake dynamics by considering wings with $\Lambda_{c/2} \approx 0^\circ$, as shown for the similar flow patterns that develop at the root region for $(\lambda, \Lambda_{\mathrm{LE}}) = (1, 0^\circ)$ and $(0.27, 18.4^\circ)$ wings. Here, with a lower taper ratio, tip vortices are considerably weakened when compared to the untapered wing tip vortices. Over the tapered wing, vortex rolls are slanted and aligned with Λ_{LE}, showing that the LE sweep angle is important to the near-wake shedding behavior.

For tapered wings, the backward-swept LE effect can be observed by fixing the $\Lambda_{\mathrm{TE}} = 0^\circ$

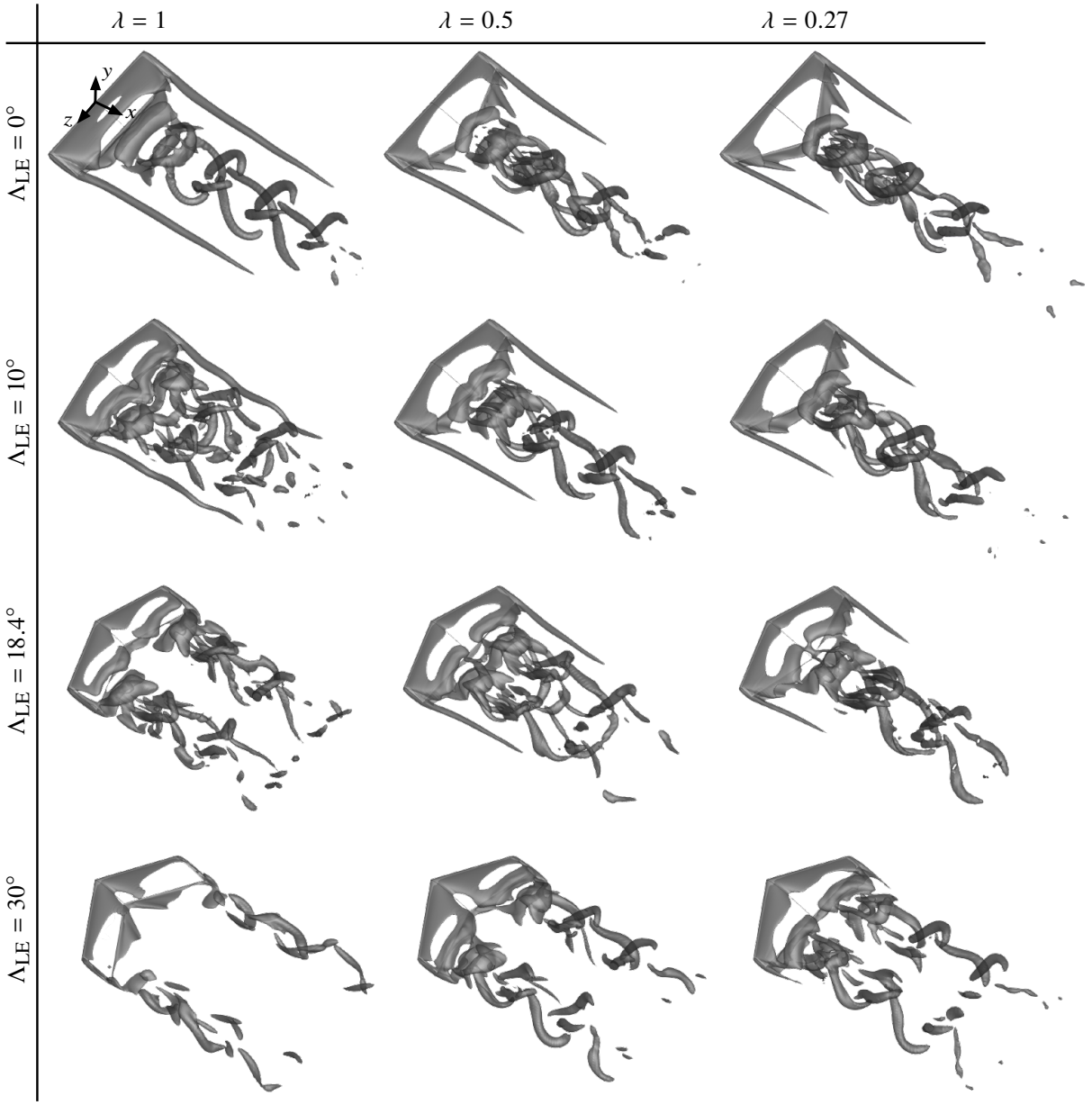

Figure 3.4: Instantaneous flows with $Re_c = 600$ around tapered wings with $sAR = 2$, $0.27 \leq \lambda \leq 1$, and $0° \leq \Lambda_{\mathrm{LE}} \leq 30°$, at $\alpha = 18°$ visualized using gray-colored isosurfaces of $Q = 1$.

while the LE is swept backward with $\Lambda_{\mathrm{LE}} = 18.4°$ and $30°$ for $\lambda = 0.5$ and 0.27, respectively. Such taper causes the wake shedding structures to move towards the wing tip region. An opposite effect is shown in the top row of figure 3.4, for flows over forward-swept TE wings. These planforms have fixed $\Lambda_{\mathrm{LE}} = 0°$, while $\Lambda_{\mathrm{TE}} = -18.4°$ and $-30°$ for $\lambda = 0.5$ and 0.27, respectively. For these cases, we observe that taper reduces the tip vortex length and affects the topology of the root-shedding structures. Let us further study the taper effect for highly swept wings, shown at the bottom row of figure 3.4, with a fixed $\Lambda_{\mathrm{LE}} = 30°$, while $\Lambda_{\mathrm{TE}} = 11.6°$ and $0°$ for $\lambda = 0.5$ and 0.27, respectively. Here, taper increases the amplitude of wake oscillations. We further detail the discussions on the effects of LE and TE sweep in sections 3.5.3, 3.5.4, and 3.5.5.

A variety of wake structures that appear around tapered wings, as seen in figure 3.4, calls for a proper characterization of the wake dynamics that associates its behavior with the wing planform geometry. The above discussions suggest that taper affects the location where unsteadiness emerges and the characteristics of the vortical structures. In the following section, we map the wake characteristics of tapered wings.

3.4 A portfolio of flow fields around tapered wings

3.4.1 Perspective view

In this section, we provide flow field visualizations of the wake structures around all tapered wings considered in the present study in a perspective view. Flows around $sAR = 1$ wings at $\alpha = 14°$, $18°$, and $22°$ are shown in figures 3.5, 3.6, and 3.7, respectively. Similarly, flows around $sAR = 2$ wings $\alpha = 14°$, $18°$, and $22°$ are shown in figures 3.8, 3.9, and 3.10, respectively. All flows are visualized using isosurfaces of $Q = 1$, colored by the streamwise velocity u_x.

3.4.2 Side view

In this section, we provide flow field visualizations of the wake structures around all tapered wings considered in the present study in a side view. Flows around $sAR = 1$ wings at $\alpha = 14°$, $18°$, and $22°$ are shown in figures 3.11, 3.12, and 3.13, respectively. Similarly, flows around $sAR = 2$ wings $\alpha = 14°$, $18°$, and $22°$ are shown in figures 3.14, 3.15, and 3.16, respectively. All flows are visualized using isosurfaces of $Q = 1$, colored by the streamwise velocity u_x.

3.4.3 Top view

In this section, we provide flow field visualizations of the wake structures around all tapered wings considered in the present study in a top view. Flows around $sAR = 1$ wings at $\alpha = 14°$, $18°$, and $22°$ are shown in figures 3.17, 3.18, and 3.19, respectively. Similarly, flows around $sAR = 2$ wings $\alpha = 14°$, $18°$, and $22°$ are shown in figures 3.20, 3.21, and 3.22, respectively. All flows are visualized using isosurfaces of $Q = 1$, colored by the streamwise velocity u_x.

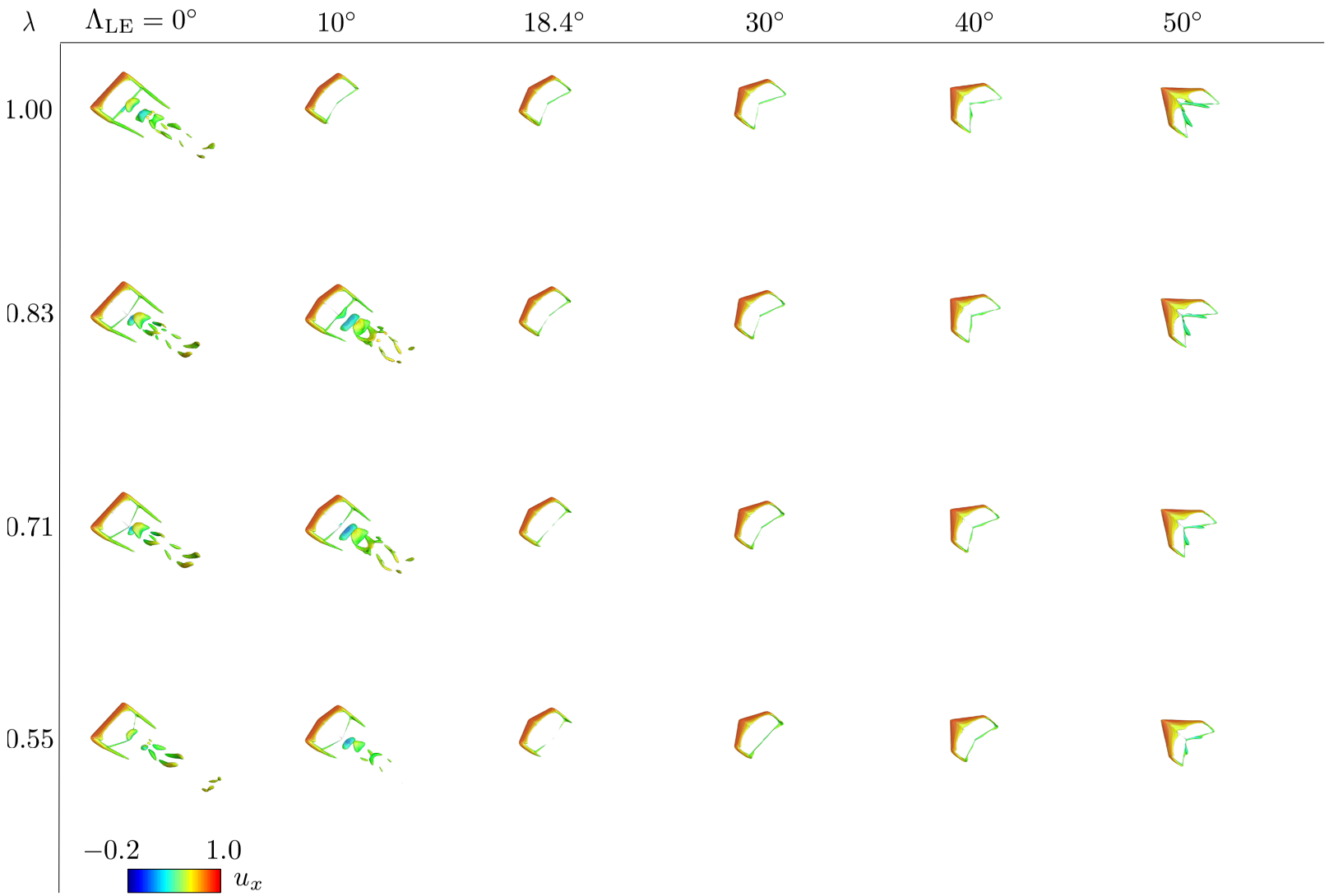

Figure 3.5: Perspective view. Isosurfaces of $Q = 1$, $Re_c = 600$ flows over $(sAR, \alpha) = (1, 14°)$ wings.

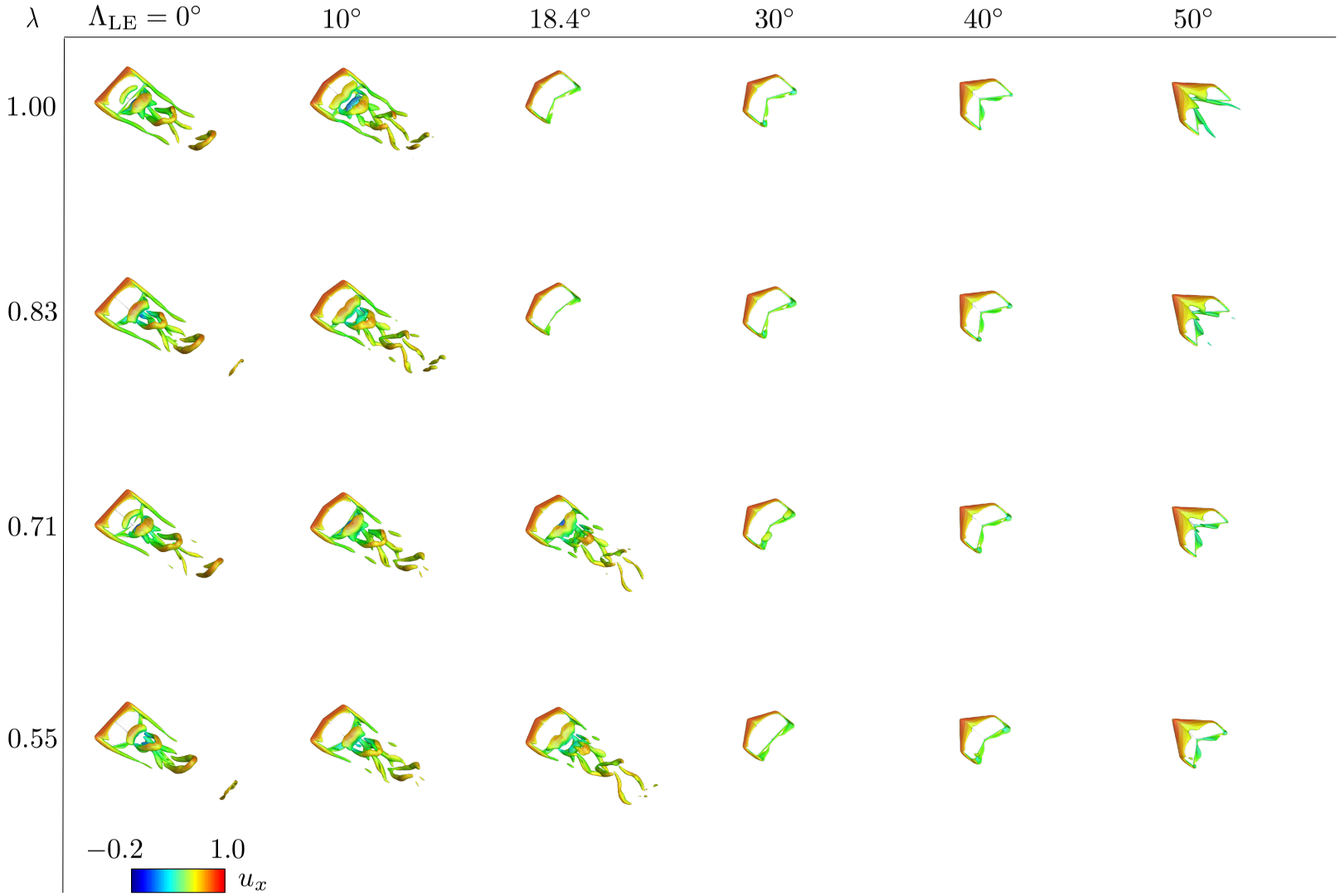

Figure 3.6: Perspective view. Isosurfaces of $Q = 1$, $Re_c = 600$ flows over $(sAR, \alpha) = (1, 18°)$ wings.

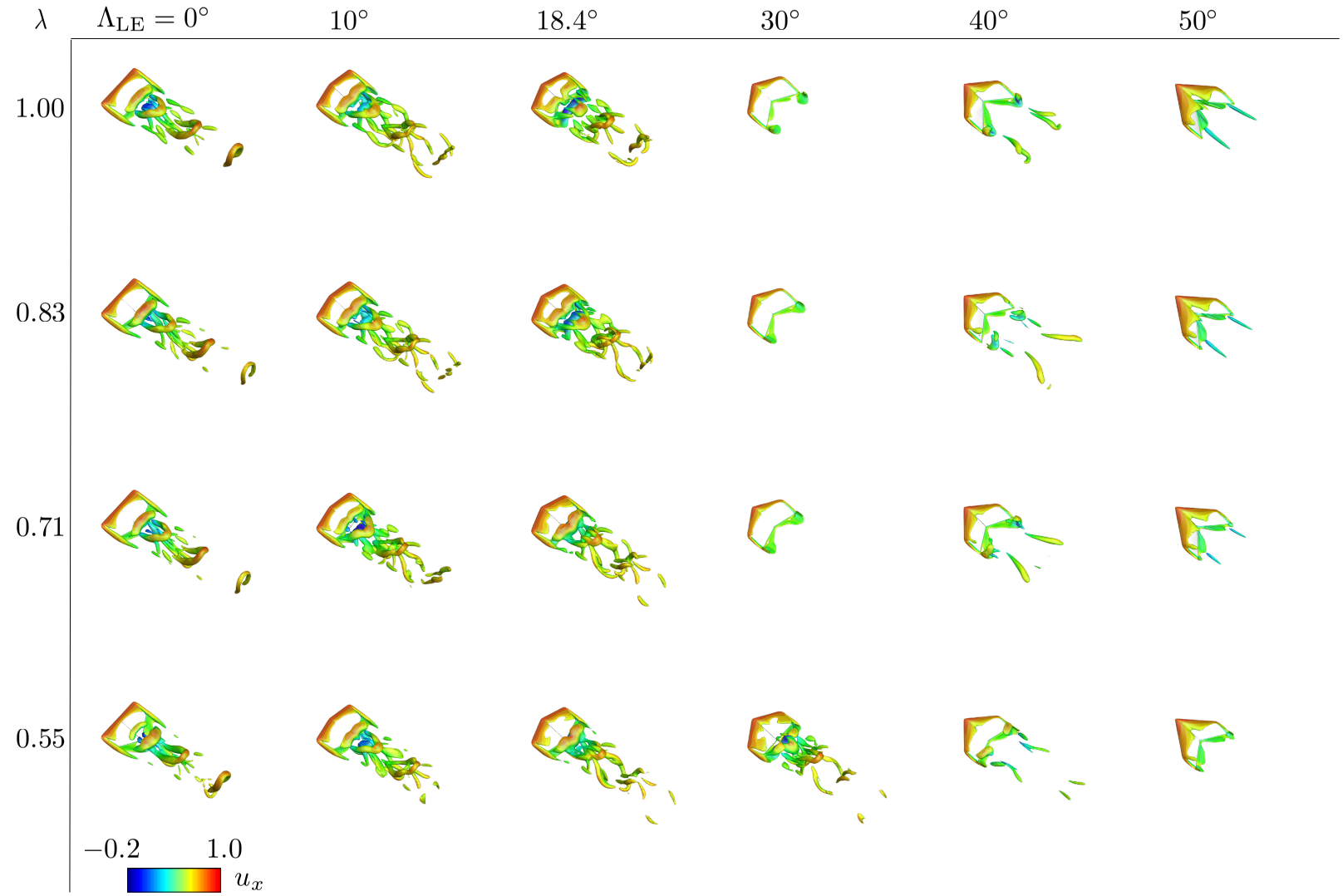

Figure 3.7: Perspective view. Isosurfaces of $Q = 1$, $Re_c = 600$ flows over $(sAR, \alpha) = (1, 22°)$ wings.

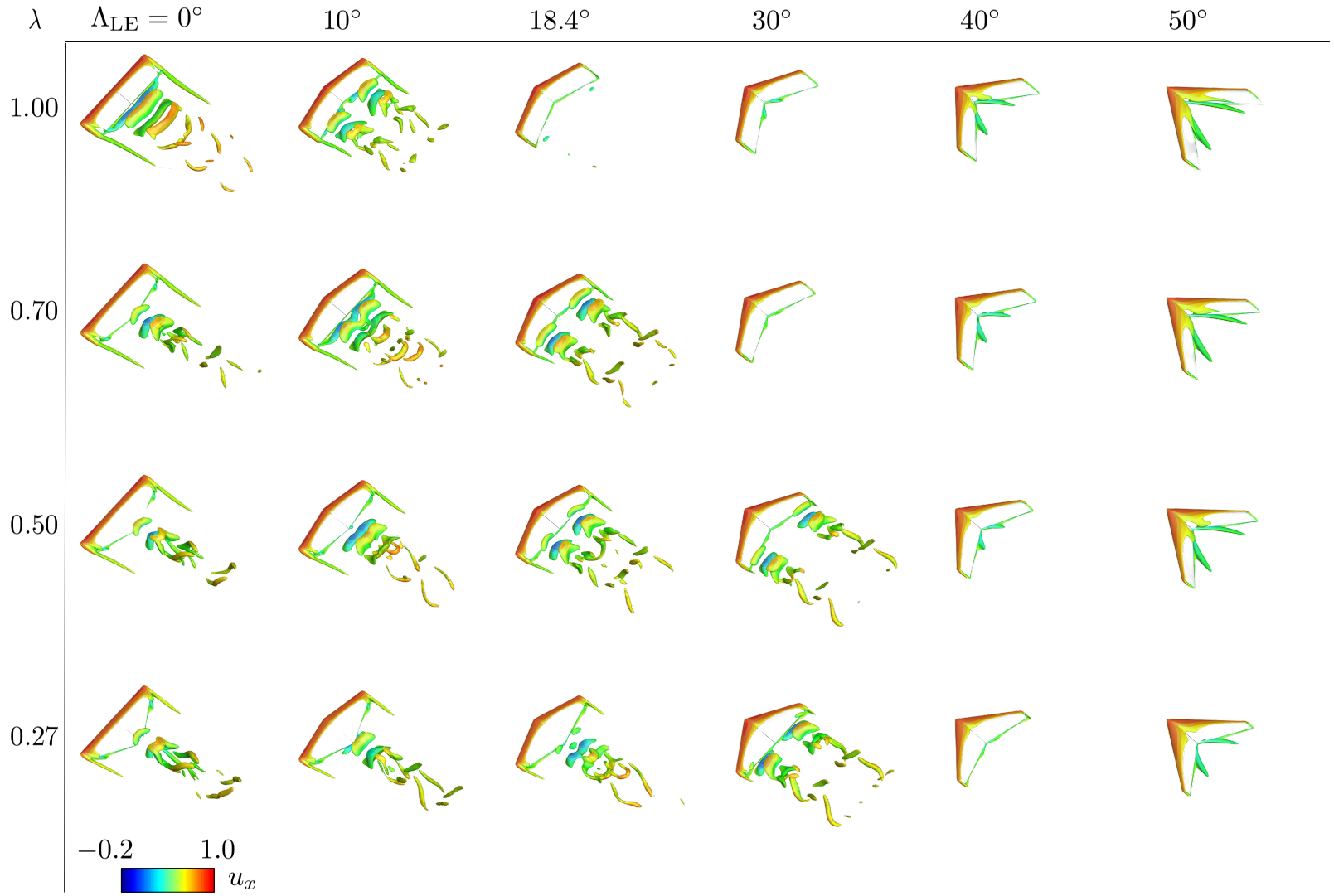

Figure 3.8: Perspective view. Isosurfaces of $Q = 1$, $Re_c = 600$ flows over $(sAR, \alpha) = (2, 14°)$ wings.

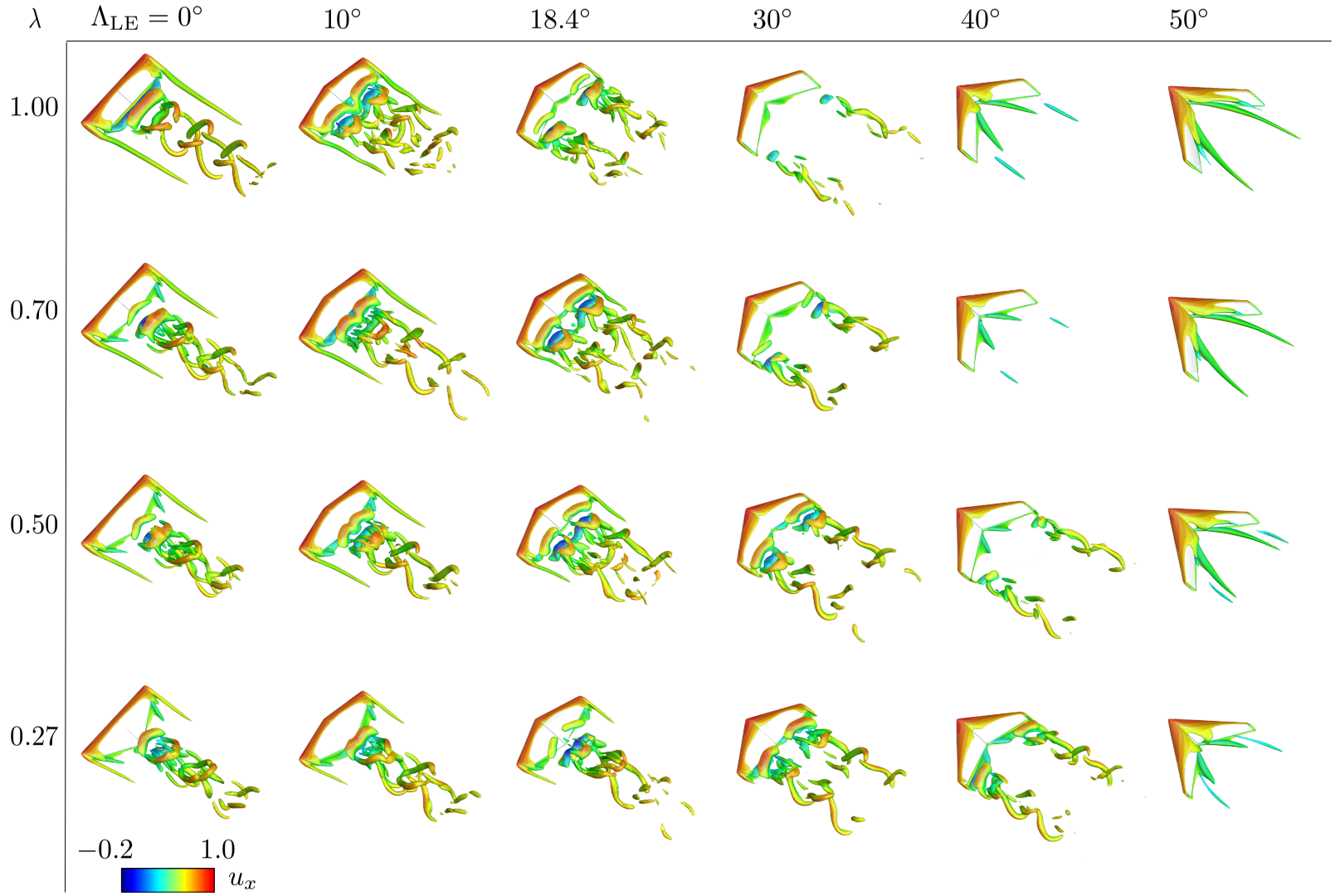

Figure 3.9: Perspective view. Isosurfaces of $Q = 1$, $Re_c = 600$ flows over $(sAR, \alpha) = (2, 18°)$ wings.

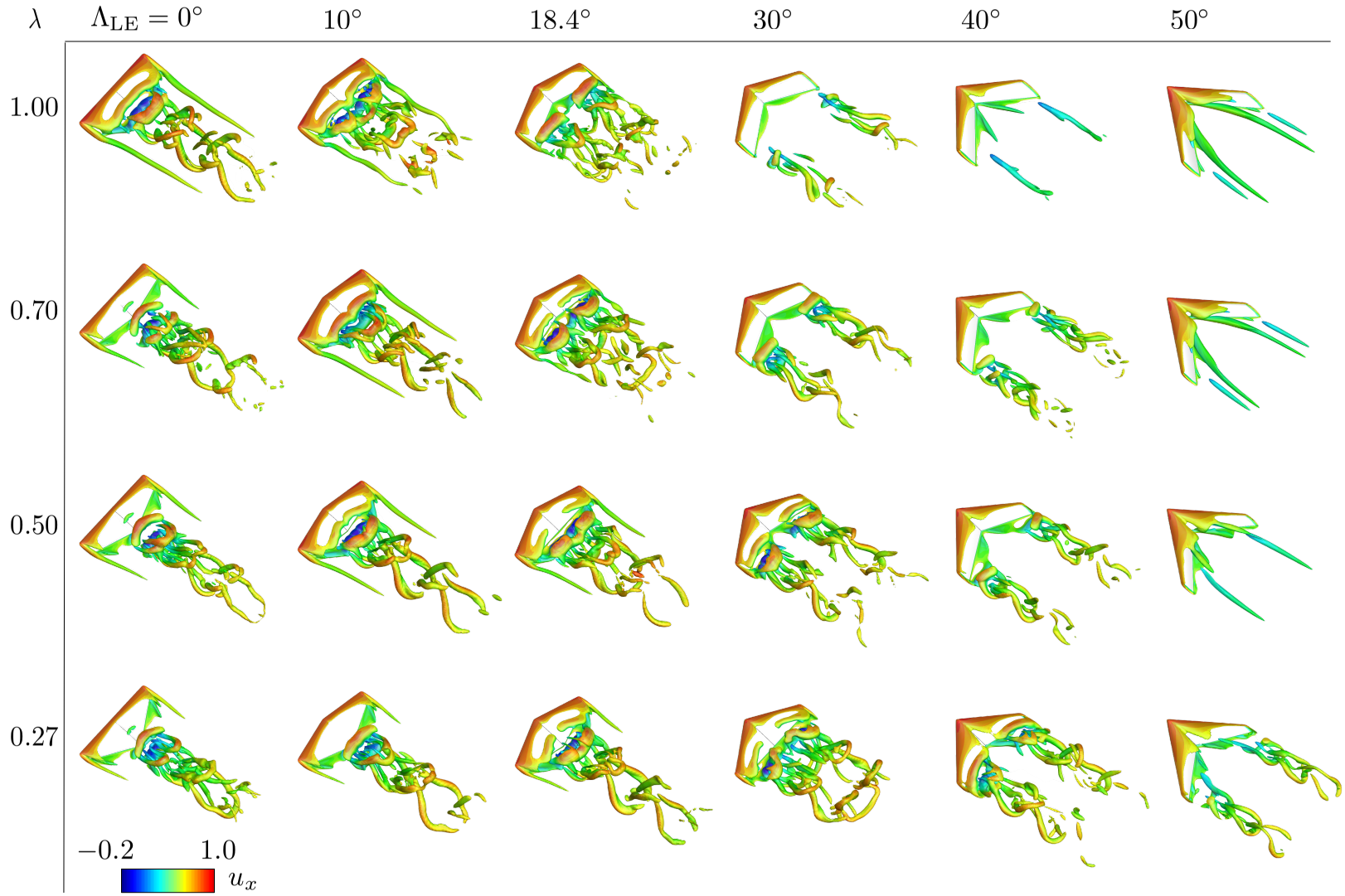

Figure 3.10: Perspective view. Isosurfaces of $Q = 1$, $Re_c = 600$ flows over $(sAR, \alpha) = (2, 22°)$ wings.

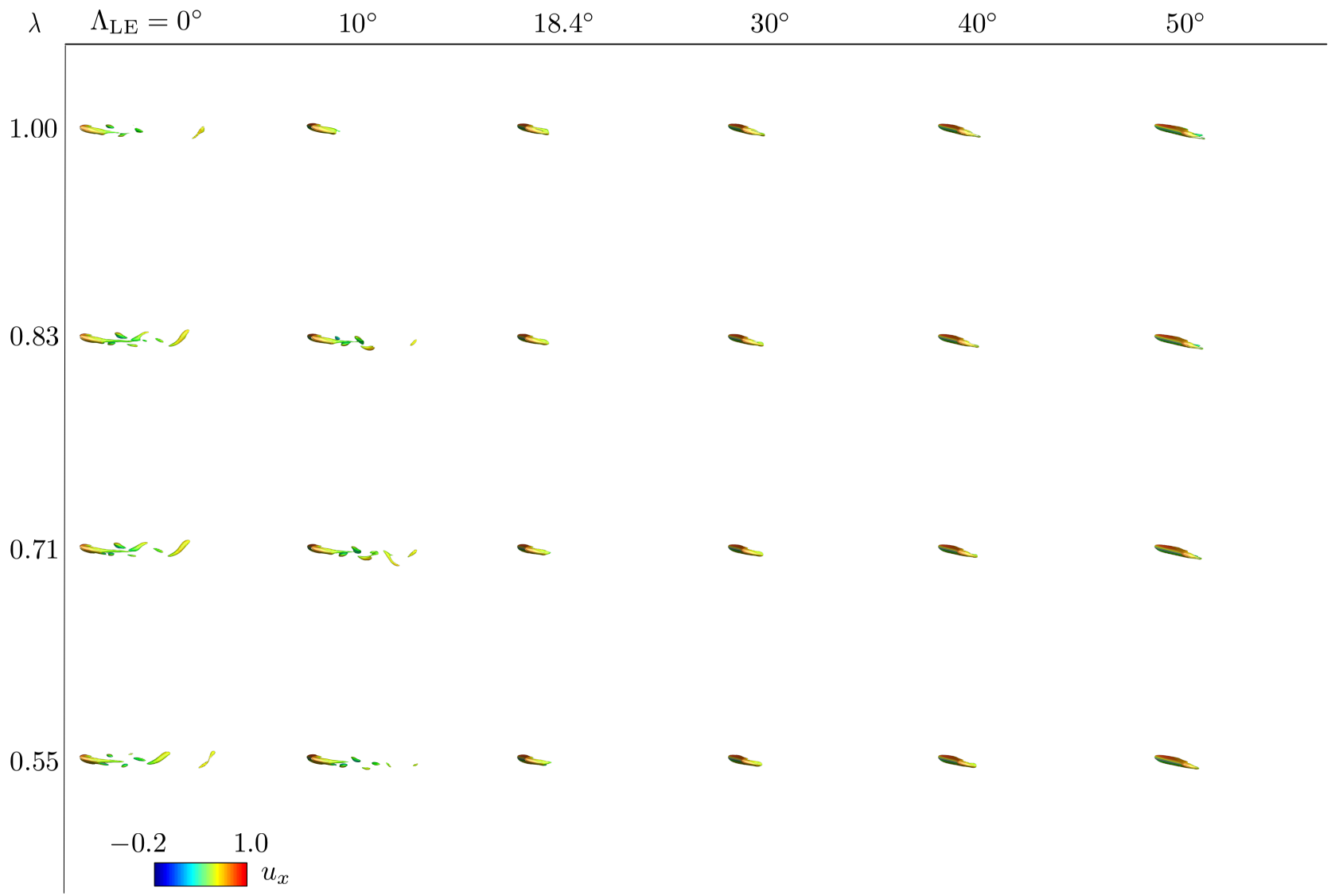

Figure 3.11: Side view. Isosurfaces of $Q = 1$, $Re_c = 600$ flows over $(sAR, \alpha) = (1, 14°)$ wings.

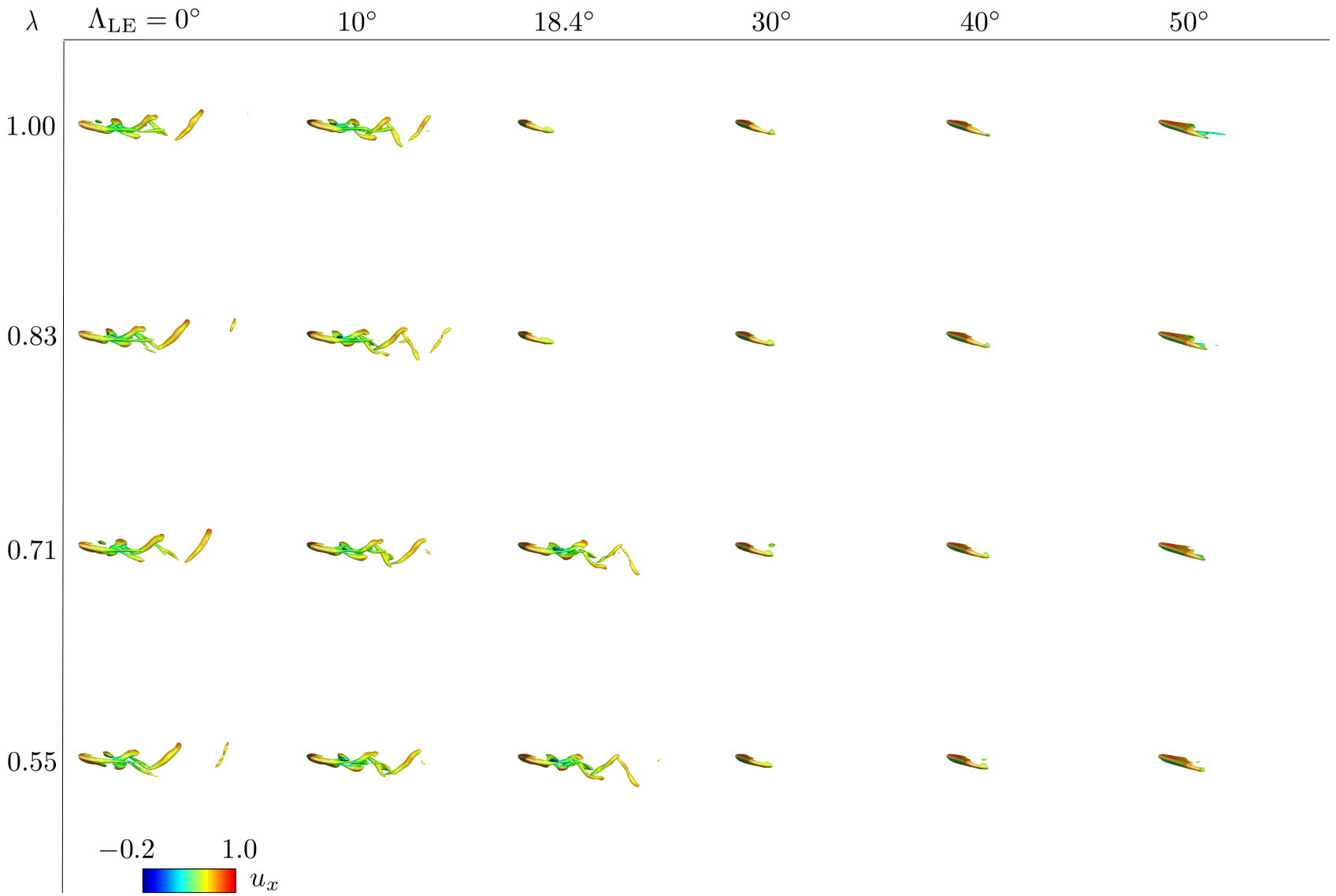

Figure 3.12: Side view. Isosurfaces of $Q = 1$, $Re_c = 600$ flows over $(sAR, \alpha) = (1, 18°)$ wings.

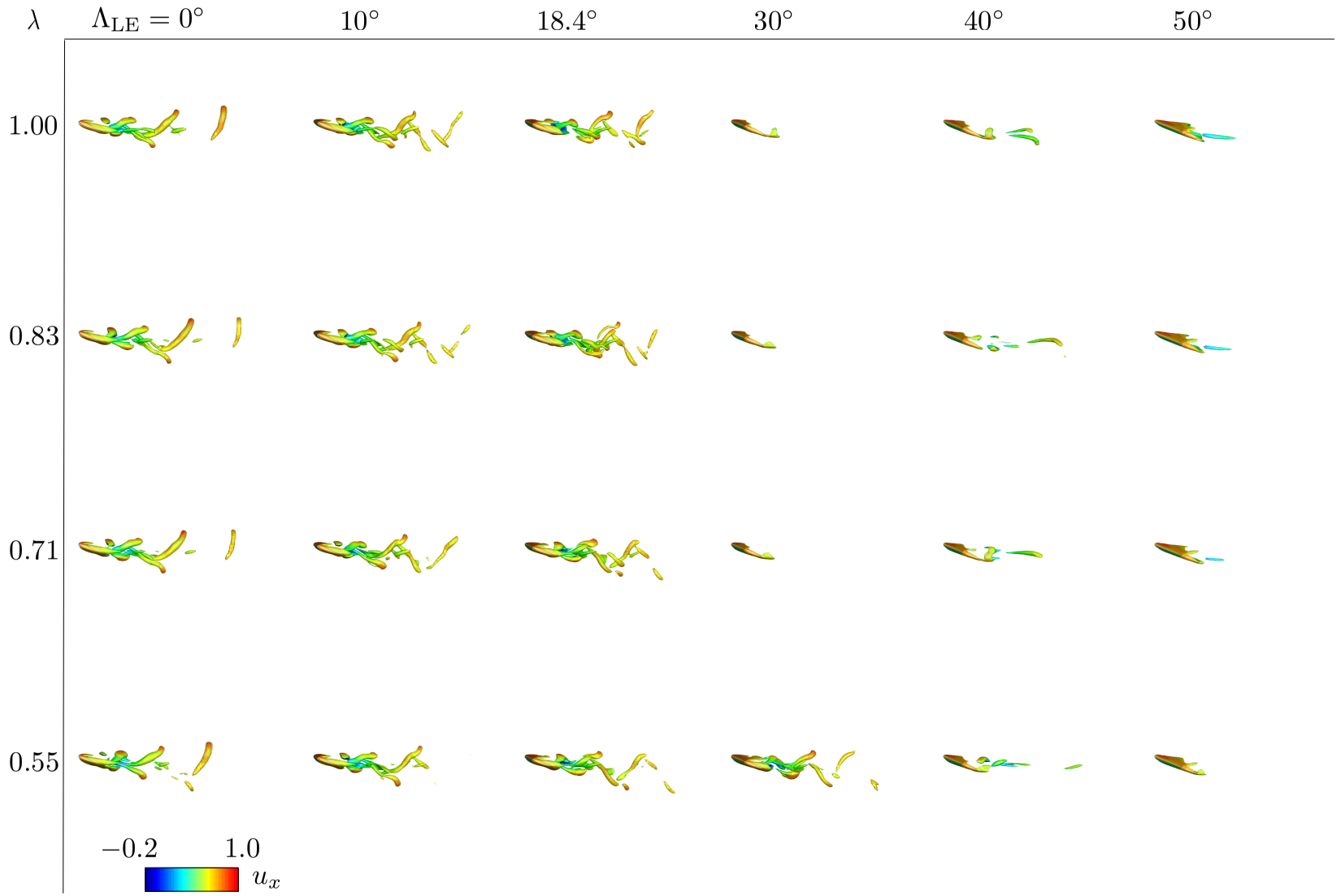

Figure 3.13: Side view. Isosurfaces of $Q = 1$, $Re_c = 600$ flows over $(sAR, \alpha) = (1, 22°)$ wings.

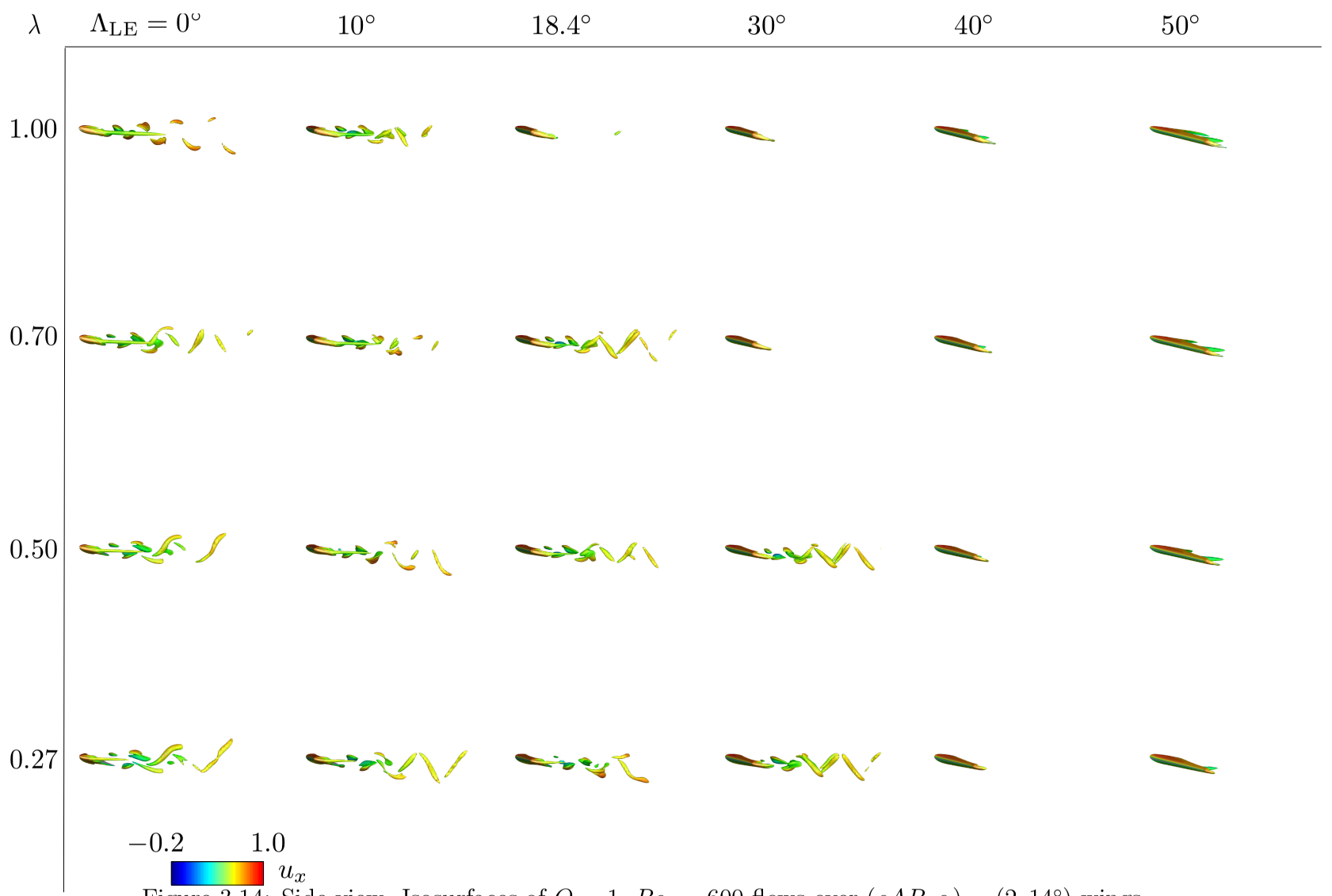

Figure 3.14: Side view. Isosurfaces of $Q = 1$, $Re_c = 600$ flows over $(sAR, \alpha) = (2, 14°)$ wings.

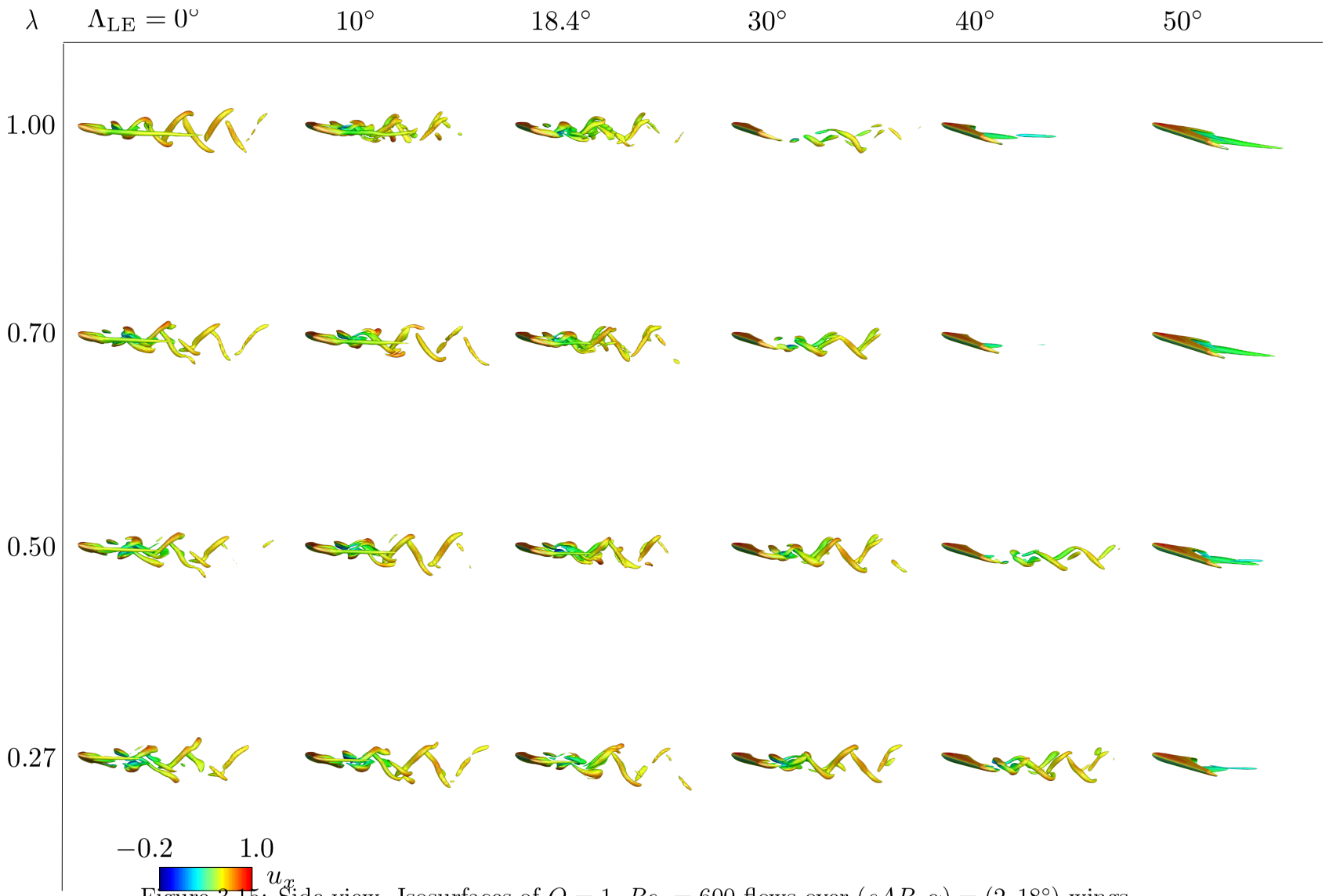

Figure 3.15: Side view. Isosurfaces of $Q = 1$, $Re_c = 600$ flows over $(sAR, \alpha) = (2, 18°)$ wings.

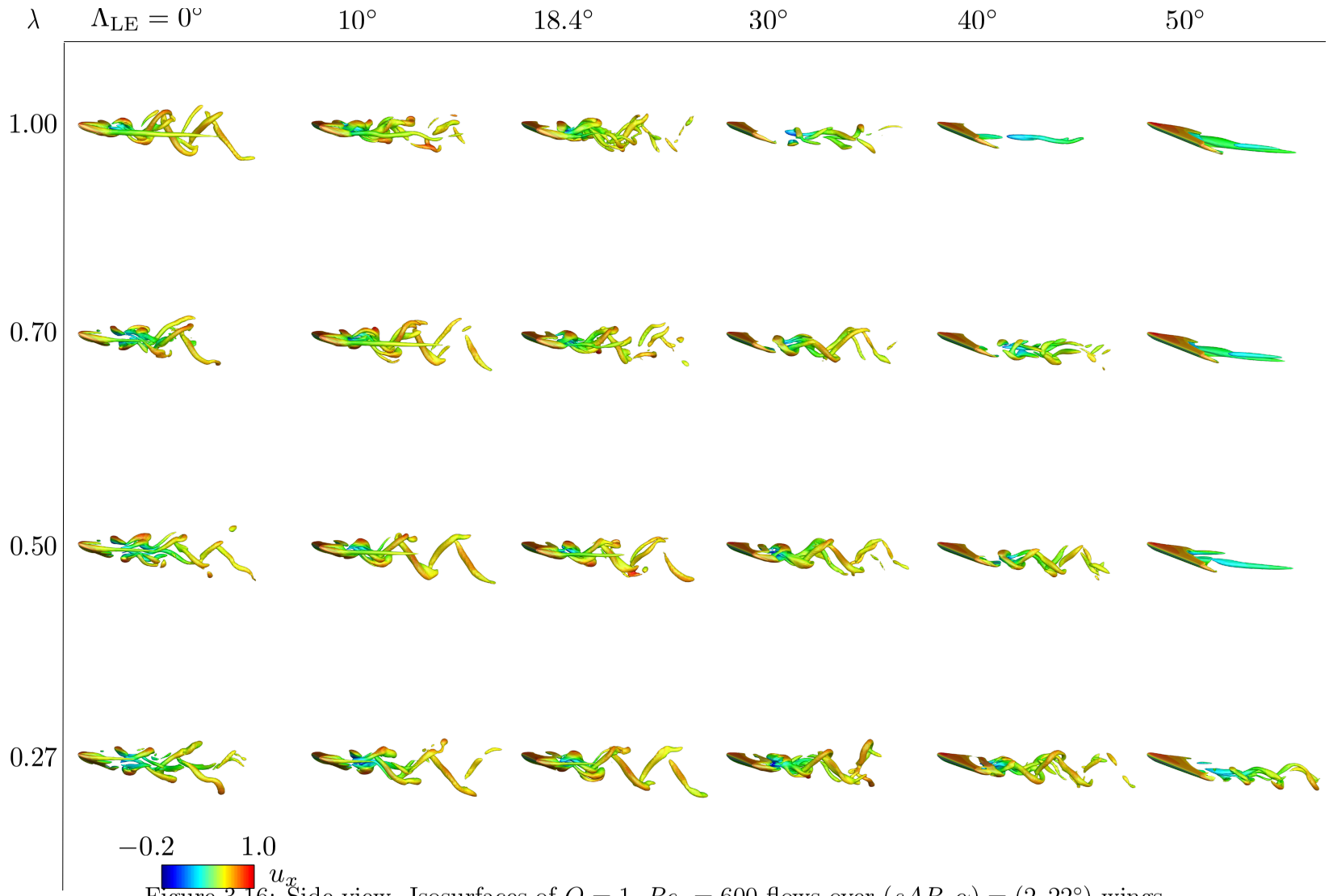

Figure 3.16: Side view. Isosurfaces of $Q = 1$, $Re_c = 600$ flows over $(sAR, \alpha) = (2, 22°)$ wings.

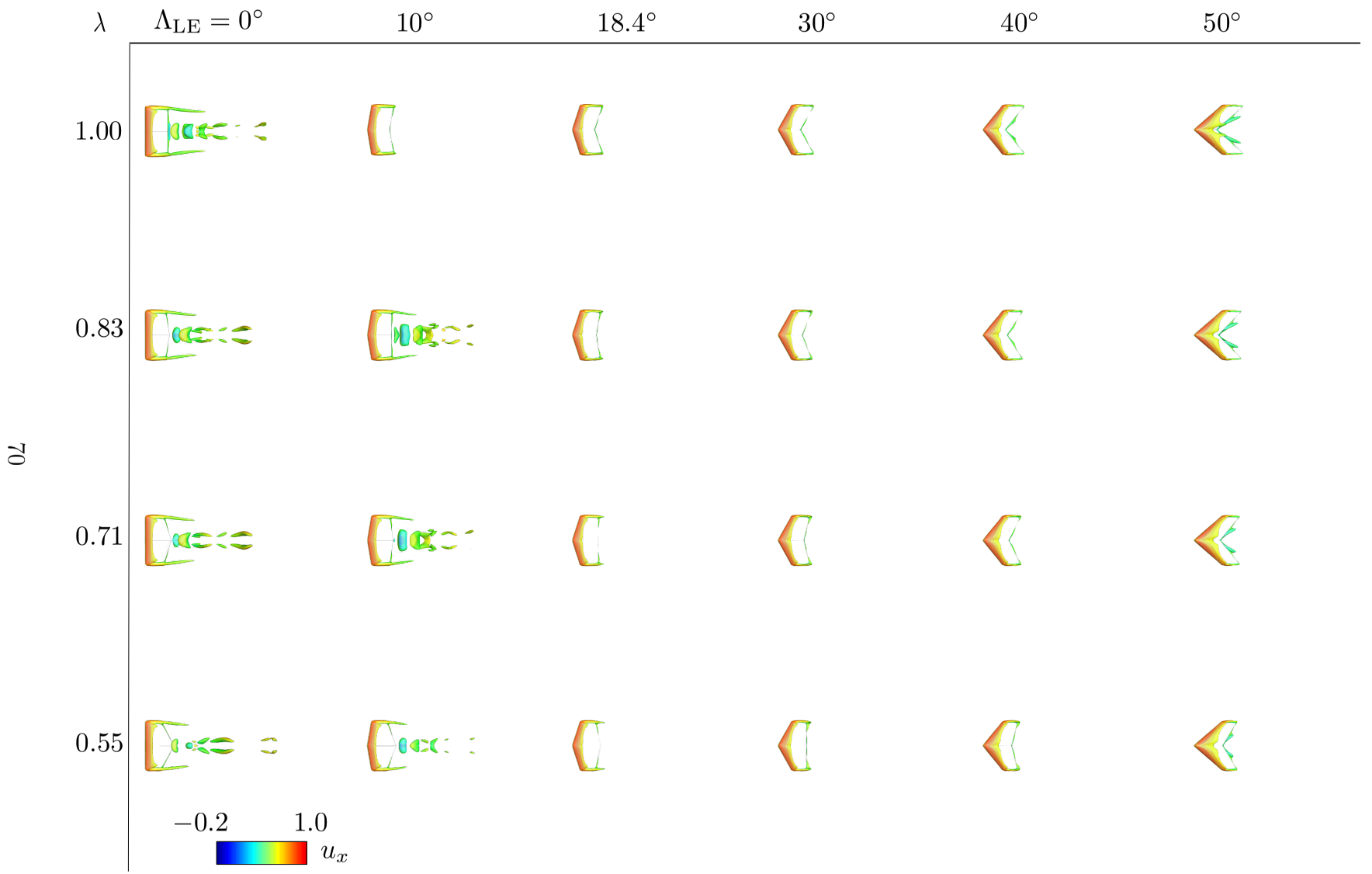

Figure 3.17: Top view. Isosurfaces of $Q = 1$, $Re_c = 600$ flows over $(sAR, \alpha) = (1, 14°)$ wings.

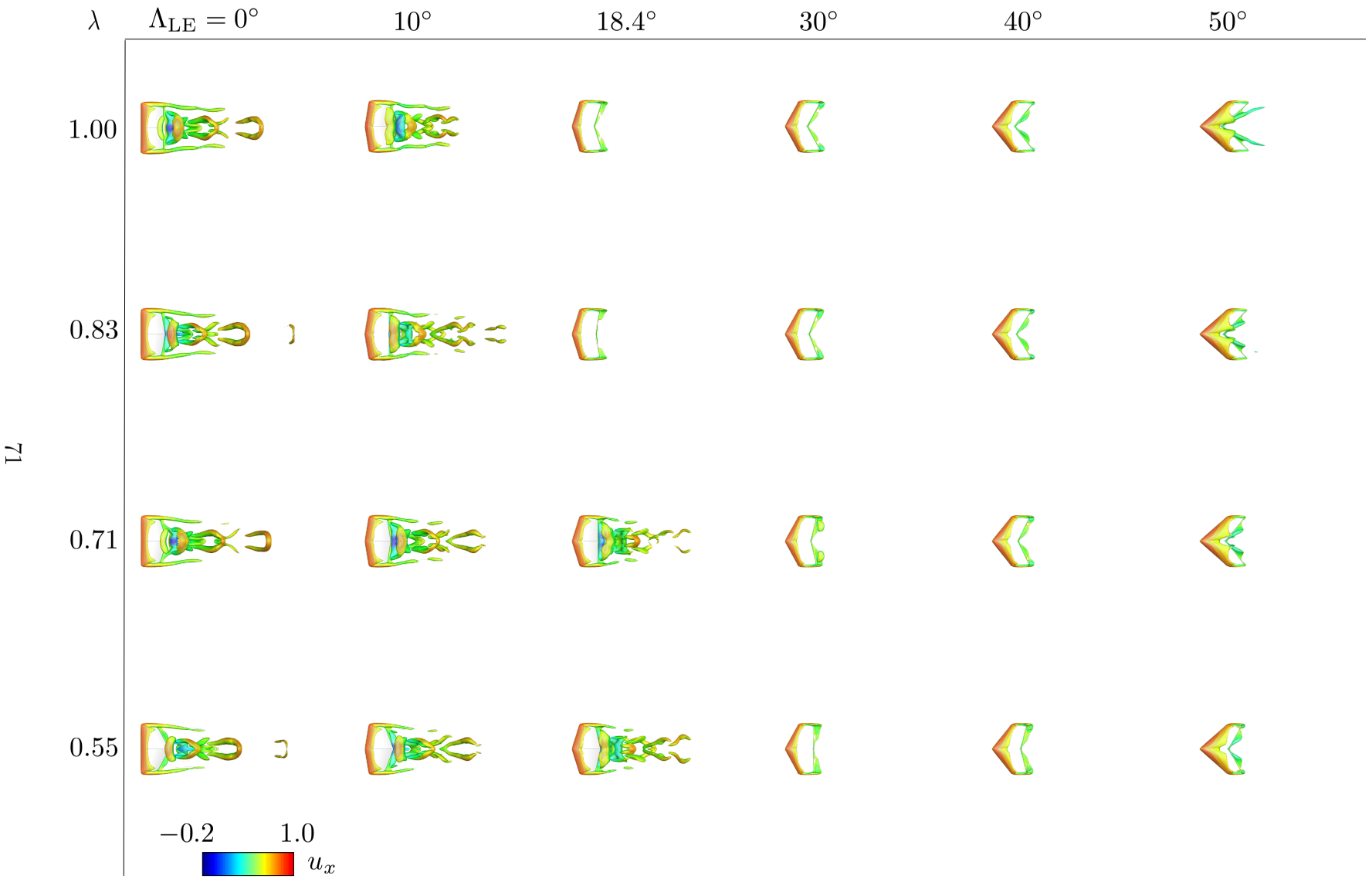

Figure 3.18: Top view. Isosurfaces of $Q = 1$, $Re_c = 600$ flows over $(sAR, \alpha) = (1, 18°)$ wings.

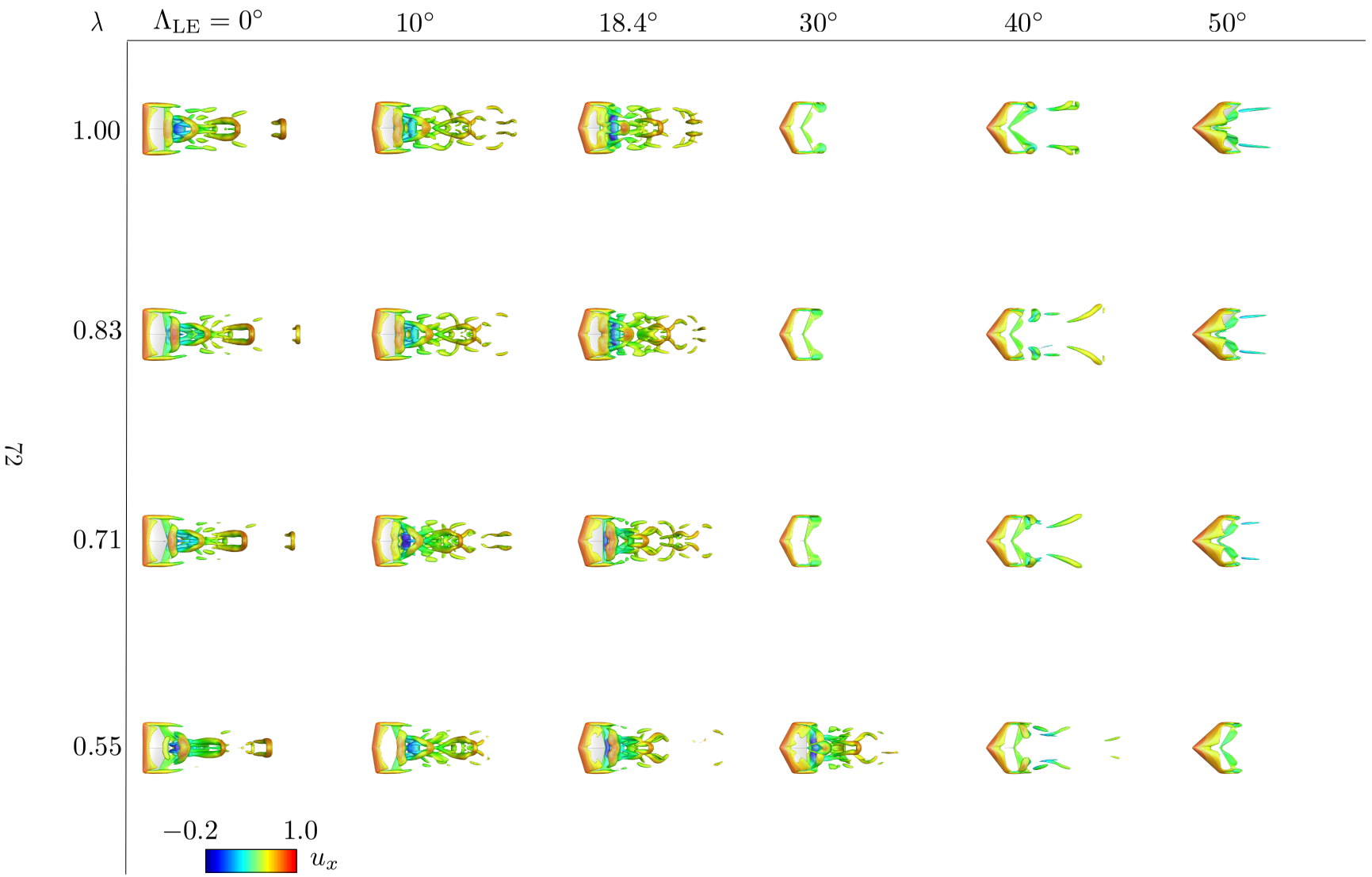

Figure 3.19: Top view. Isosurfaces of $Q = 1$, $Re_c = 600$ flows over $(sAR, \alpha) = (1, 22°)$ wings.

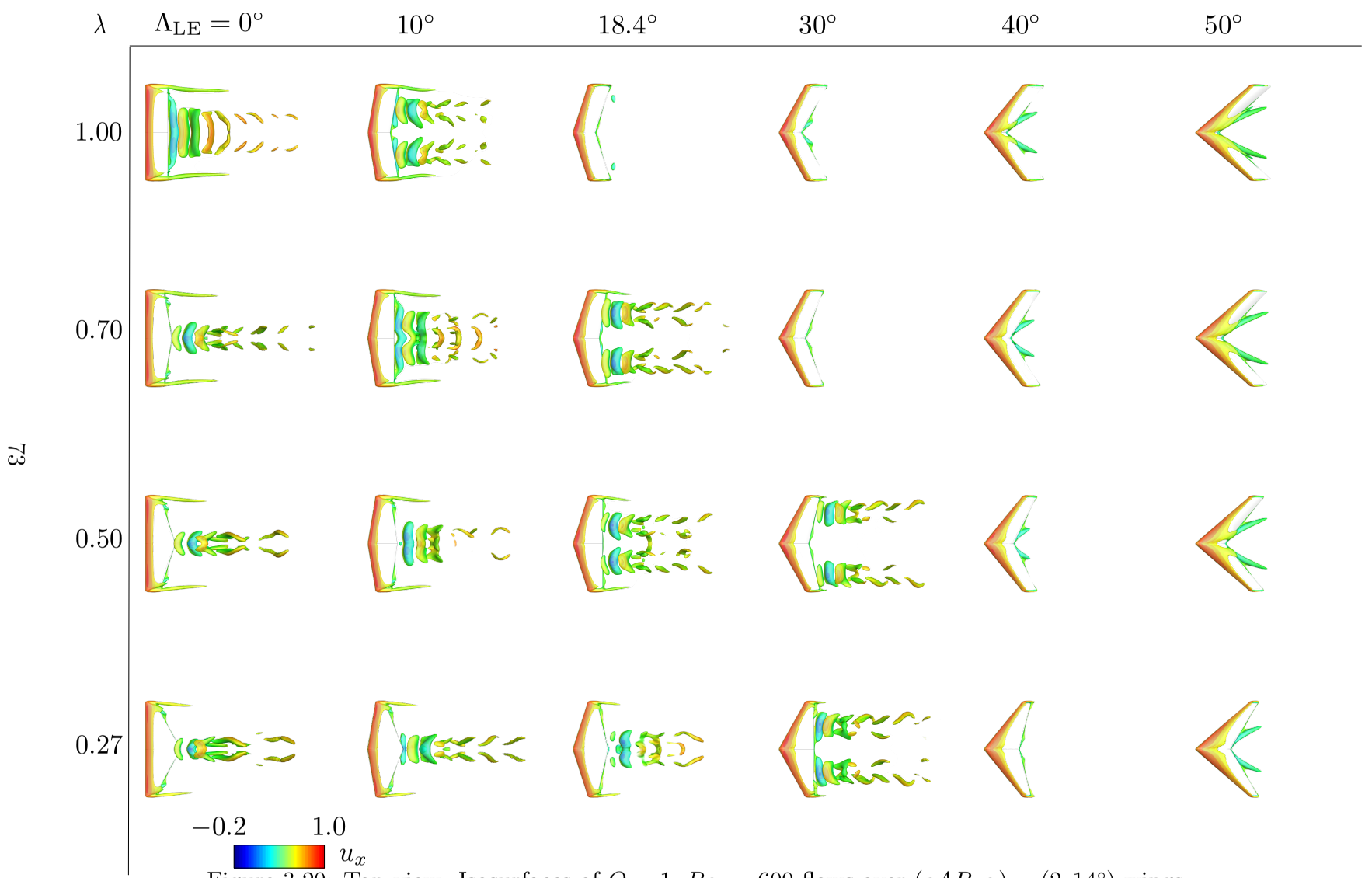

Figure 3.20: Top view. Isosurfaces of $Q = 1$, $Re_c = 600$ flows over $(sAR, \alpha) = (2, 14°)$ wings.

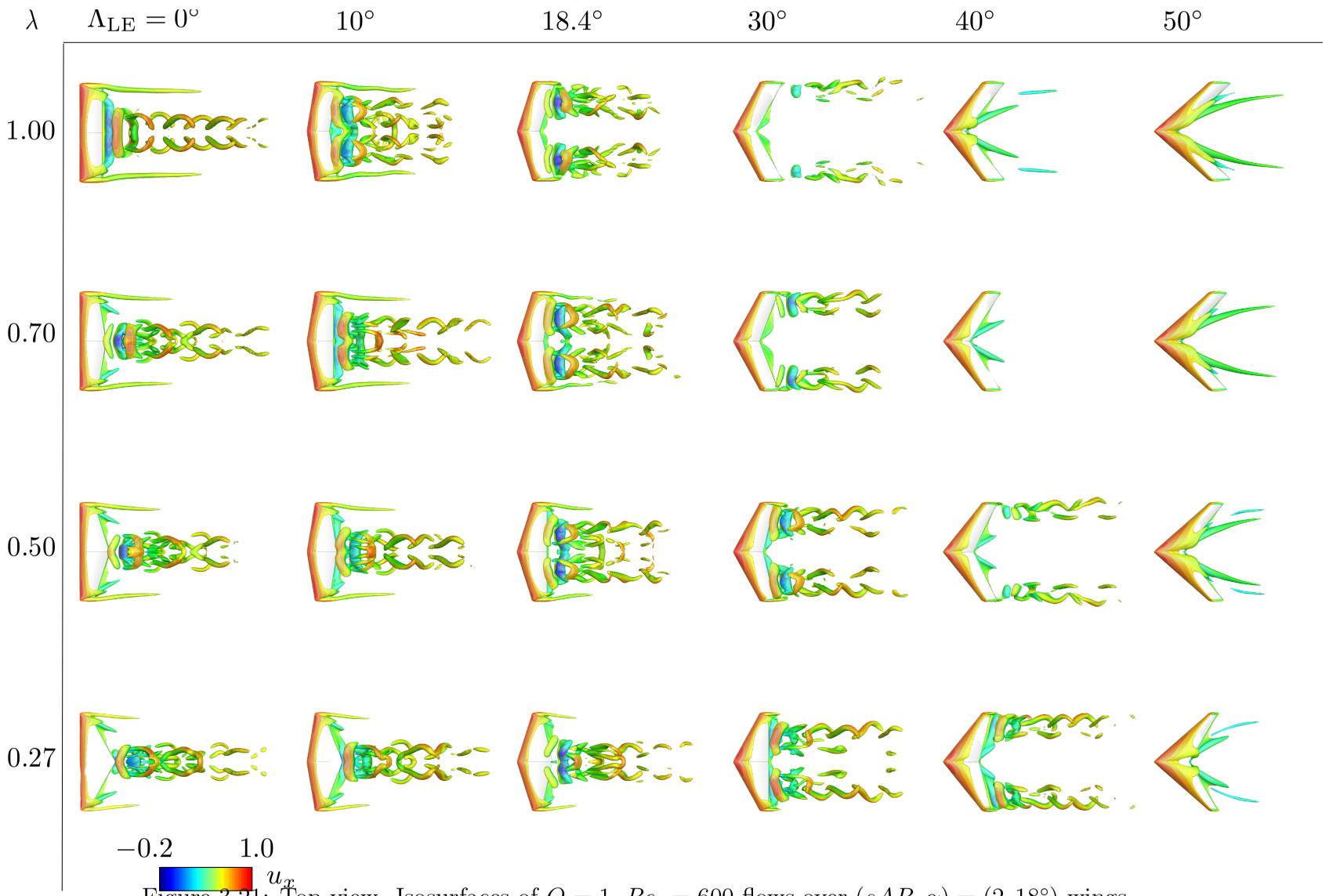

Figure 3.21: Top view. Isosurfaces of $Q = 1$, $Re_c = 600$ flows over $(sAR, \alpha) = (2, 18°)$ wings.

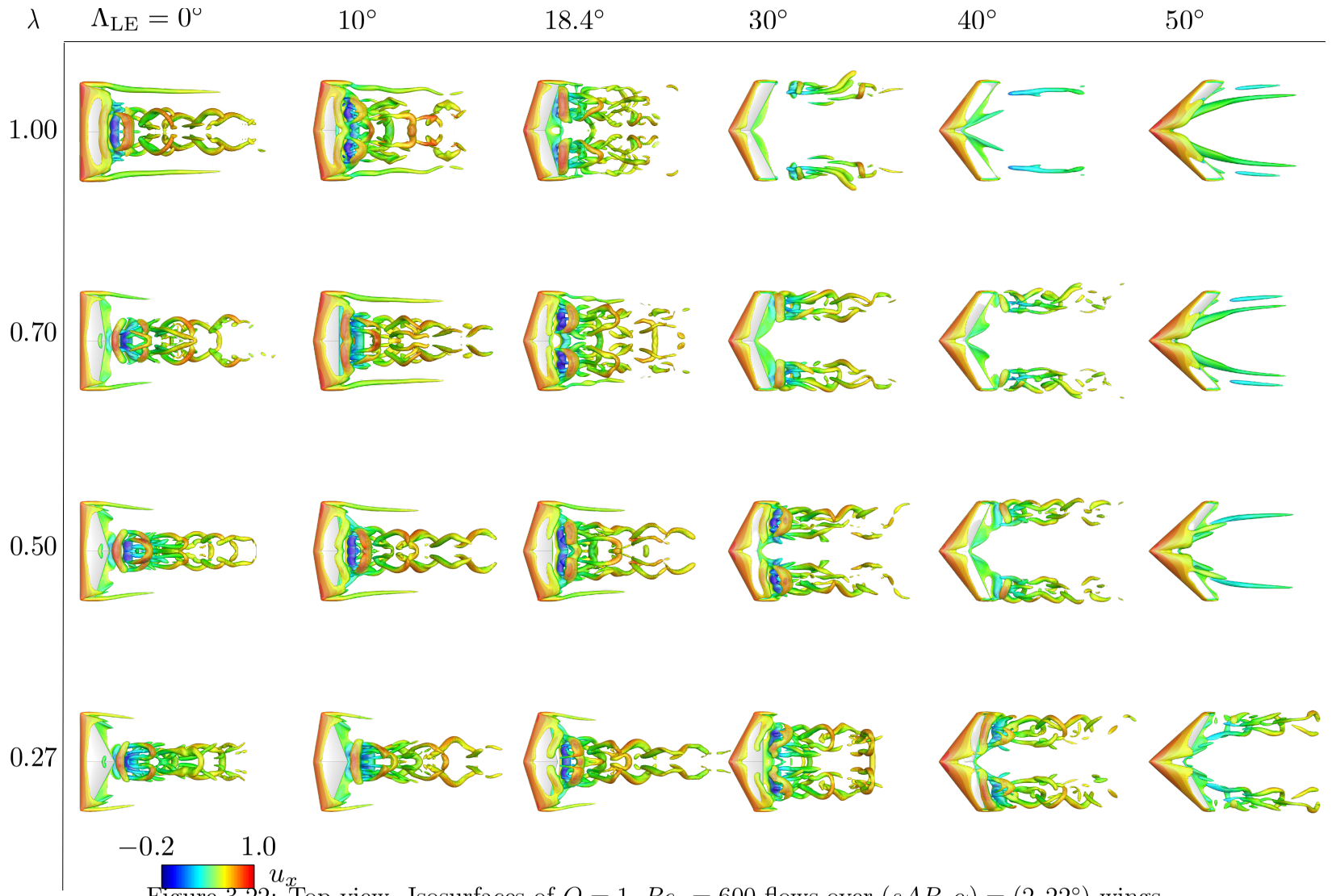

Figure 3.22: Top view. Isosurfaces of $Q = 1$, $Re_c = 600$ flows over $(sAR, \alpha) = (2, 22°)$ wings.

3.5 Characterization of tapered swept wings wakes

3.5.1 Wake classification

We now classify the wake patterns associated with tapered wing planforms. Our criterion is based on the examination of the flow characteristics downstream the airfoil on a 2-D plane at $x/c = 4$, where we identify the spatial location of maximum time-averaged $\overline{Q}$ and the maximum fluctuating component of $Q' = Q - \overline{Q}$, where Q is the second invariant of the velocity gradient tensor used to identify the vortical structures [JH95]. Maximum $\overline{Q}$ and Q' located between $0 \leq z/(c\ sAR) < 0.5$ are labeled root dominant, while points with maximum $\overline{Q}$ or Q' between $0.5 \leq z/(c\ sAR) \leq 1$ are named tip-dominant. We consider the flow as steady when the maximum fluctuating value of Q' is smaller than 0.1 at $x/c = 4$. Using the root and tip locations of $\overline{Q}$ and Q', we classify their wakes into 3 unsteady and 2 steady regimes, as shown in figure 3.23, where the steady-unsteady threshold (black dotted line) is computed via biharmonic spline interpolation and shown at the contour lever of $Q' = 0.1$. Instantaneous flow fields for all tapered wings shown in figure 3.23 are provided in the section 3.4 using isosurfaces of $Q = 1$ colored by streamwise velocity u_x.

The first flow regime (△) is composed of tapered wings wakes that have both maximum $\overline{Q}$ and Q' dominant over the root region. Such wakes appear for tapered wings with low Λ_{LE}. For such wings, the tip vortex is short in length and a $\Lambda_{\mathrm{TE}} \leq 0°$ effect concentrates shedding at the wing root. The second flow regime of unsteady wakes (◇) occurs when both maximum $\overline{Q}$ and Q' are found over the tip region. Such wakes are observed around tapered wings over a broad range of λ values, being strongly associated with high-Λ_{LE}. The flow over those wings often exhibits hairpin-type vortices in the wake.

The third flow regime of unsteady wakes (◁) around tapered wings presents maximum $\overline{Q}$ at the wing tip with maximum Q' at the root. This wake characteristic is often seen for tapered wings with high λ and wings with low Λ_{LE}, as those allow for the formation of a strong tip vortex, near the maximum $\overline{Q}$ location, and wake shedding near the root. Weak

unsteady flow oscillations can appear over the tip vortex, as shown in figure 3.23, but the most energetic vortices are generally observed over the root region.

There are two distinct flow regimes of steady wakes identified herein, as shown in figure 3.23. The first one (▼) is comprised of wakes with a steady streamwise vortex that develops into the wake. Such flows are mainly exhibited around highly swept $sAR = 2$ wings with $\lambda \geq 0.5$. The second steady wakes regime (■) is comprised of flows with no significant wake structures, with maximum $\overline{Q} \leq 0.1$ in the wake and are commonly observed for $sAR = 1$ wings and for $sAR = 2$ wings with high Λ_{LE} and low λ.

For $sAR = 2$ wings, the transition from steady to unsteady wakes is dependent of λ for each Λ_{LE}. Generally, wakes with lower taper ratios sustain unsteadiness for higher LE sweep angles than untapered wings. Let us now perform a detailed examination on the taper affects the wake unsteadiness and the separate influence of Λ_{LE} and Λ_{TE} on the wake dynamics in the following section.

3.5.2 Skin friction lines over the wing surface

The skin friction pattern shows the structure of the laminar separation bubble in the separated flow. The skin friction lines over the wing result from the near-wake vorticity field, with patterns associated with unsteady and steady coherent structures. For instance, swirl patterns near the wing tip are associated with the three-dimensionality from the tip vortex, observed in experiments and computations [WB80a, ZHA20b]. Moreover, some regions which we here call as sources appear on the skin friction field where near-wake vortices exert stronger loads over the wing and develop wake shedding, these regions are marked with blue circles in figure 3.24, where we see the effect of wing taper over the wing surface for representative cases.

Flow separation is 2-D near the symmetry plane for untapered wings, as shown in the top-left of figure 3.24, with upstream flow over a large portion of the suction side, between

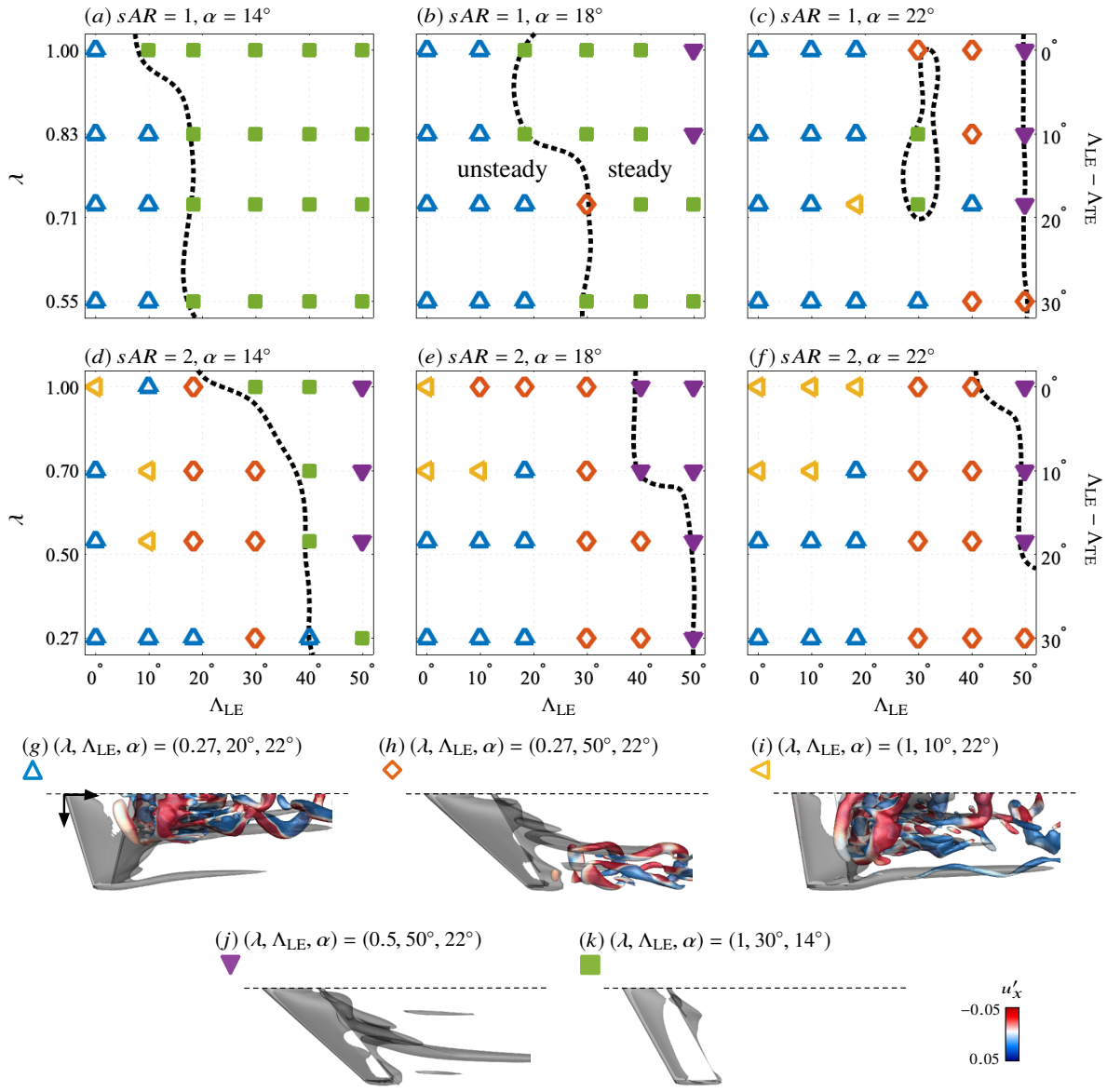

Figure 3.23: Classification map of laminar wakes over tapered wings with (*a-c*) $sAR = 1$ and (*d-f*) 2. Black dashed lines mark transition from steady to unsteady flows. (*g-k*) Five distinct wake patterns are shown for $sAR = 2$ wings visualized with time-averaged $\overline{Q} = 1$ in gray and instantaneous $Q' = 0.2$ colored by u'_x.

LE and TE. Closer to the wing tip the flow is attached, with a strong spanwise flow, and a swirl region where the tip vortex is found. With wing taper, as LE is swept backward, LE vortex is strengthened. This breaks the 2-D pattern near the root, with a strong spanwise component in that region. The skin friction source moves towards the quarter-span with the decrease in δ, as shown by blue circles in figure 3.24. Near the wing tip, the wing taper suppresses the swirl formation for $\delta \leq 0.50$, as c_{tip} reduces, exhibiting dominance of the spanwise flow component near the wing tip.

Highly swept wings with $\Lambda_{\text{LE}} = 40°$ exhibit a distinct pattern with wing taper moving the source from the tip towards the quarter-span, as shown in the bottom row of figure 3.24. For untapered wings with high sweep angles, the LE attached flow has a strong spanwise flow towards the tip at the separation line. The reversed flow is directed in the spanwise direction towards the wing root. This is associated with the ram-horn vortices that form around highly swept wings developing from the root LE and propagating as streamwise structures in the wake, as observed by [ZHA20a] and [BHH22].

For highly swept and tapered wings, the skin friction field at the LE is altered by the proximity of the TE effects. Flow is observed to arise from the skin friction source near the quarter-span. The root-directed spanwise component is weakened near the tip for $\delta = 0.50$, with the appearance of spanwise flow from quarter-span towards the tip for $\delta = 0.27$. This flow appears as the skin friction source moves from the wing tip towards the quarter-span at the TE, exhibiting a swirl pattern near the wing root. This behavior suggests that wake shedding occurs centered at the quarter-span region.

3.5.3 Tapered wings with straight LE and forward-swept TE

Let us take a closer look at the effect of wing taper for straight LE wings with forward-swept TE, as it allows us to isolate the Λ_{TE} effect on the wake dynamics. For tapered wings with $\lambda = 0.27, 0.5, 0.7$, and 1, the planforms we study in this section have $\Lambda_{\text{TE}} = -30°, -18.4°, -10°$, and $0°$, respectively. The negative Λ_{TE} indicates a forward sweep. The

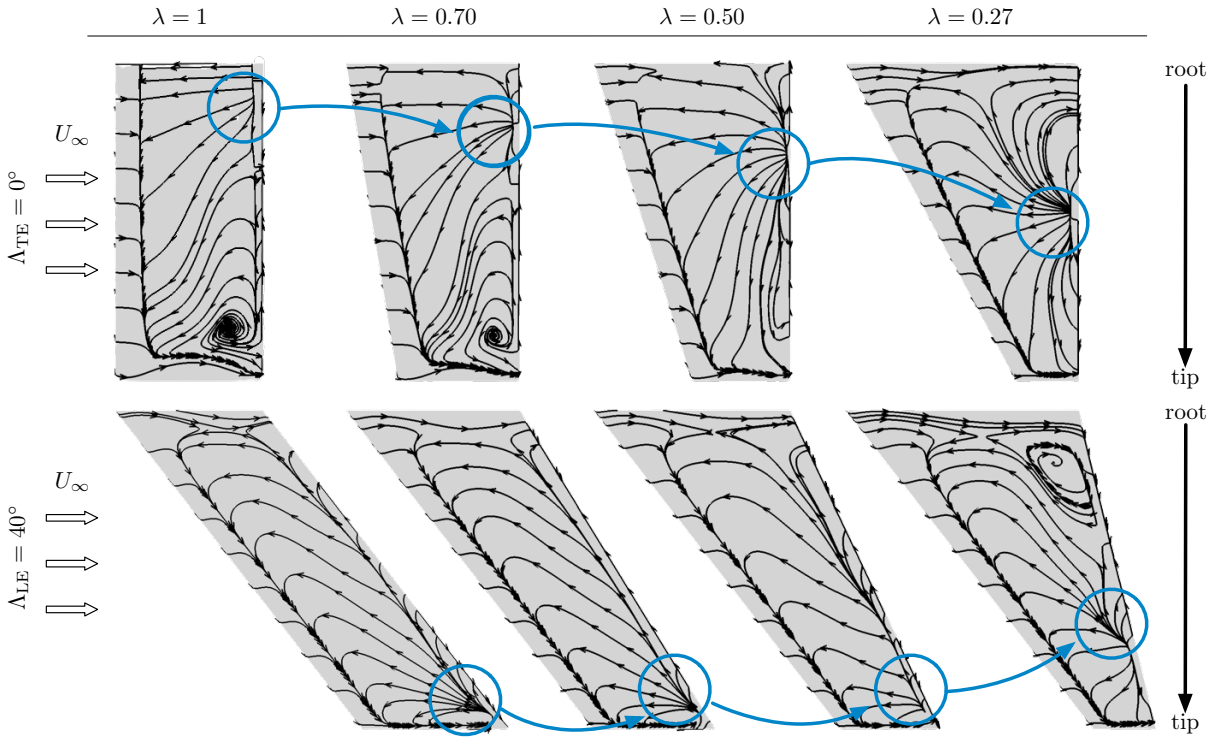

Figure 3.24: Skin friction lines on the suction surface of finite tapered wings with $0.27 \leq \delta \leq 1$, $\Lambda_{TE} = 0°$ and $\Lambda_{LE} = 40°$, and $\alpha = 22°$.

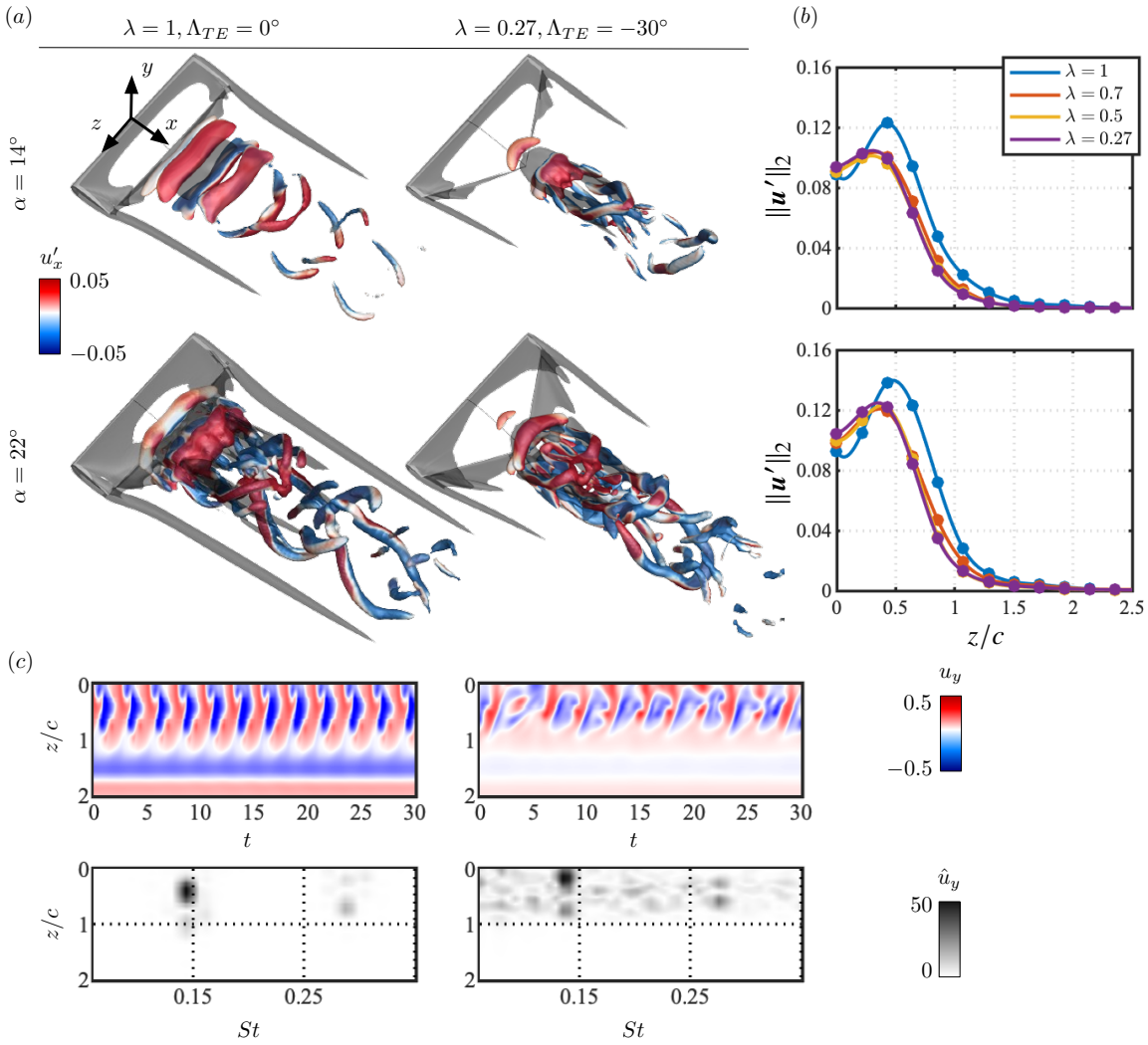

Figure 3.25: (a) Isosurfaces of flow fields around tapered wings with $sAR = 2$, $\Lambda_{\mathrm{LE}} = 0°$, $\lambda = 0.27$ and 1, $\alpha = 14°$ and $22°$. Time-averaged $\overline{Q} = 1$ isosurface is shown in gray. Instantaneous $Q' = 0.2$ isosurface is shown colored by u'_x. (b) Spanwise distribution of $\|\mathbf{u}'\|_2$ for different λ for $\Lambda_{\mathrm{LE}} = 0°$ wings. (c) Spatial-temporal (top) and PSD (bottom) of u_y distribution over the spanwise direction from probes located at $(x, y)/c = (3, -0.5)$ for the $\lambda = 0.27$ and 1 tapered wings at $\alpha = 22°$ shown above.

LE is fixed with $\Lambda_{\mathrm{LE}} = 0°$. For such wings, taper causes the wake shedding to concentrate near the root region, as shown in figure 3.25(a).

Tapered wings have a smaller tip chord length. This weakens the tip vortices and decreases its length in the streamwise direction, which alleviates the inboard downwash over the wing. Such tip vortex attenuation and the aforementioned concentration of shedding over the root region are almost independent of the angle of attack, with only minor differences observed between the flows over tapered wings at $\alpha = 14°$ and $22°$. The influence of the incidence angle appears on the formation of secondary vortices near the wing tip. For untapered wings at high incidence angle, the appearance of a secondary tip vortex emerging from the LE is known [DM17, ZHA20b]. For the tapered wings shown herein, at $\alpha = 22°$, there is also a secondary steady vortex that emerges from the TE near the wing tip region. This structure is slanted towards the root region, suggesting that perturbations arising from the TE can be advected through this vortex towards the downstream wing root region.

To gain further insights on the wake unsteadiness characteristics, we study the unsteady flow behavior over the wingspan using probe measurements of velocity fluctuations over $x/c \in [3, 4]$, $y/c \in [-1.5, 0.5]$. The x/c location is arbitrary and does not affect significantly the results. The y/c range encompasses the region where vortical structures appear. Over this region, we probe the norm of the root-mean-square (RMS) of the velocity, $\|\mathbf{u}'\|_2$. Such measurement is used as a metric to represent a spanwise distribution of flow unsteadiness, as shown in figure 3.25(b).

By examining at the spanwise $\|\mathbf{u}'\|_2$ distribution in figure 3.25(b) for untapered wings (blue), we notice that the flow unsteadiness peaks at $z/c \approx 0.5$ and decays towards the wing tip, for both angles of attack. For tapered wings, the spanwise $\|\mathbf{u}'\|_2$ curves are independent of the taper ratio for $\lambda \leq 0.7$. For such wings, taper yields an attenuation of the $\|\mathbf{u}'\|_2$ peak. The peak of $\|\mathbf{u}'\|_2$ also moves towards $z/c \approx 0$, showing a concentration of unsteadiness towards the wing root of these tapered wings.

We further characterize the effect of taper by analyzing the spatial-temporal distribution

of u_y from probes located at $(x, y)/c = (3, -0.5)$ over the spanwise direction, as it reveals how wing taper affects the shedding behavior. Herein, temporal frequency is characterized through the Strouhal number defined as $St = f(c \sin \alpha / U_\infty)$, where f is the frequency. For comparison, the wake spectra for the flow over an untapered wing is shown on the left of figure 3.25(c). For this wing, there is a narrow peak of oscillations at $St \approx 0.14$. The wake spectra is clean with a vortex shedding pattern comprised of spanwise-dominated vorticity near the root, forming hairpin vortices and a steady streamwise vortex at the wing tip. For tapered wing, the spectra is broadband as a result of the mixing of streamwise and spanwise vortices near the wing root. Even though the wake exhibits more mixing, the spanwise structures remain dominant, being related to the PSD peak at $St \approx 0.13$. We note that the PSD peak occurs at a lower St than the one observed for the untapered wing, as the flow oscillations that populate the downstream wake arise from the root region of the wing, where the chord length is enlarged.

3.5.4 Tapered wings with backward-swept LE and straight TE

Next, let us analyze the taper effects of wings with a fixed straight TE and backward-swept TE, to understand and separate the effects of the Λ_{LE} on the global wake. For such wings with $\lambda = 0.27, 0.5, 0.7$, and 1, the planforms have $\Lambda_{\mathrm{LE}} = 30°, 18.4°, 10°$, and $0°$, respectively. The positive Λ_{LE} indicates backward sweep. The TE is fixed with $\Lambda_{\mathrm{TE}} = 0°$. For such wings, taper yields an opposite effect on the wake characteristics, when compared those discussed in section 3.5.3. Herein, taper causes the wake unsteadiness to move towards the wing tip, as shown in figure 3.26(a).

Concurrently, the tip vortex weakens for tapered wings with the shortened c_{tip}, which alleviates of the inboard downwash near the tip, similar to what was observed for the wings in section 3.5.3. This increases the effective angle of attack near the tip and allows for the flow to detach from the wing surface and form wake shedding structures near $z/c \approx 1$, as shown in figure 3.26(a). We quantify the effect of wing taper on flow unsteadiness through

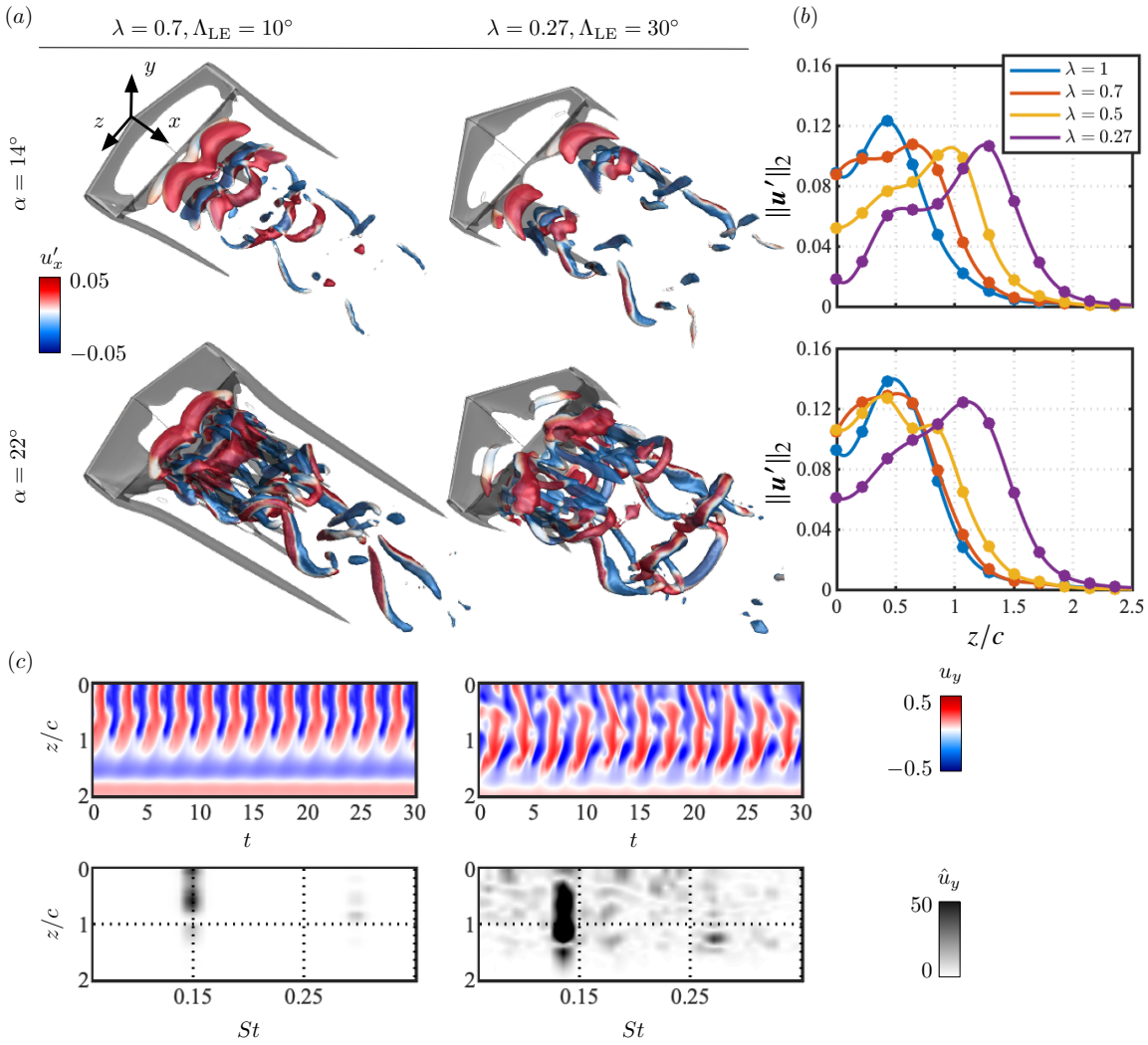

Figure 3.26: Isosurfaces of flow fields around tapered wings with $sAR = 2$, $\Lambda_{\mathrm{TE}} = 0°$, $\lambda = 0.27$ and 0.7, $\alpha = 14°$ and 22°. Time-averaged $\overline{Q} = 1$ isosurface is shown in gray. Instantaneous $Q' = 0.2$ isosurface is shown colored by u'_x. (b) Spanwise distribution of $\|\mathbf{u}'\|_2$ for different λ for $\Lambda_{\mathrm{LE}} = 0°$ wings. (c) Spatial-temporal (top) and PSD (bottom) of u_y distribution over the spanwise direction from probes located at $(x, y)/c = (3, -0.5)$ for the $\lambda = 0.27$ and 0.7 tapered wings at $\alpha = 22°$ shown above.

the wingspan distribution of $\|\mathbf{u}'\|_2$, as shown in figure 3.26(b). For both angles of attack, taper affects the wake shedding distribution over the wingspan. For $\lambda = 0.27$ (purple), at $\alpha = 22°$, the peak of $\|\mathbf{u}'\|_2$ appears near the quarter-span at $z/c \approx 1.25$, with a gradual transition towards $z/c \approx 0.5$ from $\lambda = 0.27$ to 1.

As seen in figure 3.26(b), tapered wings with forward-swept LE and straight TE exhibit unsteadiness over a larger spanwise length than untapered wings. For instance, let us observe the spanwise $\|\mathbf{u}'\|_2$ distribution for wings at $\alpha = 22°$. For the untapered wing (blue), $\mathbf{u}' \geq 0.02$ over $0 \leq z/c \leq 1$, which is the region where significant unsteady wake structures appear. Now, for the tapered wing with $\lambda = 0.27$, $\mathbf{u}' \geq 0.02$ over $0 \leq z/c \leq 1.6$, hence large unsteady structures can be observed over a larger spanwise portion of the wake.

The spatial-temporal distribution of u_y over the spanwise direction also shows that the wake of backward-swept LE and straight LE tapered wings exhibits 3-D vortical structures that result in a broadband wake spectrum, as shown in figure 3.26(c). The wake, however, is mainly dominated by large quasi-2-D spanwise aligned vortex rolls observed for all taper ratios. For $\lambda = 0.27$, as unsteadiness appears over a larger portion of the wingspan, the stronger shedding structures are hairpin-like vortices that appear between $0.5 \leq z/c \leq 1.5$, as shown on the right of figure 3.26(c).

Wing taper affects the tip vortex, which becomes consistently smaller than the tip vortex around untapered wings, as shown in figure 3.27(a). Tip vortices have high importance in terms of the aerodynamic characteristics of the wing [FK79, GA91, DRL96, BLM04, TC09, ZHA20b, DCM20, TY21, TY22] and, in the case of tapered wings, due to the small c_{tip}, tip vortices are attenuated, as a result of the reduced pressure differences between upper and lower side of the wing near the tip. Beyond that, even for wings with the same λ, the tip vortex behavior can be shifted in x-direction depending on how the wing is tapered, whether it has a backward-swept LE or a forward-swept TE, as shown in figure 3.27(b,c).

We can observe how wing taper affects the strength of the tip vortex by analyzing the $\overline{\omega_x}$ near the tip, as shown in figure 3.27(a-c). The isosurfaces of $\overline{\omega_x}$ and the contour lines at

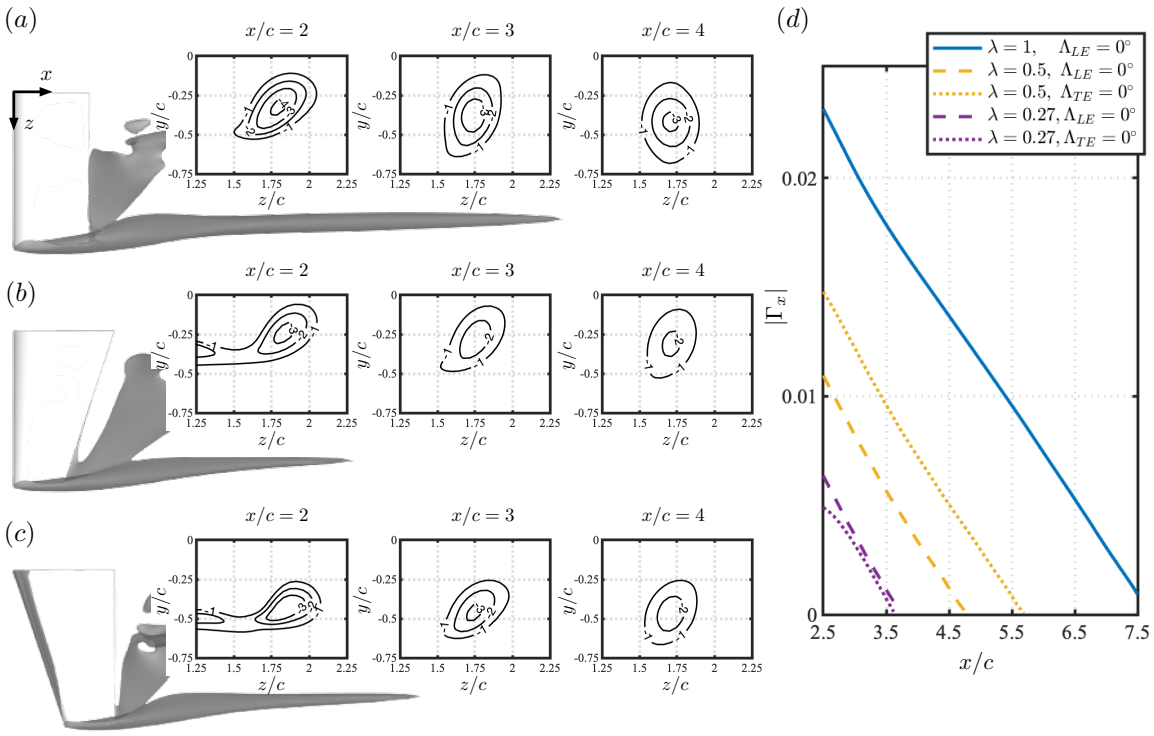

Figure 3.27: Streamwise circulation of tip vortex around (a) an untapered wing and tapered wings with $\lambda = 0.27$ with (b) straight LE and forward-swept TE and (c) backward-swept LE and straight LE. Flow field visualized with grey-colored isosurfaces of $\overline{\omega}_x = -2$ and 2-D slices with isolines of $\overline{\omega}_x$ at specific x/c locations. The magnitude of $|\Gamma_x|$ computed for the isocontour of (d) $\overline{\omega_x} = -2$ for tapered swept wings with different planform configurations.

representative x/c locations show the decay of vorticity magnitude for tapered wings with $\lambda = 0.5$. However, the effect of taper is not the same for both wings, even though they share the same taper ratio. This difference can be quantified as we compute the streamwise circulation $\Gamma = \int_C = \mathbf{u} \cdot \mathrm{d}\mathbf{l}$. Here, C is the isocontour of $\overline{\omega_x} = -2$, as shown in figure 3.27(d). The choice of $\overline{\omega_x}$ level is carefully chosen to isolate the tip vortex.

The tip vortex diffuses downstream of the wing, which makes the $|\Gamma_x|$ profiles to decay slowly [ESS18, ZHA20b]. In general, for tapered wings the reduction in c_{tip} is the main cause of the tip vortex weakening, thus the $|\Gamma_x|$ circulation decays with λ at any distance from the wing tip. The circulation $|\Gamma_x|$ further reveals how different types of wing taper can affect the of the tip vortex, as shown in figure 3.27(d). For $\lambda = 0.5$, $|\Gamma_x|$ is higher the straight TE tapered wing at any distance from the wing. For $\lambda = 0.27$, however, the taper ratio is so low that the effects of LE and TE sweep are minor on the tip vortex and $|\Gamma_x|$ distribution is similar for both wings.

3.5.5 Tapered wings with high LE sweep angles

Let us also examine how taper affects wings with high LE sweep. For the swept wings discussed herein, with $\Lambda_{\text{LE}} > 30°$, wake oscillations are strongly attenuated. For laminar flows over untapered wings with high sweep angles at moderate angles of attack, the wake becomes steady, while at high angles of attack, unsteadiness may develop in the wing tip region [ZHA20a, RYT23]. For highly swept and tapered wings, the flow exhibits wake shedding for small λ, as shown in figure 3.28(a).

Here, we analyze wings with a fixed $\Lambda_{\text{LE}} = 40°$, while the TE is swept with $\Lambda_{\text{TE}} = 10°, 21.6°, 30°$, and $40°$ for $\lambda = 0.27, 0.5, 0.7$, and 1, respectively. The onset of shedding for highly swept and tapered wings results from the distinct effects of Λ_{LE} and Λ_{TE}. For the present tapered swept wings, the vortical structures emerging from the TE promote unsteadiness in the wake near the wing tip. For lower taper ratios, wings have a low Λ_{TE}, which causes wake oscillation to appear and become large toward the root. Such effects show

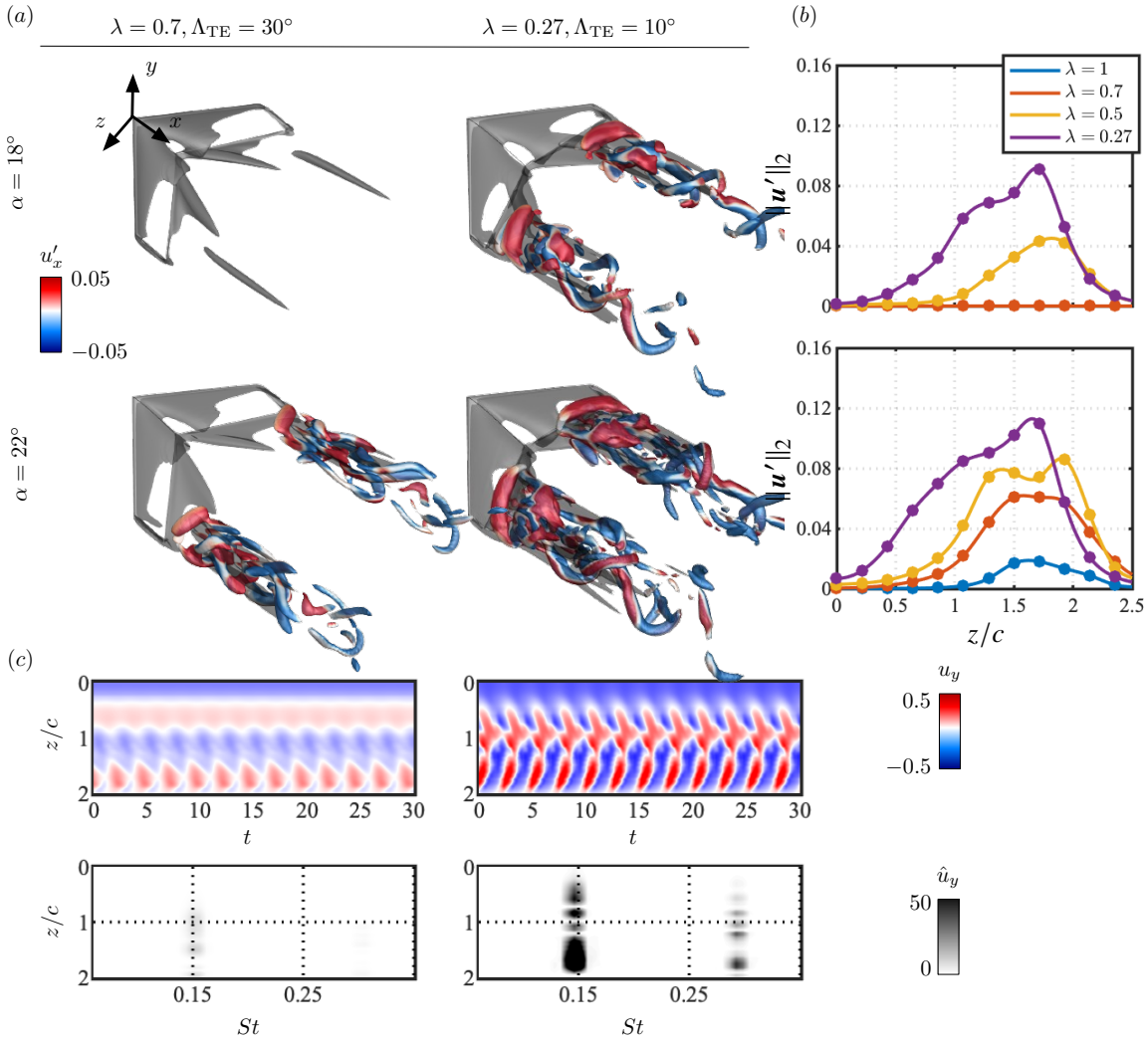

Figure 3.28: Isosurfaces of flow fields around tapered swept wings with $sAR = 2$, $\Lambda_{LE} = 40°$, $\lambda = 0.27$ and 0.7, $\alpha = 18°$ and 22°. Time-averaged $\overline{Q} = 1$ isosurface is shown in gray. Instantaneous $Q' = 0.2$ isosurface is shown colored by u'_x. (b) Spanwise distribution of $\|\mathbf{u}'\|_2$ for different λ for $\Lambda_{LE} = 0°$ wings. (c) Spatial-temporal (top) and PSD (bottom) of u_y distribution over the spanwise direction from probes located at $(x, y)/c = (3, -0.5)$ for the $\lambda = 0.27$ and 0.7 tapered wings at $\alpha = 22°$ shown above.

that while the high Λ_{LE} has the effect of stabilizing wake oscillations for untapered wings, the combination of wing taper and sweep can promote wake unsteadiness.

For instance, at $\alpha = 18^\circ$ the wake is steady for $\lambda = 0.7$ with long steady streamwise vortices developing from both LE and TE. At $\lambda = 0.5$, unsteadiness appears with vortex rolls at the wing tip, with wake shedding appearing for $\lambda = 0.27$. We quantify the wing taper effect in figure 3.28(b). For instance, for the wings with $\lambda \geq 0.7$ at $\alpha = 18^\circ$, the flow is steady and $\|\mathbf{u}'\|_2$ is negligible in the wake. At $\alpha = 22^\circ$, $\|\mathbf{u}'\|_2$ is small for untapered wings, increasing considerably in magnitude and spanwise length as the taper ratio decreases. For highly swept tapered wings, the flow fluctuations appear at the tip, further appearing over the midspan for the lower taper ratios.

The unsteady vortices exhibited in the wakes of tapered wings with high LE sweep angles behave as vortex shedding structures, as shown by the probed u_y in the wake in figure 3.28(c). For $\lambda = 0.7$, the vortices appear as a consistent oscillation near the wing tip. For $\lambda = 0.27$, the wake is dominated by spanwise-aligned roll structures that occupy a large portion of the wingspan. As these structures develop from the wingspan region near the wing tip, which has a reduced chord length, their frequency $St \approx 0.15$ is slightly higher than the shedding frequency of untapered wings.

We also present the effect of wing taper on the wake unsteadiness for other wing geometries, as shown in figure 3.29. The results show how wings with low Λ_{LE}, as shown in figure 3.29(a) can concentrate flow oscillations near the root plane, while the opposite happens for tapered wings with backward-swept LE and unswept TE, shown in figure 3.29(b). Over such wings, unsteady vortical structures are advected towards the wing tip region. For wings with a high Λ_{LE}, as shown in figure 3.29(c), the wing taper increases the magnitude of flow unsteadiness near the wing tip and vortex shedding emerges near the wing tip. The magnitude of wake oscillations increases in magnitude towards the midspan for lower λ. In the next section, we explore how these different wake patterns affect the stall region over the wing.

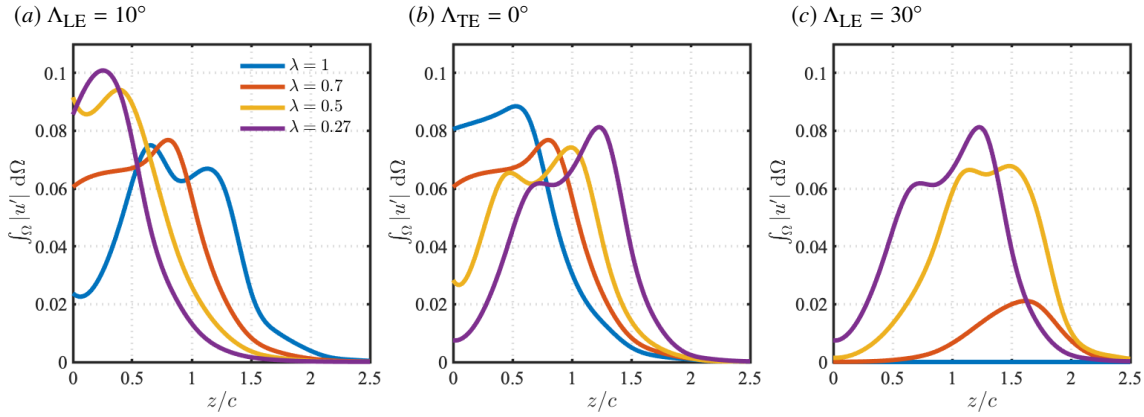

Figure 3.29: Effect of wing taper on flow unsteadiness over wingspan for $sAR = 2$ wings at $\alpha = 14°$ with low (a) $\Lambda_{LE} = 10°$, (b) unswept TE, and (c) $\Lambda_{LE} = 40°$.

3.5.6 Aerodynamic loads and force elements

The difference in tapered wing planforms results in a variety of wake patterns that further affect the aerodynamic forces over the wing and their distribution over the wingspan. Herein, we report the aerodynamic forces through their lift and drag coefficients defined as

$$C_L = \frac{F_y}{\frac{1}{2}\rho U_\infty^2 bc} \quad \text{and} \quad C_D = \frac{F_x}{\frac{1}{2}\rho U_\infty^2 bc} \, , \tag{3.2}$$

where F_x and F_y are the x and y components, respectively, of the viscous and pressure forces integrated over the wing surface. For the aerodynamic forces presented in figure 3.30, the x-axis is chosen to be the $\Lambda_{c/4}$, as this is the aerodynamic center of the wing, traditionally used in aeronautics and aircraft design to represent wing sweep for tapered wings [And10]. From figure 3.31 it is challenging to identify a trend for the effect of wing taper and sweep, although some observations can be made. The wings with high $\overline{C_L}$ are the untapered and unswept wings and the tapered wings with high $\Lambda_{c/4}$. The wings with lower $\overline{C_L}$ appear as the tapered wings with low $\Lambda_{c/4}$ and the highly swept and untapered wings.

For the tapered wings with $0° < \Lambda_{c/4} < 40°$ conclusions with respect to the overall lift can be misleading. We note, however, a trend on $\overline{C_D}$ to decrease with the increase in $\Lambda_{c/4}$, as shown in figure 3.31(b). Wings with low $\Lambda_{c/4}$ exhibit a higher overall $\overline{C_D}$ than swept wings.

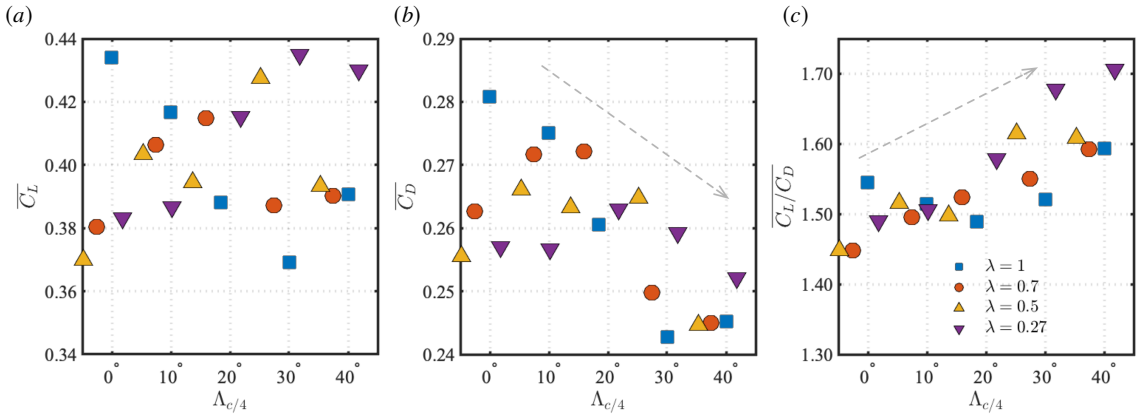

Figure 3.30: Time-averaged aerodynamic force coefficients: (a) $\overline{C_L}$, (b) $\overline{C_D}$, and (c) $\overline{C_L/C_D}$, for wings with $sAR = 2$, $0.27 \leq \lambda \leq 1$, with various sweep angles at $\alpha = 18°$. Light-gray arrows show the trend of decreasing $\overline{C_D}$ and increasing $\overline{C_L/C_D}$ with $\Lambda_{c/4}$.

In addition, wings with high $\Lambda_{c/4}$ exhibit a similar low $\overline{C_D}$ for all λ. This affects the $\overline{C_L/C_D}$ results shown in figure 3.31(c). The aerodynamic performance of the wing increases with $\Lambda_{c/4}$. The wings with higher $\overline{C_L/C_D}$ are the tapered wings with the lowest λ and high $\Lambda_{c/4}$. This enforces the idea that a combination of taper and sweep is beneficial to the aerodynamic performance of the wing in post-stall flow conditions.

To further understand the effect of taper and sweep on the aerodynamic forces, we present the time-averaged $\overline{C_L}$ and $\overline{C_L/C_D}$ for the the representative wings discussed in sections 3.5.3, 3.5.4, and 3.5.5, as shown in figure 3.31. The blue symbols present the aerodynamic loads for tapered wings with straight LE and forward-swept TE. The red symbols show the results for tapered wings with backward-swept LE and straight TE, while the yellow symbols represent tapered wings with $\Lambda_{\text{LE}} = 40°$.

The effect of wing taper in the aerodynamic loads is strongly dependent on how the wing is tapered. Whether it has a LE or a TE sweep is paramount to its overall lift and aerodynamic performance. Let us start from the untapered and unswept wings, marked by blue downward-pointing triangles at $\lambda = 1$. At each angle of attack, for lower taper ratios,

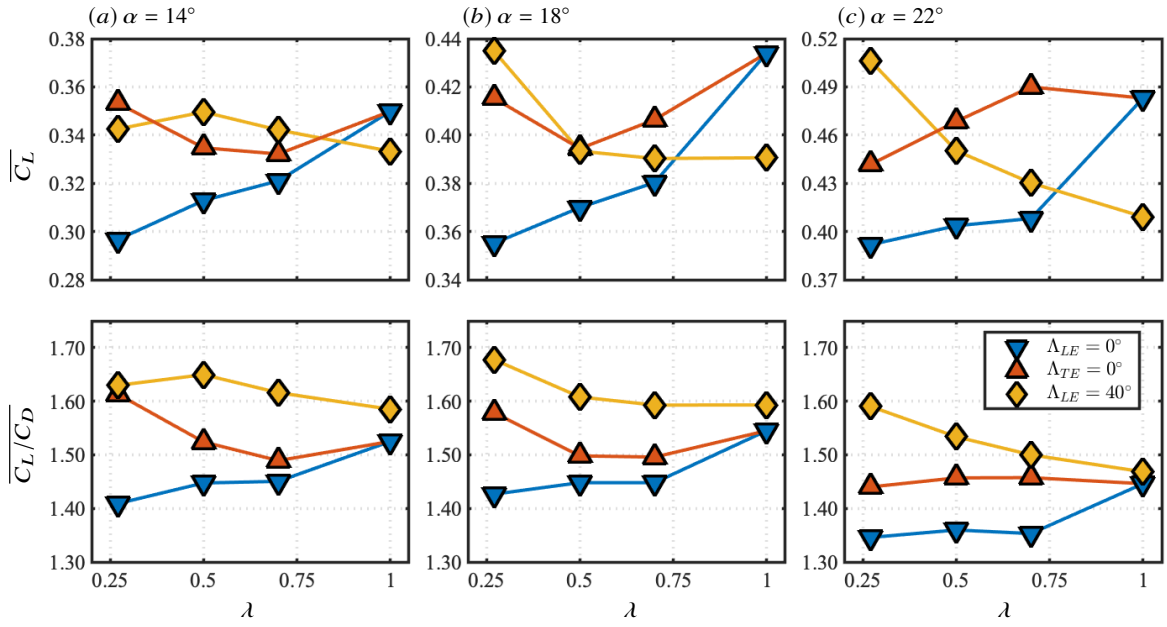

Figure 3.31: Time-averaged lift and lift-to-drag coefficients, $\overline{C_L}$ and $\overline{C_L/C_D}$, respectively, for $sAR = 2$ tapered wings with $0.27 \leq \lambda \leq 1$ at $14° \leq \alpha \leq 22°$. Blue symbols for wings with straight LE and forward-swept TE, red symbols for wings with backward-swept LE and straight TE and yellow symbols for tapered wings with $\Lambda_{\mathrm{LE}} = 40°$.

$\overline{C_L}$ and $\overline{C_L/C_D}$ are higher for tapered wings with backward-swept LE and straight TE than that of tapered wings with straight LE and forward-swept TE.

These results suggest that the backward-swept LE enhances the aerodynamic efficiency of the wing in post-stall laminar flow conditions. Untapered swept wings, however, present a lower $\overline{C_L}$ for all angles of attack. It is the combination of a high LE sweep with wing taper that causes $\overline{C_L}$ to increase, as seen by the yellow symbols in figure 3.31. In general, the aerodynamic performance $\overline{C_L/C_D}$ of tapered wings with high LE sweep and lower taper ratios is also higher than that of other wing planforms. This shows that the combination of wing taper and sweep can be beneficial for laminar separated flows.

Moreover, we analyze the effect of wing taper on the sectional lift coefficients $\overline{C_l}$, as shown in figure 3.32. The larger contribution to the overall lift comes from the wing root up to the quarter-span at $b/2$ for all wings shown herein. For tapered wings with straight LE and forward-swept TE, shown in figure 3.32(a), the contribution to lift from the root for $\lambda = 0.5$ and 0.7 increases. For $\lambda = 0.27$, the lift decreases considerably over the entire wingspan. For tapered wings with backward-swept LE and straight TE, shown in figure 3.32(b), the lift contribution from tip decreases considerably, while the lift from the root increases for tapered wings.

For highly swept wings, with $\Lambda_{\text{LE}} \geq 40°$, the largest contribution of lift comes from the wing root, decreasing over the wingspan towards the tip. For taper ratios $\lambda = 0.7$ and 0.5, lift increases mainly near the root when compared to the untapered wing load distribution. For wings with $\lambda = 0.27$, the effect of wing taper is to increase the overall contribution of lift over the entire wingspan. For this wing, the increase in lift near the wing root peaks at $z/c \approx 0.2$. The overall increase in lift is also observed at the tip, supported by the emergence of unsteady shedding near the wing tip.

To further understand how wing taper affects the lift distribution over the wingspan, we use the force element analysis of [Cha92] to identify flow structures exerting aerodynamic loads over the wing. Many other approaches have derived force elements in flows

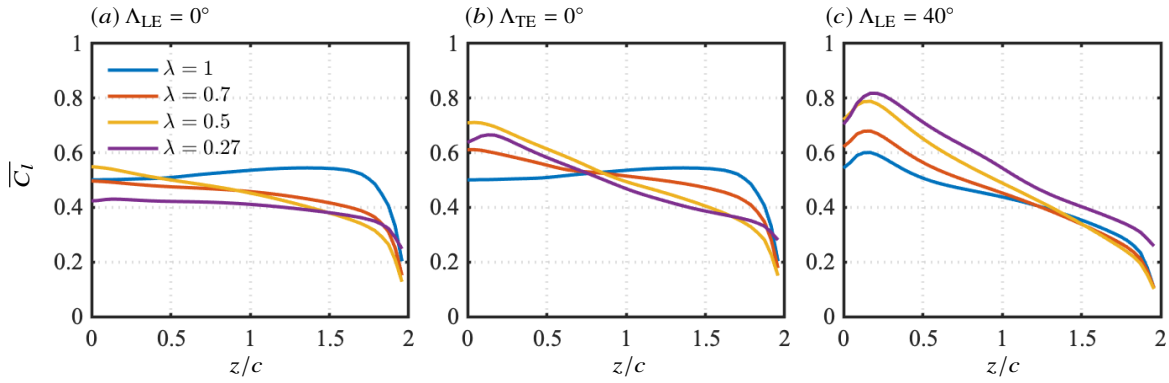

Figure 3.32: Time-averaged lift coefficients $\overline{C_l}$ distribution over the wingspan for wings with $sAR = 2$, $\alpha = 22°$, and $0.27 \leq \lambda \leq 1$ for wings with $\Lambda_{LE} = 0°$, $\Lambda_{TE} = 0°$, and $\Lambda_{LE} = 40°$.

through variational approach [QN83, PSN00], reciprocal theorem [Mag11], vortex force maps [LW18, LZG20], and force partition [MM21a, MM21b]. Force elements have provided in-depth insights on the near-wake structures and their role in the lift and drag support over impulsively started finite plates [LHC12] and wings [ZHA20b, ZT22, ZSB22].

To perform this analysis, we define an auxiliary potential with boundary condition of $-\mathbf{n} \cdot \nabla\phi_i = \mathbf{n} \cdot \mathbf{e}_i$ along the surface of the wing, where ϕ is the auxiliary potential, $\mathbf{n}$ is the unit wall normal vector, and $\mathbf{e}_i$ is normal vectors in the ith–direction. With the inner product of the Navier–Stokes equations with $\nabla\phi$ and performing an integral over the fluid domain, we can express the force exerted in the i-th direction as

$$F_i = \int_V \omega \times \mathbf{u} \cdot \nabla\phi_i \mathrm{d}V + \frac{1}{Re} \int_S \omega \times \mathbf{n} \cdot (\nabla\phi_i + \mathbf{e_i}) \mathrm{d}S, \tag{3.3}$$

where the first integral represents the volume force elements and the second integral term is comprised of the surface force elements. We illustrate the lift elements by the Hadamard product of the $\nabla\phi_i$ and the Lamb vector ($\boldsymbol{\omega} \times \mathbf{u}$). For low-Reynolds number flows, the volume elements dominate the contribution to the total force exerted over the wing. Furthermore, due to the nature of the potential velocity, the lift elements are mainly found near the wing.

To demonstrate how wing taper affects the volumetric contribution to lift, we present

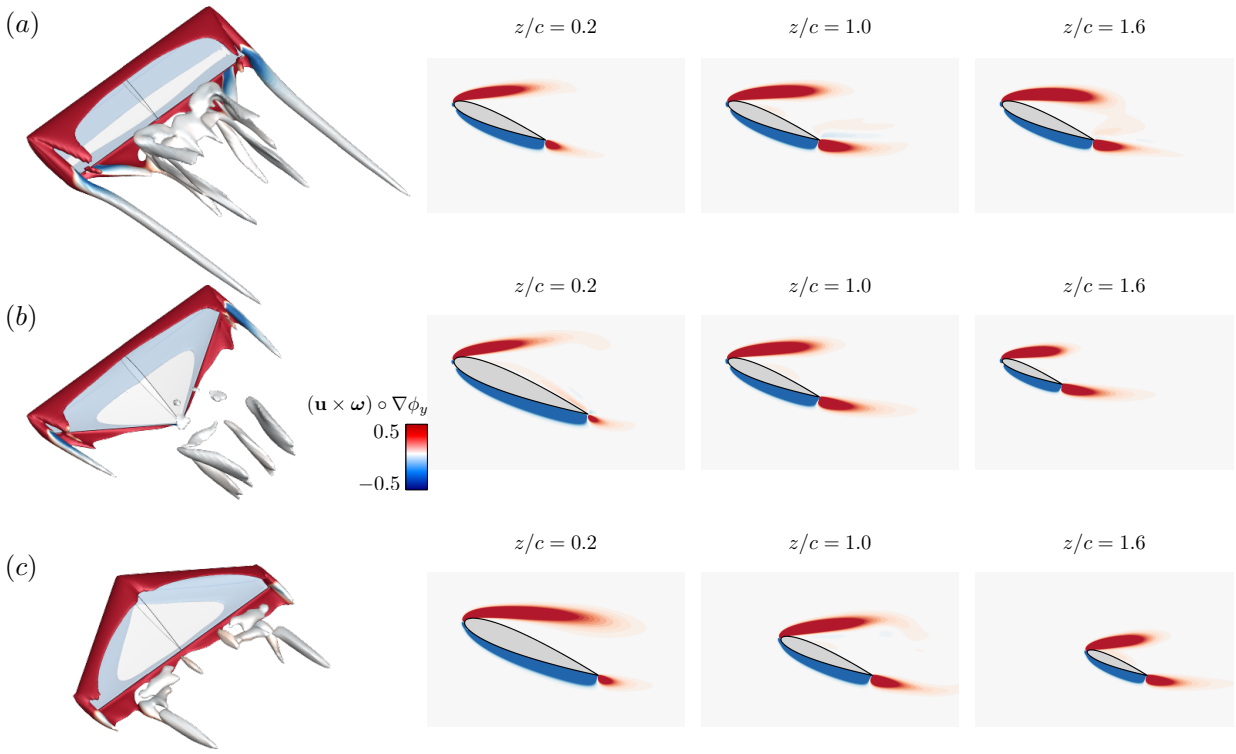

Figure 3.33: Lift elements around tapered wings with $sAR = 2$ at $\alpha = 22°$ with (a) $(\delta, \Lambda_{\text{LE}}) = (1, 0°)$, (b) $(\delta, \Lambda_{\text{LE}}) = (0.27, 0°)$, and (c) $(\delta, \Lambda_{\text{LE}}) = (0.27, 30°)$. Time-averaged isosurfaces of $\overline{Q} = 2$ colored by lift elements $(\mathbf{u} \times \boldsymbol{\omega}) \circ \nabla\phi_y \in \pm 0.5$ with sectional slices at $z/c = 0.2$, 1, and 1.6.

the lift elements on isosurfaces of $\overline{Q} = 2$ around wings with $sAR = 2$ and $\alpha = 22°$ with three distinct planforms in figure 3.33. The with-colored contours away from the wing show that the main contribution the volume lift elements comes from the near-wake structures. Furthermore, sliced visualizations for the lift element contours are shown at $z/c = 0.2$, 1.0, and 1.6 to highlight the lift contribution over the wingspan. We observe that the pressure side contribution to lift is negative, while the suction side is positive for all wings shown.

For the untapered wing, seen in figure 3.33(a), positive lift elements appear distant from the wing, while approaching the wing surface and becoming thicker as we approach the wing tip region. This explains the small increase in C_l over the z/c seen for the untapered wing in figure 3.32. For the wings with $\Lambda_{\text{LE}} = 0°$ and $\Lambda_{\text{TE}} < 30°$ for $\delta = 0.27$, shown in figure 3.33(b), the lift elements appear thinner over the suction side and far from the wing, showing that the near-wake contribution to lift is smaller with such planform when compared to the untapered wing, as was previously observed in figures 3.31 and 3.32. For the wing with backward-swept LE, the lift element contours appear thicker over the suction side near the wing root, in agreement with the increase in C_l observed in figure 3.32 for this planform. The lift elements become thinner and move away from the wing near the wing tip, showing that the main contribution to the overall lift comes from the near-wake structures at the root.

3.5.7 Spectral analysis of lift coefficient

The lift spectrum is affected by wing taper and sweep as these parameters define where unsteadiness appears over the wing. As the emergence of vortical structures is shifted over the wingspan for different wing planforms, the vortex shedding frequency changes as well as the lift coefficient spectra. Let us focus on the spectral content of aerodynamic loads over $sAR = 2$ wings, as shown in figure 3.34, with the lift coefficients power spectrum density (PSD) $\hat{C}_L$ for wings at $14° \leq \alpha \leq 22°$ and $\Lambda_{\text{LE}} = 0°$ and 18.4°. The dominant lift oscillations are associated with the vortex shedding frequency, which we characterized by the Strouhal

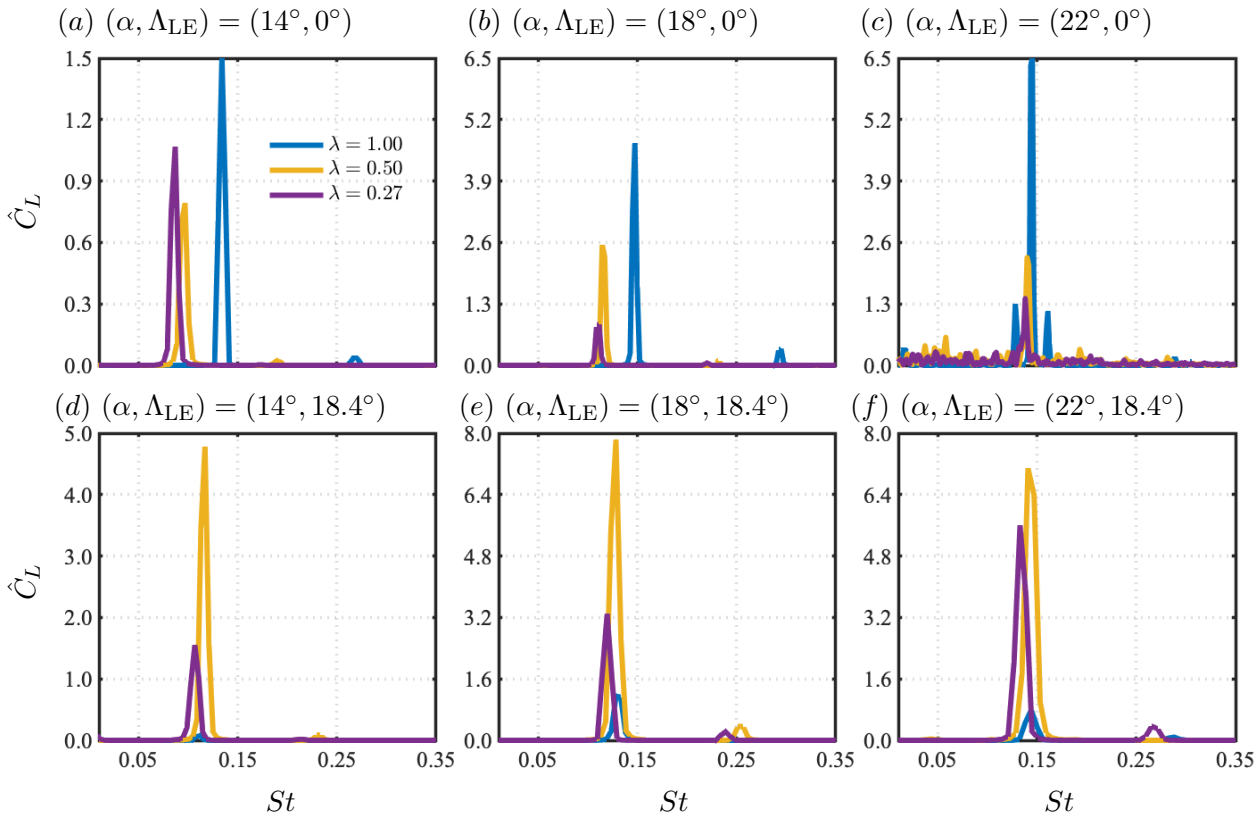

Figure 3.34: Power spectrum density of lift coefficients, $\hat{C}_L$ for wings with $sAR = 2$, $0.27 \leq \lambda \leq 1.00$, $14° \leq \alpha \leq 22°$, and $\Lambda_{\mathrm{LE}} = 0°$ and $18.4°$.

number defined as

$$St = \frac{\omega}{2\pi} \frac{c \sin \alpha}{U_\infty} \ , \tag{3.4}$$

where ω is the temporal frequency. For laminar flows around low-aspect-ratio finite wings, lift PSD is characterized by a single narrow peak at a dominant frequency [ZHA20b]. At high incidence, oscillations at other frequencies may appear with amplitudes that are an order of magnitude lower.

The frequency peak shifts towards lower St for $\lambda \leq 0.50$. This effect is stronger at the lower angles of attack. This occurs as the vortex shedding develops near the wing root, where it is slowed by the larger chord length in that region for tapered wings. For instance, for wings with $\Lambda_{\text{LE}} = 0°$, TE is swept forward with λ, concentrating wake shedding at the root, where c_{root} has the larger chord length. As a result, there is a gradual transition towards lower frequency $\hat{C}_L$ with the decrease in λ, as shown in figure 3.34 (a, b, c). Furthermore, for wings with $\Lambda_{\text{LE}} = 18.4°$ in figure 3.34(d, e, f), there is a peak lift frequency decrease with λ, as the shedding moves from the tip towards the quarter-span and the root. The magnitude of lift oscillations also increases considerably for $\lambda \leq 0.50$ (yellow and purple curves), when the TE is unswept. The present analysis shows that the dominant spectral behavior of the wing is affected by the wing taper and sweep, suggesting that the frequency of dominant perturbations might also be affected by the wing planform geometry parameters. In the next section, we provide discussions on the effect of wing taper and sweep on optimal harmonic perturbations through the lens of resolvent analysis.

The present discussion paves the way for the next chapters of this manuscript. We have shown the diverse wake features observed on flows around finite wings, considering the effects of wing taper and sweep. Now, we will deepen our understanding of these effects using vortex dynamics and resolvent analysis. Our first effort, shown in the following chapter, is to isolate the effects of the wing sweep by studying spanwise periodic swept wings. These wings have no effect of wing tip and will allow us to understand how the sole effect of sweep affects the wake characteristics of post-stall flows. For this effort, we will combine direct numerical

simulations and biglobal resolvent analysis.

CHAPTER 4

Wing sweep effects

We reveal the sole effects of sweep on the wake dynamics around NACA 0015 wings at high angles of attack using direct numerical simulations and resolvent analysis. The influence of sweep on the wake dynamics is considered for sweep angles from 0° to 45° and angles of attack from 16° to 30° for a spanwise periodic wing at a chord-based Reynolds number of 400 and a Mach number of 0.1. Wing sweep affects the wake dynamics, especially in terms of stability and spanwise fluctuations with implications for the development of three-dimensional wakes. We observe that wing sweep attenuates spanwise fluctuations. Even as the sweep angle influences the wake, force, and pressure coefficients can be collapsed for low angles of attack when examined in wall-normal and wingspan-normal independent flow components. Some small deviations at high sweep and incidence angles are attributed to vortical wake structures that impose secondary aerodynamic loads, revealed through the force element analysis. Furthermore, we conduct global resolvent analysis to uncover oblique modes with high disturbance amplification. The resolvent analysis also reveals the presence of wavemakers in the shear-dominated region associated with the emergence of three-dimensional wakes at high angles of attack. For flows at high sweep angles, the optimal convection speed of the response modes is shown to be faster than the optimal wavemakers speed suggesting a mechanism for the attenuation of perturbations. The present findings serve as a fundamental stepping stone to understanding separated flows at higher Reynolds numbers.

4.1 Motivation

Understanding the dynamics of airfoil wakes is critically important for the design of aircraft. Moreover, many nature-inspired engineering applications can benefit from the study of the complex fluid dynamics observed, for instance, in the flight of common swifts (*Apus Apus*), where wings are swept [VSP04]. The dynamics of wakes have been studied extensively to reveal the mechanisms that trigger flow separation and three-dimensionality over unswept wings [And10, TC09, ZHA20b]. The wake dynamics of swept wings, however, have not received much attention to understanding the effect of sweep on the vortical structures that emerge at high angles of attack.

Fundamental studies on flow separation have been performed on two-dimensional (2D) unswept wings. The flow structures emerging in post-stall wakes have been a subject of research for decades [Gas67, TP82]. In the early work of [Hor68], the behavior of a canonical laminar boundary layer separation was investigated through theoretical and experimental approaches. On the numerical side, 2D simulations of flow separation were performed by [PMR90], establishing a relation among vortex shedding, adverse pressure gradient, and inviscid shear layer mechanisms.

The characteristics of vortex shedding are related to the geometrical parameters of the wing and physical parameters of the flow, including the angle of attack and the Reynolds number [HWJ01, YSK09]. The Reynolds number is important for discussing the transition on vortex shedding patterns in 2D laminar flows [WR88, RCO18]. For the analysis of flow fields at the Reynolds number where such transitions occur, experiments and computations have shown that three-dimensionality emerges as stall cells develop on the suction side [WB80a]. Numerically, three-dimensionality at high angles of attack can be captured by extending the wingspan in spanwise periodic simulations [BFP01, HBV03].

Around swept wings at high incidence, vortical structures are affected by the combination of the streamwise and spanwise flows, where the latter yields a crossflow instability over the

airfoil [SK16]. The spanwise flow alters the stall characteristics and vortical interactions in the airfoil wake [HM64]. Laminar flows over swept wings have been examined through experiments [YH07] and numerical simulations [MS14, MPH21, ZHA20a, ZT22]. Turbulent flows over swept wings have also been studied through large eddy simulations [VG19, GV20]. Such efforts, however, have considered finite swept wings, hence the effects of sweep angle are not independently analyzed from the wing tip effects.

To distinguish the influence of sweep from tip effects, one may consider analyzing a spanwise periodic swept wing, as in the works of [PBD19], [CGS19], and [PDL20, PDB21], which revealed stall cells advection during transonic buffet over swept wings. Although the wake dynamics is influenced by the sweep angle, the flows of swept and unswept wings still preserve similarities in the chordwise and wall normal flow components through the boundary layer independence principle [Whi91, WTK11]. This principle has prompted many studies in turbulent flow regimes [WTT14, CRS19], although the independence principle for laminar separated flows remains to be examined.

Analyzing the flow variables on the plane normal to the leading edge, we are able to identify the collapse of laminar flow characteristics for flows over swept wings at lower angles of attack, suggesting independence of streamwise and spanwise flow components. When interaction between them is present, it is not expected that the independence principle holds. In this study, we call on the force element theory [Cha92] to reveal the flow structures that exert additional forces on the wing responsible for the departure from the independence principle.

The presence of spanwise instabilities in the wakes behind swept wings suggests the existence of self-sustained mechanisms that affect the wake dynamics. For instance, these mechanisms may be responsible for initiating three-dimensionality at the higher incidence and reducing spanwise oscillations around swept wings. This flow complexity motivates the use of modal analysis [TBD17, THB20] to provide a comprehensive understanding of the wake dynamics and evolution of disturbances in swept wings.

Among all modal analysis methods, the resolvent analysis reveals the evolution of perturbations excited by optimal harmonic inputs to the flow [TTR93b, FI94, JB05]. Resolvent analysis can be performed with respect to steady (equilibrium) and time-averaged states. The latter case assumes that the flow is statistically stationary. In such a case, resolvent analysis can be used to study laminar and turbulent flows, extending the applicability of resolvent analysis to time-averaged base flows [MS10]. [Jov04b] extended the methodology to unstable systems and [SB14] discussed the evolution of perturbations over a finite-time horizon and the modal sensitivity to small changes in the resolvent operator. These efforts enabled the use of resolvent analysis for studying various types of complex fluid flows [GBR16, STR18, YT19, YBT20, KYT20, LSY21].

For laminar separated flows, resolvent analysis reveals how flow perturbations arise, grow, and self-sustain in the flow field. For instance, disturbances generated from the vortices at the flow separation over the wing can grow and develop into wake unsteadiness downstream. This behavior can be captured by the optimal forcing and response structures, and their spatial overlap, characterized by wavemakers. Such regions of the flow field act as a source to the global stability of the flow and are optimal locations for the introduction of self-sustained perturbations in the flow field [GL07, GCL10, FSS17].

Wavemaker analysis can aid in uncovering mechanisms that sustain flow unsteadiness in particular flow regions. In the present chapter, we further reveal that optimal response structures have a lower phase speed than the optimal wavemakers, which explains the attenuation of unsteadiness and three-dimensionality for flows over swept wings. Furthermore, resolvent analysis predicts the onset of oblique shedding on flows over swept wings, as observed in flows over high-apect-ratio bodies [MS14, MPH21, ZHA20a]. As oblique vortices are observed in laminar flows over finite-length bodies and unseen over spanwise periodic bodies, there is an open question on whether sweep angle or the body tip promotes oblique shedding. In the present chapter, we address this question using revolvent analysis. The emergence of highly amplified oblique resolvent modes shows that oblique shedding can be

triggered and sustained over swept wings with an appropriate input.

This chapter aims to study the influence of the sweep angle on the wake dynamics of laminar flows over swept wings by combining direct numerical simulations and resolvent analysis. We present the problem setup and the numerical methods in section 4.2. Next, we characterize the flow over swept wings in section 4.3. We also examine the applicability of the concepts associated with the boundary layer independence principle for flows with massive separation and employ the force element theory to identify sources of vortically induced lift and drag in sections 4.3.1 and 4.3.2. Moreover, we discuss the effects of spanwise flow on the evolution of perturbations via resolvent analysis in section 4.3.4. The role of wavemakers in swept wings is also studied in sections 4.3.5. Lastly, we summarize our findings 7.1.3.

4.2 Problem setup

We study laminar separated flows over swept wings with a NACA 0015 airfoil cross-section for sweep angles $0^\circ \leq \Lambda \leq 45^\circ$ and angles of attack $16^\circ \leq \alpha \leq 30^\circ$. For all cases, we set the chord-based Reynolds number to $Re_c \equiv U_\infty L_c/\nu = 400$ and the free-stream Mach number to $M_\infty \equiv U_\infty/a_\infty = 0.1$. Here, U_∞ is the free-stream velocity, L_c is the chord length, ν is the kinematic viscosity and a_∞ is the free-stream speed of sound. We illustrate the present setup in figure 4.1 with an instantaneous flow field visualized for $\alpha = 30^\circ$ and $\Lambda = 15^\circ$.

For the present chapter, we consider a NACA 0015 profile with constant chord length in the (x, y) plane for all angles of attack and sweep, with spanwise periodicity in the z'-direction. As shown in figure 4.1, the effective chord length is defined as

$$L_c' = L_c \left(\cos^2\alpha \cos^2\Lambda + \sin^2\alpha\right)^{1/2} \leq L_c \tag{4.1}$$

and the effective angle of attack is defined as

$$\alpha_{\text{eq}} = \tan^{-1}\left(\tan\alpha/\cos\Lambda\right) \geq \alpha \tag{4.2}$$

Effective L_c' and α_{eq} are dependent on the sweep angle Λ and relate to the airfoil geometry

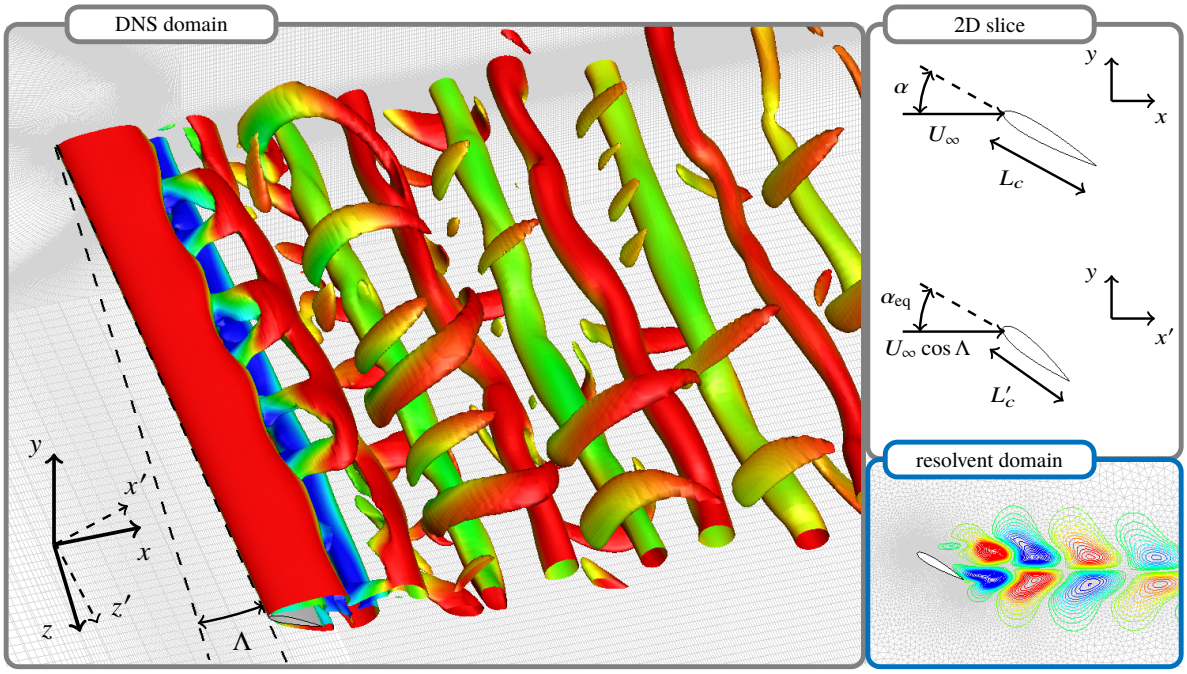

Figure 4.1: The problem setup. Instantaneous flow over a spanwise periodic NACA 0015 profile at $\alpha = 30°$ and sweep angle $\Lambda = 15°$ visualized with isosurfaces of Q criterion colored by streamwise velocity u_x. 2D slice of airfoil in coordinate systems (x, y, z) and (x', y, z'), with x' and z' perpendicular and parallel to the wingspan, respectively. DNS and resolvent grids are shown as gray lines in the background.

on the (x', y) plane.

4.2.1 Direct numerical simulations of spanwise periodic flows

To study the flows over swept NACA 0015 airfoils, we perform direct numerical simulations (DNS) with *CharLES*, a finite-volume-based compressible flow solver with second- and third-order accuracies in space and time, respectively [KHN11, BHN17b]. We position the leading edge of the airfoil at $(x'/L_c,\ y/L_c) = (0, 0)$. The C-shaped computational mesh extends over $(x'/L_c, y/L_c, z'/L_c) \in [-20, 25] \times [-20, 20] \times [0, 4]$. We build the grids with

	$\Lambda = 0°$		$\Lambda = 15°$		$\Lambda = 30°$		$\Lambda = 45°$	
	$\overline{C_L}$	$\overline{C_D}$	$\overline{C_L}$	$\overline{C_D}$	$\overline{C_L}$	$\overline{C_D}$	$\overline{C_L}$	$\overline{C_D}$
Present	0.690	0.405	0.649	0.391	0.536	0.350	0.384	0.296
[ZHA20a]	0.702	0.405	0.657	0.392	0.547	0.353	0.393	0.301

Table 4.1: Time-averaged lift and drag coefficients ($\overline{C_L}$ and $\overline{C_D}$) compared to [ZHA20a] for laminar separated flow over NACA 0015 airfoils with $\alpha = 20°$, $\Lambda = 0°$, $15°$, $30°$, and $45°$.

$(\min \Delta x, \min \Delta y, \min \Delta z)/L_c = (0.005, 0.005, 0.0625)$, with mesh refinement near the airfoil and wake. This yields a mesh with $100,000$ to $200,000$ cells on the root plane, extruded in the spanwise direction with equally spaced cell elements. We have verified our computational setup and validated the results with [ZHA20a]. Our simulations obtained close agreement for the instantaneous and time-averaged velocity components, skin friction lines, and pressure coefficients over the wing surface.

We prescribe Dirichlet boundary conditions at the inlet and farfield boundaries as

$$(\rho, u_{x'}, u_y, u_{z'}, p) = (\rho_\infty, U_\infty \cos\Lambda, 0, U_\infty \sin\Lambda, p_\infty) \ , \tag{4.3}$$

where ρ is density, p is pressure, $u_{x'}$, u_y, and $u_{z'}$ are velocity components in (x', y, z') directions, respectively, ρ_∞ is the freestream density and p_∞ is the freestream pressure. On the airfoil surface, we prescribe the adiabatic no-slip boundary condition. For the outflow, a sponge layer [Fre97] is applied over $x'/L_c \in [15, 25]$ with the target state being the running-averaged flow over 5 acoustic time units. For time integration, a fixed acoustic Courant-Friedrichs-Lewy (CFL) number of 1 is utilized. We start the simulations with a uniform flow. The initial transients are flushed out of the computational domain for 80 convective time units, after which statistics are recorded over at least 100 convective time units.

The current results are carefully validated by examining the lift, drag, and pressure

coefficients, respectively defined as

$$C_L = \frac{F_y}{\frac{1}{2}\rho U_\infty^2 L_c}, \quad C_D = \frac{F_x}{\frac{1}{2}\rho U_\infty^2 L_c}, \quad \text{and} \quad C_p = \frac{p - p_\infty}{\frac{1}{2}\rho U_\infty^2}, \tag{4.4}$$

where F_x and F_y are the x and y force components, respectively. The forces for $\alpha = 20^\circ$ are in close agreement with those reported by [ZHA20a], as shown in table 4.1. The flow fields were also compared and exhibited agreement validating the current setup.

4.2.2 Biglobal resolvent analysis

To analyze the perturbation dynamics over swept wings we use resolvent analysis, as presented in section 2.1. Here we consider the flows to be spanwise periodic. The spanwise periodicity and statistical stationarity allow for $\mathbf{q}'$ and $\mathbf{f}'$ to be represented with temporal and spanwise Fourier modes

$$[\mathbf{q}'(x', y, z', t), \mathbf{f}'(x', y, z', t)] = \int_{-\infty}^{\infty}\int_{-\infty}^{\infty} \left[\hat{\mathbf{q}}_{k_{z'},\omega}(x', y), \hat{\mathbf{f}}_{k_{z'},\omega}(x', y)\right] e^{i(k_{z'}z' - \omega t)} \mathrm{d}k_{z'}\mathrm{d}\omega \ , \tag{4.5}$$

where $k_{z'}$ is the spanwise wavenumber, and $\hat{\mathbf{q}}_{k_{z'},\omega}$ and $\hat{\mathbf{f}}_{k_{z'},\omega}$ are the biglobal modes for spanwise wavenumber $k_{z'}$ and temporal frequency ω.

We can also incorporate temporal damping into forcing and response modes as $[\hat{\mathbf{q}}_{k_{z'},\omega}, \hat{\mathbf{f}}_{k_{z'},\omega}]e^{-\beta t}$ through a discounted resolvent operator, where β is a time-discounting parameter [Jov04b, SB14]. Moreover, the pseudospectral analysis is dependent on the norm [TE05]. In this work, we use the Chu norm [Chu65] which is incorporated into the resolvent through a similarity transform $\mathbf{H}_{\bar{\mathbf{q}}} \rightarrow \mathbf{W}^{\frac{1}{2}}\mathbf{H}_{\bar{\mathbf{q}}}\mathbf{W}^{-\frac{1}{2}}$, where $\mathbf{W}$ is the weight matrix that accounts for numerical quadrature and energy weights.

The weighted resolvent is dependent on the temporal frequency ω, spanwise wavenumber $k_{z'}$, and the base flow $\bar{\mathbf{q}} = \bar{\mathbf{q}}(\alpha, \Lambda)$. These parameters define a large parameter space to characterize the effect of sweep angle on the wake dynamics. To facilitate this characterization, we employ an adjoint-based parametric sensitivity method for ω and $k_{z'}$ [SB14, FS17]. This approach is helpful when the parameter space is large as well as to capture the sensitivity of the resolvent norm to specific geometrical and flow parameters [SS19].

To perform the resolvent analysis, we construct a discrete linear operator $\mathbf{L}_{\bar{\mathbf{q}}}$ [STC17]. This operator is discretized over a 2D unstructured grid, as shown in figure 4.1, with a reduced-size spatial domain $x/L_c \in [-10, 15]$ and $y/L_c \in [-10, 10]$ to alleviate the computational costs of performing resolvent analysis without affecting the accuracy of the resolvent modes. The structured DNS base flow solution is transferred to the unstructured grid via cubic interpolation. We enforce homogeneous Dirichlet boundary conditions for the fluctuating variables ρ' and u' and homogeneous Neumann boundary conditions for T' along the farfield and airfoil boundaries as well as to all variables at the computational outlet. In addition, we apply sponges far from airfoil in conjunction with the boundary conditions.

In the present chapter, we construct $\mathbf{L}_{\bar{\mathbf{q}}}$ with m ranging between $150,000$ and $200,000$. The resolvent modes were computed using the randomized resolvent algorithm [RYT20], sketching the operator with 10 random test vectors weighted by the gradients of the baseflow $(\|\nabla\rho\|, \|\nabla u_x\|, \|\nabla u_y\|, \|\nabla u_z\|, \|\nabla p\|)$. The resolvent norm converges to at least 7 significant digits. For the spectral analysis of $\mathbf{L}_{\bar{\mathbf{q}}}$, eigenmodes were computed using the Krylov–Schur method [Ste02] with 128 vectors for the Krylov subspace and tolerance residual of 10^{-10}. The direct and adjoint linear systems were solved using the MUMPS package. The codes used to compute the resolvent modes and eigenvalues are part of the 'Linear Analysis Package' made available by [SRT22].

4.3 Effect of sweep on wake dynamics

4.3.1 Wake characterization

The wake structures are affected by sweep and incidence angles, as shown by the isosurfaces of Q colored by the vorticity ω_z in figure 4.2. For angles of attack $\alpha \leq 20°$, the flow is 2D and the wake vortices are aligned with the sweep angle. For $\alpha \geq 26°$, the vortical structures exhibit spanwise oscillations with a transition from 2D to 3D vortex shedding. At $\alpha = 26°$, a sinusoidal pattern of oscillations appears in the spanwise direction and, at

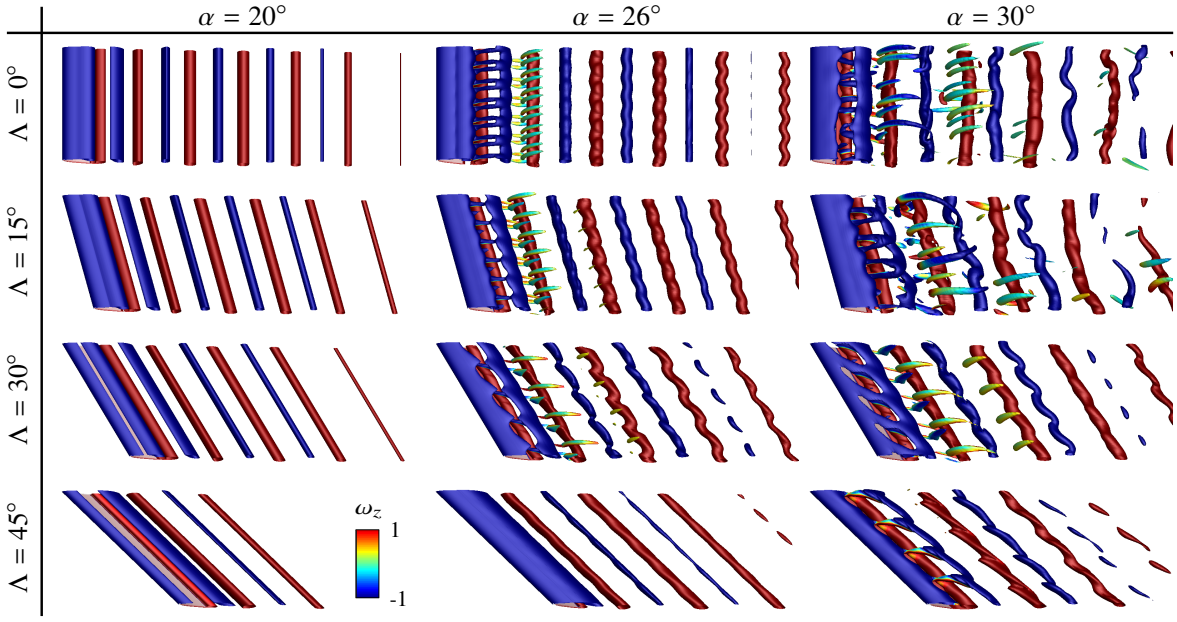

Figure 4.2: Instantaneous flow field visualization with isosurfaces of Q criterion colored by the vorticity component ω_z. For $\alpha \geq 26°$, the wake is 3D. As Λ increases, the vortices become slanted with the sweep angle and wake three-dimensionality is reduced for $\alpha \geq 26°$.

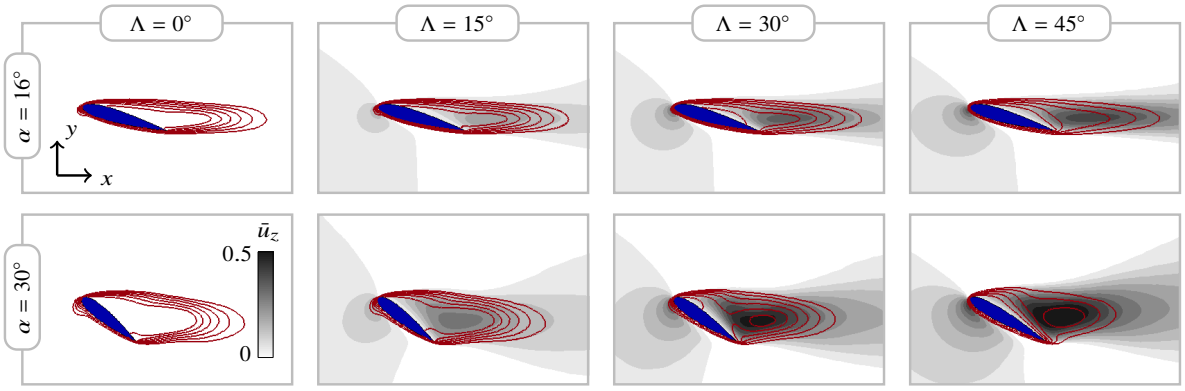

Figure 4.3: Time-averaged flow field visualization with z–velocity component, $\bar{u}_z \in [0, 0.5]$, in grayscale, for $0° \leq \Lambda \leq 45°$ and $\alpha = 16°$ and $30°$. Red solid contours mark the laminar separation bubble, with 6 equally distributed isolines of x–velocity component, $\bar{u}_x \in [0, 0.5]$. Crossflow component $\bar{u}_z$ strengthens with α and Λ.

$\alpha = 30°$, streamwise vortical structures emerge.

Highly swept wings induce spanwise flows and attenuate wake three-dimensionality as evident from the flow visualizations. When the sweep angle is $\Lambda \leq 15°$ the wake is similar to the flow over unswept wings for all angles of attack. The wake is significantly altered for sweep angles $\Lambda \geq 30°$, especially at high angles of attack, when spanwise oscillations are advected by the spanwise flow. For instance, at $\Lambda = 45°$ and $\alpha = 26°$, the spanwise oscillations are almost suppressed. The attenuation of spanwise fluctuations also occurs for $\alpha = 30°$, as we observe a similar effect for $\Lambda \geq 30°$.

Even though sweep attenuates three-dimensionality, the sustained unsteadiness of the wake suggests the existence of self-supported mechanisms that yield distinct vortex shedding patterns in swept wings at high incidence angles. We gain further insights into the separated flows by analyzing the time-averaged flow field contours of streamwise and spanwise velocities, as seen in figure 4.3. In general, as we increase the sweep angle, the $\bar{u}_x = 0$ contour line approaches the wing surface. For $\alpha = 30°$, we also notice a circular $\bar{u}_z$ profile

appearing in the wake region where the spanwise flow is stronger.

The aerodynamic loads exerted on the wing are also affected by the sweep angle [ZHA20a, ZT22]. However, it is possible to observe similarities among force characteristics with different sweep angles through the independence principle. This leads to the application of proper scaling factors to collapse aerodynamic properties for a variety of swept wings where adverse pressure gradients and spanwise fluctuations are negligible [WTK11].

For the present flows, however, the adverse pressure gradients cannot be neglected due to the massive separation. In figure 4.4, we show that $\overline{C_L}$ and $\overline{C_D}$ differ for the same α if we analyze the flow variables in (x, y, z). The coefficients collapse if we consider scaling the same force coefficients in (x', y, z'). Here, the vector-valued variables in (x, y, z) aligned with x are scaled with $\cos\Lambda$ and the effective chord length

$$L'_c = L_c \left(\cos^2\alpha \cos^2\Lambda + \sin^2\alpha\right)^{1/2} \leq L_c \tag{4.6}$$

is used to form the scaled C'_L and C'_D coefficients as

$$C'_L = \frac{F_y}{\frac{1}{2}\rho(U_\infty \cos\Lambda)^2 \; L'_c}, \quad C'_D = \frac{F_x \cos\Lambda}{\frac{1}{2}\rho(U_\infty \cos\Lambda)^2 \; L'_c} \; , \tag{4.7}$$

where $F_x \cos\Lambda = F_{x'}$ is the x' component of the pressure and viscous forces integrated over the airfoil surface per unit depth. As shown in figure 4.4(d–f), these scaled coefficients collapse over the angles of attack. Deviations are noticed only for sweep angles $\Lambda \geq 30^\circ$ at high angles of attack $\alpha \geq 26^\circ$.

The shown scaling can also be applied to the Fage–Johansen Strouhal number in the (x', y) plane as

$$St' = \frac{\omega}{2\pi} \frac{L'_c \sin\alpha_{\text{eq}}}{U_\infty \cos\Lambda} \; . \tag{4.8}$$

As presented in figure 4.5, the power spectrum density profiles of C'_L for swept wings exhibit peaks at their characteristic Strouhal number of the vortex shedding and its harmonics. When the adapted Fage–Johansen Strouhal number St' is considered, the spectral peaks collapse at the same frequencies as observed for the unswept wings. For $\alpha = 16^\circ$, the flow

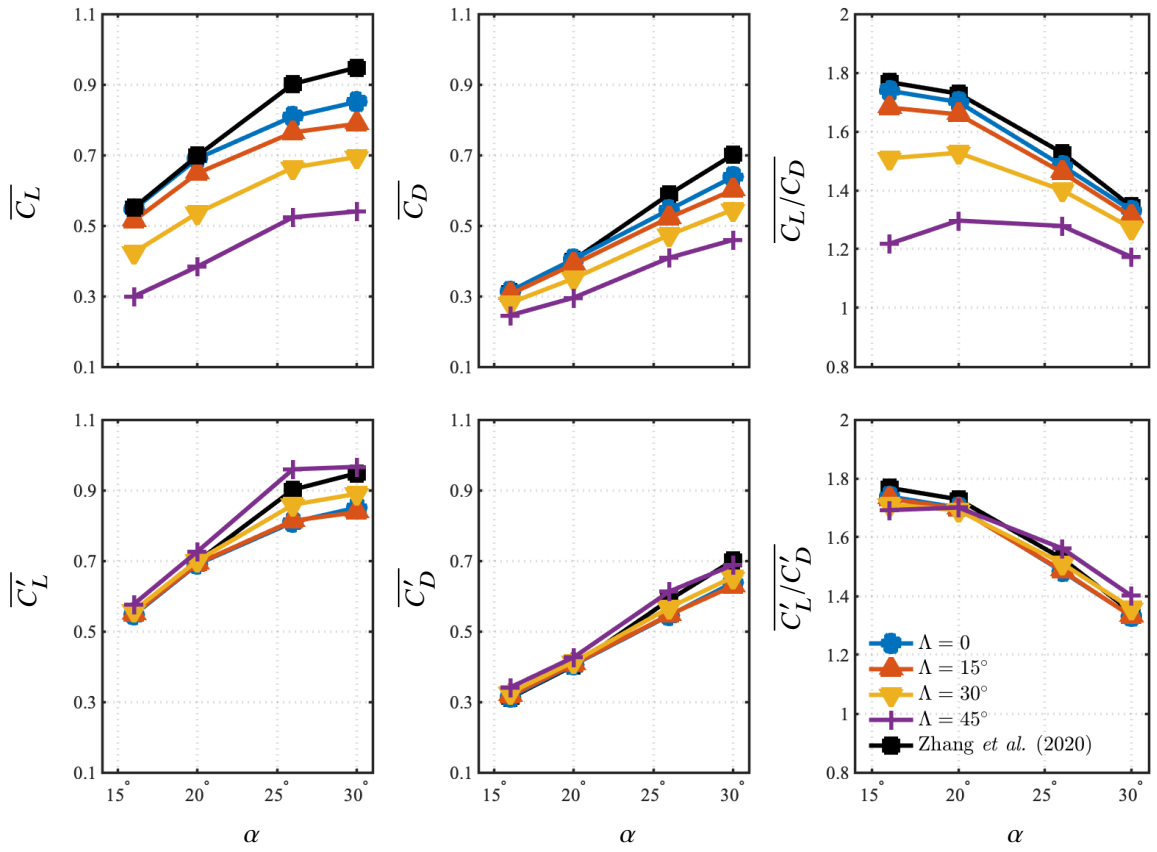

Figure 4.4: Time-averaged lift, $\overline{C_L}$, drag, $\overline{C_D}$, and coefficient ratio $\overline{C_L/C_D}$, for all α, Λ pair of the present study compared to 2D incompressible results shown by [ZHA20b]. The bottom row shows the scaled time-averaged coefficients where the flow is analyzed in (x', y, z'), and the results collapse for each α, for all sweep angles.

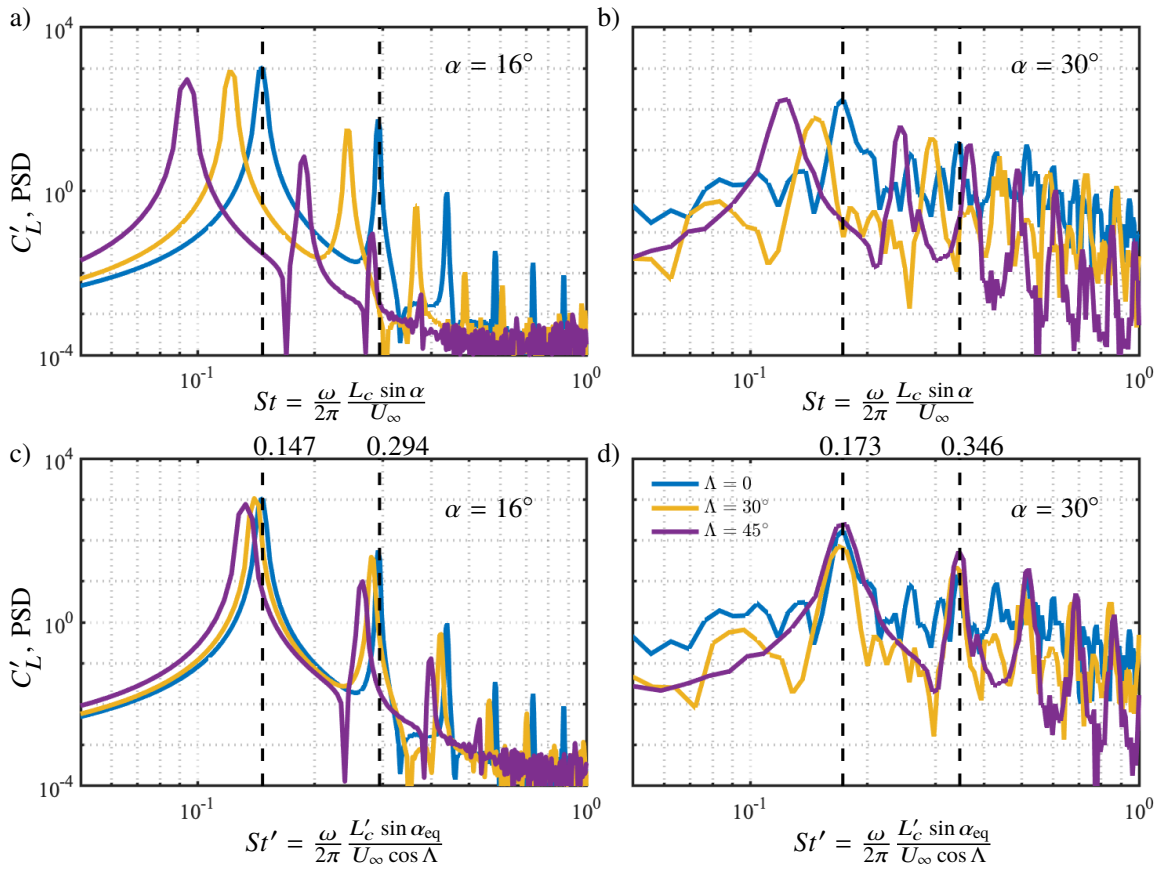

Figure 4.5: Scaled lift power spectrum density for (a,c) $\alpha = 16°$ and (b,d) $\alpha = 30°$ at sweep angles $\Lambda = 0°$, $30°$, and $45°$. In (c,d) the Fage–Johansen Strouhal number is analyzed in the (x', y) plane and the dominant and harmonic frequencies for swept wings collapse with the unswept wings.

is characterized by a single 2D vortex shedding and the C_L' spectra is smooth with distinct peak values. For $\alpha = 30°$, the spectra exhibits secondary peaks for $\Lambda \leq 30°$ and is smooth for $\Lambda = 45°$, when three-dimensionality is attenuated.

We can also similarly normalize the pressure coefficients C_p by considering the $U_\infty \cos\Lambda$ in place of U_∞ in equation 4.4. Indeed, large differences in C_p distribution over the wing are shown in figure 4.6(a,b), however, if we consider the scaled-C_p, we reveal that the pressure distributions collapse for moderate angles of attack, even though these flows exhibit massive separation, as shown in figure 4.6(c,d). Although we can bring pressure coefficients closer using $C_p/\cos^2\Lambda$, we notice some deviations for higher angles of sweep and attack, as observed for $\Lambda = 45°$ and $\alpha = 30°$. This motivates us to further understand how massively separated streamwise flow and the strong spanwise flow may impose additional loads over the wing. These deviations indeed suggest that even when the three-dimensionality is attenuated, the wake over laminar swept wings can exert additional aerodynamic forces over the wing for $\Lambda \geq 30°$ and $\alpha \geq 26°$.

4.3.2 Force element analysis

To further understand the sources of deviations in the independence principle, we use the force element theory of [Cha92] to relate the near-body vortical structures to aerodynamic forces (see description of force element theory in section 3.5.6). Through this method, we identify lift and drag force elements in the near-wake region of the current low-Reynolds number flows and analyze the distribution of force elements near the surface as the wing is swept. This analysis captures the emerging wake structures over swept wings at high angles of attack that exert nonlinear post-stall forces onto the wing.

We observe that the emergence of these force elements is associated with a departure from the collapsed force and pressure coefficients. The sweep-angle dependent scaling in equations 4.7 and 4.8 assumes independence of streamwise and spanwise flow components. The interaction between them can cause a departure from the collapsed force and pressure

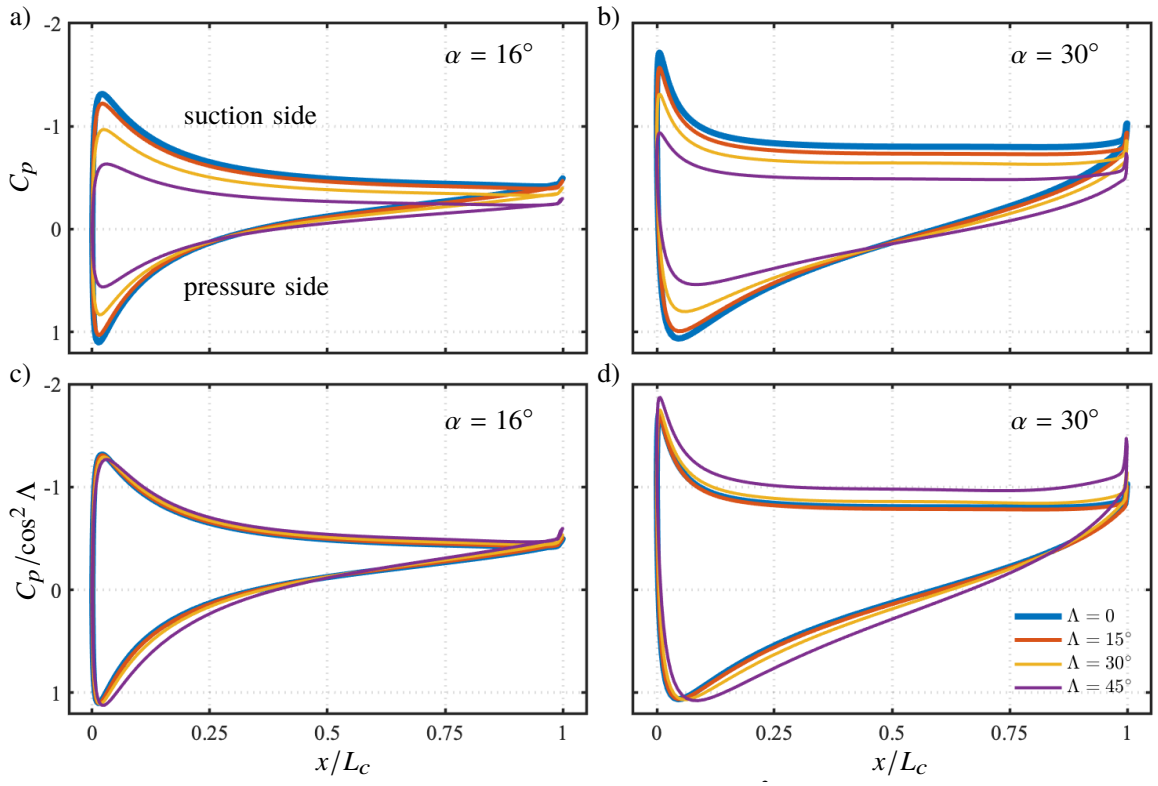

Figure 4.6: Time-averaged pressure coefficients top C_p and bottom $C_p/\cos^2\Lambda$ over the airfoil surface at (a,c) $\alpha = 16°$ and (b,d) 30°.

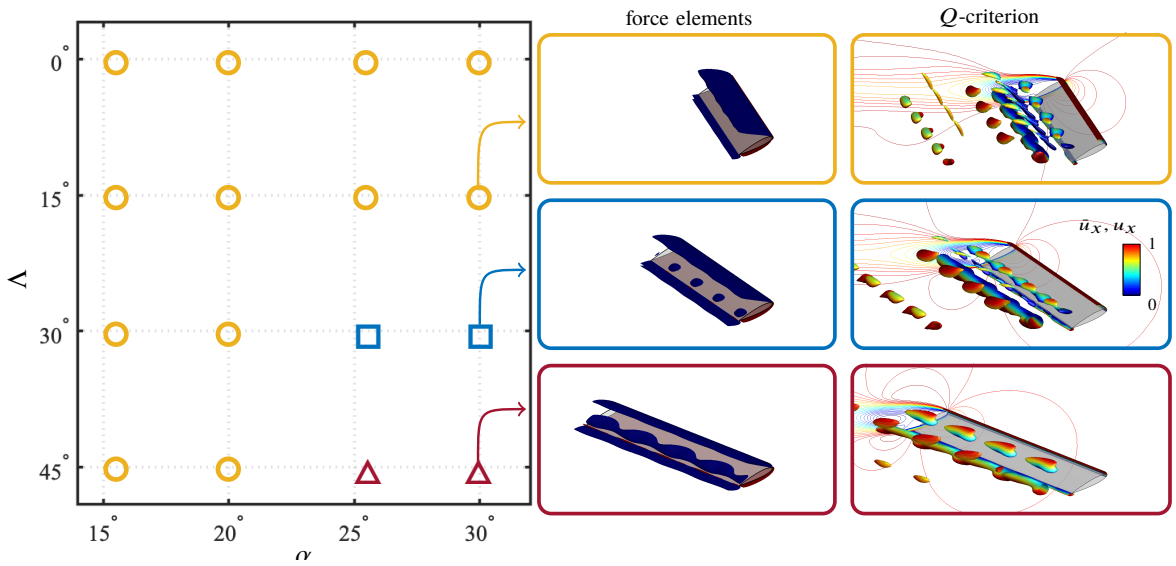

Figure 4.7: Characterization of force elements on swept wings. The symbols refer to: ○ force elements only near the leading and trailing edges, □ additional equally-spaced small lift elements, and △ large force structures observed on the suction side. On the right, we show isosurfaces of lift force elements, $(\boldsymbol{\omega} \times \mathbf{u}) \cdot \nabla \phi_L \in [-0.3, 0.3]$ and isosurfaces of Q values colored by streamwise velocity component $\bar{u}_x$ with range $[0, 1]$ for the time step with the highest lift coefficient C'_L for $\alpha = 30°$ and $15° \leq \Lambda \leq 45°$.

coefficients. By using the force element analysis, we uncover near-wake structures that are responsible for the extra forces at high angles of sweep and attack.

Sweep has a strong influence in limiting the validity of the independence principle at high angles of incidence and it favors the emergence of additional force elements near the wing surface. To show this, let us reveal the vortical structures that generate lift $(\boldsymbol{\omega} \times \mathbf{u}) \cdot \nabla \phi_y$ at the instance when the maximum lift is achieved, as shown in figure 4.7. Drag elements have similar behavior as the lift and are not shown for brevity. For $\alpha \leq 20°$, the force elements are located near the airfoils leading and trailing edges, in the shear-dominated region of the flow, along the edge of the laminar separation bubble.

Additional lift elements appear for higher angles of sweep and attack, as shown in figure 4.7. These lift elements are observed over the final quarter chord of the airfoil on the suction side, and as the sweep angle increases, they also increase in size. The force elements can be contrasted with the vortical structures in Q criterion visualization in figure 4.7. As such coherent structures are present inside the laminar separation bubble, with size and shape similar to the force elements they can be identified as the lift elements related to the larger deviations in figure 4.6(c,d).

We observe that sweep affects the coherent structures, time-averaged flow fields, and aerodynamic loads and, although some similarities are perceived, sweep has a strong influence on the wake flow downstream at the higher angles of attack. This suggests that flow perturbations originating near the airfoil in the laminar flows over swept wings can be related to the features observed in the nonlinear simulations. To further understand how sweep alters the vortex dynamics we conduct global resolvent analysis to identify the sources of self-sustained mechanisms near the wing that affect the wake behavior.

4.3.3 Dominant eigenvalues of the linearized operators

The eigenspectrum of the linearized Navier–Stokes operator $\mathbf{L}_{\bar{\mathbf{q}}}$ is comprised of eigenvalues $-i\omega = -i\omega_r + \omega_i$, with growth rate ω_i and temporal frequency ω_r. The dominant eigenmode reveals the spatial structures that can emerge in the flow. We track the dominant eigenvalue in the complex plane as we increase the spanwise wavenumber $k_{z'}$ for each (α, Λ) pair to examine if some of these parameters may cause the linear operator to become unstable, as shown in figure 4.8.

There is a distinct behavior for $\alpha \leq 20^\circ$ and $\alpha \geq 26^\circ$. For the lower angles of attack, swept wings have a greater growth rate for each $k_{z'}$, while for the higher angles of attack, we observe the opposite trend. For $\alpha \leq 20^\circ$, swept wings wakes are close to the stability threshold as we increase $k_{z'}$. On the other hand, for $\alpha \geq 26^\circ$ unstable modes move into the stable region as we increase $k_{z'}$ for all swept wings. As the linearized operators are

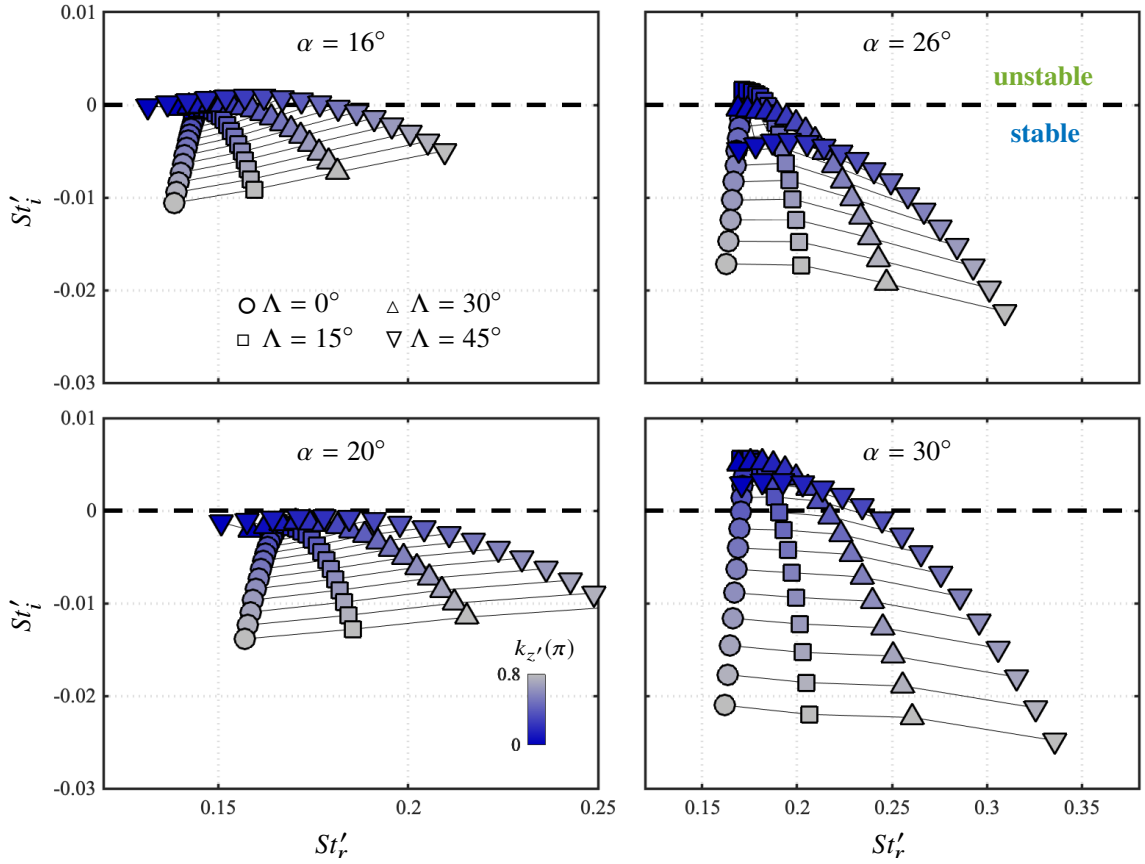

Figure 4.8: Dominant eigenvalues of $\mathbf{L}_{\bar{\mathbf{q}}}$ for (a) $\alpha = 16°$, (b) 20°, (c) 26°, and (d) 30°, for different sweep angles Λ, and spanwise wavenumbers $k_{z'}$. St_r' and St_i' are the St' numbers for growth rate and temporal frequency, respectively. Black solid lines connect the eigenvalues for the same $k_{z'}$.

unstable for $\alpha = 30^\circ$ and $k_{z'} \approx 0$, small perturbations can be amplified and sustained by the wavemakers generating the 3D wake flow observed in the numerical simulations.

Even when the modes are unstable, they are close to the stable region in the complex plane. We keep the same finite time window for resolvent analysis for all angles of sweep and attack. We find the highest growth rate among all cases to set the discounted resolvent operator with a finite time shorter than the associated time scale of the largest ω_i, which is observed for the unswept wing at $\alpha = 30^\circ$. For this reason, we use a fixed time window of $t_s U_\infty \sin\alpha / L_c \cos\Lambda = 50$ for the discounted resolvent analysis of all angles of attack and sweep.

4.3.4 Biglobal resolvent analysis of wing sweep effects

To identify the existence of regions susceptible to the growth of perturbations in the flows over swept wings, we study the effect of sweep using resolvent analysis. Details on the stability of the linear operators and the usage of time-discounting are provided in the section 4.3.3. We characterize the present flows through the dominant singular value σ_1 of the resolvent operator and its corresponding singular vectors $\hat{q}_{k_{z'},\omega}$ and $\hat{f}_{k_{z'},\omega}$. The influence of sweep on the vortex dynamics in the wake is analyzed through the forcing and response modes in figure 4.9. The shown modal structures highlight the regions of the flow field which are more sensitive and responsive to the growth of perturbations.

Forcing modes are more localized than response modes, which are supported in the shear-dominated region of the flow, where perturbations can be highly amplified. On the other hand, the response modes are seen in the wake. For swept wings, the response modes are deformed spatially towards the airfoil surface and, for $\alpha = 30^\circ$, we notice the emergence of a characteristic responsive region near the airfoil leading edge. Such response structures appear over swept wings only at high angles of attack, as seen in figure 4.9 (top). We observe the contours of the magnitude of modal streamwise velocity component $|\hat{u}_x|$ to reveal the regions of the flow that have more responsive to introduced perturbations. We visualize

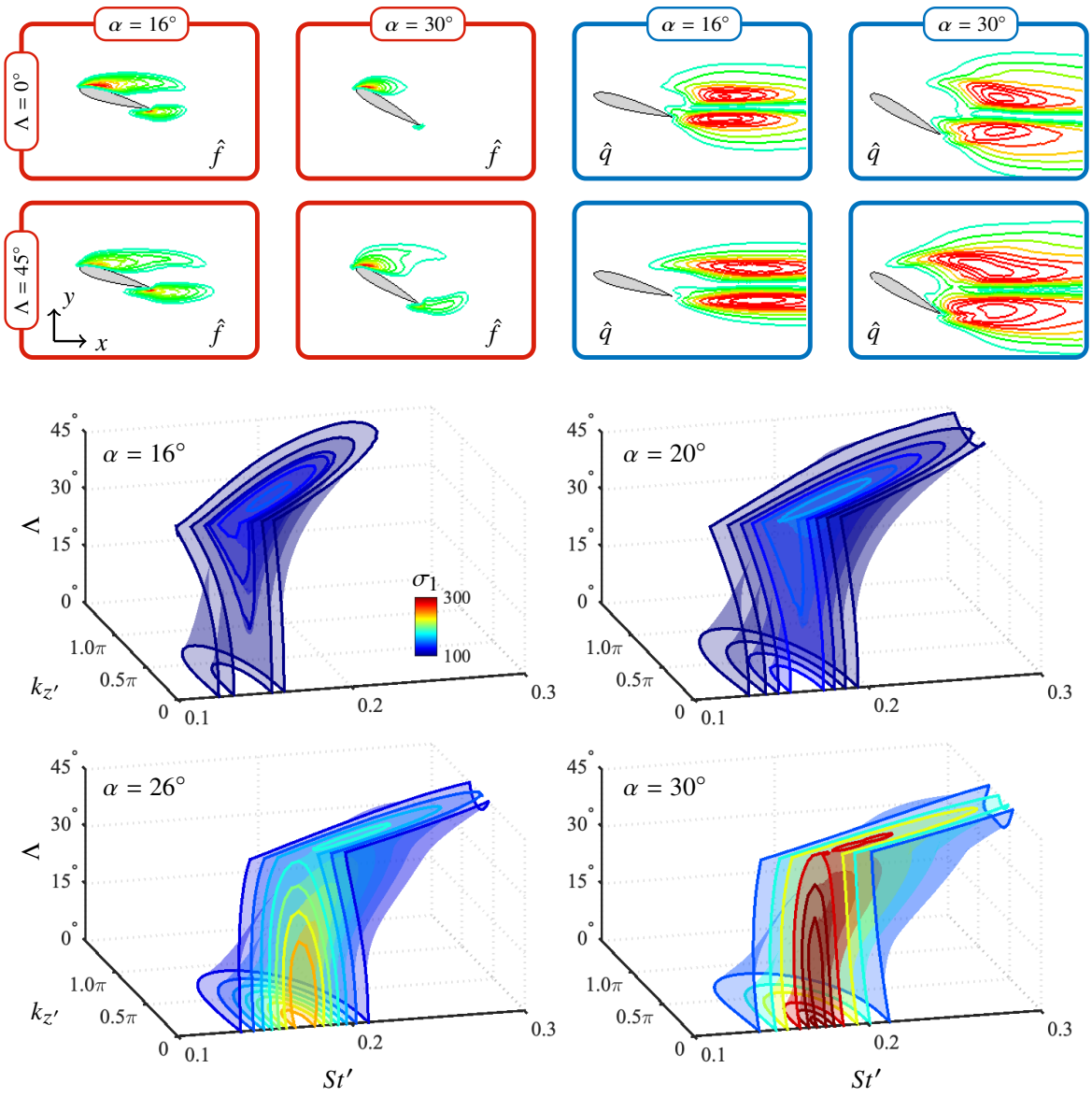

Figure 4.9: Forcing (in red boxes) and response (in blue boxes) contours for the $|u_x|/\|u_x\|_\infty \in [0.1, 1]$ in blue-green-red scale at the largest σ_1 with $k_{z'} = 0$ at $\Lambda = 0°$ and 45°. Forcing modes extend in the wake and response modes become closer to the airfoil in swept wings. Isosurfaces of dominant resolvent gain σ_1 in the Λ–St'–$k_{z'}$ space for $\alpha = 16°$ to 30°.

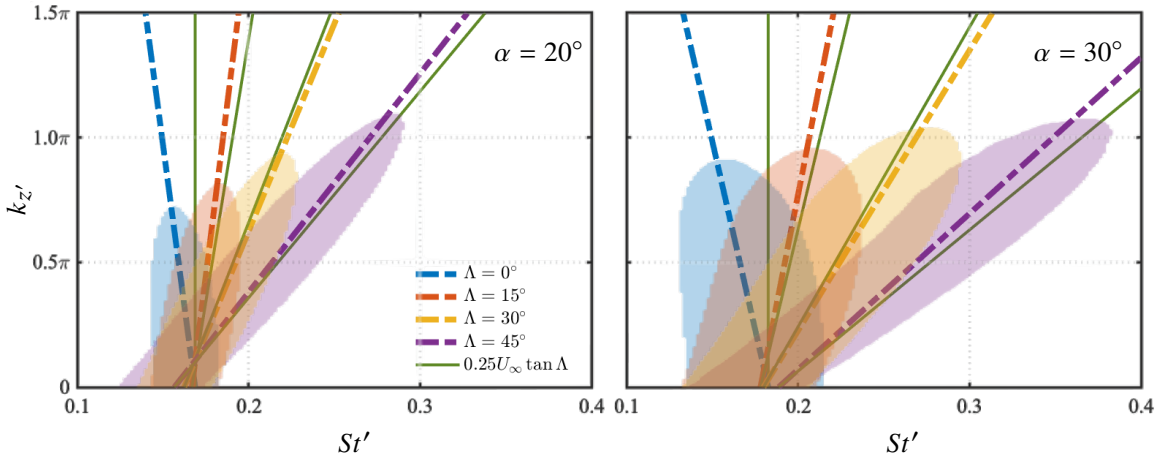

Figure 4.10: The leading resolvent gain contours at $\alpha = 20°$ and $30°$ for $0° \leq \Lambda \leq 45°$. The dash-dotted slopes represent spanwise convection speeds. Green line exhibits the convection speed prediction with $0.25U_\infty \tan\Lambda$.

similar contours for the forcing counterpart and see that the modes extend slightly into the wake, over the laminar separation bubble. This behavior reveals that the flow over swept wings can amplify optimal disturbances closer to the airfoil suction side, which can be used to alter the formation of the laminar separation bubble.

Furthermore, the present resolvent analysis predicts the formation of an oblique vortex shedding, as observed in [MPH21] and [ZHA20a], even though the present study is performed on spanwise periodic wings. Previous works have shown that oblique coherent structures become spatially periodic for large aspect ratio wings, making spanwise periodic analysis valid to study such three-dimensional structures. Through resolvent analysis, we can explain how oblique coherent structures are advected by the flow stream using the spatiotemporal frequencies of the optimal response modes.

The frequency at maximum σ_1 for each spanwise wavenumber is a function of the sweep angle and is characterized by the convection speed of the optimal oblique modes. We compute this phase speed as $c = \mathrm{d}\omega/\mathrm{d}k_{z'}$, the slope of the optimal response frequencies for each

spanwise wavenumber. This value is a function of Λ and $k_{z'}$ [PBD19, PDB21, HT21]. For flow regimes studied in the present chapter, $f \approx 0.25 U_\infty \tan\Lambda$ gives a reasonable prediction for the frequency of the maximum σ_1 for each spanwise wavenumber and sweep angle for all angles of incidence, as shown in figure 4.10. This function can be used to predict the optimal forcing and response modes for laminar separated flows over swept wings. Additionally, the mode shapes of the optimal forcing and response are similar for low $k_{z'}$. The present results reveal the optimal actuation location and response as well as the spatiotemporal behavior of the flow perturbations over laminar separated flows on swept wings.

In general, oblique modes are the most amplified optimal disturbances for all swept wings. The effect of sweep on σ_1, however, depends on the angle of attack, as shown in figure 4.9 and summarized in table 4.11. For $\alpha \leq 20°$, swept wings have higher amplification than unswept wings. This is a distinct behavior when compared to $\alpha \geq 26°$, in which swept wings have a lower resolvent norm than unswept wings. This behavior suggests that it is more challenging to perturb highly swept wings at high angles of attack.

The spatial and temporal frequency of the maximum resolvent gain $\max(\sigma_1)$ in the St'–$k_{z'}$ space depends on the sweep angle, as shown in table 4.11. For unswept wings, the largest resolvent gain σ_1 is found for the 2D setting of $k_{z'} = 0$ associated with the temporal frequency of the characteristic vortex shedding. However, both $k_{z'}$ and St' of the optimal disturbances $\max(\sigma_1)$ increase with the sweep angle. Thus, the 3D oblique modal structures are not only predicted by the present resolvent analysis but also found to be the most amplified flow mechanism in swept wings, as shown in figure 4.12.

Although all flows analyzed in this chapter are spanwise periodic, and oblique shedding is absent in the DNS, the large σ_1 in $k_{z'} > 0$ modes suggest that the spanwise flow over swept wings supports the formation and shedding of 3D oblique vortices in infinite wings. To analyze the spatial behavior of oblique modes, let us focus on the resolvent analysis at the angle of attack $\alpha = 20°$ and sweep angle $\Lambda = 45°$, as seen in figure 4.12. As noticed at $k_{z'} = 0$, the 2D forcing and response modes are aligned with the wingspan, however, the

	α = 16°			α = 20°		
Λ	max(σ_1)	St'	$k_{z'}$	max(σ_1)	St'	$k_{z'}$
0°	107.7	0.143	0.000π	137.0	0.165	0.000π
15°	110.7	0.146	0.161π	140.6	0.169	0.171π
30°	121.3	0.154	0.281π	150.3	0.175	0.221π
45°	145.3	0.170	0.392π	166.5	0.190	0.302π

α	α = 26°			α = 30°		
Λ	max(σ_1)	St'	$k_{z'}$	max(σ_1)	St'	$k_{z'}$
0°	250.1	0.173	0.000π	368.5	0.174	0.000π
15°	257.2	0.178	0.131π	375.9	0.175	0.090π
30°	228.2	0.189	0.191π	363.8	0.182	0.101π
45°	186.6	0.207	0.211π	299.4	0.195	0.111π

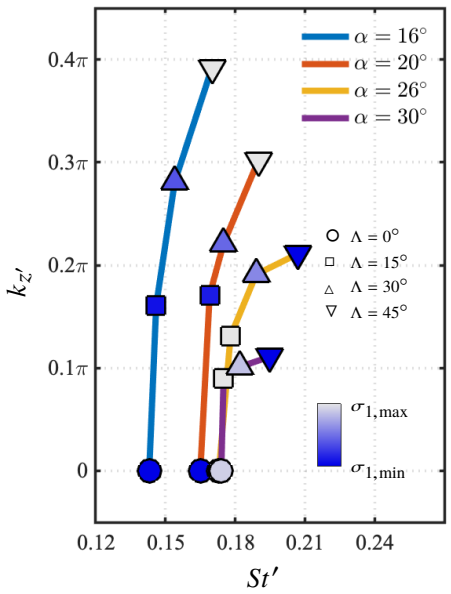

Figure 4.11: The maximum leading resolvent gain max(σ_1) for each α, Λ pair. On the right, we plot max(σ_1) in St'–$k_{z'}$ space colored in blue scale with respect to the minimum and maximum σ_1 for each α.

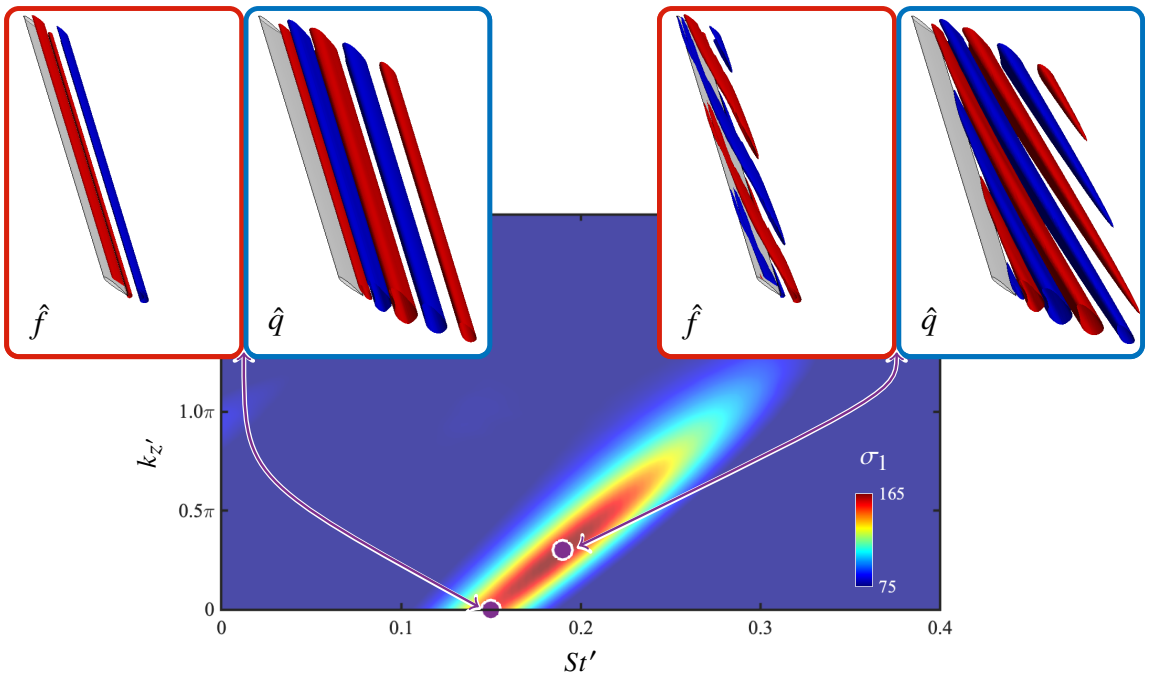

Figure 4.12: Forcing ($\hat{f}$, in red boxes) and response ($\hat{q}$, in blue boxes) modes isosurfaces with y–velocity components $\hat{u}_y/\|\hat{u}_y\|_\infty \in \pm 0.2$ in red-blue color scale for $\alpha = 20°$ and $\Lambda = 45°$. Wingspan length is 10 L_c. Forcing and response modes are associated with the largest resolvent gain for each $k_{z'}$ as shown in the σ_1 contours over St'–$k_{z'}$ plane.

maximum resolvent gain σ_1 in the St'–$k_{z'}$ for this flow is found at $k_{z'} = 0.3\pi$ and $St = 0.19$, where modes are oblique with respect to the wingspan. For this reason, the flow over swept wings has a higher propensity to develop oblique shedding when compared to the flow over unswept wings and such characteristic is revealed through resolvent analysis to be associated with the sweep angle.

The flow mechanisms that are responsible for oblique shedding and the attenuation of the spanwise oscillations for swept wings were described as the growth of response modes towards the airfoil surface and the extension of forcing modes into the wake and over the laminar separation bubble. This phenomenon also creates an overlapping region of the flow where both forcing and response modes are supported. This overlap of forcing and response structures is more prominent at the higher sweep angles, although it is also present in unswept wings. The overlap of forcing and response modes and their associated resolvent gain can both be relevant to characterize how the flow over swept wings at high incidence gives rise to perturbations on the flow as we discuss such phenomena through the lens of wavemakers.

4.3.5 Biglobal resolvent wavemakers

Wavemakers have been described as regions of the flow field characterized by both high sensitivity and responsiveness to perturbation growth [GL07, GCL10, FSS17]. Such regions are optimal for the introduction of self-sustained instabilities, acting as the source of global instabilities of the system, and motivating the analysis of structural sensitivity of the modal forcing and response structures.

In global stability analysis, wavemakers are generally derived with direct and adjoint modes. Here, we quantify the strength of the wavemakers with the inner product of the forcing and response modes $\langle \hat{q}_{k_{z'},\omega}, \hat{f}_{k_{z'},\omega} \rangle$ and visualize the corresponding wavemaker modes with their Hadamard product. Wavemaker modes exhibit a higher magnitude downstream of the airfoil, as shown in figure 4.13, in the region where 3D flow develops for $\alpha = 30°$. Thus, the emergence of strong wavemakers near the leading edge and over the separation

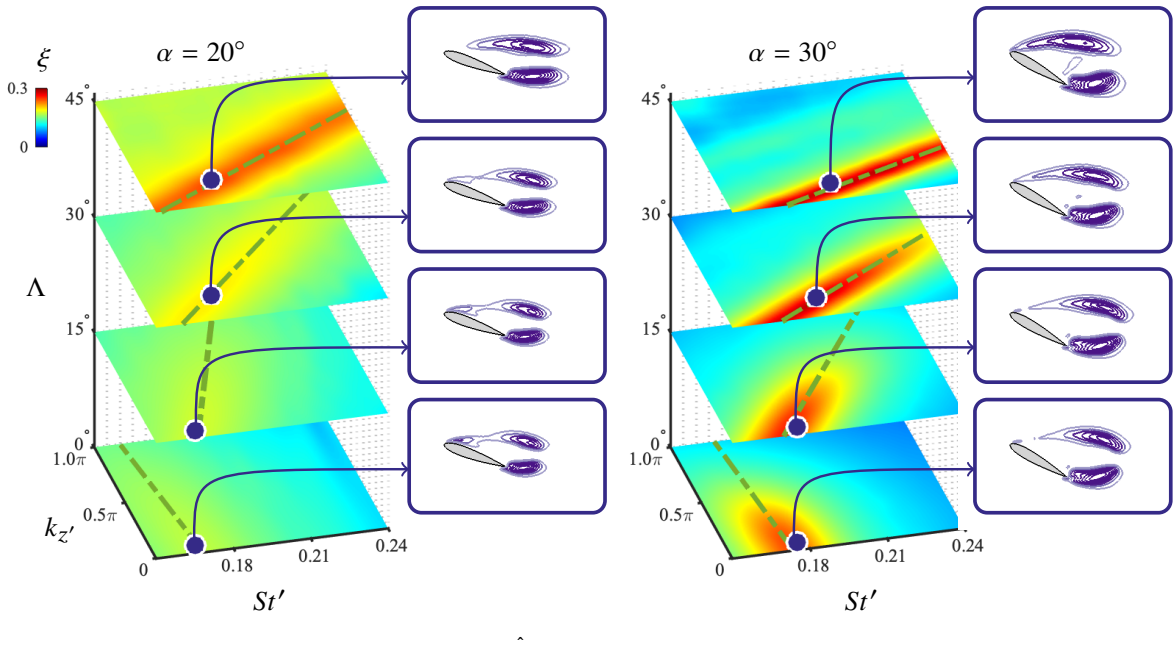

Figure 4.13: Contours of $\xi = (\sigma_1/max(\sigma_1))\langle\hat{q}_i, \hat{f}_i\rangle$, the inner product between forcing and response modes, scaled by the ratio of σ_1 and the maximum σ_1 for each α. Green line shows the convection speed $c = \mathrm{d}\omega/\mathrm{d}k_{z'}$ for the optimal wavemakers. Spatial modes shown by the Hadamard product of $\hat{q}_i$ and $\hat{f}_i$, in magnitude, normalized by their maximum value, and colored in purple scale.

bubble highlights the presence of self-sustained oscillations in the flow field. As the sweep angle tends to empower forcing and response modes overlap, wavemakers tend to be spatially wider in swept wings.

We evaluate the strength of wavemakers in the Λ–St'–$k_{z'}$ space with the inner product of pseudomodes $\langle\hat{q}_{k_{z'},\omega}, \hat{f}_{k_{z'},\omega}\rangle$ and their associated resolvent gain σ_1. In this way, we avoid accounting for the wavemakers where σ_1 is too small to amplify perturbations. Hence, to understand which combination of temporal frequencies, spanwise wavenumber, and sweep angle is most likely to generate wavemakers, we consider the coefficient $\xi = (\sigma/max(\sigma_1))\langle\hat{q}_i, \hat{f}_i\rangle$, where $max(\sigma_1)$ is evaluated for each angle of attack over the St'–$k_{z'}$–Λ space, with contours

shown in figure 4.13 for $\alpha = 20°$ and $30°$.

The resolvent modes with higher values of ξ are observed for swept wings at higher angles of attack. The wavemaker modes appear where vortex shedding develops in the wake. Hence a higher ξ suggests perturbations are introduced with higher gain to be amplified in this region for flows over wings at high incidence. Furthermore, those disturbances feed the flow with self-generated disturbances that maintain the three-dimensionality of the wake, as observed for instance at $\alpha = 30°$. In unswept wings, the St'–$k_{z'}$ frequencies with strong wavemaker modes is found for 2D wavemakers.

For swept wings, the modes with the highest ξ coefficient for each angle of attack are located at $\Lambda = 45°$ and nonzero $k_{z'}$, hence being associated with oblique modes. This finding is in agreement with the previous observations on the overlap of forcing and response modes, in figure 4.9. Hence, even if the amplification gain σ_1 is reduced for swept wings at $\alpha = 30°$, the overlap of forcing and response modes is stronger, which introduces wavemakers over swept wings that are stronger than wavemakers for unswept wings, which explains the three-dimensionality observed in these flow fields.

This finding, however, is in contrast with the DNS results that show an attenuation of spanwise oscillations with the sweep angle. To understand why such alleviation occurs, we must observe that optimal responses and optimal wavemakers also have an associated wave speed, characterized by their spatial and temporal frequencies, that is associated with the transport of disturbances over the periodic direction.

We note that an optimal wavemaker speed being faster than the optimal response wave speed leads to an attenuation on three-dimensionality. Wavemakers yield self-sustained instabilities in swept wings with an associated wavemaker phase speed $c_w = \mathrm{d}\omega/\mathrm{d}k_{z'}$, which we characterize by the slope of the slash-dotted green lines in figure 4.13. As observed in table 4.14, when c_w is large for high sweep angles and the optimal response c is small, the reduction of spanwise oscillations is seen in the flowfield. In such cases, a misalignment appears between optimal responses and wavemakers which can not support spanwise oscillations. For this

	$\alpha = 26°$				$\alpha = 30°$			
	$\Lambda = 0°$	15°	30°	45°	0°	15°	30°	45°
Opt. response	−0.021	0.022	0.089	0.253	−0.042	0.039	0.150	0.406
Opt. wavemaker	0.117	0.185	0.316	0.595	−0.008	0.073	0.204	0.537

Figure 4.14: Convective speed $c = \mathrm{d}\omega/\mathrm{d}k_{z'}$ for the optimal response and the optimal wavemakers for the 3D flows at $\alpha = 26°$ and 30° and sweep angles $0° \leq \Lambda \leq 45°$.

reason, wavemakers cannot sustain three-dimensional disturbances over swept wings.

Finally, even for $\alpha = 20°$, in which the flow field is 2D, resolvent analysis reveals the presence of wavemakers. Those are associated with the sustained unsteady 2D vortex shedding. To sustain three-dimensionality, wavemakers must introduce sufficiently strong three-dimensional structures to the flow with high amplification gain. For swept wings at high incidence, even though optimal wavemakers have a high gain, they are advected faster than the optimal responses, which reduces the flow three-dimensionality.

CHAPTER 5

Triglobal resolvent analysis

Through triglobal resolvent analysis, we reveal the effects of the wing tip, taper, and sweep angle on laminar separated wakes over swept wings. For the present study, we consider wings with semi-aspect ratios from 1 to 4, sweep angles from 0° to 45°, and angles of attack of 20° and 30° at a chord-based Reynolds number of 400 and 600, and a Mach number of 0.1. Triglobal resolvent analysis is employed to gain further insights into the mechanisms of flow unsteadiness and to identify the optimal spatial input-output mode pairs and the associated gains over a range of frequencies. The three-dimensional forcing and response modes reveal that harmonic fluctuations are directed toward the root for unswept wings and toward the wing tip for swept wings. The overlapping region of the forcing-response mode pairs uncovers triglobal resolvent wavemakers associated with self-sustained unsteady wakes of swept wings. The effect of wing taper is also shown through the forcing-to-response dynamics and resolvent wavemakers support. Furthermore, we show that for low aspect ratio wings optimal perturbations develop globally over the entire wingspan. The present study uncovers physical insights on the effects of tip and sweep on the growth of optimal harmonic perturbations and the wake dynamics of separated flows over swept wings.

5.1 Motivation

Understanding flow separation over finite swept wings is essential to the study of aircraft and biological flight [And10, VSP04, LMS07]. The aspect ratio, angle of attack, and sweep play important roles in influencing stall and wake characteristics [ZHA20a, ZHA20b]. Although

a number of studies have deepened our knowledge of laminar separated wakes around swept wings, coherent flow structures associated with the three-dimensional (3-D) flow separation have not been characterized in a comprehensive manner. Such findings would be crucial to explain the role played by the perturbations in characterizing the wakes and support efforts to control flow separation around finite wings.

Previous studies have shown the effect of sweep on post-stall wake characteristics with a focus on the role of spanwise flow over wings [HM64]. The spanwise flow induced by sweep delays the emergence of stall [YH07, YH09] and stabilizes wake oscillations, as shown for high-Reynolds number flows over transonic buffets in biglobal [CGS19, PBD19, PDB21] and triglobal linear stability analysis [Tim20, HT21]. Similar observations have been made for flows around aircraft models in experiments [MTP20] and computations [HTS22].

At a low Reynolds number, direct numerical simulations (DNS) from [ZHA20a] showed that sweep angle can significantly alter the wake patterns. For wings with low sweep angles, vortex shedding develops near the wing tip, while unsteadiness is suppressed for flows over highly swept wings. Similar attenuation of flow unsteadiness was further studied for forward-swept wings [ZT22] revealing that wing sweep has a strong effect on stabilizing wake oscillations in laminar flows. Furthermore, linear instabilities around swept wings were examined for a variety of swept and unswept wings, showing that the sweep angle suppresses the emergence of wake modes [BHH22, RYZ22a].

The aspect ratio of the wing also affects the wake dynamics on separated flows due to the wing tip vortex in steady [DRL96, TM04, TC09] and unsteady wing motion [BS06, YR12]. For low-aspect-ratio wings, the tip vortex may suppress the leading-edge vortex formation, reducing the wake unsteadiness [TC09]. Tip vortices can also produce adverse effects on the wing, with induced drag and a reduced lift.

To alter the wake dynamics with a proper actuation input, we need to identify the optimal forcing structures that can be amplified in the flow field [EST18, ESS18]. For this task, we may use modal analysis techniques [TBD17, THB20] to study the dynamics of

flow instabilities. Resolvent analysis is an attractive tool for the present study because it identifies the optimal input perturbations in the flow field, their energy amplification, and the characteristics of their unsteady response [TTR93b, JB05]. Furthermore, with the diverse steady and unsteady wakes observed around swept wings, resolvent analysis can provide a comprehensive study of the input-output dynamics around wings with different aspect ratios, angles of attack, and sweep.

Resolvent analysis has been used to study a broad range of fluid flows [MST13a, TP18, STR18, SS19, YBT20, RWT22]. This approach was initially formulated for steady base flows, to identify modal structures that can be amplified in stable flow regimes [TTR93b]. This perspective on fluid dynamics was later extended to unstable systems by [JB05] and to unsteady and turbulent flows by [MS10]. In these formulations, a time-averaged flow is used as a base state and nonlinear terms act as sustained forcing in the flow field. In both steady and unsteady flows, resolvent analysis identifies harmonic forcings that produce an amplified response in the flow.

In this study, we identify the optimal spatial input-output modes around the wing through a 3-D global (triglobal) resolvent analysis, that assumes no spatial homogeneity. Moreover, we gain insights into the self-sustained fluctuations that support unsteadiness on laminar separated flows using resolvent wavemakers, which are similar to the eigenvalue-based wavemakers [GL07, GCL10]. The resolvent wavemakers, also named structural sensitivity, are obtained from the overlap of forcing and response mode pairs [QS17, SYS22]. These findings provide a comprehensive analysis of the energy amplification mechanisms in flows around swept wings through an input-output process, identifying the optimal locations where perturbations can be introduced to alter the wake behavior. Therefore, these findings are crucial for the development of efficient flow control strategies [YT19, LSY21] that aim to improve the aerodynamic performance of swept wings experiencing massive flow separation.

The present chapter on triglobal resolvent analysis is organized as follows. In section 5.2, we describe the problem setup for the current work. In section 5.3, we discuss our main

findings from triglobal resolvent analysis. We identify the emergence of wake unsteadiness caused by the overlap of optimal forcing and response modes in the near wake. Perturbations are directed toward the region where vortex shedding takes place. The locations of the optimal forcing and response modes over the wingspan also suggest that wakes of highly swept wings are more resilient to external perturbations. Furthermore, we find that low-aspect-ratio wings limit the growth of perturbations to global modes extending over the entire wingspan. Finally, our conclusions are presented in section 7.1.4.

5.2 Tree-dimensional global (triglobal) resolvent analysis

We consider laminar flows over wings with NACA 0015 cross-sectional profile, as shown in figure 5.1. We perform a three-dimensional resolvent analysis over such wings and explore the effects of wing sweep, taper, aspect ratio, and angle of attack. The resolvent methodology is described in section 2.1. For a detailed discussion of the flow fields analyzed herein, we refer to the chapter 3.

The $\mathbf{H}_{\bar{\mathbf{q}},\omega}$ operators were discretized over 3-D structured grids with the leading edge at the root positioned at $(x/c,\ y/c,\ z/c) = (0, 0, 0)$, extending over $(x/c, y/c, z/c) \in [-10, 15] \times [-10, 10] \times [0, 10]$ with near wake grids shown at the bottom left of figure 5.1.The grids used for resolvent are smaller than the grids used for DNS. To obtain the base flow within the mesh for resolvent analysis, we perform a linear interpolation from the flow field defined in the DNS mesh to the resolvent mesh. We prescribe homogeneous Neumann boundary conditions for T' and homogeneous Dirichlet boundary conditions for the fluctuating variables ρ' and u' along the farfield, airfoil surface, and outlet. Sponges are applied far from the airfoil and in conjunction with the boundary conditions [Fre97].

For the large linear operators in the present work, efficient numerical tools are needed for SVD [HMT11b]. We use the randomized resolvent analysis algorithm from [RYT20], sketching $\mathbf{H}_{\bar{\mathbf{q}},\omega}$ with 10 random test vectors. Each entry of the test vectors is associated

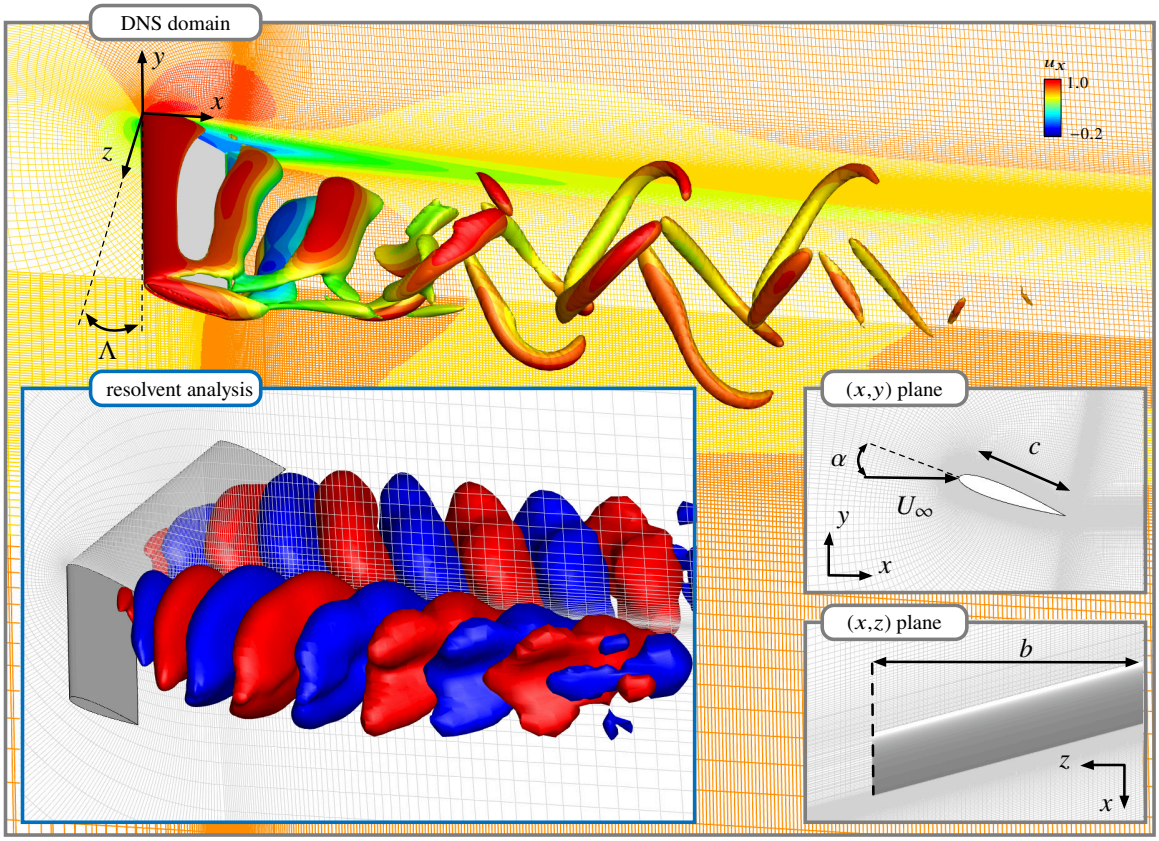

Figure 5.1: Setup for finite swept wing simulation at $Re_c = 400$. In the gray boxes, the instantaneous $Re_c = 400$ flow field for $\alpha = 20°$, $\Lambda = 15°$, and $sAR = b/c = 4$, with $Q = 2$ isosurfaces colored by instantaneous u_x. Mesh colored by time-averaged $\bar{u}_x$. In the blue box, isosurfaces of the primary response mode with mesh in light gray.

with a particular grid point and the five state variables. We compute the norm of the base flow gradients, i.e., $\|\nabla\rho\|, \|\nabla u_x\|, \|\nabla u_y\|, \|\nabla u_z\|, \|\nabla T\|$, and scale the test vectors at their specific entry associated with each spatial location and state variable [RYT20, HSR22].

The computation of resolvent modes for large linear operators can be challenging for the resolvent analysis of high-Reynolds number flows that require a large grid. The bottleneck is related to the time and memory requirements of the linear systems solvers within the SVD. Building an optimal basis to avoid linear system solvers is possible [BGM22], although a generalization for complex geometries is still challenging. It is possible, however, to obtain accurate resolvent modes with time-stepping instead of direct solvers. Those methods tend to penalize the time costs, although a considerable reduction in memory requirements can be achieved [BBS08, MAB10, GBR16]. The computational time required by time-steppers can also be reduced by incorporating streaming discrete Fourier transforms [MRT21, FTM21]. The use of iterative solvers has shown promising results to compute resolvent modes around a commercial aircraft model [HTS22].

In the present work, the direct and adjoint linear systems were directly solved using the MUMPS (multifrontal massively parallel sparse direct solver) package [ADD96]. Moreover, we incorporate the adjoint-based sensitivity analysis to interpolate the resolvent norm over frequencies ω [SB14, FS17]. This approach is used to calculate the gradient of σ with respect to ω, allowing an accurate interpolation among frequencies [SS19]. The codes used to compute the resolvent modes are part of the 'linear analysis package' made available by [SRT22].

5.2.1 Choice of resolvent discounting parameter

Prior to performing the resolvent analysis, we examine the stability characteristics of $\mathbf{L}_{\bar{\mathbf{q}}}$ and the need of a discounting parameter. For this task we analyze the eigenspectrum of the linear operator with respect to the time-average base flow. Since this base flow is not the equilibrium point, the eigenvalues of $\mathbf{L}_{\bar{\mathbf{q}}}$ do not necessarily present stability characteristics.

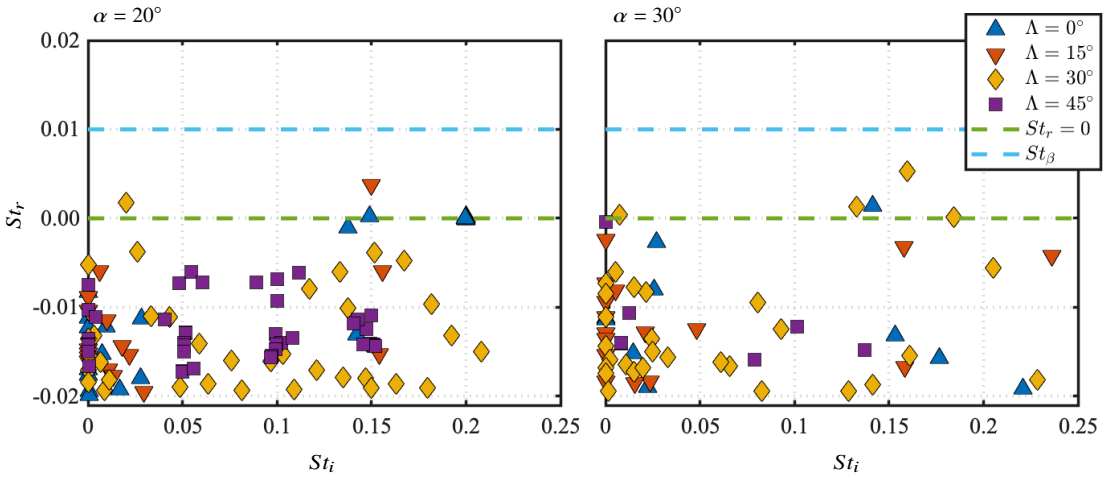

Figure 5.2: Eigenvalues of $\mathbf{L}_{\bar{\mathbf{q}}}$ for $sAR = 4$ wings with $\alpha = 20°$ and $30°$, and $0 \leq \Lambda \leq 45°$. Here St_r and St_i represent the growth rate and temporal frequency, respectively. Green–dashed line shows $St_r = 0$. Cyan-dashed line shows where discounting parameter is set.

However, eigenvalue properties are needed to enable the examination of the amplification mechanisms of perturbation over the appropriate time scale. The eigenvalues of $\mathbf{L}_{\bar{\mathbf{q}}}$ are computed using the Krylov–Schur method [Ste02] with 128 vectors for the Krylov subspace and a tolerance residual of 10^{-10}. This analysis reveals eigenvalues $-i\omega = -i\omega_r + \omega_i$, where ω_i is the growth rate and ω_r is the temporal frequency. The Strouhal number scaling (equation 4.8) is used throughout this study to report ω_i and ω_r as St_i and St_r, respectively, as shown in figure 5.2. The discounting parameter is defined in a similar manner as $St_\beta = (\beta/2\pi)(c \sin\alpha / U_\infty \cos\Lambda)$. In this manner, St_β is directly associated with a physical time window $t_\beta = (2\pi/\beta)$, which is chosen to be shorter than the time scale associated with the largest St_r. As shown in figure 5.2 for flows over $sAR = 4$ wings with $\alpha = 20°$ and $30°$, and $0 \leq \Lambda \leq 45°$, modes which appear with positive St_r (above green-dashed line) are so-called unstable.

Through the global stability analysis of all $\mathbf{L}_{\bar{\mathbf{q}}}$ operators examined in the present study, we observe that eigenvalues of the unstable modes with higher growth rate lie near the stability

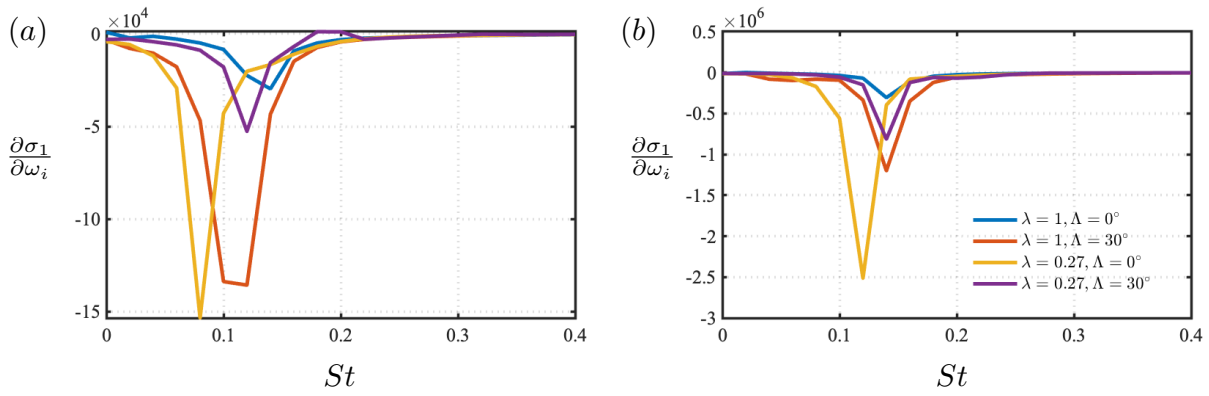

Figure 5.3: Decay of resolvent norm with ω_r indicating that the current discounting parameter accounts for a stable time-period for the growth of perturbations.

margin. The discounting parameter St_β must be chosen such that $St_\beta > \max(St_r)$ for all linear operators considered. For $St_\beta = 0.01$, the resolvent discounting is able to encompass all the unstable modes in the present study, as shown in figure 5.2 with a cyan-dashed line. This discounting corresponds to a physical time window of $t_\beta(U_\infty \cos\Lambda/c \sin\alpha) = 100$.

For the tapered wings of the present study, we have checked whether the time window t_β is sufficient by analyzing the parametric sensitivity of the resolvent gains with respect to ω_i, as shown in figure 5.3. For $St_\beta > \max(St_r)$, as we increase β, the gain σ_1 should decay [JB05, YT19], yielding negative $\partial\sigma_1/\partial\omega_i$. In this way, the negative values of $\partial\sigma_1/\partial\omega_i$ in figure 5.3 indicate that the β parameter was sufficiently large such that $St_\beta > \max(St_r)$ for the present linear operators. Through the discounted resolvent analysis, valuable insights have been provided in past studies for the dynamics and control of flows over airfoils [YT19, YBT20, RWT22, RYZ22b].

5.2.2 Convergence test for resolvent analysis

We document the randomized resolvent analysis computations in table 5.1, for a selected case of $(sAR, \alpha, \Lambda) = (2, 30°, 15°)$. The convergence of randomized SVD algorithm depends on the number of test vectors k used for sketching [HMT11b, RYT20]. As our discussions

	$k = 5$	$k = 10$	$k = 20$
σ_1	3058.119140625	3058.1840820312	3058.0112304688
σ_2	395.9677734375	397.50375366211	397.54058837891
σ_3	283.04278564453	285.14834594727	285.30682373047
σ_4	172.99363708496	178.36595153809	179.13203430176
σ_5	131.17066955566	155.90252685547	156.57176208496

Table 5.1: Convergence of the randomized resolvent analysis using $k = 5$, 10, and 20 test vectors shown for the five leading singular values with $(sAR, \alpha, \Lambda) = (2, 30°, 15°)$ at $St = 0.14$.

focus on the modal characteristics of the dominant and sub-dominant resolvent modes, we have analyzed their convergence using $k = 5$, 10, and 20. The use of $k = 10$ test vectors was shown to be sufficient to guarantee converged leading modes with error smaller than 1% for the leading 5 resolvent gains.

5.3 Results

5.3.1 Forcing and response modes structures

Let us first examine the dominant gains, forcing, and response modes for the $Re_c = 400$ flow over a $(sAR, \alpha, \Lambda) = (4, 20°, 0°)$ wing, as shown in figure 5.4. In the present section, we consider flows with chord-based Reynolds number fixed at $Re_c = 400$ and their wake dynamics was discussed in section 3.3.1. The dominant resolvent modes are observed at $St = 0.14$, where $St = (\omega/2\pi)(c \sin\alpha/U_\infty \cos\Lambda)$ is the Fage–Johanssen Strouhal number with a $1/\cos\Lambda$ scaling that incorporates the sweep angle, as discussed in section 4.3 This frequency matches the peak frequency for the lift coefficient shown in figure 5.4 (bottom left). The dominant frequency for σ_1 and $\hat{C}_L$ agrees for all unsteady flows presented herein.

The spatial structures of forcing-response mode pairs are shown in figure 5.4 (right) for

representative frequencies. For $St = 0.14$, primary modes exhibit modal structures near the root plane. The forcing mode appears near and upstream of the wing, while the response mode develops downstream in the wake. The modal structures for the primary forcing and response modes are aligned with the wingspan, with the response mode similar to the unsteady vortices revealed from DNS. At this frequency, the secondary modes are comprised of spanwise-aligned vortices near the root plane, similar to the primary modes.

As we increase the frequency, the resolvent gains decay in magnitude and σ_1 decays faster than σ_2. Their magnitudes become approximately the same at $St = 0.16$. At this frequency, the spatial characteristics of the primary and secondary forcing-response mode pairs exhibit distinct behavior. The primary forcing and response modes are aligned with the wingspan and near the root plane, similar to those at lower St. The secondary modes, however, exhibit modal structures near the wing tip, in contrast to the secondary modes at lower frequencies which reside near the wing root.

For $St = 0.18$, the primary forcing-response mode pair appears near the wing tip, while the secondary mode pair develops at the root plane. Such behavior persists as we increase the frequency to $St = 0.20$. For $St \geq 0.18$, primary modes are tip-dominated while secondary modes are root-dominated around this wing. This means that root and wing tip modes switch their order of amplification at $St \approx 0.18$, i.e., mode switching.

5.3.2 Wing sweep effects on resolvent modes

Here we consider flows with chord-based Reynolds number fixed at $Re_c = 400$ and their wake dynamics was discussed in section 3.3.1. The mode switching phenomenon discussed in the previous section is also observed for swept wings with $\Lambda = 15°$. For such wings, root-supported structures appear as the primary forcing-response pairs at $St = 0.14$, as shown in figure 5.5 (left). A distinct mode switching is observed over this wing, as the forcing-response pairs gradually transition toward the root at $z/c \approx 0$ with the increase in St. This type of concentrated resolvent mode at the wing root also appears for the unswept wings at

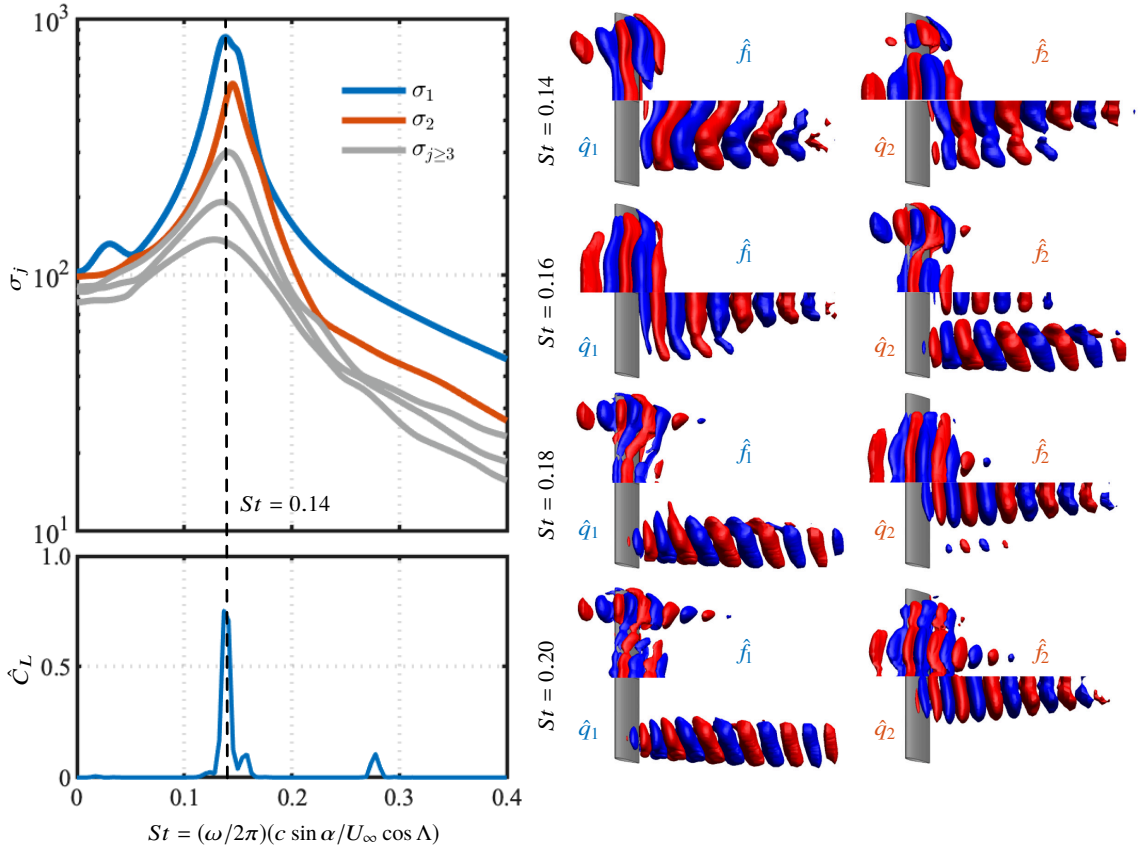

Figure 5.4: Resolvent gains and forcing-response mode pairs for the $Re_c = 400$ flow over a $(sAR, \alpha, \Lambda) = (4, 20°, 0°)$ wing. For each mode, forcing ($\hat{\mathbf{f}}$) is the top-half while response ($\hat{\mathbf{q}}$) it the bottom-half with isosurfaces of velocity $\hat{u}_y \in [-0.2, 0.2]$, with freestream directed to the right. On bottom left, power spectrum density of lift coefficient $\hat{C}_L$.

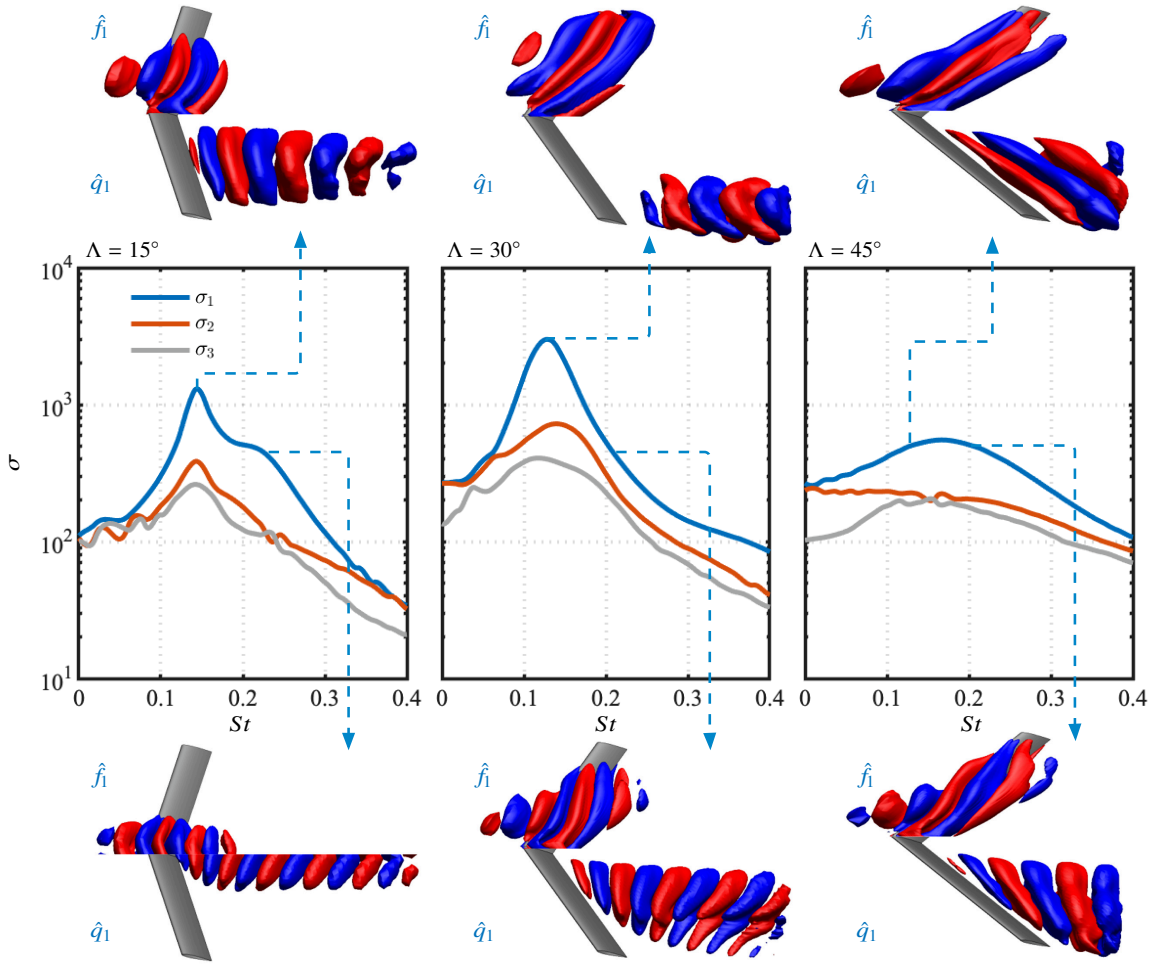

Figure 5.5: Resolvent gain distribution for the top three mode pairs and forcing-response mode pairs for selected frequencies for $(sAR, \alpha) = (4, 20°)$ and $\Lambda = 15°$, $30°$, and $45°$. The chord-based Reynolds number for these base flows is $Re_c = 400$. Primary forcing ($\hat{f}$) and response ($\hat{q}$) modes shown with isosurfaces of velocity $\hat{u}_y \in [-0.2, 0.2]$.

$St = 0.20$ as a secondary mode, as shown in figure 5.4 (bottom, right).

For $\Lambda = 30°$, mode switching also occurs toward the root with the increase in St, in an opposite trend to the unswept wings. The dominant response modes at lower frequencies appear at the wing tip, as shown in figure 5.5 (middle). There is a gradual transition to root-supported modes as the frequency increases. At a higher sweep angle, $\Lambda = 45°$, no mode switching occurs. The region of the dominance of the forcing and response modes is slightly invariant for the frequencies shown herein.

In contrast with the lower sweep angle wings, for $\Lambda = 45°$, forcing and response modes are dominant at distinct wingspan locations, as shown in figure 5.5 (right). Response modes are tip-dominated while forcing structures appear upstream near the root plane, extending over the wingspan aligned with the sweep angle. For all $(sAR, \alpha) = (4, 20°)$ wings, the highest amplification is found for $\Lambda = 30°$, at $St \approx 0.12$. At $\Lambda = 45°$, the dominant gain is an order of magnitude lower. This finding suggests that it is challenging to perturb flows over $\Lambda = 45°$ wings. These wings are steady because self-sustained flow disturbances cannot introduce sufficient energy into the wake to generate vortex shedding.

5.3.3 Wing taper effects on resolvent modes

The triglobal resolvent modes further reveal the spatial sensitivity, the response structures, and the harmonic behavior over the wake behind tapered wings. The present flows consider the wake dynamics around wings presented in section 3.3.2, with a mean-chord-based Reynolds number of $Re_c = 600$. To this end, we will study perturbations through the overlap between the forcing and response modes in the spanwise direction. We integrate the magnitude of velocity components of $\hat{\mathbf{f}}$ and $\hat{\mathbf{q}}$ over z-normal planes as

$$\boldsymbol{\Omega}_{\hat{\mathbf{f}}}(z) = \int_{S(x,y)} \|\hat{\mathbf{f}}\|_2 \, \mathrm{d}S(x,y) \quad \text{and} \quad \boldsymbol{\Omega}_{\hat{\mathbf{q}}}(z) = \int_{S(x,y)} \|\hat{\mathbf{q}}\|_2 \, \mathrm{d}S(x,y) \, , \tag{5.1}$$

where $\|\hat{\mathbf{f}}\|_2$ and $\|\hat{\mathbf{q}}\|_2$ are the 2-norm of $[\hat{\mathbf{f}}_{u_x}, \hat{\mathbf{f}}_{u_y}, \hat{\mathbf{f}}_{u_z}]$ and $[\hat{\mathbf{q}}_{u_x}, \hat{\mathbf{q}}_{u_y}, \hat{\mathbf{q}}_{u_z}]$, respectively, at each grid point of the computational domain. By performing the integral over $S(x, y)$, we obtain

$\mathbf{\Omega_{\hat{f}}}$ and $\mathbf{\Omega_{\hat{q}}}$ computed for each spanwise slice and for each frequency. Here, we plot their contours normalized by the maximum $\mathbf{\Omega_{\hat{f}}}$ and $\mathbf{\Omega_{\hat{q}}}$ at each St, to emphasize the spatial support of forcing and response over the wingspan.

So far, all base flows considered for the present triglobal resolvent study have a chord-based Reynolds number set to $Re_c = 400$, which were briefly discussed in section 3.3.1. From now on, we will also introduce the triglobal resolvent modes computed for the base flows over tapered wings at $Re_c = 600$. In figure 5.6, we present the forcing and response modes over two wings with unswept TE and $\lambda = 1$ (untapered) and 0.27 at $Re_c = 600$. The gain (σ_j) curves, shown in figures 5.6(a, d), exhibit the distribution over St for each wing. The curves are similar and they have a large resolvent gain peak at approximately the same St number.

In figures 5.6(c, f) we show three forcing (top,right half span) and response (bottom, left half span) mode pairs at $St = 0.14$, 0.20, and 0.30. Generally, we observe that forcing and response modes are aligned in the streamwise direction while forcing modes appear upstream and response modes dominate the downstream wake region. Now, let us look at the resolvent gain distribution over St, shown in figure 5.6(a, d). For both wings, the resolvent gain peaks at a similar St. We note that the response structures at the peak frequency exhibit a mode shape similar to the shedding structures that were observed in the DNS, at a slightly different $\alpha = 18°$, as shown in figure 3.4.

Although both wings have a peak resolvent gain frequency at approximately the same Strouhal number, the σ_1 spectra change as frequency increases which also has implications on the spatial modal structures. For instance, we observe a secondary peak in the σ_1 spectra that appear only for the tapered wing at $St \approx 0.2$, as shown in figure 5.6(d). This secondary peak coincides with the same frequency where the $\Omega_{\hat{\mathbf{f}}}$ and $\Omega_{\hat{\mathbf{q}}}$ contours, shown in figure 5.6(e), exhibit a mode switching from $z/c \approx 1$ dominant modes at low St to root-dominant modes at $St \approx 0.2$.

As the frequency increases to $St \approx 0.3$, there is another mode switching which now

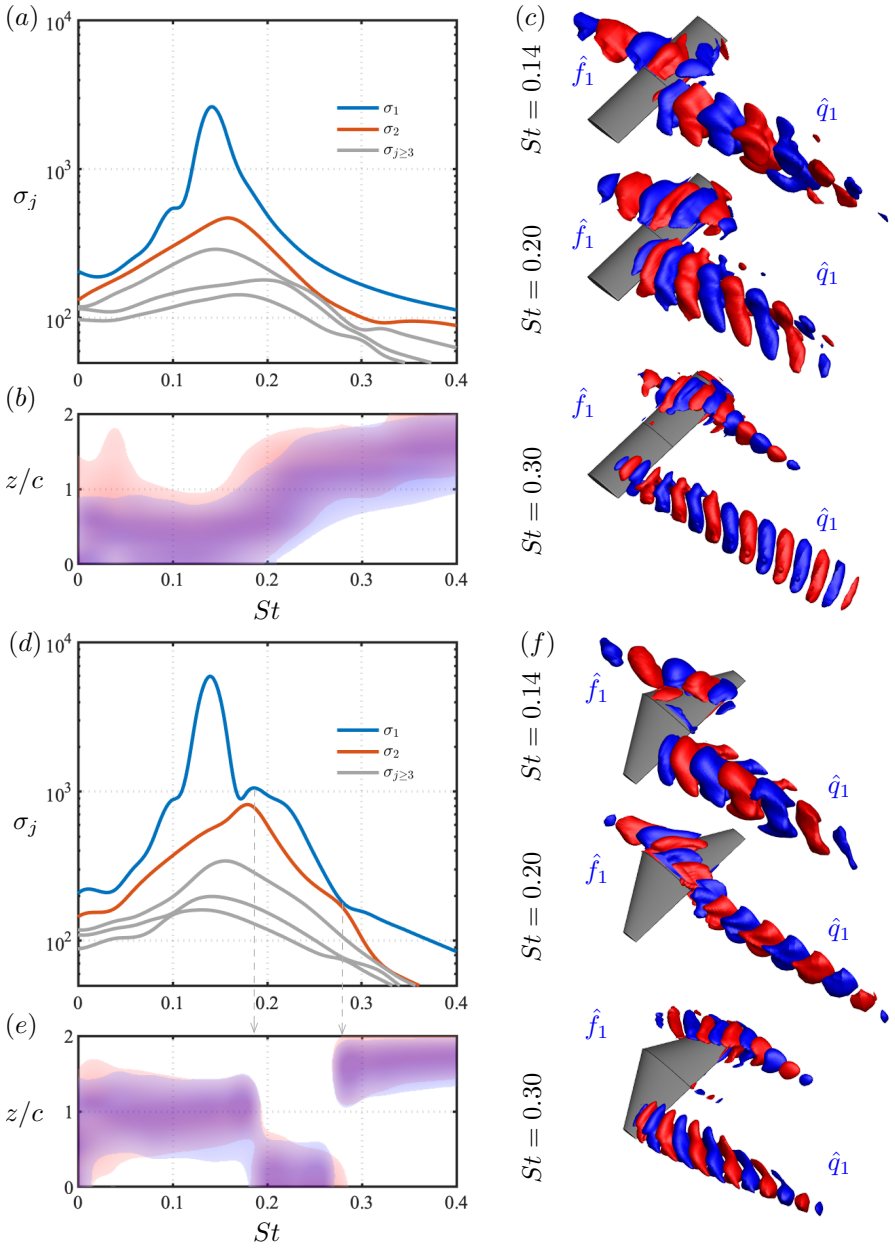

Figure 5.6: Effect of wing taper on resolvent modes, for $Re_c = 600$ flows over tapered wings. (a, d) Gain curves (σ_j), (b, e) contours of $\mathbf{\Omega}_{\hat{\mathbf{f}}}$ (red) and $\mathbf{\Omega}_{\hat{\mathbf{q}}}$ (blue) to highlight the wingspan (z/c) location of dominant forcing and response modes, (c, f) and isosurfaces of $\hat{u}_y = \pm 0.5$ for leading forcing $(\hat{f}_1)$ and response $(\hat{q}_1)$ modes at $St = 0.14$, 0.2, and 0.3. Results shown for (a, b, c) untapered wing and (d, e, f) tapered wing with unswept TE and backward-swept LE at $\alpha = 22°$. Light gray arrows indicate mode switching in (d) and how it appears in (e).

occurs from the root-dominant modes at $St \approx 0.2$ toward the wing tip dominant modes at $St \approx 0.3$. This sequence of mode switching over a short frequency range was observed previously for $sAR = 4$ untapered and unswept wings but not for $sAR = 2$ wings. Such low-aspect-ratio wings exhibit a smooth transition between root and tip regions as the frequency increases [RYT23]. This finding suggests similarities in the input-output dynamics observed around low-aspect-ratio tapered wings and high-aspect-ratio untapered and unswept wings. For the present $sAR = 2$ untapered wing, as shown in figure 5.6(a, b), mode switching is absent. There is a gradual transition from root-dominated modes to tip modes as the Strouhal number increases.

We also show the effect of sweep on the optimal perturbations for highly swept wings, that is, wings with high LE sweep angle $\Lambda_{\text{LE}} = 40°$. DNS has shown that wing taper promotes unsteadiness in the wake. This yields a significant impact on the resolvent modes, as shown in figure 5.7. Here, we analyze 3 highly swept wing planforms with $\Lambda_{\text{LE}} = 40°$ and taper ratios (a, b) $\lambda = 1$, (c, d) $\lambda = 0.5$, and (e, f) $\lambda = 0.27$ through their triglobal resolvent modes. The peak resolvent frequency shifts toward a slightly higher St for lower λ and the dominant σ_1 decays. To understand this behavior, we need to resort to the wake dynamics characteristics observed in the DNS, as shown in figure 3.4. At $\alpha = 22°$, there are small oscillations that appear downstream in the wake, far from the wing. These flow oscillations may not be characterized as wake shedding structures, they possess a low-frequency content, being highlighted in the resolvent analysis by the backbone-shaped modes captured in the primary and secondary resolvent modes in figure 5.7(b).

At the σ_1 peak frequency, we further study the ratio between σ_1 and σ_2, as these modes are characterized by a high amplification and a low-rank behavior of the resolvent operator. For lower λ, the σ_1/σ_2 ratio increases at the peak gain, which coincides with the appearance of shedding structures emerging from the separation bubble, as observed in figure 3.4. It is noteworthy that, for lower λ, the dominant response modes are shifted closer to the wing and exhibit a shedding structure shape, similar to the wake structures characterized in the

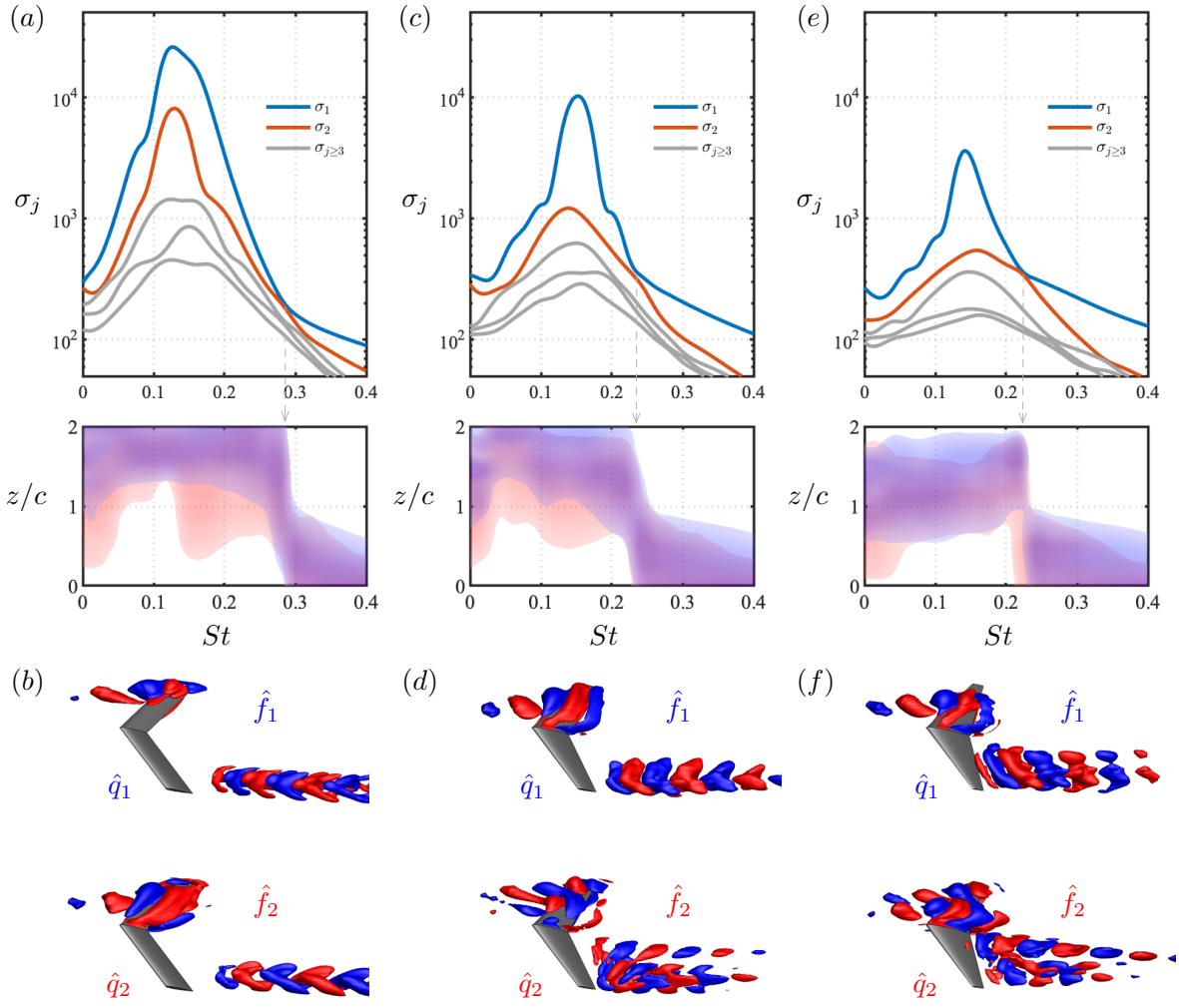

Figure 5.7: Effect of wing taper on resolvent modes for flows with $Re_c = 600$. (a, c, e) Gain curves (σ_j) on top and contours of $\mathbf{\Omega}_{\hat{\mathbf{f}}}$ and $\mathbf{\Omega}_{\hat{\mathbf{q}}}$ on bottom to highlight the wingspan (z/c) location of dominant forcing (red) and response (blue) modes. (b, d, f) Isosurfaces of $\hat{u}_y = \pm 0.5$ for dominant and subdominant forcing $(\hat{f})$ and response $(\hat{q})$ modes at their peak gain. Results shown for (a, b) untapered swept wing with $\Lambda_{\text{LE}} = 40°$, (c, d) tapered swept wing $\Lambda_{\text{LE}} = 40°$ and $\lambda = 0.5$, and (e, f) tapered swept wing $\Lambda_{\text{LE}} = 40°$ and $\lambda = 0.27$ at $\alpha = 22°$. Light gray arrows in (a, c, e) point to mode switching observed in the resolvent gain spectra and how it appears in the spatial modes shown below.

DNS, while the response modes for the wings with $\lambda = 0.5$ and 1 emerge far from the wing tip and exhibit the backbone-shaped modal structure which is characteristic of tip-dominant modes [RYT23].

The secondary modes exhibit similar behavior as the dominant modes, being developed at the same wingspan region as the primary modes. The mode shapes associated with σ_2 modes, however, can be very different. For instance, the secondary forcing mode for the untapered wing at the peak gain, shown at the bottom of figure 5.7(b) spans over the entire wing surface, while the leading forcing is localized near the wing tip. The presence of forcing mode spread over the wingspan appears also for the lower taper ratios at their peak frequency, as shown in figures 5.7(d, f).

The $\Omega_{\hat{\mathbf{f}}}$ and $\Omega_{\hat{\mathbf{q}}}$ contours for the highly swept wings shows similarities for all taper ratios. There is a single characteristic mode switching for all wings at $St \geq 0.2$. We note, however, that the dominance of forcing-response mode pairs for the $\lambda = 0.27$ wing appears at $z/c \approx 1$, for $St \leq 0.2$, while for higher taper ratios, the tip region near $z/c \approx 2$ is characterized by the dominance of forcing-response modes at lower frequencies.

5.3.4 Forcing-to-response dynamics over high-aspect-ratio swept wings

Here we initially consider flows with chord-based Reynolds number fixed at $Re_c = 400$ and their wake dynamics discussed in section 3.3.1 for $sAR = 4$ wings. Using the contours plots of $\mathbf{\Omega}_{\hat{\mathbf{f}}}$ and $\mathbf{\Omega}_{\hat{\mathbf{q}}}$ at each St, we identify the locations of the maximum strength of forcing and response modes as shown by the dot-dashed lines in figure 5.8. Black arrows indicate the direction from the maximum forcing to the maximum response at $St = 0.15$. This analysis depicts the preferential direction in which optimal forcing is transferred to optimal response over the wingspan at each frequency.

For unswept wings, shown in figure 5.8 (left), the optimal forcing structures appear closer to the wing tip than the response modes, which are slightly shifted toward the root,

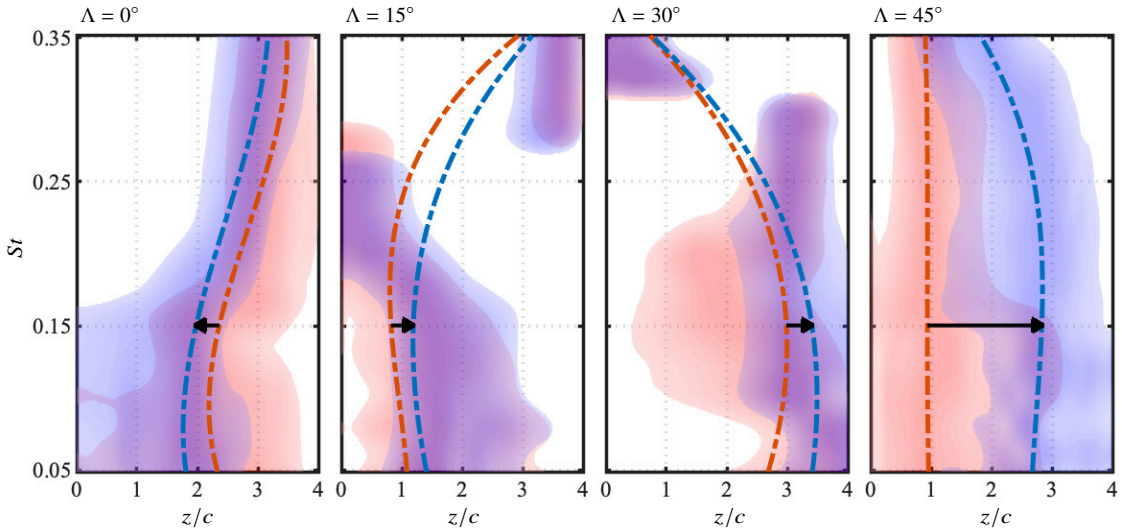

Figure 5.8: Wingspan locations of dominant forcing (red) and response (blue) with contours of $\mathbf{\Omega}_{\hat{\mathbf{f}}}$ and $\mathbf{\Omega}_{\hat{\mathbf{q}}} \in [0.4, 1.0]$ for $0.05 \leq St \leq 0.35$ for $Re_c = 400$ flows over $sAR = 4$ wings with $\alpha = 30°$ with $0° \leq \Lambda \leq 45°$. Dot-dashed lines are polynomial fit of maximum z/c of forcing and response at each St. Arrows show direction of optimal forcing-to-response at $St = 0.15$.

suggesting that fluctuations are directed toward the root. Indeed, as seen in the DNS, unsteadiness is concentrated toward the root, as evident from figure 3.3, also in agreement with the results reported by [ZHA20b]. In addition, the flow around the wing tip for unswept wings is characterized by an almost steady tip vortex, suggesting that it is hard to amplify flow instabilities near the tip.

For swept wings, fluctuations are directed toward the wing tip. For $\Lambda = 15°$, both forcing and response modes appear near the wing root. At the vortex shedding frequency for this wing, $St \approx 0.15$, we observe forcing and response modes to be dominant at $z/c \approx 1$, with the forcing mode supported closer to the wing root than the response mode. This concurs with the flow field we observe in the DNS, as vortices are formed near the wing root and evolve toward the wing tip where spanwise vortices appear and propagate in the wake. For the $\Lambda = 30°$ wing, the dominant forcing-response mode pair emerges near the wing tip at low St,

as seen in figure 5.8. For this wing, low-frequency vortical structures emerge downstream in the wake aligned at the tip, as shown in figure 3.3.

For the $\Lambda = 45°$ wing, the distance between the maximum forcing and response modes significantly increases. For this sweep angle, the region of forcing is centered at $z/c \approx 1$, while the response is supported mostly at $z/c \approx 3$. As the peak σ_1 is smaller for this wing compared to lower sweep angle planforms, we can argue that a significant amount of energy is required for an external forcing to perturb the wakes of highly swept wings. For all wings with $sAR = 4$, this distance between the dominant forcing-response mode pairs is strongly associated with the sweep angle, while having a minor dependency on the angle of attack and presenting a gradual decrease with the frequency.

The direction from forcing-to-response revealed by the optimal triglobal resolvent modes suggests a spanwise advection of flow structures associated with the sweep angle. As shown previously, we can relate the forcing-to-response characteristics to the vortical fluctuations observed in the DNS. We can further relate these findings to the modal convective speed from biglobal stability analysis over swept wings [CGS19, PBD19, PDB21]. Triglobal resolvent modes also reveal the advection of perturbations over the wingspan related to the sweep angle, the attenuation of flow unsteadiness, and the resilience to grow perturbations at high sweep angles. Even for unswept wings, the triglobal analysis uncovers a preferential root-direction for the advection of instabilities.

5.3.5 Forcing-to-response dynamics over tapered wings

We further examine the $\Omega_{\hat{\mathbf{f}}}$ and $\Omega_{\hat{\mathbf{q}}}$ contours over a broad range of wing planforms and show the mode-switching phenomena as well as the mode transition between root and tip dominant modes for the $Re_c = 600$ flows observed around tapered swept wings, as shown in figure 5.9. The present flows consider the wake dynamics around wings presented in sections 3.3.2 to 3.5.5, with a mean-chord-based Reynolds number of $Re_c = 600$. Here, the locations of the maximum strength of forcing and response modes are shown by the dot-dashed lines.

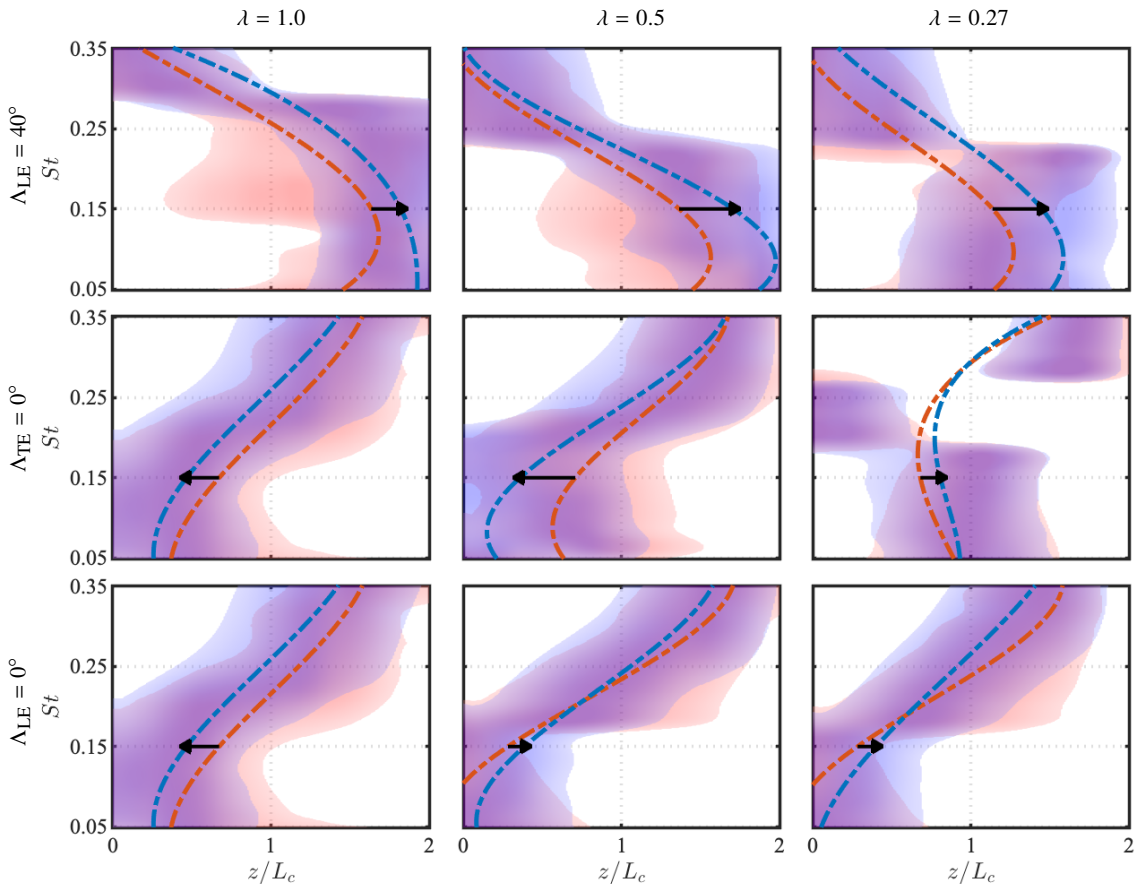

Figure 5.9: Effect of wing taper on forcing and response modes over wingspan for the $Re_c = 600$ flows over wings at $\alpha = 22°$ with unswept LE and forward-swept TE, backward-swept LE and unswept TE, and tapered wings with $\Lambda_{\mathrm{LE}} = 40°$. Black arrows show the direction from the maximum strength of forcing (red) to the maximum strength of response (blue).

Black arrows indicate the direction from the maximum forcing to the maximum response at $St = 0.15$.

For highly swept wings, shown in the top row of figure 5.9, wing taper influences the forcing modes, which tend to appear closer to the quarter span at $St = 0.15$ for tapered wings, in contrast with the untapered and swept wings that have both forcing and response localized in the wing tip region. For the case of wings with unswept TE and backward-swept LE, wing taper causes forcing and response to overlap at the quarter-span for $\lambda = 0.27$ wings, where the shedding is observed over this wing. This shows that external forcing over this wing promotes the amplification of flow perturbations aligned in the streamwise direction at the quarter-span of the wing for $St = 0.15$, with small spanwise dislocation. For higher taper ratios, there is a preferential direction of perturbations to be amplified toward the wing root, where shedding structures emerge.

For the case of unswept LE wings with forward-swept TE, shown in the bottom row of figure 5.9, forcing and response modes collapse near the root at small St numbers. There are no strong forcing or response modes localized at the tip region, for the frequencies shown, the maximum wingspan location of forcing modes is observed at $z/c \approx 1.5$. This shows that the wing tip is challenging to amplify disturbances over the wing tip for this planform, as also suggested by the observations of the flow field from DNS.

5.3.6 Perturbation dynamics around low-aspect-ratio wings

High sweep angle and low aspect ratio restrict the emergence of fluctuations in flows over finite wings. As shown in figure 5.8, tip- and root-dominated modes may extend over 1 or 2 chord-lengths over the wingspan. For this reason, for flows over wings with $sAR < 2$, the dominance of the global modes may not be associated with root or tip regions, as they extend over the entire wingspan. To analyze the effect of aspect ratio on the resolvent modes, we analyze the flows over finite swept wings without taper at $Re_c = 400$, as we have obtained base flows for semi-aspect-ratios ranging from 1 to 4 at this particular chord-based Reynolds

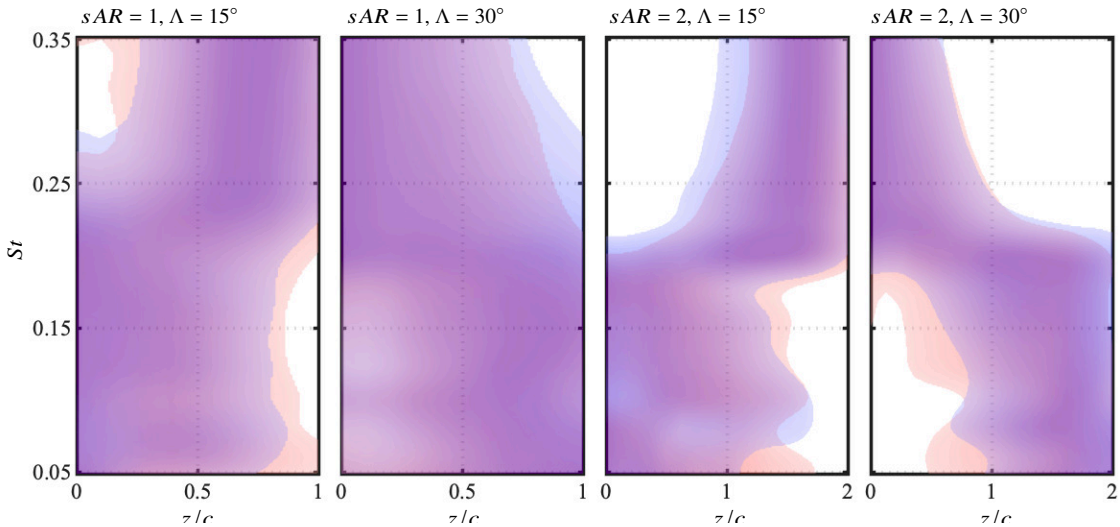

Figure 5.10: Wingspan locations of dominant forcing (red) and response (blue) with contours of $\mathbf{\Omega}_{\hat{\mathbf{f}}}$ and $\mathbf{\Omega}_{\hat{\mathbf{q}}} \in [0.4, 1.0]$ for $0.05 \leq St \leq 0.35$ for wings at $\alpha = 30°$, $sAR = 2$ and 1, and $\Lambda = 15°$ and $30°$. The chord-based Reynolds number is set to $Re_c = 400$.

number.

For flows over $sAR = 2$ wings, we observe a gradual transition between root-dominated and tip-dominated forcing and response modes, as shown in figure 5.10. For $\Lambda = 15°$, the optimal forcing-response mode pair appears near the root for lower frequencies and at the wing tip for higher frequencies, characterizing a root-to-tip mode switching. For $\Lambda = 30°$, the trend is opposite, with wing tip modes at lower frequencies and root modes at higher frequencies, characterizing a tip-to-root mode switching. These features are similar to the mode switching observed for these sweep angles with $sAR = 4$, as shown in figure 5.8.

For wings with a low aspect ratio, the growth of root-dominated and tip-dominated perturbations is constrained and mode switching does not occur for $sAR = 1$, as shown in figure 5.11. Distinguishing between root-dominated and tip-dominated modes may be challenging for flows over $sAR = 1$ wings as forcing and response mode pairs appear globally, extending over the entire wingspan, independently of the sweep angle. Therefore, flows

around wings with $sAR = 1$ tend to exhibit similar wake characteristics over different sweep angles. Indeed, the wake patterns for flows over $sAR = 1$ wings at a particular angle of attack and sweep exhibit different characteristics from the flows over higher aspect ratio wings, i.e., $sAR = 2$ and 4.

For high-aspect-ratio wings, for instance, the flow around $(sAR, \alpha, \Lambda) = (4, 30°, 15°)$ wings, we observe in the DNS that the wake shedding structures appear over the entire wingspan. The resolvent modes depict these structures in three different flow mechanisms. As shown in figure 5.11 (right) for $sAR = 4$, there are two types of root-dominated modes, which were also previously identified for this wing at $\alpha = 20°$, shown in figure 5.5 (left). The first one is characterized by root-dominated structures and appears at $St = 0.15$, while the second type, with a high σ_1, develops at $St = 0.25$ with compact root-concentrated modes. The third type is comprised of tip-dominated modes that become primary as the frequency increases to $St = 0.28$. These modes were primary at $\alpha = 20°$ at $St \approx 0.40$, as shown in figure 5.5, although for $\alpha = 30°$ they present a higher amplification gain.

For $sAR = 2$, root-dominated modes are primary for $St < 0.20$. Root-concentrated modes are absent and tip-dominated modes are the primary perturbations for $St \geq 0.20$, as shown in figure 5.11 (middle), characterizing a root-to-tip mode switching. The overall mode switching for $sAR = 2$ is the same, with root-to-tip transition. For $sAR = 1$, shown in figure 5.11 (left), mode switching is absent. Both primary and secondary modes develop over the entire wingspan for all frequencies, as shown for the primary modes at $St = 0.14$. Although mode switching is absent we can still reveal two distinct root- and tip-dominated mechanisms on a single mode over low-aspect-ratio wings. For instance, at $St = 0.24$, modes emerge from the leading edge at the root and from the trailing edge near the tip. Combined, these two flow instabilities yield a global mode that appears over the entire wingspan.

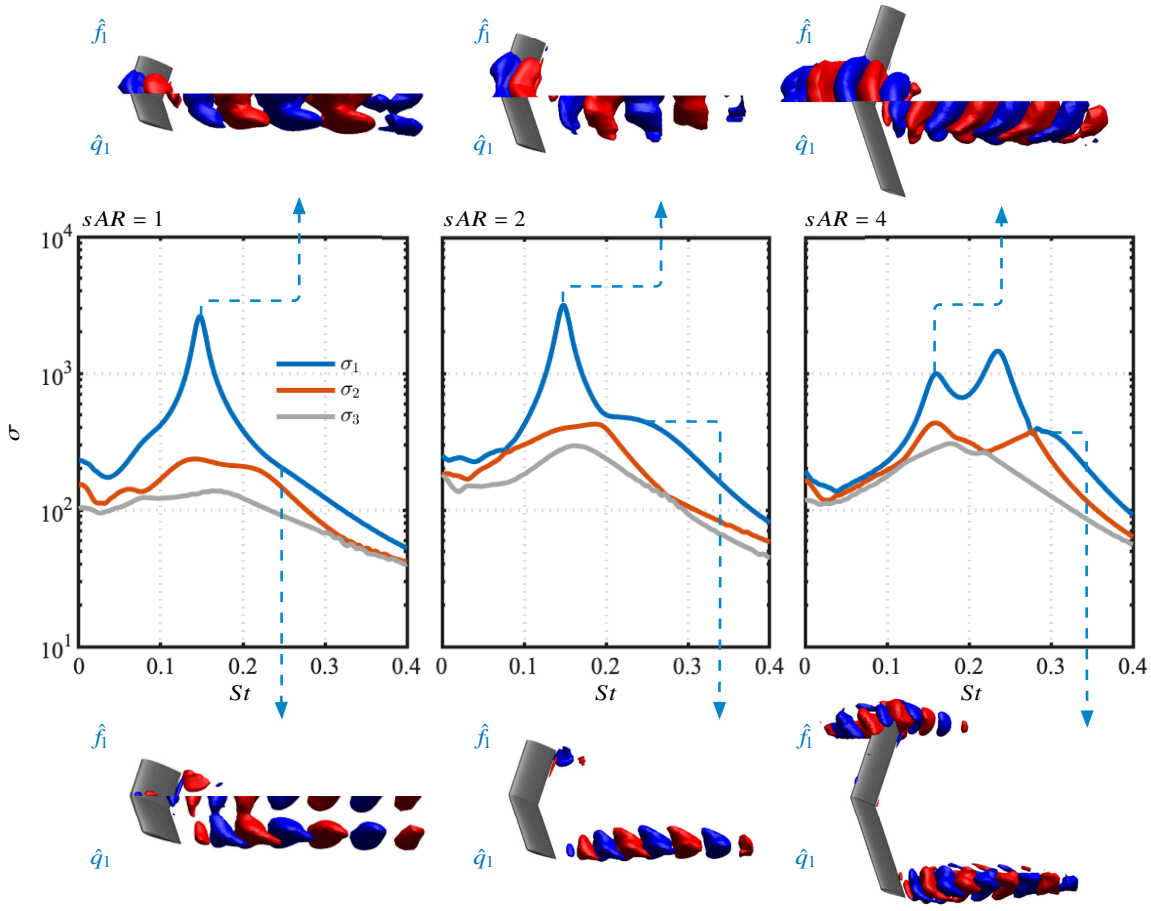

Figure 5.11: Resolvent gain distribution and forcing-response mode pairs over frequency for $(\alpha, \Lambda) = (30°, 15°)$ and $1 \leq sAR \leq 4$. Forcing $(\hat{f})$ and response $(\hat{q})$ modes shown with isosurfaces of velocity $\hat{u}_y \in [-0.2, 0.2]$. Mode switching is absent for $sAR = 1$ due to merging of root and wingtip perturbations on the wake.

5.3.7 Resolvent wavemakers

To characterize the self-sustained unsteadiness in the flows over swept wings, we study the forcing and response modes spatial overlap that supports the continuous formation of vortical structures. Since the forcing modes show regions receptive to external perturbations and the response modes reveal the structures being excited due to the forcing, the region over which forcing and response modes overlap can be interpreted as a mechanism for self-sustained oscillations to present in the flow. This idea is similar to the wavemaker concept deduced from direct and adjoint eigenmodes presented in [GL07].

Through the wavemaker analysis, previous studies identified critical points responsible for sustaining wake shedding on laminar wakes around cylinders [SS90, Hil92] and regions associated with their primary and secondary instability modes [GL07, GCL10]. Moreover, wavemakers revealed the physical mechanisms responsible for tonal noise generation in high-Reynolds number flows over airfoils [FSS17] and self-sustained flow instabilities in transonic buffet regimes [PBD19].

In the aforementioned studies, wavemakers were derived from direct and adjoint global stability eigenmodes. Our formulation derives wavemakers from global resolvent modes and is closely related to the structural sensitivity devised by [QS17] and to the resolvent wavemaker obtained by [SYS22]. The present resolvent wavemaker is not identical to the eigenvalue-based wavemaker. With the time-averaged base flow, the forcing terms model nonlinear effects as a internal feedback mechanism within the flow field. Hence, the spatial overlap between forcing and response provides useful insights on the support of self-sustained oscillations in the wake. Herein, the resolvent wavemaker modes are directly obtained from resolvent modes, as the Hadamard product of forcing and response

$$\hat{\mathbf{w}} = \hat{\mathbf{f}} \circ \hat{\mathbf{q}} \ , \tag{5.2}$$

where $\hat{\mathbf{w}}$ is the resolvent wavemaker mode. The resolvent modes presented herein are defined with the five state variables, $\hat{\mathbf{f}} = [\hat{\mathbf{f}}_\rho, \hat{\mathbf{f}}_{u_x}, \hat{\mathbf{f}}_{u_y}, \hat{\mathbf{f}}_{u_z}, \hat{\mathbf{f}}_T]$ and $\hat{\mathbf{q}} = [\hat{\mathbf{q}}_\rho, \hat{\mathbf{q}}_{u_x}, \hat{\mathbf{q}}_{u_y}, \hat{\mathbf{q}}_{u_z}, \hat{\mathbf{q}}_T]$. For the

resolvent wavemaker, we consider only the velocity components, $\hat{\mathbf{w}} = [\hat{\mathbf{w}}_{u_x}, \hat{\mathbf{w}}_{u_y}, \hat{\mathbf{w}}_{u_z}]$, as for weakly compressible low-Reynolds number flows, the inclusion of ρ and T terms does not alter the findings. We define our resolvent wavemaker gain ξ as

$$\xi = \sigma^2 \int_S |\hat{\mathbf{w}}(\mathbf{x})| \, \mathrm{d}S \, , \tag{5.3}$$

which is in close agreement with $\xi = \sigma^2 |\langle \hat{\mathbf{f}}, \hat{\mathbf{q}} \rangle|$, derived by [SYS22] and obtained when S is defined over the entire computational domain. The resolvent wavemaker gain ξ can also be computed for each spanwise slice and each frequency. To this end, we consider $S = S(x, y)$, as z-normal planes at different spanwise locations, to build the ξ-contours shown in figure 5.12. Through this analysis, we highlight the resolvent wavemaker spatial support over the wingspan.

Let us focus our resolvent wavemaker analysis on the flow over the unswept wing with $(sAR, \alpha, \Lambda) = (4, 20^\circ, 0^\circ)$, as shown in figure 5.12 (top, left). At $St = 0.14$, triglobal resolvent wavemakers with high ξ appear between $2 \lesssim z/c \lesssim 3$ in the near wake. The resolvent wavemakers at this region support the formation of unsteady root vortices that propagate downstream in the wake. This resolvent wavemaker region is also characterized by the formation of braid-like structures that connect to the root shedding as vortex loops [ZHA20a]. Resolvent wavemakers for $(sAR, \alpha, \Lambda) = (4, 20^\circ, 15^\circ)$ also show similar shedding behavior, as seen in figure 5.12 (top, right).

Resolvent wavemakers are also revealed for steady flows. The overlap of forcing and response for flows over wings with $(sAR, \alpha, \Lambda) = (4, 20^\circ, 30^\circ)$, as shown in figure 5.12 (bottom, left), develops over the wing and extends into the wake aligned with the wing tip. These resolvent wavemakers extend over the entire wingspan, being stronger and larger than the ones exhibited around wings with lower sweep angles. The ξ peak appears at the wing tip at $St = 0.12$, indicating that the tip region is more susceptible to develop unsteadiness around this wing.

For $\Lambda = 45^\circ$, shown in figure 5.12 (bottom, right), we reveal that resolvent wavemakers

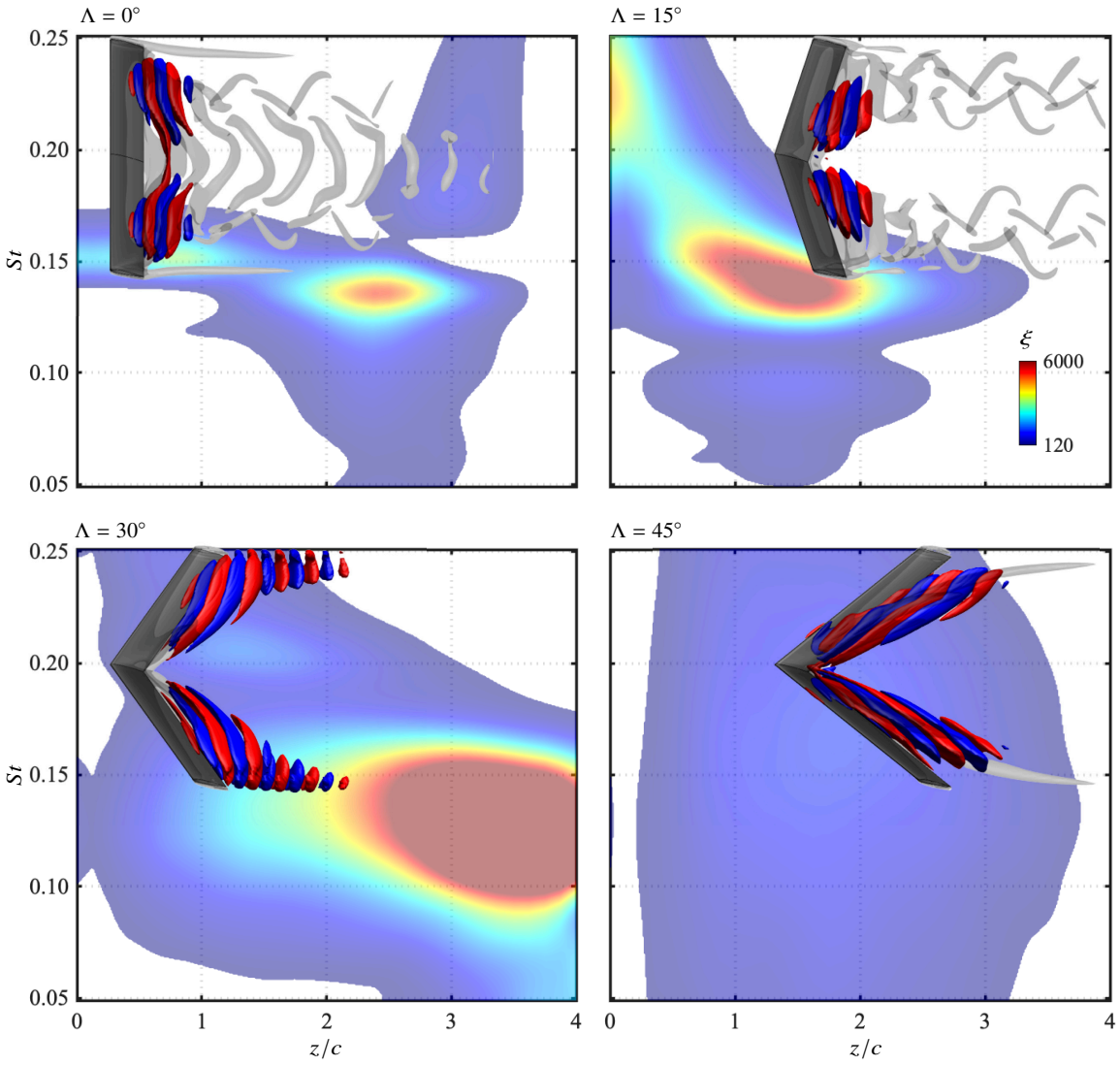

Figure 5.12: Wingspan location of primary resolvent wavemakers with isocontours of ξ for $0.05 \leq St \leq 0.25$ for the $Re_c = 400$ flow over $(sAR, \alpha) = (4, 20°)$ wings with $0° \leq \Lambda \leq 45°$. Resolvent wavemaker modes are shown with isosurfaces of $\hat{u}_y/\|\hat{u}_y\|_\infty = \pm 0.1$ and instantaneous $Q = 1$ are gray-colored isosurfaces.

emerge from the leading edge near the root plane toward the wing tip and downstream at the wake, overlapping the region where steady ram-horn-shaped vortices appear in the DNS. These resolvent wavemakers exhibit a region of the flow field with high receptiveness to amplify forcing structures and disturb the steady ram-horn vortex. Because the dominant resolvent wavemaker around the $\Lambda = 45°$ wing have a low ξ, in spite of occupying a large region of the wake, the energy they introduce to the flow field is insufficient to disturb the wake.

The resolvent wavemakers further exhibit the root- and tip-dominated modal characteristics and the mode switching phenomenon in figure 5.12, in agreement with the forcing-response modal behavior shown in figures 5.4 and 5.5. For instance, the resolvent wavemaker modes at the peak ξ values for the unswept wing appear near $z/c \approx 2$, with a gradual transition from root-supported to tip-dominated modes as St increases. Moreover, for the $\Lambda = 15°$ wing, there is a transition in the dominant region of resolvent wavemaker support from $z/c \approx 1.5$ at lower frequencies to $z/c \approx 0$ at higher frequencies, as shown in figure 5.12 (top, right). Lastly, for the $\Lambda = 30°$ wing, there is a tip-to-root transition with the increase in St while the peak resolvent wavemakers for $\Lambda = 45°$ are invariant over the frequencies, appearing near $z/c \approx 2$.

For tapered wings, we consider lower aspect ratios of $sAR = 2$ and the mean-chord-based Reynolds number is set to $Re_c = 600$. For these flows, the discussion of the wavemaker characteristics also helps us to interpret the mechanisms that sustain wake unsteadiness in the stalled region, as shown figure 5.13. We observe that for all wings shown, the wavemakers appear over the regions where the shedding is formed within the stalled region. The peak ξ coincides with the shedding frequency of each wing observed in the DNS results. The wavemaker ξ contours show that self-sustained oscillations are shifted from the wing root toward the $z/c = 1$ region for backward-swept LE and unswept TE wings. This result shows that the wavemakers are being shifted toward the tip by the higher LE sweep that further moves the peak of unsteadiness to the tip region.

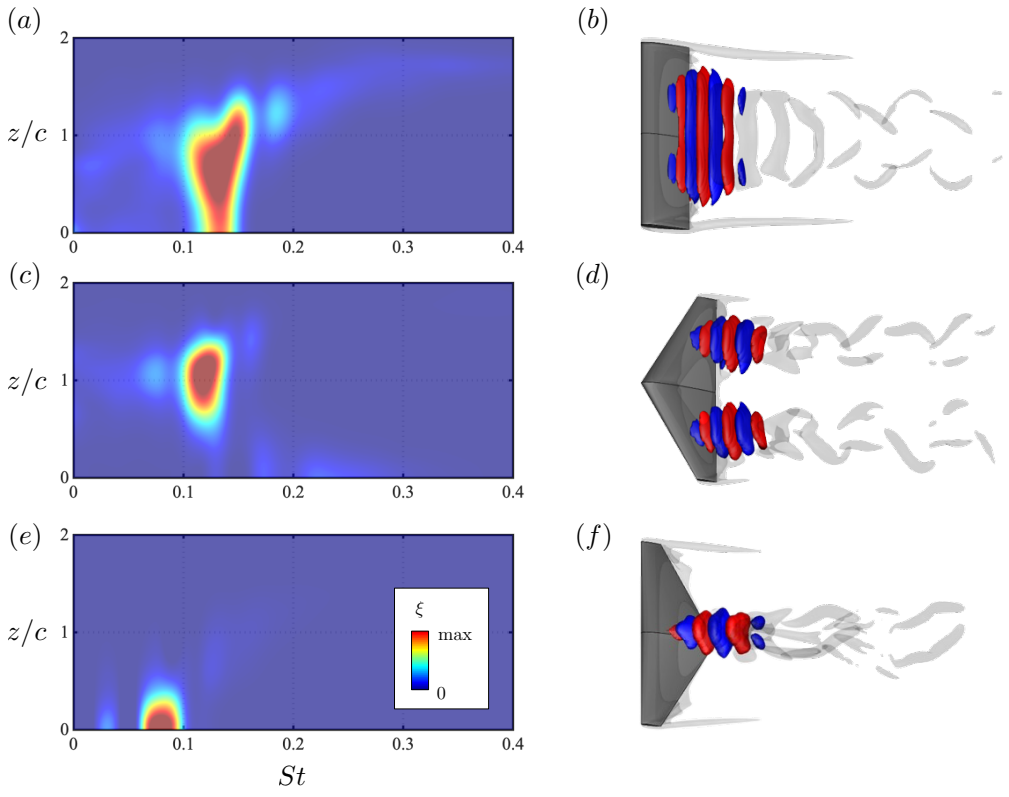

Figure 5.13: Resolvent wavemakers for the $Re_c = 600$ flows around tapered wings. (a, c, e) Contours of ξ to highlight the wingspan (z/c) wavemaker dominance. (b, d, f) Isosurfaces of $\hat{\mathbf{w}}_{u_y} = \pm 0.5$ for dominant wavemaker $(\hat{w})$ modes at $St = 0.14$. Results are shown for (a, b) untapered unswept wing at $\alpha = 14°$, (c, d) tapered swept wing $\Lambda_{\text{LE}} = 18.4°$ and $\lambda = 0.5$, and (e, f) tapered swept wing $\Lambda_{\text{LE}} = 30°$ and $\lambda = 0.27$. Instantaneous $Q = 1$ isosurface is also shown in light gray.

For wings with unswept LE and forward-swept TE, the opposite happens. As the shedding structures concentrate near the root region, the wavemakers are also collapsed into a thin region near the root. The wavemakers exhibit a triangular shape pointing to the wing with a slight enlargement in the spanwise direction downstream in the wake. This result suggests that the flow around unswept LE and forward-swept TE wings concentrates self-sustained perturbations to a narrow space, which results in the root-concentrated shedding observed in the DNS, as discussed in section 3.3. The conclusions for this chapter are presented in section 7.1.4.

5.4 A portfolio of resolvent modes around tapered wings

In the next chapter we will present the resolvent-based flow control around tapered wings. For this reason, in the last part of the present section, we provide a portfolio of all the optimal resolvent mode pairs considered in the control analysis from a perspective view. Resolvent modes around wings at $\alpha = 14^\circ$ are shown in figures 5.14, 5.15, and 5.16, respectively. Similarly, resolvent modes around wings at $\alpha = 22^\circ$ are shown in figures 5.17, 5.18, and 5.19, respectively. The mode pairs are visualized using isosurfaces of with isosurfaces of $\hat{\mathbf{f}}_{uy} = \pm 1$ for the forcing modes and $\hat{\mathbf{q}}_{uy} = \pm 0.5$ for the response modes.

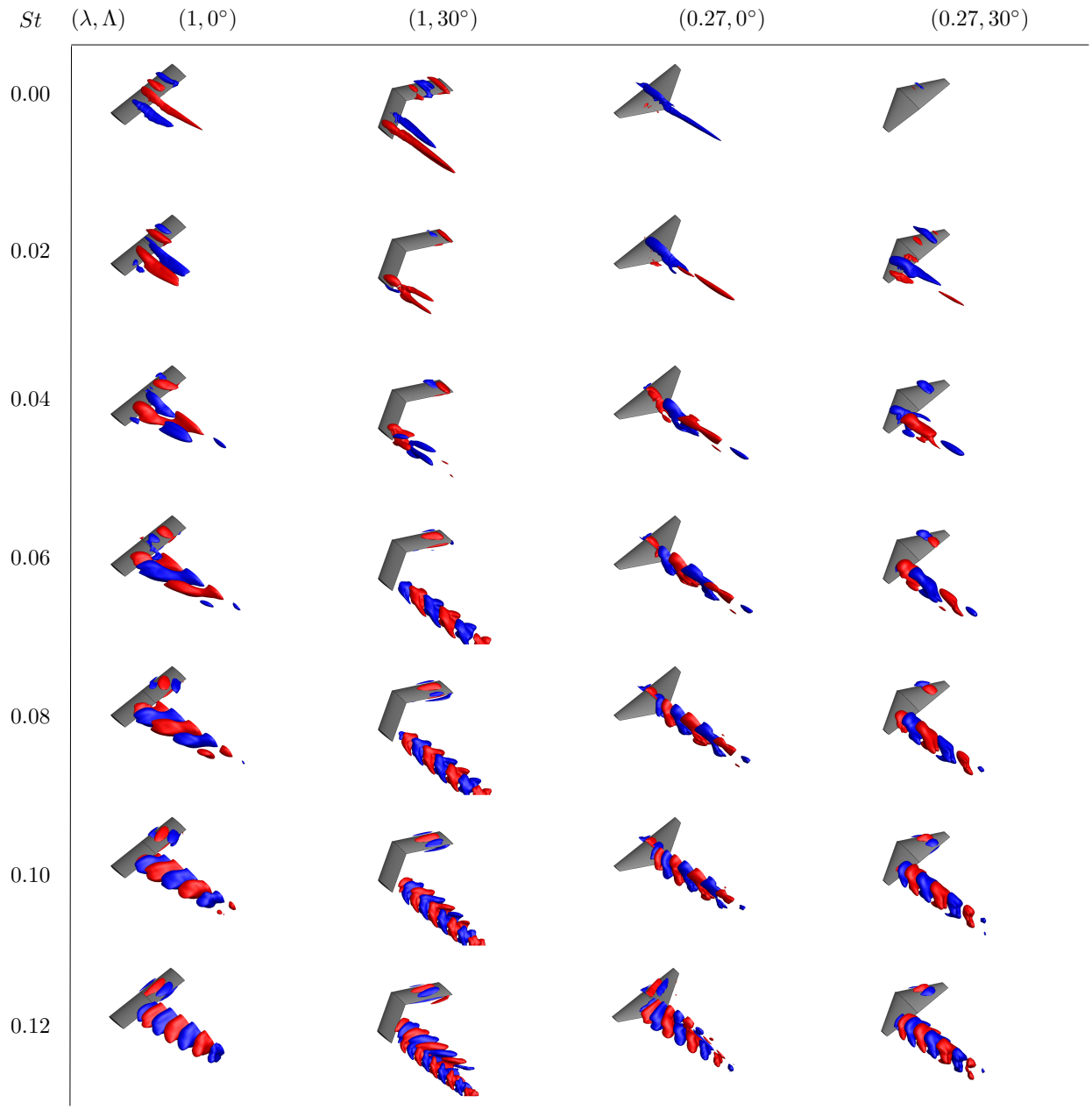

Figure 5.14: Optimal forcing (top, right halfspan) and response (bottom, right halfspan) modes visualized with isosurfaces of $\hat{\mathbf{f}}_{uy} = \pm 1$ and $\hat{\mathbf{q}}_{uy} = \pm 0.5$ for $Re_c = 600$ flows around wings of $sAR = 2$ at $\alpha = 14°$ and frequencies $0 \leq St \leq 0.12$.

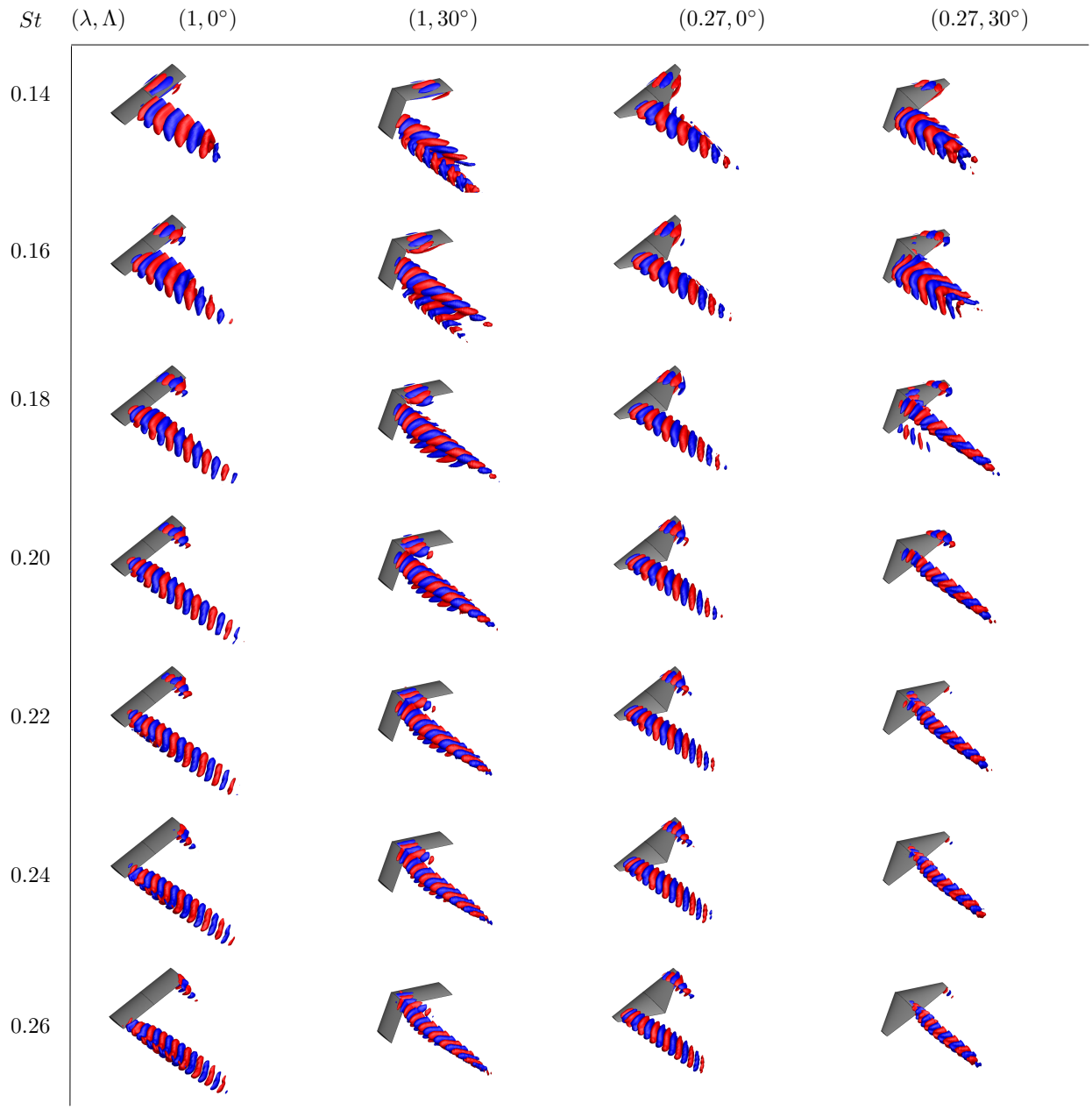

Figure 5.15: Optimal forcing (top, right halfspan) and response (bottom, right halfspan) modes visualized with isosurfaces of $\hat{\mathbf{f}}_{uy} = \pm 1$ and $\hat{\mathbf{q}}_{uy} = \pm 0.5$ for $Re_c = 600$ flows around wings of $sAR = 2$ at $\alpha = 14°$ and frequencies $0.14 \leq St \leq 0.26$.

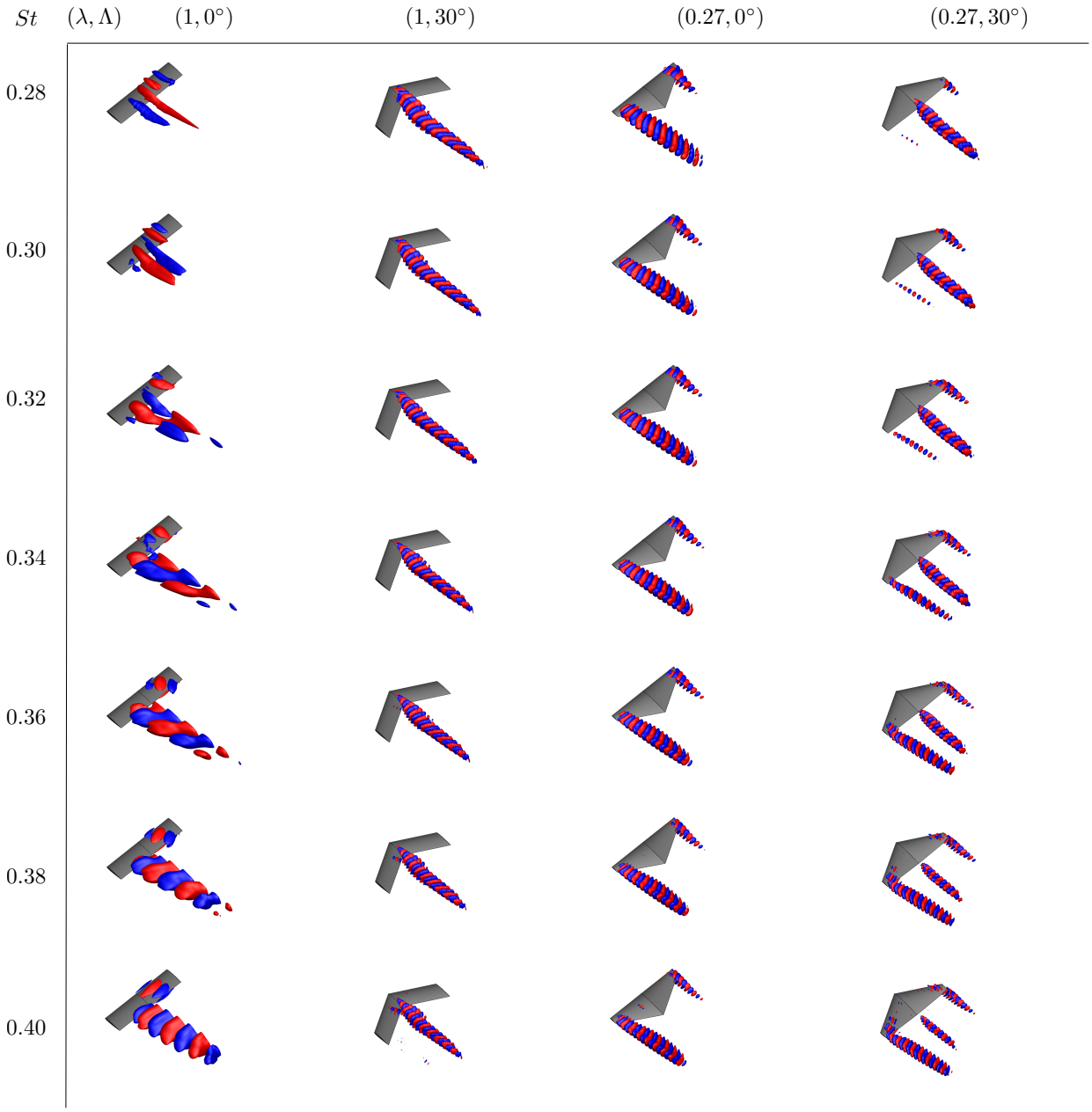

Figure 5.16: Optimal forcing (top, right halfspan) and response (bottom, right halfspan) modes visualized with isosurfaces of $\hat{\mathbf{f}}_{uy} = \pm 1$ and $\hat{\mathbf{q}}_{uy} = \pm 0.5$ for $Re_c = 600$ flows around wings of $sAR = 2$ at $\alpha = 14°$ and frequencies $0.26 \leq St \leq 0.40$.

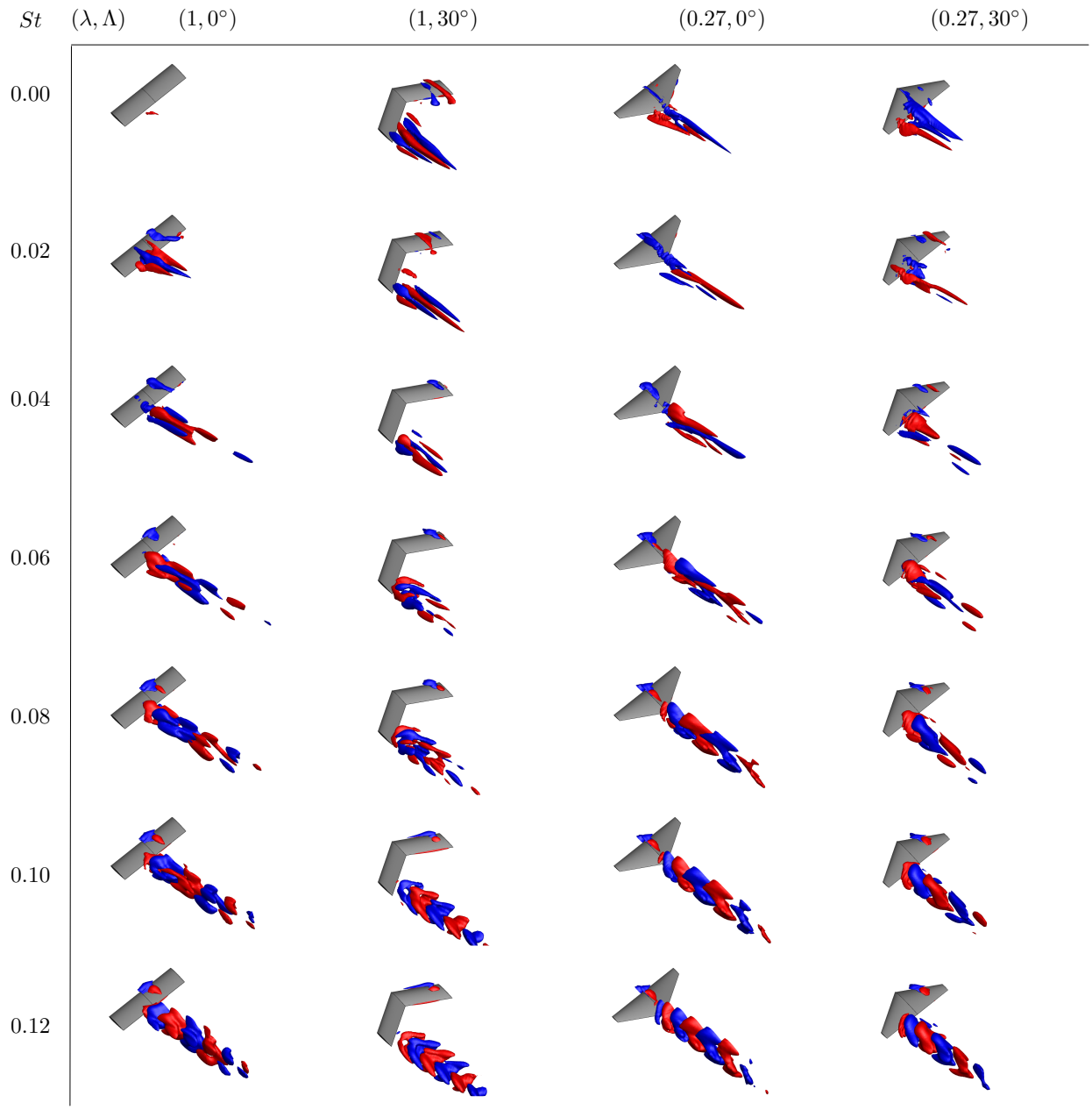

Figure 5.17: Optimal forcing (top, right halfspan) and response (bottom, right halfspan) modes visualized with isosurfaces of $\hat{\mathbf{f}}_{uy} = \pm 1$ and $\hat{\mathbf{q}}_{uy} = \pm 0.5$ for $Re_c = 600$ flows around wings of $sAR = 2$ at $\alpha = 22°$ and frequencies $0 \leq St \leq 0.12$.

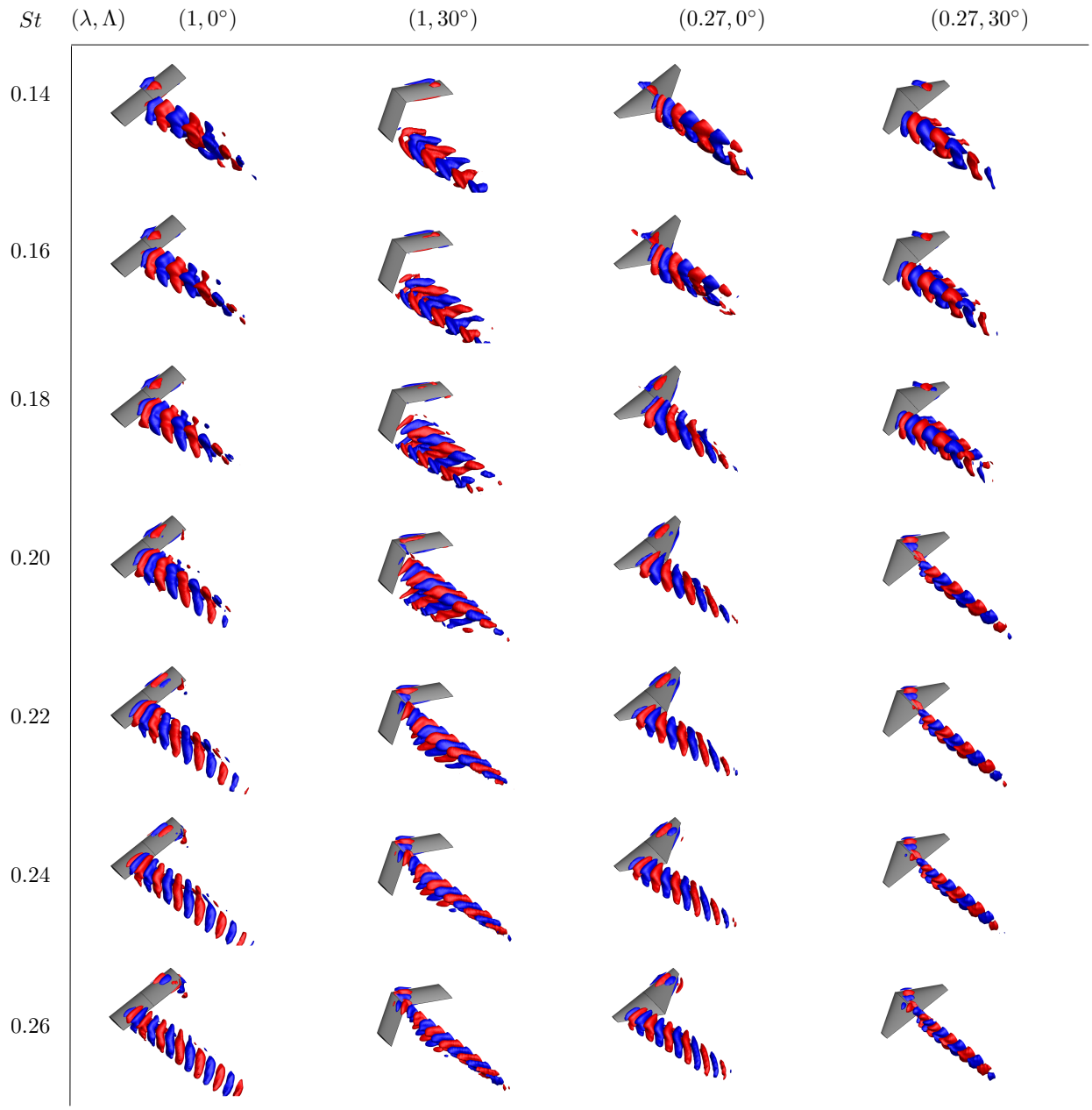

Figure 5.18: Optimal forcing (top, right halfspan) and response (bottom, right halfspan) modes visualized with isosurfaces of $\hat{\mathbf{f}}_{uy} = \pm 1$ and $\hat{\mathbf{q}}_{uy} = \pm 0.5$ for $Re_c = 600$ flows around wings of $sAR = 2$ at $\alpha = 22°$ and frequencies $0.14 \leq St \leq 0.26$.

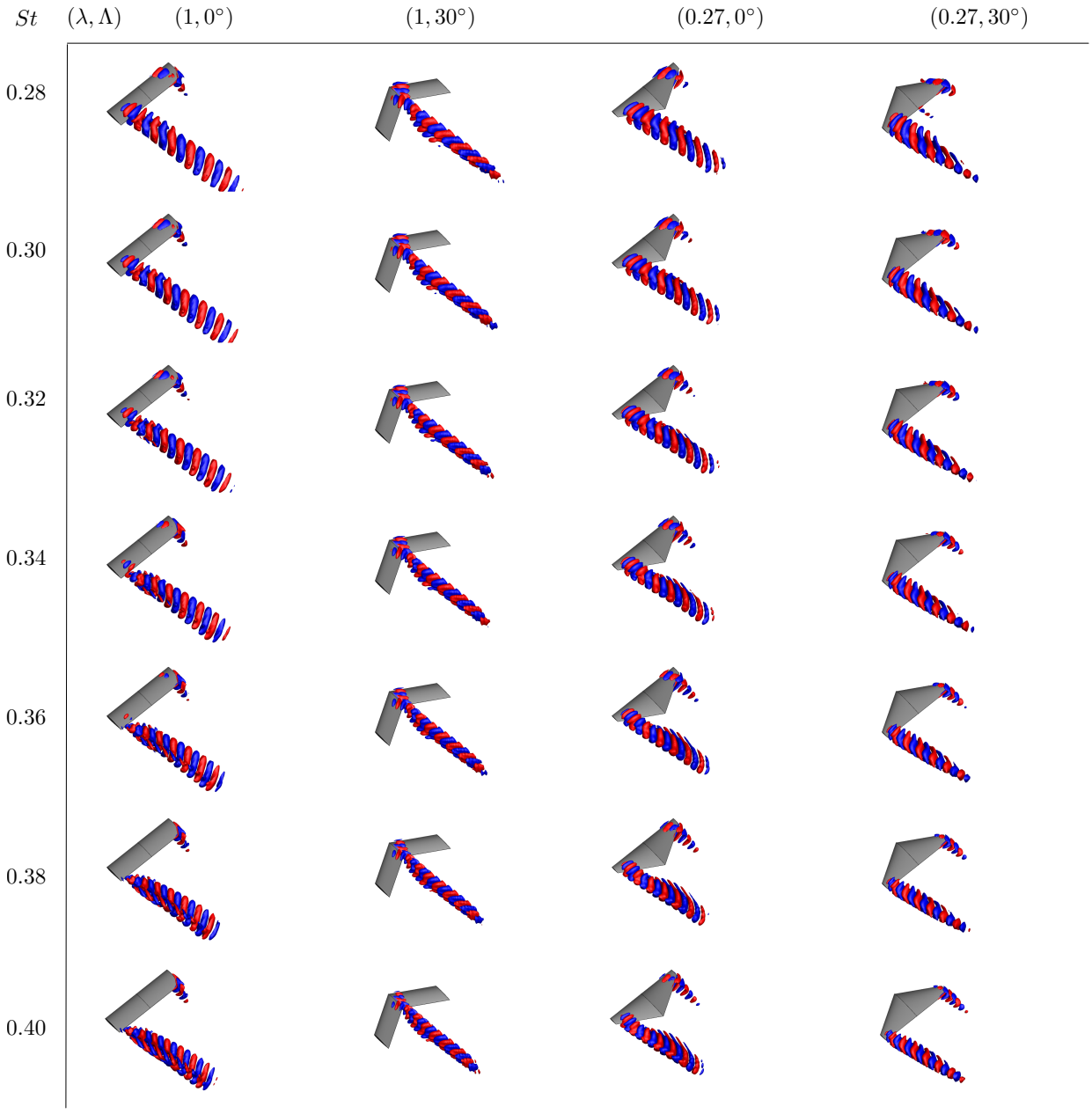

Figure 5.19: Optimal forcing (top, right halfspan) and response (bottom, right halfspan) modes visualized with isosurfaces of $\hat{\mathbf{f}}_{uy} = \pm 1$ and $\hat{\mathbf{q}}_{uy} = \pm 0.5$ for $Re_c = 600$ flows around wings of $sAR = 2$ at $\alpha = 22°$ and frequencies $0.26 \leq St \leq 0.40$.

CHAPTER 6

Resolvent-based active flow control over finite wings

We use triglobal resolvent analysis to develop three-dimensional active flow control over finite wings in post-stall laminar flow conditions. For the present study, we consider wings with semi-aspect ratios from 2 at angles of attack of 14° and 22°, taper ratios 0.27 and 1, and leading-edge sweep angles of 0° and 30°, at a mean-chord-based Reynolds number of 600. The triglobal resolvent analysis provides a pair of forcing and response spatial modes with their amplification gain at each frequency. The forcing modes show the regions with high sensitivity where perturbations can potentially be amplified in the flow field with spatio-temporal behavior related to the response modes. Here, the response modes provide insights on the spatial regions that can be modified by the optimal forcing modes, which are used as body forces within the direct numerical simulations. As the spatial location of forcing modes is frequency-dependent, the actuation frequency is used as a selection parameter for the control objective. For instance, we note that for untapered and unswept wings, suboptimal modes at high frequencies perturb and attenuate the wing tip vortex, while the optimal frequency is used to increase flow oscillations within the separation bubble, which significantly improves the overall aerodynamic performance of the wing. For tapered swept wings, it is shown that a local actuation near the root perturbs the upstream formation of the stall region, increasing both lift and lift-to-drag ratio. This study reveals the sensitivity of the flow field to coherent structures that have the potential to modify massively separated wakes and improve their aerodynamic performance.

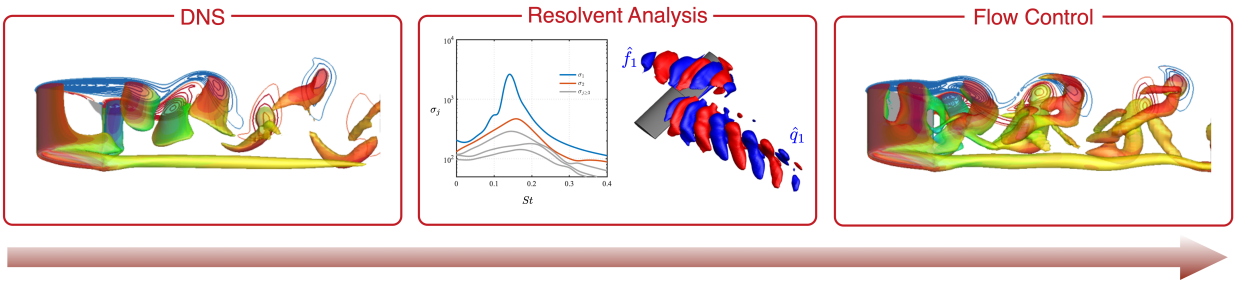

Figure 6.1: Schematics of the present work. Through a combination of DNS and resolvent analysis, we develop and evaluate the effect of resolvent-based actuation to the development of flow control strategies that improve the aerodynamic performance of the wing.

6.1 Motivation

Altering the dynamics of flows has tremendous importance in aerospace engineering and can significantly impact the economy and safety of future aircraft [Gad00]. Control design, however, may prove to be an outstanding challenge due to the nonlinear, high-dimensional, and complex nature of the flow fields behind finite wings in post-stall angles of attack [And10, TC09, ZHA20b]. In such flow conditions, control inspired by the intuition and experience of control engineers may often lead to an ineffective flow modification and undesirable outcomes, as the evolution of flow perturbations is not trivial. To properly study the perturbation dynamics, we use triglobal resolvent analysis, which provides insights that support the design flow control strategies that modify the wake characteristics according to a predefined goal. The present work reveals the sensitivity of massively separated flows over wings to resolvent-based external forcing structures.

In this chapter, we develop a flow control strategy to modify the wake using body force actuation, as shown in figure 6.1. The body force is harmonic and modeled using the optimal forcing modes at each frequency, obtained by triglobal resolvent analysis. The main control objective is to increase lift and improve the aerodynamic performance of the wing. Furthermore, we explain how to use the actuation frequency as a selection parameter to perturb

different areas of the wake and distinct wingspan locations. For instance, to attenuate the tip vortex, it is shown that a high-frequency actuation is more effective. The setup used in the present chapter is the same one used to study tapered wings in section 3.2. The present chapter is organized as follows. In section 6.2, we present the numerical approach used for the present work, the direct numerical simulations and triglobal resolvent analysis. In section 6.3, we describe our active flow control approach, inspired by resolvent modes, and show its application to tapered swept wings and the difference of the control actuation at two different angles of attack.

6.2 Methodology

6.2.1 Direct numerical simulations

6.2.1.1 Formulation

We study the three-dimensional flow over finite wings by numerically solving the incompressible Navier–Stokes equations

$$\frac{\partial \boldsymbol{u}}{\partial t} + \boldsymbol{u} \cdot \boldsymbol{\nabla} \boldsymbol{u} = -\boldsymbol{\nabla} p + \frac{1}{Re_c} \boldsymbol{\nabla}^2 \boldsymbol{u} + \boldsymbol{e} \ , \tag{6.1}$$

$$\boldsymbol{\nabla} \cdot \boldsymbol{u} = 0 \ , \tag{6.2}$$

where $\boldsymbol{u} = (u_x, u_y, u_z)$ is the velocity vector in Cartesian coordinates, p is the pressure, $\boldsymbol{e}$ is external forcing. The external forcing is modeled as a body-force harmonic actuation using the spatiotemporal characteristics of the triglobal forcing modes obtained from resolvent analysis (described in detail in section 6.2.2). The set of equations 6.2 is solved using *Cliff*, the incompressible flow solver from the *CharLES* package, developed by Cascade Technologies, Inc. This solver uses collocated node-based second-order finite volume to compute mass and momentum equations and a fractional step scheme for time integration [HI04, HMI06].

With the origin of the Cartesian system placed at the leading edge of the wing root $(x, y, z)/c = (0, 0, 0)$, the computational domain extends over $(x, y, z)/c \in [-20, 25] \times$

$[-20, 20] \times [0, 20]$. The meshes used in the present work are the same used in chapter 3. A symmetry boundary condition is imposed at the root. At the inlet, we prescribe a freestream velocity vector $\boldsymbol{u} = (U_\infty, 0, 0)$. At the outlet, we specify convective boundary conditions. A slip boundary condition is applied on all other farfield boundaries. Moreover, we enforce a no-slip wall boundary condition at the wing surface.

We perform DNS for baseline ($\boldsymbol{e} = 0$ in equation 6.2) and controlled flows ($\boldsymbol{e}$ modeled with harmonic forcing modes). For both cases, simulations are initiated from uniform flow with no external forcing, being performed with a constant acoustic Courant-Friedrichs-Lewy (CFL) number of 1 until transients are washed out of the computational domain, which takes approximately 90 convective time units. After the transients are washed out the domain, flows are simulated, with and without external forcing, with a constant time step defined such that CFL is smaller than one. Statistics are collected for approximately 100 convective time units to ensure convergence. We recall that for the numerical results presented in chapter 3, we have used the compressible solver with a freestream Mach number set to $M_\infty \equiv U_\infty / a_\infty = 0.1$, where a_∞ is the freestream speed of sound. The differences between incompressible and weakly compressible flow fields are negligible, one may refer to chapter 3 for insights into the baseline flows.

6.2.2 Triglobal resolvent analysis for flow control

For this chapter we use the resolvent modes shown in section 5.4. These modes were obtained from a weakly compressible base flow. For this reason, the modes are defined with the five state variables, $\hat{\mathbf{f}} = (\hat{\mathbf{f}}_\rho, \hat{\mathbf{f}}_{u_x}, \hat{\mathbf{f}}_{u_y}, \hat{\mathbf{f}}_{u_z}, \hat{\mathbf{f}}_T)$ and $\hat{\mathbf{q}} = (\hat{\mathbf{q}}_\rho, \hat{\mathbf{q}}_{u_x}, \hat{\mathbf{q}}_{u_y}, \hat{\mathbf{q}}_{u_z}, \hat{\mathbf{q}}_T)$, under the Chu norm [Chu65]. The compressibility effects are negligible at the present low-Mach number flow, allowing for the velocity components of the forcing modes, namely $(\hat{\mathbf{f}}_{u_x}, \hat{\mathbf{f}}_{u_y}, \hat{\mathbf{f}}_{u_z})$, to be used as body forces within the incompressible DNS.

For the present resolvent analysis formulation (see section 2.1), forcing modes represent the optimal structures that can modify the flow field, while the response modes describe the

evolution of the flow perturbations in the flow field. In a linear analysis perspective, such evolution is the result of the input actuation given by the forcing modes at each frequency. This idea leads naturally to flow control, as we have insights on the perturbations that can be amplified by the flow field as the forcing modes and how they behave in the wake as the response modes. Nonetheless, to understand whether these modes can significantly change the wake structures in practice we introduce the forcing modes within the flow field as a harmonic external actuation mechanism.

For the controlled flows, forcing modes obtained from resolvent analysis are modeled as the external forcing $\boldsymbol{f}$ in equation 6.2. The spatial distribution of the forcing modes and their frequency ω is used within the definition of the body-force $\boldsymbol{e}$ expressed as

$$\boldsymbol{f}(\boldsymbol{x},t) = A(\mathrm{Re}(\hat{\boldsymbol{f}}(\boldsymbol{x}))\sin(\omega t+\phi) + \mathrm{Im}(\hat{\boldsymbol{f}}(\boldsymbol{x}))\cos(\omega t+\phi)) \ , \tag{6.3}$$

where $\hat{\boldsymbol{f}}(\boldsymbol{x})$ is the spatial forcing mode, with real $\mathrm{Re}(\cdot)$ and imaginary $\mathrm{Im}(\cdot)$ parts, A is the amplitude, and ϕ is the phase. The velocity components of the forcing mode $\hat{\boldsymbol{f}} = (\hat{\boldsymbol{f}}_{ux}, \hat{\boldsymbol{f}}_{uy}, \hat{\boldsymbol{f}}_{uz})$, with unit magnitude, that is $\|\hat{\boldsymbol{f}}\|_2 = 1$, are added to the momentum equations 6.2 as body force.

The objective of control is to achieve notable flow modifications to improve the overall aerodynamic performance of the wing using a small forcing input. The amplitude A is $\mathcal{O}(1)$, similar to previous modal-based body-force actuation works [ESS18]. To quantify the control input, we perform simulations with active control in a quiescent flow field and estimate the momentum coefficient C_μ as

$$C_\mu = \frac{\rho\frac{S_{\mathrm{act}}}{V_{\mathrm{act}}}\int_{V_{\mathrm{act}}}\left({u'_x}^2+{u'_y}^2+{u'_z}^2\right)\mathrm{d}V}{\frac{1}{2}\rho U_\infty^2 bc} \ , \tag{6.4}$$

where u'_x, u'_y, and u'_z are the velocity components, and S_{act} and V_{act} are the surface and volume of the active 3-D forcing. The maximum C_μ used in the present study is 0.05.

One can use the global forcing modes for actuation, as the forcing and response modes are defined over the entire computational domain. In this way, by actuating the flow field with

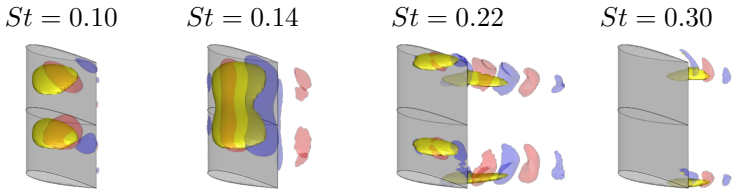

Figure 6.2: Actuation location for representative frequencies and forcing modes shown by the yellow contours, defined using equation 6.5 and the threshold $K_{\hat{\mathbf{f}}}(\mathbf{x},\omega) \geq 0.5\max(K_{\hat{\mathbf{f}}}(\omega))$.

a specific forcing mode, we are introducing an input over the entire flow field. Although this idea seems interesting, it is not practical to be replicated in different experiments. The spatial distribution of the forcing modes, however, is also not even over the computational domain. The subset of the forcing modes with high magnitude is usually located in a small region near the wing. The forcing modes are almost sparse in the 3-D domain. For this reason, the resolvent modes can give insights for a localized actuation in a subset of the spatial domain V_{act}, instead of using the whole global domain forcing. The volume of actuation is defined using an auxiliary spatially defined variable $K_{\hat{\mathbf{f}}}(\mathbf{x})$, which is a velocity-based metric of the forcing modes, defined as

$$K_{\hat{\mathbf{f}}}(\mathbf{x},\omega) = |\hat{\mathbf{f}}^*_{u_x}\hat{\mathbf{f}}_{u_x} + \hat{\mathbf{f}}^*_{u_y}\hat{\mathbf{f}}_{u_y} + \hat{\mathbf{f}}^*_{u_z}\hat{\mathbf{f}}_{u_z}| \ , \tag{6.5}$$

which is the absolute value of the sum of the forcing velocity components inner products at each grid location. Using this variable, the V_{act} is defined for the spatial region that has $K_{\hat{\mathbf{f}}}(\mathbf{x})$ above the 50th percentile, that is, where $K_{\hat{\mathbf{f}}}(\mathbf{x},\omega) \geq 0.5\max(K_{\hat{\mathbf{f}}}(\omega))$. The effect of the control input defined at this subset instead of the entire domain yields minor differences in the modified flow. In figure 6.2 we show a yellow isosurface that marks the region where $K_{\hat{\mathbf{f}}}(\mathbf{x},\omega) \geq 0.5\max(K_{\hat{\mathbf{f}}}(\omega))$ for specific forcing modes. Red and blue isosurfaces show the global modes defined over the flow field with $\hat{\mathbf{f}}_{ux}/\|\hat{\mathbf{f}}_{ux}\|_\infty = \pm 0.1$.

Furthermore, we can also get insights from the response modes to know how the flow field will respond to the forcing input at each given frequency. The spatial characteristics

of the response modes indicate how the active flow control using a specific forcing mode modifies the wake. In this context, the frequency ω of the response modes is a selection parameter of the locations where the active control operates, as the spatial characteristics of the response modes are distinct as a function of their temporal behavior. It is interesting, for the present study, to extract information from the response modes on how much mixing they can generate, for this reason, we use the modal streamwise, transverse, and spanwise Reynolds stresses respectively defined as

$$\hat{R}_x(\mathbf{x},\omega) = \mathrm{Re}(\hat{\mathbf{q}}^*_{u_y}\hat{\mathbf{q}}_{u_z}), \quad \hat{R}_y(\mathbf{x},\omega) = \mathrm{Re}(\hat{\mathbf{q}}^*_{u_z}\hat{\mathbf{q}}_{u_x}), \quad \hat{R}_z(\mathbf{x},\omega) = \mathrm{Re}(\hat{\mathbf{q}}^*_{u_x}\hat{\mathbf{q}}_{u_y}) \ , \tag{6.6}$$

where $\mathrm{Re}(\cdot)$ is the real part of the complex-valued variable. To quantify the momentum mixing and vortex merging that we expect to obtain for a specific control input, we compute a momentum mixing-merging metric using the Reynolds stresses of the response mode as

$$M(\omega) = \int_{V_M} [\sigma_1^2(\hat{R}_x(\mathbf{x},\omega) + \hat{R}_y(\mathbf{x},\omega) + \hat{R}_y(\mathbf{z},\omega)]^{1/2}\mathrm{d}V \ , \tag{6.7}$$

where V_M is a predefined volume, where we intend to analyze the capability of the forcing modes to promote perturbations and modify the flow. The key idea is that the highest the value of M, the stronger the effect of the actuation is within the volume V_M. In the next section, we will study how the metric M can give us insights on the flow field modification for an untapered and unswept wing. We will deeply discuss the evolution of the perturbed flow within the DNS for one case and present control strategies to increase the aerodynamic performance of tapered and swept wings.

6.3 Direct numerical simulations of controlled flows

6.3.1 Flow field response to external actuation

To study how the present flow fields respond to the resolvent-based actuation, we perform DNS with body forces modeled from the localized forcing modes for an untapered and

unswept wing at $\alpha = 14°$. In figure 6.3 we observe the flow field over the half span wing, at the time step of the maximum lift, visualized with isosurfaces of $Q = 1$ colored by the streamwise velocity component u_x and a 2-D slice of spanwise vorticity component ω_z contours at the wing root. In figure 6.3(a) we have the baseline flow, as we have observed in the top left corner of figures 3.8, 3.14, and 3.20, with a long steady streamwise vortex core at the wing tip and shedding developing over the separation bubble near the wing root with spanwise vortex rolls. We note that unsteady vortices only appear in the wake, downstream of the wing, as the separation bubble is large over the suction side.

On the right, it is presented the temporal and spectral characteristics of probed u_y over the wingspan at $(x, y)/c = (3, -0.5)$. The location of the probes is arbitrary and does not affect the discussions in a significant manner. Over a period of $50 \leq t \leq 70$ we observe on the oscillatory behavior of the spanwise rolls near the root with a characteristic frequency captured near the frequency of $St \approx 0.14$. The unsteady vortices are spread over approximately a quarter-span.

For the actuation using the peak gain resolvent modes, at $St = 0.14$, there are considerable modifications in the near wake, as seen in figure 6.3(b). As presented in the 3-D flow field, vortical structures emerge over the suction side of the wing, increasing the unsteadiness levels and promoting a highly 3-D wake ‘downstream. The perturbed flow field alters the steady structure at the free end as a wobble motion is observed on the tip vortex far from the wing. The probed u_y velocity is apparently similar to the baseline case, but a closer inspection on the spectral content reveals that the dominant shedding frequency has shifted to $St = 0.14$, suggesting that the actuation frequency has synchronized to the vortex shedding. By analyzing the spectral signature of u_y, we notice that the unsteady flow region is larger in the spanwise direction with wake oscillations appearing near the tip.

Now let us look at the effect of resolvent-based actuation at a higher frequency of $St = 0.26$, as seen in figure 6.3(c). The optimal response modes at $St = 0.26$ develop aligned at the wing tip, suggesting that their forcing pair can be used to perturb the tip vortex. As the

actuation is localized, this perturbation has a minor influence on the wake structures near the wing root. They are, in fact, similar to the wake structures of the baseline case. The flow field near the wing tip, however, is significantly altered. Instead of the quasi-steady streamwise tip vortex that appears for the baseline, the perturbed flow develops a helical structure near the tip which is visibly shorter than the baseline tip vortex. As the tip vortex is attenuated, the effective angle of attack near the tip also increases, allowing for vortex shedding to occur at this region.

These features are further studied through the probed u_y temporal and spectral content. We observe in the temporal probed data that oscillatory patterns are now present over the entire wingspan. The root shedding oscillations appear near $St \approx 0.14$, similar to the baseline case, while between $1 \leq z/c \leq 2$, there is a lower frequency signature at a subharmonic of the actuation frequency at $St \approx 0.13$. This pattern is associated with the helical motion and resembles the vortex dislocation studied as a natural phenomenon around larger aspect ratio cylinders and wings.

6.3.2 A priori assessment of control effect through response modes

The flow field is sensitive to the actuation through triglobal forcing modes, as seen in the aforementioned results. Using the input-output perspective provided by resolvent analysis, we can use the modal characteristics to achieve a specific goal. In figure 6.4(a) we compute the M metric from equation 6.7 for each response mode in two different spatial regions, shown in 6.4(b). We note that the value of M computed over different volumes may not be compared, as the volumes are different. We evaluate the frequency St where peaks of M appear for each region of the flow field separately.

For the blue curve, M is computed over the separation bubble, defined in the region of $\overline{u_x} \leq 0$. For this region of integration, M exhibits a small peak at $St = 0.06$. The flow field and separation bubble for the actuated flow field at this frequency is shown in figure 6.4(d). This actuation is able to reduce the separation bubble size and perturbs the propagation

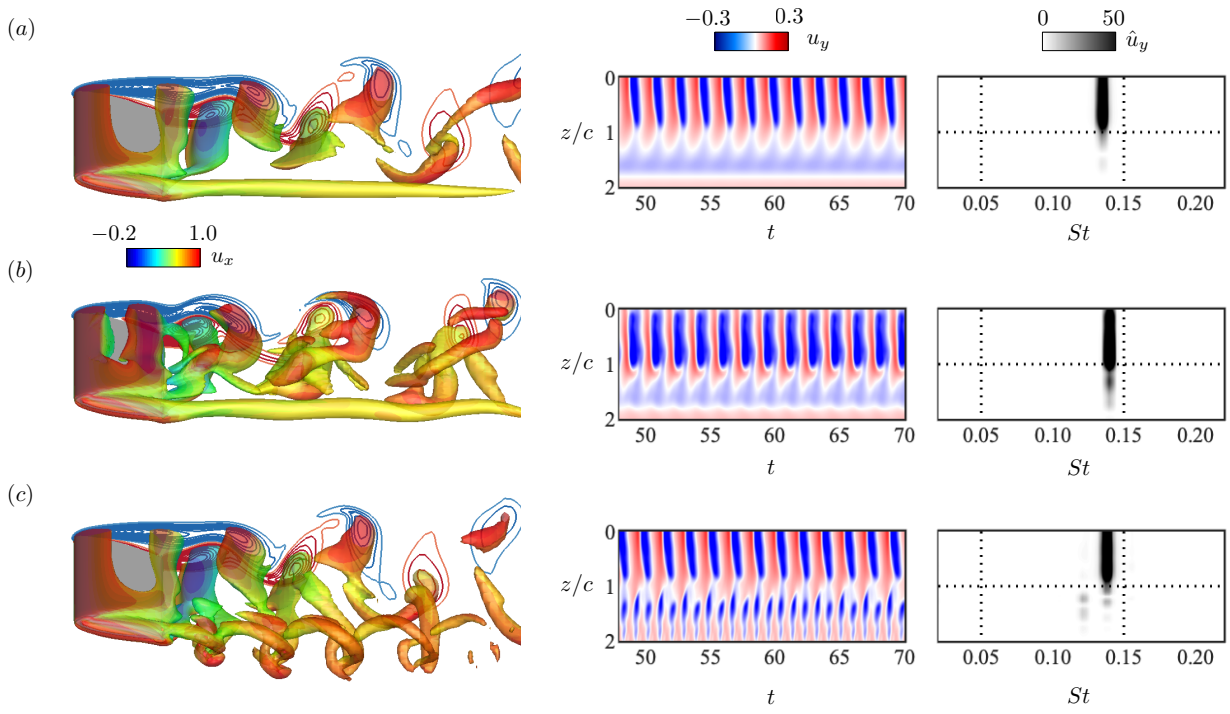

Figure 6.3: Effect of resolvent-based body-force actuation on the flow field for (a) baseline, (b) actuation with $St = 0.14$, and (c) $St = 0.26$, for wing at $\alpha = 14°$. On the left, instantaneous flow fields visualized with isosurfaces of $Q = 1$ colored by streamwise velocity u_x. Middle and right shows temporal and spectral behavior of u_y probed at $x/c = 3$ and $y/c = -0.5$ over the wingspan.

of the spanwise vortex rolls in the wake. The highest M peak occurs near $St \approx 0.14$, which is near the vortex shedding frequency of the baseline case and the frequency of the maximum σ_1. This indicates that to achieve the objective of increasing vortex merging and perturbing the separation bubble, the actuation at $St \approx 0.14$ is the most effective. Indeed, the actuated flow field at this frequency presents an even smaller separation bubble than the lower-frequency actuation. The wake pattern is also distinct, as shown in figure 6.4(e), when compared to the baseline and the actuated flow field at $St = 0.06$. Although the spanwise vortex rolls are formed, there is an increased vortex merging downstream of the wing, which is dominated by a highly 3-D vorticity field.

For the red curve, M is evaluated over the tip vortex, within the $\overline{\omega_x} \leq -0.5$ isosurface for $z/c \geq 1.65$. The red curve in figure 6.4(a) exhibits its higher values between $0.26 \leq St \leq 0.32$. This suggests that the optimal forcing modes at these frequencies is able to promote perturbations near the region highlighted in red in figure 6.4(b). The objective of this actuation is to perturb and attenuate the tip vortex. This goal is achieved, as shown in figure 6.4(f), the flow field near the free end exhibits a helical pattern consistently different to the baseline case. Furthermore, the flow modification near the tip has a minor impact on the inboard wake and separation bubble, which shows that the control effect is local and restricted to the tip region.

Whether the objective is to increase the aerodynamic performance of the wing or to perturb and attenuate the tip vortex, the aforementioned results show that both goals are achievable through resolvent-based control, as shown in figure 6.4(c). More important, by comparing the response modes assessment in figure 6.4(a) and the assessment of the flow modification in figure 6.4(c), we see that the metric M over St provides a good estimate of the effect of the resolvent-based forcing actuation on the flow field modification. From the aforementioned results, we note that the reduction in the separation bubble volume is directly associated with the increase in lift and lift-to-drag ratio. The maximum separation bubble volume reduction and the maximum increase in lift and lift-to-drag ratio are obtained

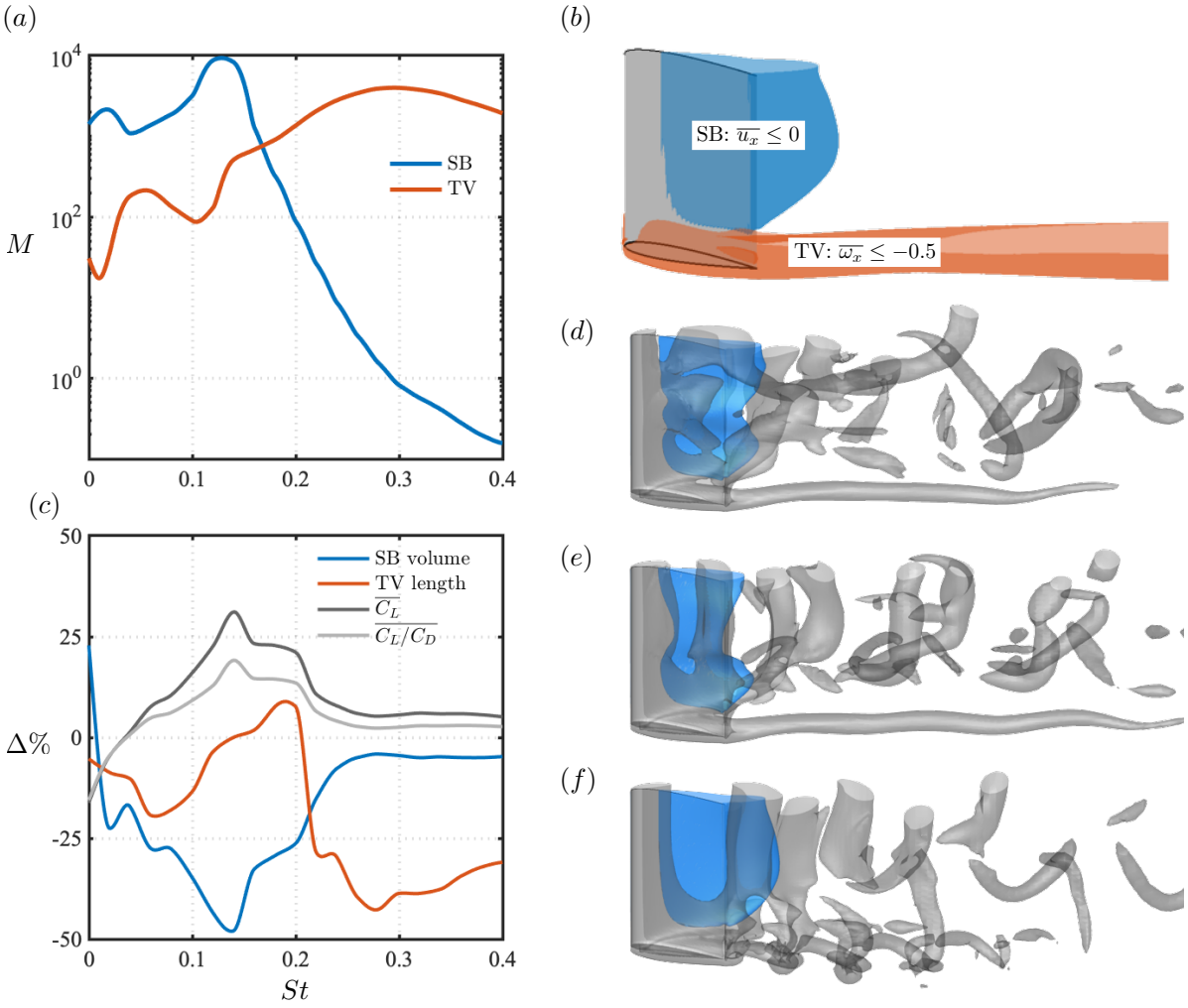

Figure 6.4: Flow modification as a result of body force actuation using forcing modes at each St for wing at $\alpha = 14°$. (a) Momentum mixing M from response modes for each frequency shows a prediction of the flow modification. (b) Separation bubble (SB) and tip vortex (TV) as regions of interest for flow field modification. (c) Percentual change in flow field and aerodynamic characteristics obtained from controlled flow fields. Instantaneous flows fields visualized with gray-colored isosurfaces of $Q = 1$ and time-averaged separation bubble shown with the blue-colored isosurfaces of $\overline{u_x} = 0$ for controlled flows with actuation from (d) $St = 0.06$, (e) $St = 0.14$, and (f) $St = 0.28$ optimal forcing modes.

for the actuation at $St = 0.14$. This might be expected, but it is not trivial for massively separated flows. In another analysis, the maximum reduction in the tip vortex length is obtained at $St = 0.26$, near the region of maximum M computed over the tip region. Due to its distinct importance to the wake dynamics, the effort of tip vortex attenuation will be discussed separately in the following section.

6.3.3 Tip vortex attenuation

The idea of controlling and effectively reducing a tip vortex length has many practical implications to air travel safety and productivity [Spa98] and has attracted the attention of many researchers. In similar flow conditions, using stability analysis modes as body forces, a 21% reduction was achieved in previous works [EST18, ESS18]. For this approach, the tip vortex was perturbed in the wake, which caused it to merge with the inboard vortices. As a result, the decay rate of the streamwise circulation was increased, reducing the tip vortex length.

For the actuated flow fields in the present work, there is a small decrease in the tip vortex length for actuation with the optimal forcing modes at frequencies $St \leq 0.14$. This small reduction coincides with a small peak in M computed at the tip vortex region in figure 6.4(a). From $St = 0.16$ to 0.20, the tip vortex length increases. As we increase the frequency of actuation and the forcing-response mode pairs gradually transition toward the wing tip, the tip vortex is drastically reduced, achieving a maximum attenuation for the optimal forcing mode at $St = 0.26$ of approximately 42% reduction in tip vortex length.

The M peak at the tip vortex region for the frequency $St = 0.06$ coincides with a small 8%reduction in the tip vortex length for the actuated flow. We note in the flow in figure 6.4(d) that the actuation substantially changes the separation bubble and the wake flow patterns, generating energetic streamwise vortices in the wake. To study how this tip vortex reduction occurs, we compute the streamwise circulation $\Gamma = \int_C = \mathbf{u} \cdot \mathrm{d}\mathbf{l}$, where C is the isocontour of $\overline{\omega_x} = -1$, as shown in figure 6.5(a). In this analysis, we see that the difference between the flow actuated at $St = 0.06$ and the baseline flow is mainly associated with a higher

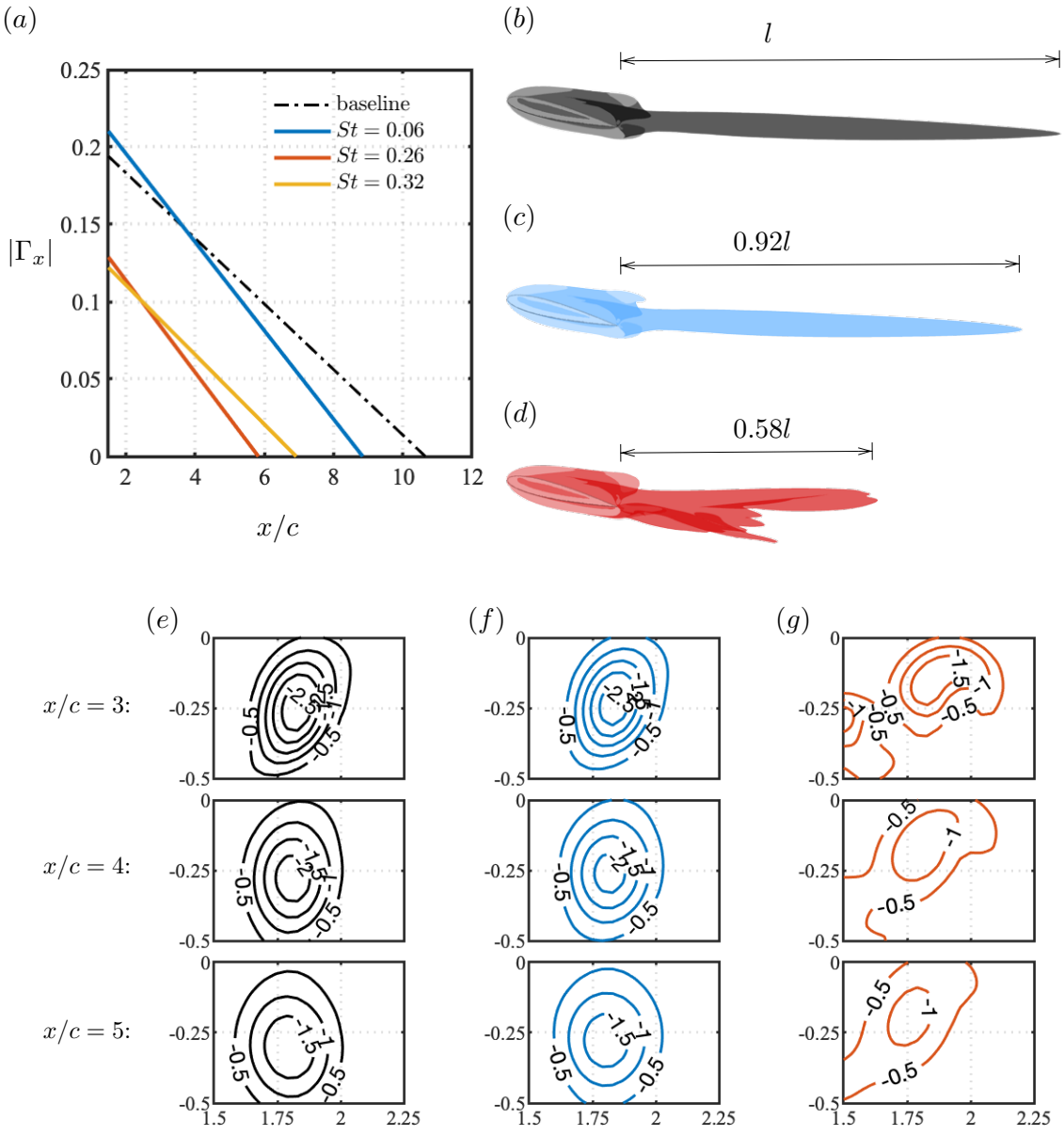

Figure 6.5: Tip vortex attenuation for optimal forcing modes actuation at specific frequencies for wing at $\alpha = 14°$. Throughout the figure, color black is used for baseline case, color blue is used for $St = 0.06$ actuation, color red is used for $St = 0.26$, and color yellow for $St = 0.32$. (a) Tip vortex streamwise circulation $|\Gamma_x|$ over x/c. (b, c, d) Side view of the time-averaged flow structures using isosurfaces of $\overline{Q} = 1$. (e) Streamwise vorticity countours shown in 2-D slices (y-z plane) at $x/c = 3, 4$, and 5.

circulation decay rate $d|\Gamma_x|/dx$. This indicates that the tip vortex attenuation obtained here results from an increased merging of inboard flow structures with the tip vortex downstream of the wing, similar to the mode of tip vortex attenuation obtained by [ESS18].

It is possible, however, to obtain a higher tip vortex attenuation by introducing perturbations near the wing. The higher values of M for tip vortex attenuation are found at $0.26 \leq St \leq 0.32$, as seen in figure 6.4(a). The maximum tip vortex reduction is obtained by the actuated flow at $St = 0.26$. Here we note a difference between the $St = 0.06$ and the $0.26 \leq St \leq 0.32$ actuated flows. At the higher frequencies, there is a strong reduction of $|\Gamma_x|$ near the wing, which indicates that the high-frequency actuation perturbs the tip vortex close to the wing, in the region where the flow structure is formed. By introducing the perturbations at this location we can modify the tip vortex and achieve the higher attenuation than that obtained by actuating at the wake of the wing [ESS18]. By analyzing the vorticity contours in 2-D slices aligned in the streamwise direction, shown in figure 6.5(e, f, g), we note that the high-frequency actuation considerably modifies the vortex core, especially in the lower part of the 2-D planes, between $-0.5 \leq y/c \leq -0.25$, when compared to the baseline and low-frequency actuation cases. This behavior results from the tip vortex actuation being localized in the pressure side of the wing.

Local actuation at the wing tip pressure side near the TE is effective to attenuate the tip vortex at higher angles of attack, as shown in figure 6.6, for a wing at $\alpha = 22°$. At higher incidence, the tip vortex increases in length in the streamwise direction for the baseline flows, as seen in figure 6.8(a, c). The tip vortex circulation decay for this case, due to interactions with the inboard flow field, may not be linear as the one obtained at lower incidence angles. As shown in figure 6.8(b), through the time-averaged vorticity contours at a 2-D slice at $x/c = 3$, the tip vortex is significantly altered by the actuation at high frequencies. An actuation with the optimal forcing modes at $St = 0.14$, where the σ_1 peak is found at the same frequency of the baseline vortex shedding, is able to reduce the size of the separation bubble, as shown in figure 6.8(d). Furthermore, this actuation perturbs the tip vortex region,

yielding a wobbling motion downstream in the wake, but only has a minor effect on its length. By actuating the flow field with the optimal forcing mode from a higher frequency $St = 0.40$, we generate the same helical vortex pattern observed previously at a lower angle of attack and significantly reduce the circulation at any streamwise distance from the wing, as seen in figures 6.8(a, e).

The present results show that it is possible to achieve a large reduction in the tip vortex length with a localized high-frequency actuation near the pressure side of the wing tip. As the flow modification is designed to be local, the inboard global structures are mostly unaffected by the tip vortex reduction. For the objective of changing the inboard wake patterns and obtaining a higher lift and lift-to-drag ratio, we may look at actuation near the natural vortex shedding frequency of the wing, as shown in figure 6.4(a, c). For the following discussions, we will study the controlled flows with this objective and investigate why this flow actuation is able to obtain higher aerodynamic performance.

6.3.4 Active flow control for improved aerodynamic performance

To achieve the objective of increasing the lift and lift-to-drag ratio, we aim to suppress the laminar separation bubble that forms on the suction side of the wing. This region is characterized by a quasi-steady reverse flow bubble where $\overline{u_x} < 0$. The modes that possess the capability of perturbing this region are found at the peaks of the blue curve of M shown in figure 6.4(a). The high-frequency modes are more effective to modify the wake near the tip region, with minor effects over the inboard wake. Even so, for the high-frequency actuated flows, the attenuation of the tip vortex reduces the inboard downwash caused by this structure in the baseline flow field. As a result, these flows exhibit an evenly distributed lift increase over the wingspan, as seen in figures 6.7(a, b), where we present the local change in lift over the wingspan $\Delta C_l(z)$ and the absolute C_l values for baseline and some actuated flows at specific frequencies.

We observe that the higher changes in C_l appear for the actuated flows with actuation

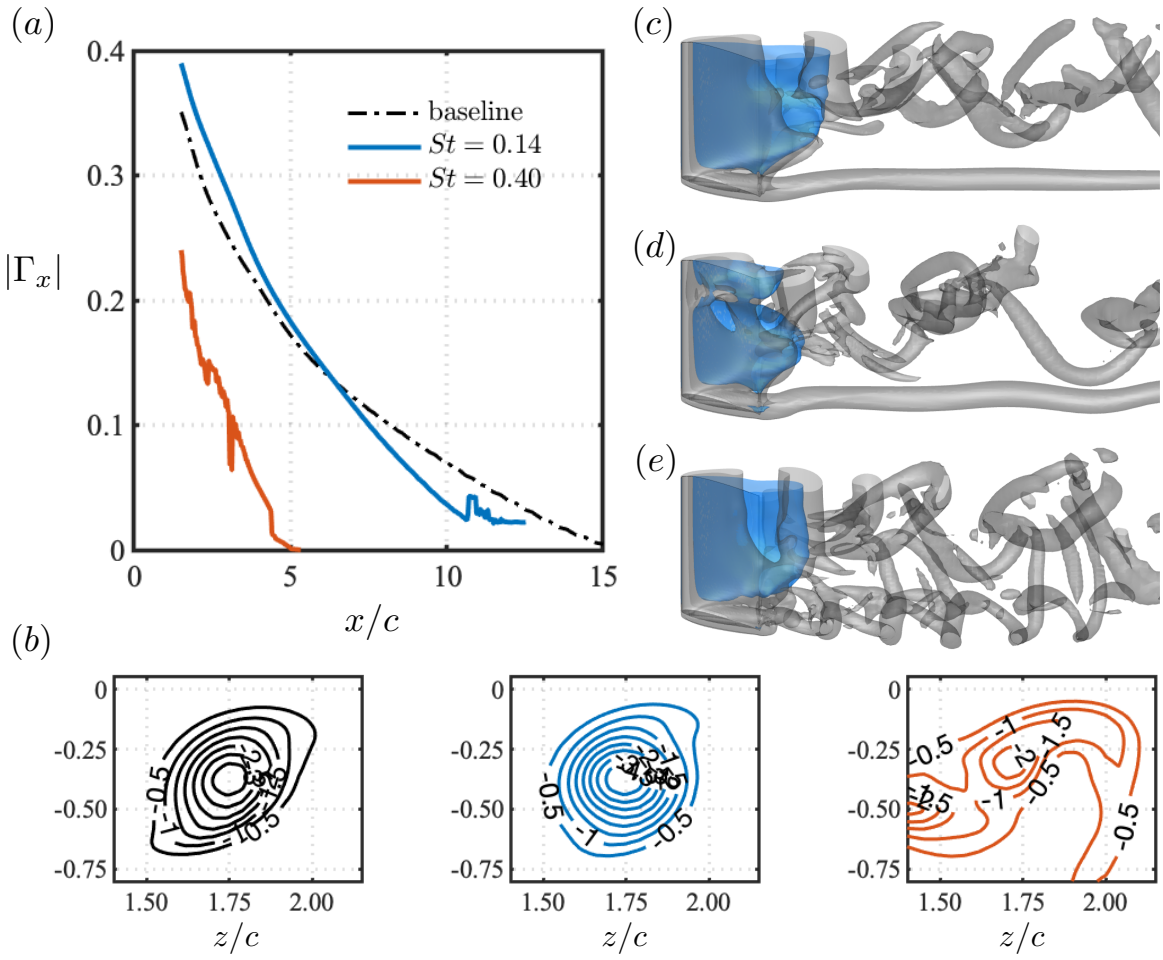

Figure 6.6: Tip vortex attenuation for optimal forcing modes actuation at specific frequencies for wing at $\alpha = 22°$. Throughout the figure, color black is used for baseline case, color blue is used for $St = 0.14$ actuation, color red is used for $St = 0.40$. (a) Tip vortex streamwise circulation $|\Gamma_x|$ over x/c. (b) Streamwise vorticity countours shown in 2-D slices (y-z plane) at $x/c = 3$. Instantaneous flows fields visualized with gray-colored isosurfaces of $Q = 1$ and time-averaged separation bubble shown with the blue-colored isosurfaces of $\overline{u_x} = 0$ for (c) baseline and controlled flows with actuation from (d) $St = 0.14$ and (e) $St = 0.40$ optimal forcing modes.

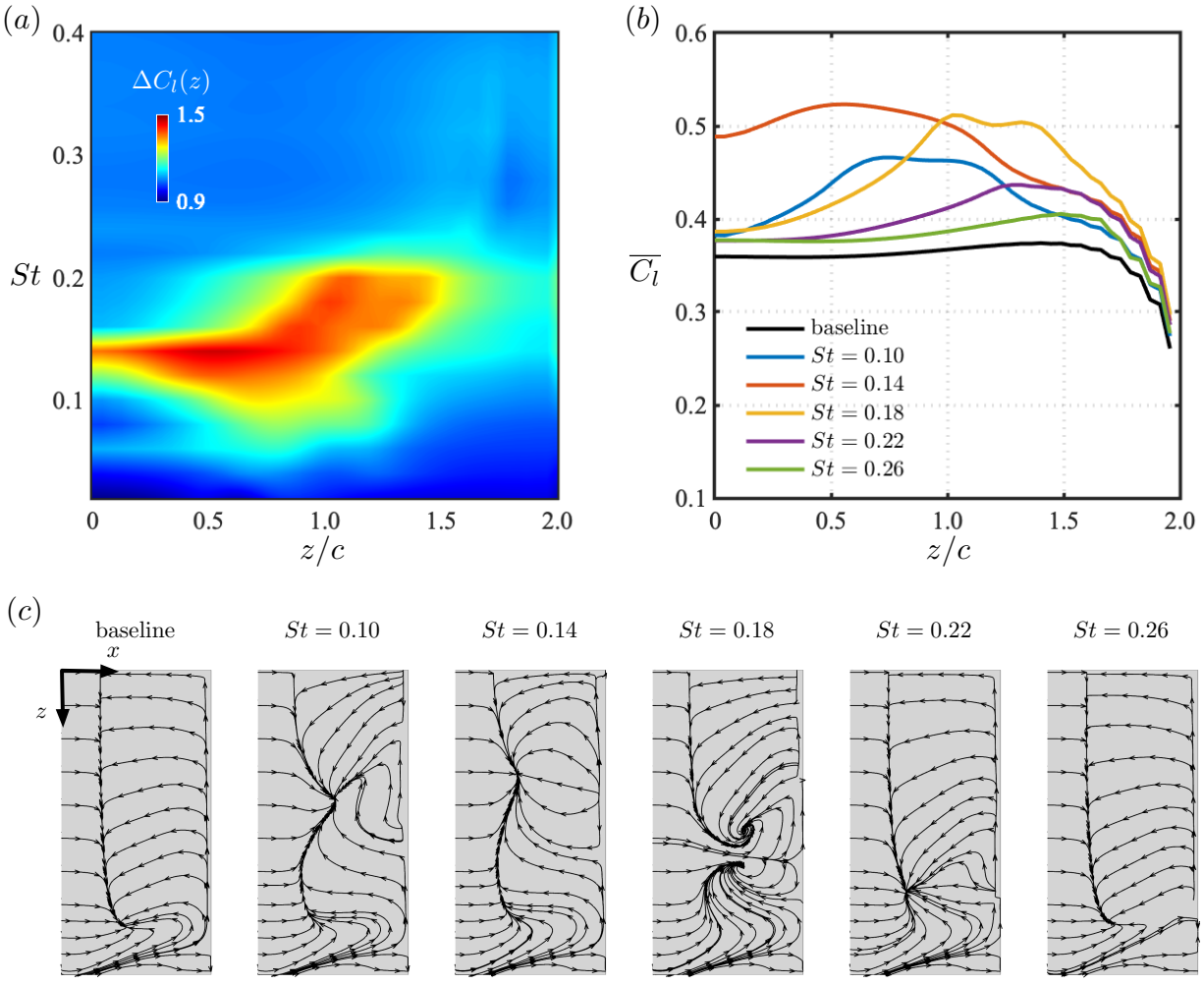

Figure 6.7: Spanwise distribution of lift for optimal forcing modes actuation at specific frequencies. (a) The overall change in local lift $\overline{C_l}$ and (b) the absolute values of $\overline{C_l}$ for specific actuation frequencies. (c) Time-averaged surface flow over the wing shown by skin friction lines revealing how different actuation modifies the surface flow patterns.

frequencies between $0.1 \leq St \leq 0.2$. The harmonic actuation at these frequencies can significantly reduce the separation bubble volume and increase the overall lift and lift-to-drag ratio, as seen in figure $6.4(c, d, e)$. The spanwise region of increased lift contribution gradually transitions from the root toward the tip region, as we increase the frequencies. This is related to the spanwise location of the forcing modes actuation, which also gradually transitions toward the tip region. For instance, while the lift contribution increases over the entire wingspan for the actuated flow with $St = 0.14$, the larger increase appears between $0 \leq z/c \leq 1.5$. For the actuated flow with $St = 0.18$, which is near the root. The largest increase in lift contribution comes from the wingspan region defined between $0.7 \leq z/c \leq 1.7$, which is closer to the tip.

At a higher incidence angle of $\alpha = 22°$, shown in figure 6.8, the findings are similar. By actuating the flow field with the proper optimal forcing mode to perturb the separation bubble, we significantly increase the near-root support for the overall lift, causing it to be higher than the lift support from the tip region. We note that having a higher lift near the wing root is generally known to be beneficial for flight stability. An actuation at higher frequencies, with the optimal forcing mode at $St = 0.40$, attenuates the tip vortex and reduces the inboard downwash, causing an overall increase in the lift over the entire wingspan.

The effect of actuation is further observed in the surface flows through the skin friction lines shown over the wing surface in figures $6.7(c)$ and $6.8(b)$. By focusing on the flows at $\alpha = 14°$, at $St = 0.26$, the optimal one for tip vortex attenuation, the skin friction field over the surface of the wing is similar to the baseline case. This is expected as the inboard flow is only slightly altered for the flow with actuation at $St = 0.26$ near the tip. Also, as the forcing mode is located on the pressure side, the surface flow on the suction side near the tip must also remain similar to the baseline flow.

The main modifications on the surface flow appear near the inboard quarter-span, near the root, at lower frequencies, and near the outboard quarter-span, closer to the tip, at

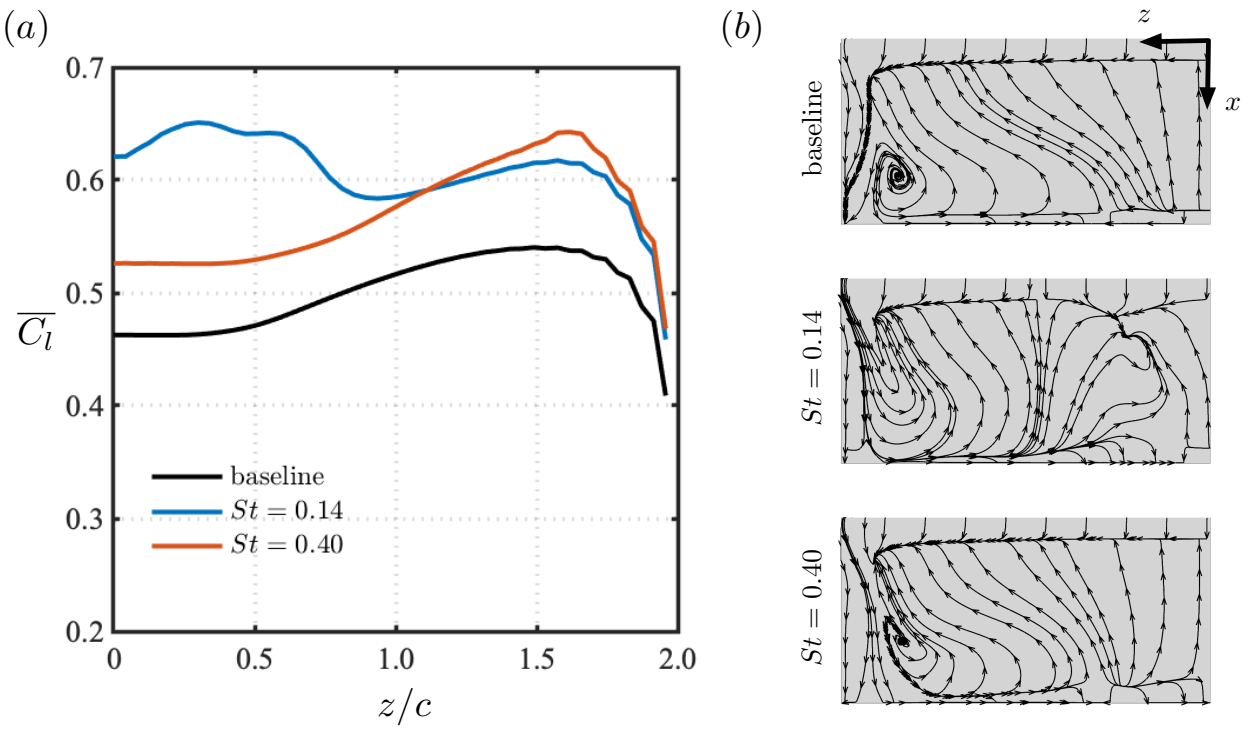

Figure 6.8: Spanwise distribution of lift for optimal forcing modes actuation at specific frequencies for wings at $\alpha = 22°$. (a) Absolute values of $\overline{C_l}$ for specific actuation frequencies. (b) Time-averaged surface flow over the wing shown by skin friction lines revealing how different actuation modifies the surface flow patterns.

higher frequencies. Although these mild changes are exhibited in the actuated surface flows, the length scales and the surface area of the reversed flow exhibits overall similarities with the baseline case. Similar observations can be drawn for the surface flows at $\alpha = 22°$, shown in figure 6.8(b) This suggests that the structures responsible for the lift increase must be spotted in the near wake and not at the wing surface. To study how the actuation modifies the near wake structures directly responsible for the generation of lift, we resort to the force element analysis (see section 3.5.6)). It has been noted that lift elements closer to the surface, exhibit a higher contribution to the total force exerted on the wing [ZT22].

The 3-D distribution of lift elements over the near-wake is shown in figure 6.9 for the (a)

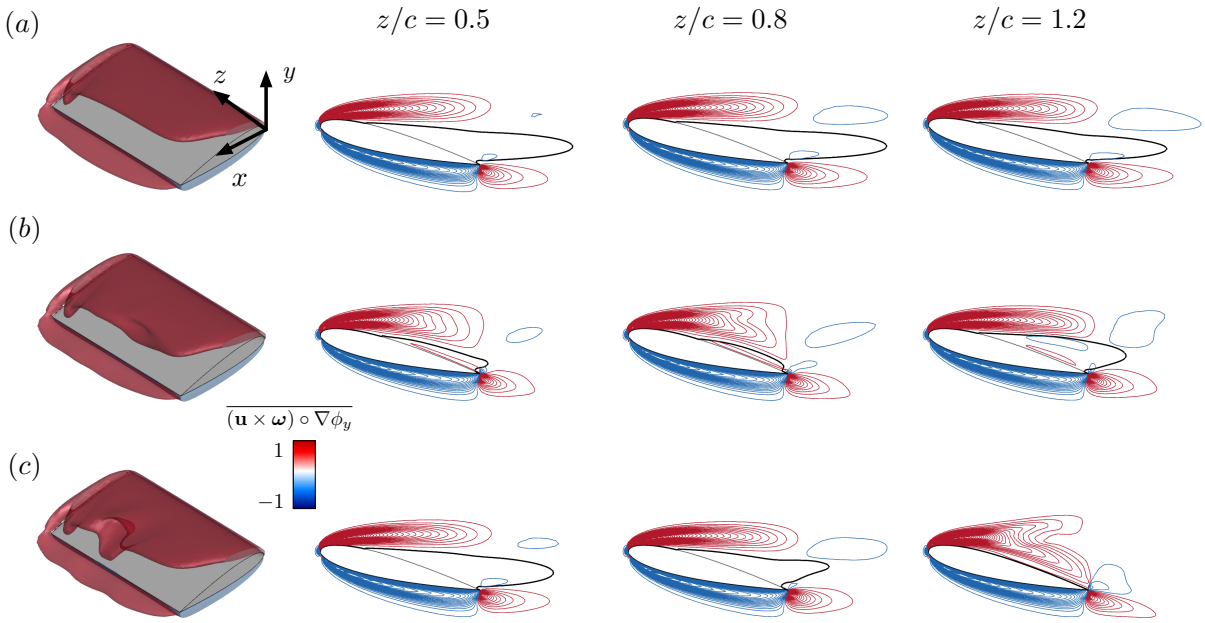

Figure 6.9: Lift elements over the wing at $\alpha = 14°$ for (a) baseline, (b) controlled flow with $St = 0.14$ and (c) 0.18 optimal forcing modes. The leftmost figures show 3-D time-averaged lift elements, 2-D slices at middle and right positions at $z/c = 0.5$, 0.8, and 1.2, respectively.A black solid line marks the contour of $\overline{u_x} = 0$.

baseline case and (b) $St = 0.14$, and (c) $St = 0.18$ actuated flows. A black line is drawn at the isocontour level of $\overline{u_x} = 0$ to represent the separation bubble on the 2-D slices of the (x, y) plane at 3 wingspan locations. Drag elements are similar to lift ones and omitted for brevity. Although the actuation frequency is similar, their effects on the lift distribution are distinct. The lift elements show that the major lift contribution (positive, red) comes from flow structures immediately over the separation bubble. For the baseline flow field, these elements appear far from the wing over a large portion of the wingspan. For the actuated flows, at the frequencies shown of $St = 0.14$ and 0.18, the flow modification reduces the separation bubble volume, which causes lift elements to emerge closer to the wing surface, which subsequently increases the lift.

For the actuated flow at $St = 0.14$, the separation bubble shrinks considerably at $z/c = 0.5$ and 0.8 and the lift elements become larger and closer to the wing when compared to the baseline case. At $z/c = 1.2$, the separation bubble increases slightly, compared to the inboard 2-D planes, shifting the lift elements upwards in the transverse y-direction. For this reason, we observe in figure 6.7(a, b) that the highest lift increase over the wingspan is observed near the inboard quarter-span of the wing. Even so, at $z/c = 1.2$, the lift elements appear closer to the wing than those of the baseline flow, which causes the lift over the outboard quarter-span of the wing, near the tip, to still be larger than the baseline lift at the same spanwise location.

The inboard quarter-span of the wing, for the actuated flow at $St = 0.18$ remains similar to the baseline case with a large separated flow region which maintains the lift elements far from the wing. The stall region is reduced for $z/c = 0.8$ and 1.2, which causes the lift elements to appear closer to the wing, significantly increasing the lift contribution from this region. The present results show that the increase in lift is directly associated with the reduction of the laminar separation bubble because it causes lift elements to emerge closer to the wing surface. For this reason, to increase the contribution to the overall lift for laminar flows with massive separation, one may pursue actuation strategies that reduce or suppress

the separation bubble.

For laminar flows, at high angles of attack, where a massive separation is formed, the idea of suppressing the separation bubble completely over the suction side may be unrealistic for the present resolvent-based flow actuation. The current results, show, however, that even if the stall bubble is not completely suppressed, the sole reduction of its volume is directly associated with an increase in lift and lift-to-drag ratio. These results give us important insights on how to achieve a better aerodynamic performance for the present wings through an active flow control strategy. It further provides the fundamental knowledge and tools to achieve the desirable wake modifications that can efficiently alter the flow field characteristics and improve the aerodynamic performance of laminar separated flows over tapered and swept wings in the following sections.

6.3.5 Active flow control over swept wings

For laminar post-stall flows over untapered swept wings, the separation bubble is shifted toward the wing tip region and a streamwise tip vortex core is absent. For a wing at $\alpha = 14°$, wake unsteadiness is suppressed and the flow becomes steady. At a higher incidence $\alpha = 22°$, flow unsteadiness appears near the wing tip. Our previous results, specifically for the tip vortex actuation, show that perturbing the upstream portion of a flow structure is more efficient to promote oscillation within it. For the flows over swept wings, the upstream portion of the separation bubble appears near the wing root. This yields the hypothesis that perturbing the upstream region of the separation bubble might be a proper choice to improve the aerodynamic performance of the wing. Over this wing, the forcing-response mode pairs gradually transition over the wingspan, as we increase the frequencies, from tip-dominated modes at lower St, to root-dominated modes at high St.

The effect of control at the optimal modes to introduce perturbations at the separation bubble and root region is studied in figure 6.10. Here, we make an a priori assessment of the control effects by evaluating M from equation 6.7 over the separation bubble (blue, peak at

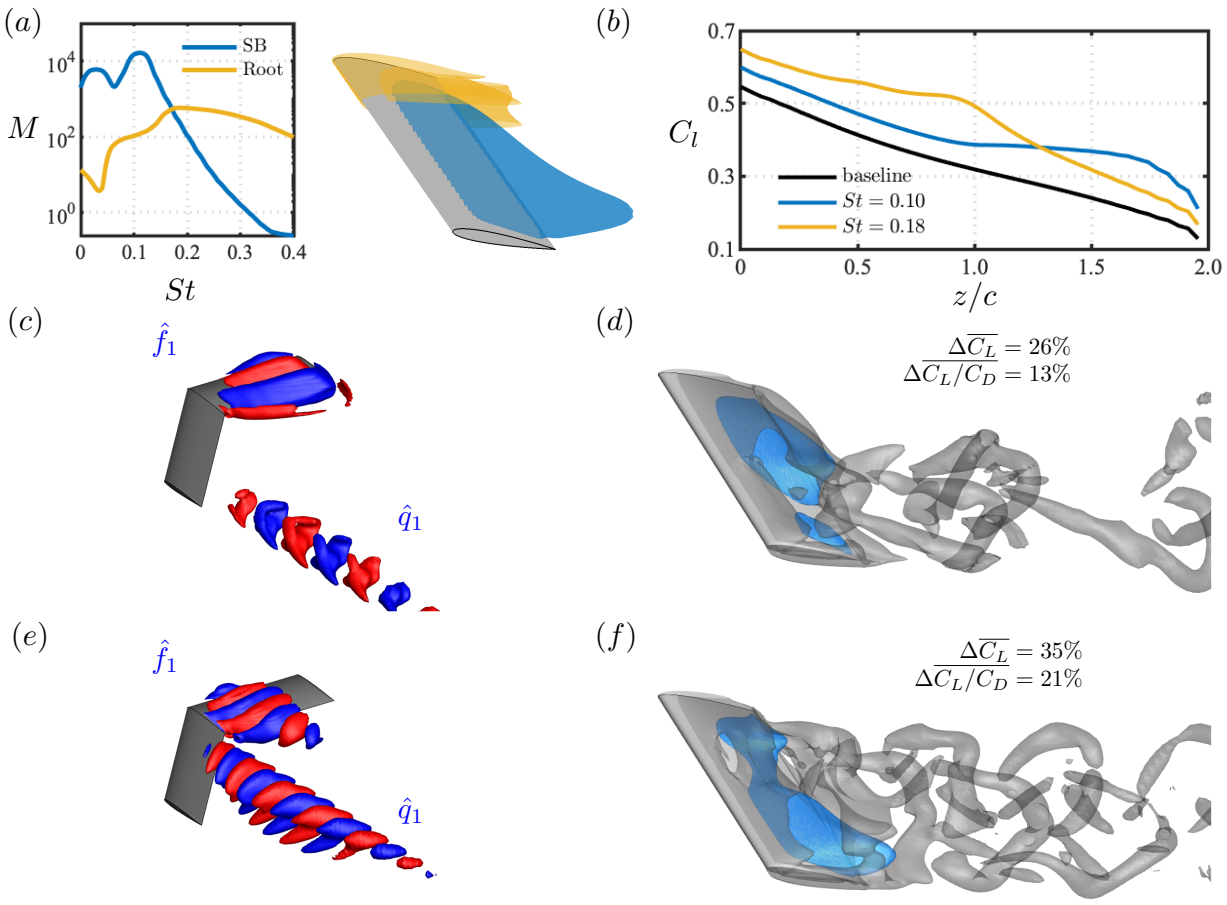

Figure 6.10: Assessment of flow control to improve the aerodynamic performance of swept wings at $\alpha = 14°$. (a) M metric over frequencies computed over the separation bubble (blue, peak at $St = 0.10$) and root region defined for $z/c \leq 0.5$ and $|\omega_z| \geq 0.5$ (yellow, peak at $St = 0.18$). (b) Lift over wingspan for baseline and actuated flows at peak M values. (c, e) Forcing-response mode pairs at $St = 0.10$ and 0.18, respectively. (d, f) Actuated flows visualized with gray isosurfaces of $Q = 1$ and blue isosurfaces of $\overline{u_x} = 0$ for $St = 0.10$ and 0.18 forcing modes actuation, respectively. Improvements in the overall lift, $\Delta\overline{C_L}$, and lift-to-drag ratio, $\Delta\overline{C_L/C_D}$, are shown

$St = 0.10$), and the root region (yellow, peak at $St = 0.18$), as shown in figure 6.10. The respective forcing-response mode pairs are shown in figures 6.10(c) for $St = 0.10$ and (e) for $St = 0.18$. By actuating the flow field with both of these optimal forcing modes, we obtain a time-averaged lift increase over the wingspan, shown in figure 6.10(b) and the flow fields become unsteady, as shown in (d, f), respectively. Both types of actuation increase the overall time-averaged lift and lift-to-drag ratio. Particularly, the actuated flow at $St = 0.10$, which aims to increase vortex merging at the separation bubble region, yields an unsteady flow field near the wing tip, while the actuated flow at $St = 0.18$, which introduces local flow perturbations near the root, yields a global unsteady flow over the entire wingspan. By perturbing the upstream formation of the separation bubble, the root-aimed control at $St = 0.18$ yields a higher reduction of the stalled region and a higher increase in the lift and lift-to-drag ratio, which shows that a local root actuation is efficient to improve the aerodynamic performance of swept wings.

At a higher angle of attack, $\alpha = 22°$, the baseline flow field is unsteady with vortical structures developing near the free end, as shown in the 4th left-to-right figure in the top row of figures 3.10, 3.16, and 3.22. The wake near the root is steady. The laminar separation bubble develops over a large portion of the swept wingspan, but it is mainly concentrated near the tip region, where the unsteady vortices emerge. To suppress the stall region, we look for the optimal resolvent modes that have the capability to promote oscillations over the separation bubble. Those are the forcing-response pair whose metric M computed for the response modes over the separation bubble peaks at $St = 0.14$, shown in figure 6.11(b). By actuating the flow with the optimal forcing modes at $St = 0.14$, we reduce considerably the size of the separation bubble and increase both lift and lift-to-drag ratio. The actuated flow field, shown in figure 6.11(c) exhibits higher levels of unsteadiness near the tip region, while the larger portion of the reminiscent stalled region appears near the wing root.

Although the stalled region in the baseline flow occupies a large portion of the wingspan, the upstream portion of it lies near the wing root. This leads us to study the effects of a

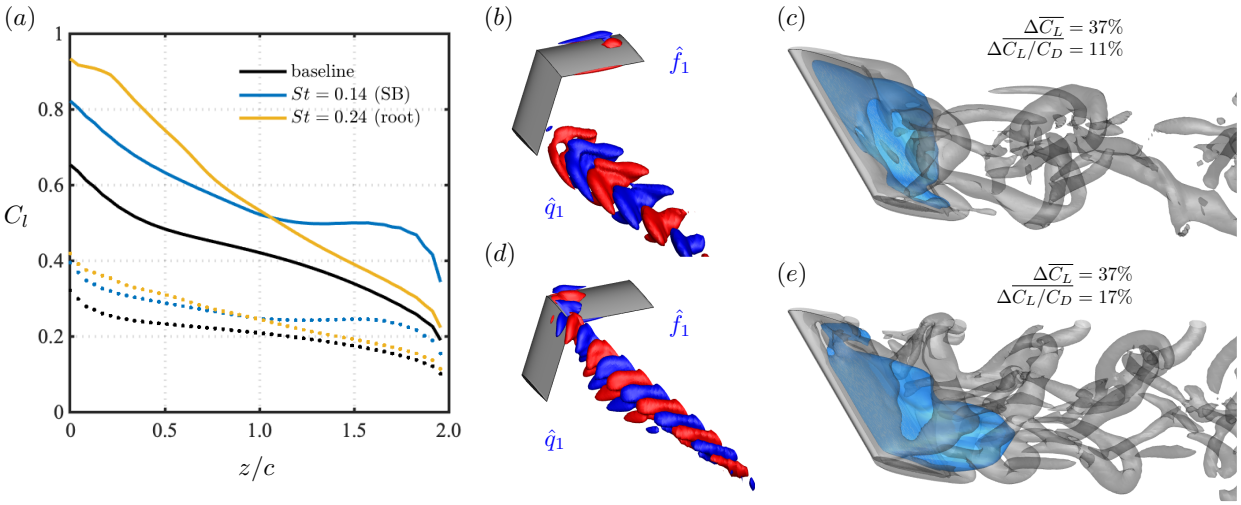

Figure 6.11: Assessment of flow control to improve the aerodynamic performance of swept wings at $\alpha = 22°$. (a) Lift (solid lines) and drag (dotted lines) coefficients over wingspan for baseline and actuated flows at peak M values computed over separation bubble (blue) and wing root (yellow). Forcing-response mode pairs at (b) $St = 0.10$ and (d) $St = 0.18$ and respective actuated flows (c, e) visualized with gray isosurfaces of $Q = 1$ and blue isosurfaces of $\overline{u_x} = 0$. Improvements in the overall lift, $\Delta\overline{C_L}$, and lift-to-drag ratio, $\Delta\overline{C_L/C_D}$, are shown.

localized root perturbation on the wake dynamics. To that end, we must look at modes at higher frequencies than the one used for the actuation at the separation bubble, as the forcing-response mode pairs gradually transition from the tip toward the root region as we increase the frequencies. Similarly to what was observed at $\alpha = 14°$, the actuation using the optimal forcing modes that perturb the root region is also effective. The forcing modes associated with it appear at $St = 0.24$ and are shown in figure 6.11(d). The actuation at the root region introduces unsteadiness over the entire wingspan and significantly reduces the separated flow region near the root, as seen in figure 6.11.

It is noteworthy that the increase in lift is the same as the actuated flow at $St = 0.14$, although the lift-to-drag ratio is higher for the actuated flow at $St = 0.24$. The spanwise lift and drag distribution, shown in figure 6.11(a), shows that lift (solid lines), increases more near root and tip depending on the location of the actuation over the wingspan, being always higher than the baseline lift. The spanwise drag also increases with respect to the baseline, but there is a significant increase in the tip contribution to the overall drag for the actuated flow at $St = 0.14$, which is tip-actuated. The major contribution to the enhancement in the aerodynamic performance for the actuated flow at $St = 0.24$ arises from the root region, where the actuation is localized at this frequency, substantially increasing its overall lift. In the next section, we extend the application of the current flow control methodology to the improvement of the aerodynamic performance of tapered wings.

6.3.6 Active flow control over tapered wings

A root local actuation with an optimal forcing mode from a higher frequency than one of the peak σ_1 is shown to also obtain the highest enhancement in both lift and lift-to-drag ratio when compared to other modal actuation, as shown in figure 6.12. The peak σ_1 for this wing occurs at $St = 0.14$, where we also observe the peak M when evaluated at the separation bubble. Once more we remind that this mode has the aim to suppress the stall formation over the suction side, as seen in figure 6.12(c). The actuation using the $St = 0.14$ shows a

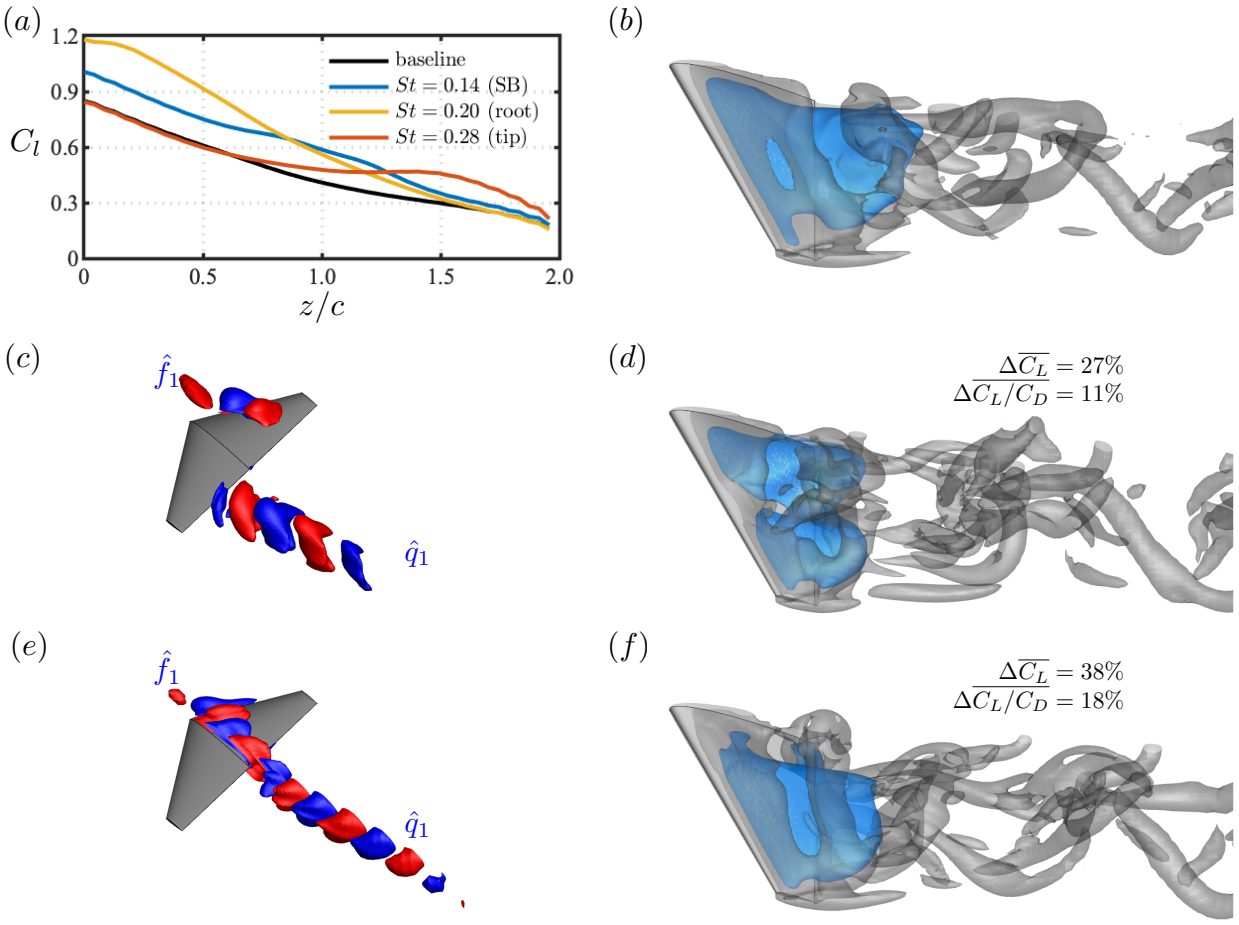

Figure 6.12: Assessment of flow control to improve the aerodynamic performance of tapered swept wings at $\alpha = 22°$. (a) Lift over wingspan for baseline and actuated flows at peak M values, $St = 0.14$ for separation bubble, $St = 0.20$ for wing root, $St = 0.28$ for wing tip. (c, e) Forcing-response mode pairs at $St = 0.14$ and 0.20, respectively. (b, d, f) Baseline and actuated flows with $St = 0.14$ and 0.20 visualized with gray isosurfaces of $Q = 1$ and blue isosurfaces of $\overline{u_x} = 0$. Improvements in the overall lift, $\Delta\overline{C_L}$, and lift-to-drag ratio, $\Delta\overline{C_L/C_D}$, are shown.

considerable increase in the lift and lift-to-drag ratio by reducing the size of the separation bubble that appears to envelop a near wake volume in the actuated flow over the wing, when compared to the baseline, as seen in figure 6.12(d). Furthermore, the forcing mode actuation at $St = 0.14$ breaks the formation of the spanwise vortex rolls over the wing that appears on the baseline flow. As a result, unsteady wake structures emerge closer to the wing.

At a higher frequency of $St = 0.28$ we can perturb the tip region, which was shown to be not effective as it only increases the tip contribution to the overall lift with minor effects on the global aerodynamic performance. The optimal actuation for the improvement of the aerodynamic performance and lift is the one using the optimal forcing mode at $St = 0.20$, shown in figure 6.12(e). For this actuated flow, we note that the separation bubble has its volume reduced and it is shifted toward the outboard portion of the half span, near the tip, seen in figure 6.12(f). This actuation introduces unsteady structures near the root and significantly increases the root contribution to the overall lift, as shown in figure 6.12(a), which is known to be beneficial to flight stability. For this reason, similar to the untapered swept wings shown in section 6.3.5, the root actuation at $St = 0.20$ is the one that yields in the most improved aerodynamic characteristics over the wing.

Lastly, we study the effects of the resolvent-based flow actuation over tapered unswept wings, that is, the one with unswept LE. For these tapered wings, the TE is swept forward and the unsteadiness concentrates at the wing root, as seen in the baseline flow field 6.13(b). As the tip vortex decays and the main structures appear near the root, the most relevant modal actuation is associated with root-dominant forcing modes. A root-based actuation at the peak σ_1, using the resolvent modes shown in figure 6.13(c), causes a considerable increase in lift and lift-t-drag ratio with a significant reduction in the size of the separation bubble, especially in the streamwise direction, as seen in figure 6.13(d). This behavior was studied in previous wings and it is known to increase the root contribution to lift.

Optimal forcing modes ar higher frequencies, namely at $St = 0.26$, as shown in figure 6.13(e) appear over the quarter-span. A $St = 0.26$ actuation increases the unsteadiness levels

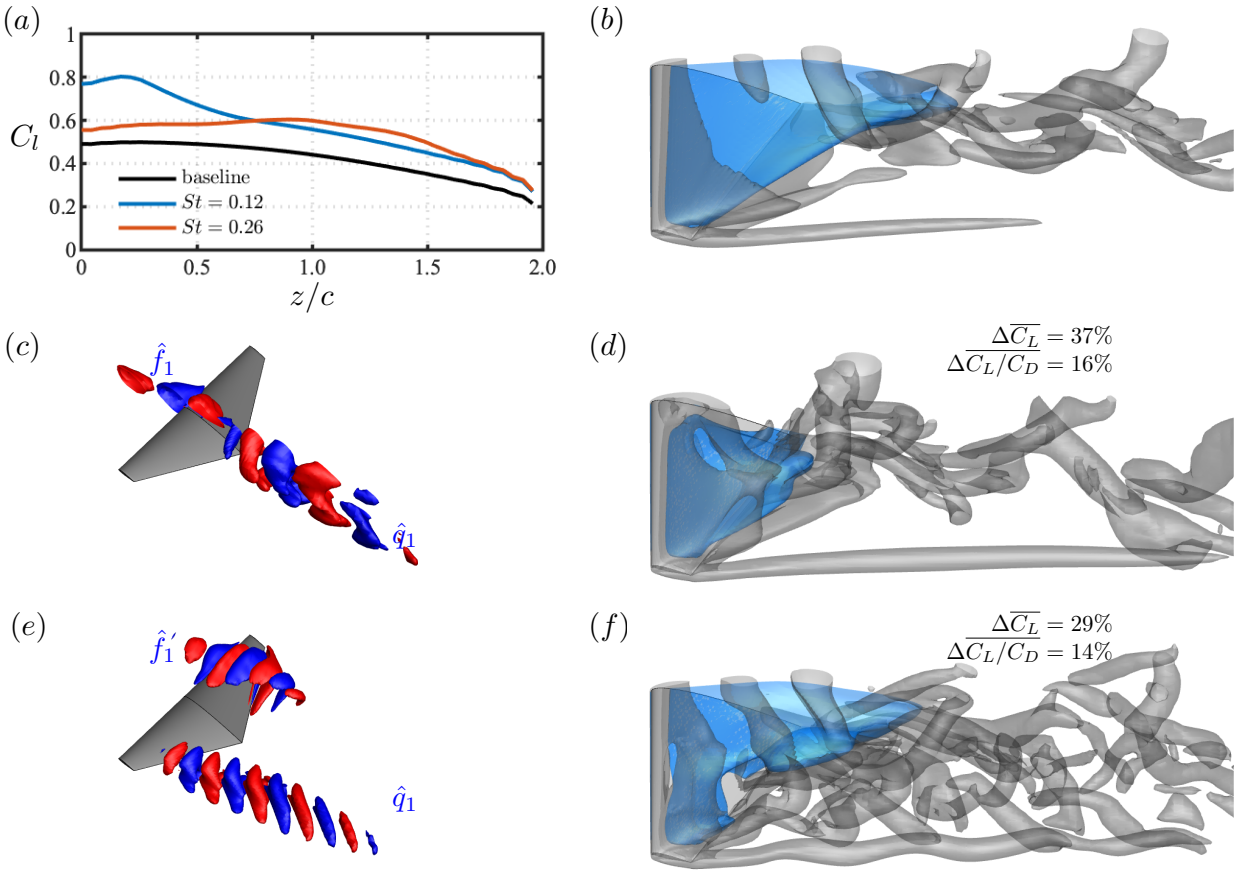

Figure 6.13: Assessment of flow control to improve the aerodynamic performance of tapered wings with unswept leading edges at $\alpha = 22°$. (a) Lift over wingspan for baseline and actuated flows at peak M values, $St = 0.12$ for separation bubble, $St = 0.26$ near wing tip. (c, e) Forcing-response mode pairs at $St = 0.12$ and 0.26, respectively. (b, d, f) Baseline and actuated flows with $St = 0.14$ and 0.20 visualized with gray isosurfaces of $Q = 1$ and blue isosurfaces of $\overline{u_x} = 0$. Improvements in the overall lift, $\Delta\overline{C_L}$, and lift-to-drag ratio, $\Delta\overline{C_L/C_D}$, are shown.

over the entire wingspan, as shown in figure 6.12(f). This causes an even increase of the lift contribution over the wingspan, as seen in figure 6.12(a). The modifications observed in the actuated flows over the unswept tapered wings yield steady and unsteady structures that were smaller in size in the baseline case, such as the tip vortex. Insights on how to control and attenuate this structures may be obtained from previous discussions in sections 6.3.3, 6.3.4, and 6.3.5. For instance, the modal actuation that is used to attenuate the tip vortex in section 6.3.3, may be used to suppress the tip vortex that appears downstream the actuated wakes seen in figures 6.13(d, f). Moreover, one could perform resolvent analysis on the controlled flows to obtain new modes that can be used to further improve the aerodynamic performance of the already actuated flows over tapered unswept wings.

CHAPTER 7

Conclusions

7.1 Summary of contributions

We have presented a comprehensive analysis of fluid flows using direct numerical simulations and triglobal resolvent analysis, characterizing the effects of aspect and taper ratio, as well as angles of attack and sweep in the wake dynamics and perturbations around finite wings. In order to perform resolvent analysis over high-dimensional flow fields, we have developed an algorithm that adapts the randomized SVD approach, through randomized numerical linear algebra, to speed up and reduce the computational burden of the resolvent modes computation. With the randomized resolvent analysis, we were able to study the perturbation dynamics in a 3-D global sense. Using the insights from DNS and resolvent we have elaborated a 3-D active flow control strategy to improve the aerodynamic performance of the wing and change their wake characteristics. In the following sections, we discuss the main contributions and conclusions of each part of the present work.

7.1.1 Resolvent analysis

Resolvent analysis has proven to be a powerful technique to reveal the input-output characteristics of fluid flows. However, the computational cost and memory allocation of the resolvent analysis can be taxing for high-Reynolds number flows, making it prohibitive to be applied to complex turbulent base flows. The major computational cost of the analysis is associated with the SVD of the resolvent operator. To remove this bottleneck, the random-

ized approach has been adopted to reduce the computational cost of SVD by considering the low-rank approximation of the resolvent operator. This was achieved by constructing the low-rank basis based on the insights gained from the sketch of the resolvent, which is obtained from a linear system solver.

For flows with fast singular value decays, e.g., flows with strong shear and separation, the randomized resolvent analysis reveals its power to accurately capture the response and forcing modes as well as the gain. Moreover, we consider the use of the velocity gradient to scale the random test matrix. Such scaling enhanced the accuracy of the randomized resolvent analysis. The necessary computation time was significantly reduced as the number of linear systems to be solved is considerably smaller. To demonstrate the capability of the randomized resolvent analysis, we analyzed the turbulent separated flow over a NACA 0012 airfoil. Excellent agreement of the leading forcing and response modes and the gains were shown between the full and randomized resolvent methods. By incorporating the knowledge of the base flow in terms of its velocity gradient into the randomized test matrix, additional speed up and accuracy enhancement were achieved. With the computational cost and memory allocation being relieved with the randomized approach, the application of the resolvent analysis can be significantly extended to higher-Reynolds number 2D and 3D base flows.

7.1.2 Wake dynamics around finite tapered and swept wings

We have examined the influence of taper and sweep on the dynamics of wake structures for finite NACA 0015 wings with straight-cut tip at a Reynolds number of 600 and a Mach number 0.1. For this study, we have performed an extensive campaign of direct numerical simulations of flows over half-span wings with symmetry boundary condition imposed at the wing root. The present numerical study spans over a wide parameter space with angles of attack between $14^\circ \leq \alpha \leq 22^\circ$, aspect ratios $sAR = 1$ and 2, leading edge sweep angles $0^\circ \leq \Lambda_{\mathrm{LE}} \leq 50^\circ$, and taper ratios between $0.27 \leq \lambda \leq 1$. This parameter space was chosen to characterize the effects of the leading edge sweep and the trailing edge sweep for tapered

wings.

Through direct numerical simulations, we observe that the flow over unswept and untapered wings forms a strong tip vortex, which interacts with the spanwise vortex detaching from the wing surface at the root region. This flow yields a three-dimensional and unsteady wake for all angles of attack considered herein. Untapered and swept wings are observed to advect the shedding region towards the wing tip for lower angles of sweep, as a result of the sweep-induced spanwise flow within the stall region. At higher sweep angles, the wake oscillations are attenuated yielding a steady wake around wings at lower angles of attack.

Wing taper has a strong influence on the wake dynamics. For such wings, LE and TE are not parallel and have a distinct influence on the flow structures within the stall region. For wings with fixed $\Lambda_{\mathrm{LE}} = 0^\circ$ and $\Lambda_{\mathrm{TE}} < 0^\circ$ for $\lambda < 1$, we studied the influence of the forward-swept TE. For such wings, taper concentrates shedding structures towards the wing root and yields a broadband spectral content in the wake, promoting mixing at the root region. Beyond the unsteady wake shedding, the tip vortex is heavily affected by wing taper, reducing its length considerably for tapered wings, as the chord length decreases towards the tip. Such attenuation of the tip vortex is observed to be stronger for wings with fixed $\Lambda_{\mathrm{TE}} = 0^\circ$ and $\Lambda_{\mathrm{LE}} > 0^\circ$ for $\lambda < 1$. This is shown to be influenced by the shedding dislocation from the wing root towards the tip for tapered wings.

It was further shown that backward-swept LE wings also stretch the wake structures in the spanwise direction and promote shedding over a larger portion of the wingspan. Moreover, for wings with high LE sweep, over which the flow tends to be steady for $\lambda = 1$, we have revealed that taper causes wake unsteadiness to appear. Those are developed initially near the wing tip for moderate taper ratios. For low-λ, wings with high LE sweep angles are able to sustain the formation of wake shedding structures that occupy a large portion of the wingspan. Through the detailed analysis of the wake structures, we also provide a map that classifies the wake behavior of tapered wings for the parameter space studied herein, as a function of the LE and TE sweep angles, semi-aspect-ratios, angles of attack, and taper

ratios. The map provides a unique description of the overall flow physics of the wakes around tapered wings and the steady-unsteady flow behavior. The present study reveals the effect of taper, isolating effects of leading and trailing edge sweep and evaluates its impact on the formation and nonlinear evolution of the wake structures.

Lastly, we show how the wing taper affects the aerodynamic forces over the wing. We show that wings with the same taper ratio may present distinct overall lift and aerodynamic performance. It is the combination of a high LE sweep with a low taper ratio that considerably improves lift and lift-to-drag ratio for laminar post-stall flows over tapered wings. The insights gained on the effect of wing taper in the absence of turbulence serve as a stepping stone for future efforts that aim to study, interpret and control higher Reynolds number post-stall flows over tapered swept wings.

7.1.3 Wing sweep effects on laminar separated flows

We reported on the wake dynamics under the influence of sweep for laminar flows over two-dimensional wings through the use of direct numerical simulations and resolvent analysis. The study focused on the onset of 3-D wake structures at a high incidence and the reduction of spanwise oscillations at high sweep. DNS revealed the influence of sweep in terms of attenuating spanwise fluctuations over the wing and giving rise to three-dimensional wakes in agreement with the literature on finite wings. Although the wake dynamics exhibit larger differences between swept and unswept wings, a sweep-angle-based scaling can be used to collapse aerodynamic characteristics when we consider streamwise and spanwise flows to be independent.

As some differences in pressure, lift, and drag for the lower angle of attack settings are perceived at the higher angles of sweep and attack, we resort to the force element theory and identify the vortical structures with spanwise periodicity formed closer to the wing within the laminar separation bubble. Such elements are observed to increase in size and shape with an increase in angles of sweep and attack, a behavior associated with the deviations

of scaled force and pressure coefficients for massively separated flows. This finding revealed force elements that impose additional forces over the wing and showed that spanwise and streamwise flow components cannot be independently analyzed for massively separated flows over swept wings.

Through resolvent analysis, we showed how the sweep angle induces a convection speed to the optimal resolvent modes and provide a linear model to predict the optimal forcing and response spatiotemporal frequencies for laminar flows over swept wings. The forcing and response spatial mode pairs are also affected by the sweep as well as wavemakers that sustain and promote unsteadiness in the wake. We revealed that a misalignment between the optimal response convection speed and the wavemaker speed leads to the reduction in spanwise oscillations for a higher sweep angle. Additionally, we observed that resolvent modes with large amplification gain on swept wings represent the oblique vortex shedding, as observed for laminar flows over high aspect ratio wings in the literature. The present results reveal the fundamental influence of the sweep angle on the airfoil wake dynamics and support future studies on the control of wake oscillations on swept wings at higher angles of attack.

7.1.4 Triglobal resolvent analysis

We presented the triglobal resolvent analysis of laminar separated flows over swept wings and characterized the effects of wing tip and sweep angle on the wake dynamics. We revealed the forcing and response structures that can be amplified from harmonic oscillations or external actuation over finite wings. In the present triglobal analysis, we have identified the wingspan locations where forcing structures can be amplified near the wing and the regions where the unsteady response develops. We have further characterized the region of the dominance of modal structures over the wingspan, with forcing-response mode pairs appearing near the wing root or tip as a function of their characteristic frequency.

Through resolvent resolvent wavemakers, we studied the steady to unsteady flow charac-

teristics over swept wings. We showed the regions where self-sustained instabilities appear over swept wings and related those to the vortex shedding structures observed in the DNS. We also revealed the most sensitive regions for perturbation growth in steady wakes over highly swept wings. The forcing-response mode pairs further revealed the mechanisms of spanwise advection of flow structures, which is further related to the spanwise convective speed found for two- and three-dimensional stability and resolvent analysis over swept wings and also associated with the nonlinear flow characteristics observed in DNS.

For tapered wings, we revealed the locations of optimal perturbations over the wingspan. We have seen that tapered wings can promote multiple mode switching as the frequency increases, which suggests that wing taper can affect the types of vortical structures that are amplified in the wake. For highly swept wings, we have observed that the response modes appear closer to the wing surface with a characteristic shedding pattern for low taper ratios. This is indicative of the mechanisms that sustain wake shedding, while untapered wings exhibit wakes with attenuated flow oscillations. Through the resolvent wavemaker analysis, we relate the regions where unsteadiness is dominant to the regions with strong support from the forcing-response overlap. We characterize how the forcing and response are affected by the taper ratio λ. These results suggest that wakes around tapered wings in post-stall flow conditions are a result of conflicting effects of LE and TE sweep angles as well.

At last, we showed for low-aspect-ratio wings that localized perturbations with root- or tip-dominant characteristics are limited as modes evolve globally over the entire wingspan. In fact, we have shown that root- and tip-dominant structures can appear over the wing in a single mode for low-aspect-ratio wings. This behavior explains the characteristics of the laminar flows around these wings, as observed in DNS, to be different from the flows over $sAR = 2$ and 4 wings. These findings provide fundamental insights into future studies on flow separation over swept wings at higher Reynolds numbers, in which a wider spectrum of fluctuations are present.

7.1.5 Flow control

We have performed direct numerical simulations with external actuation using the optimal forcing modes from triglobal resolvent analysis. We have employed control strategies to improve the aerodynamic performance of laminar post-stall flows over finite tapered and swept wings. For the baseline flows, we notice that untapered and unswept wings develop root shedding with spanwise vortex rolls at the root, while swept wings exhibit steady wakes at the lower incidence and unsteady wakes localized at the wing tip at higher angles of attack. Tapered wings exhibit distinct behavior depending on the LE sweep angle. For unswept LE wings with taper, the tip vortex is attenuated and the shedding structures concentrate at the root region. For tapered swept wings, the shedding region is shifted towards the wing tip.

All the baseline flows develop a large stalled flow region on the suction side and the aim of the present study is to show how optimal perturbations can modify the separated wake and increase the aerodynamic performance of the wing and its overall lift. To achieve the goal to modify the wake, we study the response modes and their modal Reynolds stresses to see which spatial regions are prone to grow perturbations from a given forcing mode. This analysis allows us to predict the regions of flow modification and select the proper forcing modes and actuation frequencies to achieve the control objective. For instance, for an untapered and unswept wing, we have shown that forcing modes located near the root region with frequency content near the baseline vortex shedding frequency can significantly reduce the separation volume, which causes unsteady structures to develop closer to the wing, significantly increasing the overall lift. At higher frequencies, the optimal perturbations appear closer to the wing tip, developing from the trailing edge at the pressure side. These disturbances cause a tremendous reduction in the tip vortex strength, yielding an unsteady helical vortex formation that suppresses the formation of the streamwise vortex core seen in the baseline flow and reduces its circulation at any distance from the wing.

With the knowledge of the forcing-response mode pairs and the baseline flow physics, we have applied the resolvent-based flow modification to swept and tapered wings. For swept tapered and untapered wings, we have seen that the forcing modes that efficiently promote perturbations near the root are more effective to modify the near wake and increase the lift and lift-to-drag ratio. Furthermore, they tend to increase the local lift contribution from the wing root to be always higher than the tip contribution to lift, which is good for flight stability. For tapered unswept wings, we have seen that the main modes of actuation are located near the root and that is possible to increase the overall lift and aerodynamic performance by increasing the near wake unsteadiness and reducing the separation bubble size. The present results show that laminar separated flows are receptive to external perturbations and that optimal spatiotemporal inputs can significantly alter the wake dynamics and improve the aerodynamic performance of the wing.

7.2 Future work

We have examined the 3-D flow perturbations over wings at high angles of attack and to provide pathways to the resolvent-based active flow control over such wings. There are many research avenues that can be extended from the present work. For instance, we have aimed to understand whether a mechanism of transport of vorticity exists within the stalled region that would be responsible for the advection of flow unsteadiness towards root or tip over distinct wing geometries. Further investigation may be needed to address this question and fully understand the flow mechanisms that yield the diverse wake patterns over tapered swept wings. This work has shown the structures that can be used to perturb the wake according to a desired and predetermined control objective, once the resolvent modes are known. This approach still needs to be studied experimentally to confirm the practical application of the present flow structures to modify flow fields. It also remains a challenge to extend the present methodology to higher Reynolds number flows.

REFERENCES

[AB17] J. M. Akkala and J. H. J. Buchholz. "Vorticity transport mechanisms governing the development of leading-edge vortices." *J. Fluid Mech.*, **829**:512–537, 2017.

[ADD96] P. R. Amestoy, T. A. Davis, and I. S. Duff. "An approximate minimum degree ordering algorithm." *SIAM. J. Matrix Anal. Appl*, **17**(4):886–905, 1996.

[AHL88] N. Aubry, P. Holmes, J. L. Lumley, and E. Stone. "The dynamics of coherent structures in the wall region of a turbulent boundary layer." *J. Fluid Mech.*, **192**:115–173, 1988.

[AL85] J. Adler and M. Luttges. "Three-dimensionality in unsteady flow about a wing." In *AIAA Paper 85-0132*, 1985.

[And36] R. F. Anderson. "Determination of the characteristics of tapered wings." Technical Report NACA-TR-572, NASA Langley, 1936.

[And99] J. D. Anderson. *Aircraft performance and design*. WCB/McGraw-Hill Boston, 1999.

[And10] J. D. Anderson. *Fundamentals of aerodynamics*. McGraw-Hill, 2010.

[ASS15] G. K. Ananda, P. P. Sukumar, and M. S. Selig. "Measured aerodynamic characteristics of wings at low Reynolds numbers." *Aerosp. Sci. Technol.*, **42**:392–406, 2015.

[AV59] I. H. Abbott and A. E. Von Doenhoff. *Theory of wing sections: including a summary of airfoil data*. Dover, 1959.

[BBS08] D. Barkley, H. M. Blackburn, and S. J. Sherwin. "Direct optimal growth analysis for timesteppers." *Int. J. Numer. Meth. Fluids*, **57**(9):1435–1458, 2008.

[BD01] J. M. Birch and M. H. Dickinson. "Spanwise flow and the attachment of the leading-edge vortices on insect wings." *Nature*, **412**:729–733, 2001.

[BFP01] M. Braza, D. Faghani, and H. Persillon. "Successive stages and the role of natural vortex dislocations in three-dimensional wake transition." *J. Fluid Mech.*, **439**:1–41, 2001.

[BGM22] B. Barthel, S. Gomez, and B. J. McKeon. "Variational formulation of resolvent analysis." *Phys. Rev. Fluids*, **7**(1):013905, 2022.

[BHH22] A. Burtsev, W. He, S. Hayostek, K. Zhang, V. Theofilis, K. Taira, and M. Amitay. "Linear modal instabilities around post-stall swept finite wings at low Reynolds numbers." *J. Fluid Mech.*, **944**:A6, 2022.

[BHN17a] G. A. Brès, F. E. Ham, J. W. Nichols, and S. K. Lele. "Unstructured Large-Eddy Simulations of Supersonic Jets." *AIAA J.*, **55**(4):1164–1184, 2017.

[BHN17b] G. A. Brès, F. E. Ham, J. W. Nichols, and S. K. Lele. "Unstructured large-eddy simulations of supersonic jets." *AIAA J.*, **55**(4):1164–1184, 2017.

[BL01] C. Breitsamter and B. Laschka. "Vortical flowfield structure at forward swept-wing configurations." *J. Aircraft*, **38**(2):193–207, 2001.

[Bla56] J. Black. "Flow studies of the leading edge stall on a swept-back wing at high incidence." *Aeronaut. J.*, **60**(541):51–60, 1956.

[BLM04] D. Birch, T. Lee, F. Mokhtarian, and F. Kafyeke. "Structure and induced drag of a tip vortex." *J. Aircraft*, **41**(5):1138–1145, 2004.

[BR74] G. L. Brown and A. Roshko. "On density effects and large structure in turbulent mixing layers." *J. Fluid Mech.*, **64**(4):775–816, 1974.

[BRT12] H. R. Beem, D. E. Rival, and M. S. Triantafyllou. "On the stabilization of leading-edge vortices with spanwise flow." *Exp. Fluids*, **52**(2):511–517, 2012.

[BS06] J. H. J. Buchholz and A. J. Smits. "On the evolution of the wake structure produced by a low-aspect-ratio pitching panel." *J. Fluid Mech.*, **546**:433–443, 2006.

[BT80] H. Bippes and M. Turk. "Windkanalmessungen in einem Rechteckflügel bei anliegender und abgelöster Strömung." Technical report, DFVLR Forschungsbericht IB 251-80 A 18, 1980.

[BTR23] A. Burtsev, V. Theofilis, J. H. M. Ribeiro, K. Taira, J. M. Neal, and M. Amitay. "Wake dynamics of tapered wings. Part III: triglobal linear stability analysis." In *AIAA Paper 2023-2299*, 2023.

[BVG15] C. J. Barnes, M. R. Visbal, and R. E. Gordnier. "Analysis of streamwise-oriented vortex interactions for two wings in close proximity." *Phys. Fluids*, **27**(1):015103, 2015.

[Can81] B. J. Cantwell. "Organized motion in turbulent flow." *Annu. Rev. Fluid Mech.*, **13**(1):457–515, 1981.

[CCT10] K. K. Chen, T. Colonius, and K. Taira. "The leading-edge vortex and quasi-steady vortex shedding on an accelerating plate." *Phys. Fluids*, **22**:033601, 2010.

[CGS19] J. D. Crouch, A. Garbaruk, and M. Strelets. "Global instability in the onset of transonic-wing buffet." *J. Fluid Mech.*, **881**:3–22, 2019.

[Cha92] C.-C. Chang. "Potential flow and forces for incompressible viscous flow." *Proc. R. Soc. Lond. A*, **437**(1901):517–525, 1992.

[Chu65] B.-T. Chu. "On the energy transfer to small disturbances in fluid flow (Part I)." *Acta Mechanica*, **1**(3):215–234, 1965.

[CRS19] G. N. Coleman, C. L. Rumsey, and P. R. Spalart. "Numerical study of a turbulent separation bubble with sweep." *J. Fluid Mech.*, **880**:684–706, 2019.

[CW09] K. L. Clarkson and D. P. Woodruff. "Numerical linear algebra in the streaming model." In *Proceedings of the forty-first annual ACM symposium on Theory of computing*, pp. 205–214. ACM, 2009.

[DCM20] L. Dong, K.-S. Choi, and X. Mao. "Interplay of the leading-edge vortex and the tip vortex of a low-aspect-ratio thin wing." *Exp. Fluids*, **61**(9):1–15, 2020.

[DD04] W. B. Dickson and M. H. Dickinson. "The effect of advance ratio on the aerodynamics of revolving wings." *J. Exp. Biol.*, **207**(24):4269–4281, 2004.

[DDH07] J. Demmel, I. Dumitriu, and O. Holtz. "Fast linear algebra is stable." *Num. Math.*, **108**(1):59–91, 2007.

[Del01] J. M. Délery. "Robert Legendre and Henri Werlé: toward the elucidation of three-dimensional separation." *Annu. Rev. Fluid Mech.*, **33**:128, 2001.

[Del13] J. M. Délery. *Three-dimensional separated flow topology: critical points, separation lines and vortical structures*. John Wiley & Sons, 2013.

[DLS99] M. H. Dickinson, F.-O. Lehmann, and S. P. Sane. "Wing rotation and the aerodynamic basis of insect flight." *Science*, **284**(5422):1954–1960, 1999.

[DM16] P. Drineas and M. W. Mahoney. "RandNLA: randomized numerical linear algebra." *Comm. ACM*, **59**(6):80–90, 2016.

[DM17] A. C. DeVoria and K. Mohseni. "On the mechanism of high-incidence lift generation for steadily translating low-aspect-ratio wings." *J. Fluid Mech.*, **813**:110–126, 2017.

[DMN06] H. Dong, R. Mittal, and F. M. Najjar. "Wake topology and hydrodynamic performance of low-aspect-ratio flapping foils." *Journal of Fluid Mechanics*, **566**:309–343, 2006.

[DRL96] W. J. Devenport, M. C. Rife, S. I. Liapis, and G. J. Follin. "The structure and development of a wing-tip vortex." *J. Fluid Mech.*, **312**:67–106, 1996.

[DSN19] A. Dwivedi, G. S. Sidharth, J. W. Nichols, G. V. Candler, and M. R. Jovanović. "Reattachment streaks in hypersonic compression ramp flow: an input–output analysis." *J. Fluid Mech.*, **880**:113–135, 2019.

[Dur05] K. Duraisamy. *Studies in tip vortex formation, evolution and control.* PhD thesis, 2005.

[DW22] T. C. Déda and W. R. Wolf. "Extremum seeking control applied to airfoil trailing-edge noise suppression." *AIAA J.*, **60**(2):823–843, 2022.

[EBW96] C. P. Ellington, C. Van Den Berg, A. P. Willmott, and A. L. R. Thomas. "Leading-edge vortices in insect flight." *Nature*, **384**(6610):626–630, 1996.

[EJ19] J. D. Eldredge and A. R. Jones. "Leading-edge vortices: mechanics and modeling." *Annu. Rev. Fluid Mech.*, **51**:75–104, 2019.

[EMK19] N. B. Erichson, L. Mathelin, J. N. Kutz, and S. L. Brunton. "Randomized dynamic mode decomposition." *SIAM J. App. Dyn. Syst.*, **18**(4):1867–1891, 2019.

[ESS18] A. M. Edstrand, Y. Sun, P. J. Schmid, K. Taira, and L. N. Cattafesta. "Active attenuation of a trailing vortex inspired by a parabolized stability analysis." *J. Fluid Mech.*, **855**:R2, 2018.

[EST18] A. M. Edstrand, P. J. Schmid, K. Taira, and L. N. Cattafesta III. "A parallel stability analysis of a trailing vortex wake." *J. Fluid Mech.*, **837**:858, 2018.

[EVB19] N. B. Erichson, S. Voronin, S. L. Brunton, and J. N. Kutz. "Randomized matrix decompositions using R." *J. Stat. Soft.*, **89**(11):1–48, 2019.

[Fal50] V. M. Falkner. "Sweepback and Wing Taper: The Effect of Sweepback on the Lift, Drag, and Aerodynamic Centre of a Tapered Wing." *Aircraft Eng. Aero. Tech.*, **22**(10):296–300, 1950.

[FFB86a] P. Freymuth, F. Finaish, and W. Bank. "Visualization of wing tip vortices in accelerating and steady flow." *J. Aircraft*, **23**(9):730–733, 1986.

[FFB86b] P. Freymuth, F. Finaish, and W. Bank. "Wing Tip Vortex System in a Starting Flow." **10**:116–118, 1986.

[FFB87] P. Freymuth, F. Finaish, and W. Bank. "Further visualization of combined wing tip and starting vortex systems." *AIAA J.*, **25**(9):1153–1159, 1987.

[FI94] B. F. Farrell and P.J. Ioannou. "Variance maintained by stochastic forcing of non-normal dynamical systems associated with linearly stable shear flows." *Phys. Rev. Let.*, **72**(8):1188–1191, 1994.

[FK79] M. S. Francis and D. A. Kennedy. "Formation of a trailing vortex." *J. Aircraft*, **16**(3):148–154, 1979.

[Fre85] P. Freymuth. "The vortex patterns of dynamic separation: a parametric and comparative study." *Prog. Aero. Sci.*, **22**(3):161–208, 1985.

[Fre86] P. Freymuth. "Visualizing the combined system of wing tip and starting vortices." *TSI Flowlines*, **1**, 1986.

[Fre97] J. B. Freund. "Proposed inflow/outflow boundary condition for direct computation of aerodynamic sound." *AIAA J.*, **35**(4):740–742, 1997.

[FS17] M. Fosas de Pando and P. J. Schmid. "Optimal frequency-response sensitivity of compressible flow over roughness elements." *J. Turb.*, **18**(4):338–351, 2017.

[FSS17] M. Fosas de Pando, P. J. Schmid, and D. Sipp. "On the receptivity of aerofoil tonal noise: an adjoint analysis." *J. Fluid Mech.*, **812**:771–791, 2017.

[FTM21] A. Farghadan, A. Towne, E. Martini, and A. Cavalieri. "A randomized time-domain algorithm for efficiently computing resolvent modes." AIAA Paper 2021-2896, 2021.

[GA91] S. I. Green and A. J. Acosta. "Unsteady flow in trailing vortices." *J. Fluid Mech.*, **227**:107–134, 1991.

[Gad00] M. Gad-el-Hak. *Flow control: passive, active, and reactive flow management*. Cambridge Univ. Press, 2000.

[Gas67] M. Gaster. "The structure and behaviour of laminar separation bubbles." pp. 813–854, 1967.

[GBM22] K. Goc, S. T. Bose, and P. Moin. "Large Eddy Simulation of the NASA High-Lift Common Research Model." In *AIAA Paper 2022-1556*, 2022.

[GBR16] F. Gómez, H. M. Blackburn, M. Rudman, A. S. Sharma, and B. J. McKeon. "A reduced-order model of three-dimensional unsteady flow in a cavity based on the resolvent operator." *J. Fluid Mech.*, **798**:R2, 2016.

[GC47] R. R. Graham and D. W. Conner. "Investigation of High-Lift and Stall-Control Devices on an NACA 64-Series 42 deg Sweptback Wing with and Without Fuselage." Technical Report NASA RM L7G09, NASA Langley, 1947.

[GCL10] F. Giannetti, S. Camarri, and P. Luchini. "Structural sensitivity of the secondary instability in the wake of a circular cylinder." *J. Fluid Mech.*, **651**:319–337, 2010.

[GGV05] I. Gursul, R. Gordnier, and M. Visbal. "Unsteady aerodynamics of nonslender delta wings." *Prog. Aero. Sci.*, **41**(7):515–557, 2005.

[Giu13] M. Giuni. *Formation and early development of wingtip vortices*. PhD thesis, 2013.

[GL07] F. Giannetti and P. Luchini. "Structural sensitivity of the first instability of the cylinder wake." *J. Fluid Mech.*, **581**(1):167–197, 2007.

[GLH06] R. Gurka, A. Liberzon, and G. Hetsroni. "POD of vorticity fields: A method for spatial characterization of coherent structures." *Int. J. Heat Fluid Flow*, **27**(3):416–423, 2006.

[GQO71] N. Gregory, V. G. Quincey, C. L. O'Reilly, and D. J. Hall. *Progress report on observations of three-dimensional flow patterns obtained during stall development on aerofoils, and on the problem of measuring two-dimensional characteristics*. Citeseer, 1971.

[Gre12] D. Greenblatt. "Fluidic control of a wing tip vortex." *AIAA J.*, **50**(2):375–386, 2012.

[GSK22] A. S. Ghate, G.-D. Stich, G. K. Kenway, J. A. Housman, and C. C. Kiris. "A Wall-Modeled LES Perspective for the High Lift Common Research Model Using LAVA." In *AIAA 2022-3434*, 2022.

[Gu15] M. Gu. "Subspace iteration randomization and singular value problems." *SIAM J. Sci. Comput.*, **37**(3):A1139–A1173, 2015.

[GV15] D. J. Garmann and M. R. Visbal. "Interactions of a streamwise-oriented vortex with a finite wing." *J. Fluid Mech.*, **767**:782–810, 2015.

[GV17] D. J. Garmann and M. R. Visbal. "Analysis of tip vortex near-wake evolution for stationary and oscillating wings." *AIAA J.*, pp. 2686–2702, 2017.

[GV20] D. J. Garmann and M. R. Visbal. "Examination of pitch-plunge equivalence for dynamic stall over swept finite wings." AIAA Paper 2020–1759, 2020.

[GW18] I. Gursul and Z. Wang. "Flow control of tip/edge vortices." *AIAA J.*, **56**(5):1731–1749, 2018.

[HA21] S. Hayostek and M. Amitay. "Flowfield around Low Aspect Ratio Finite Span-Wings at low Reynolds Number: Effect of Sweep." In *AIAA Paper 2021-2862*, 2021.

[HBV03] Y. Hoarau, M. Braza, Y. Ventikos, D. Faghani, and G. Tzabiras. "Organized modes and the three-dimensional transition to turbulence in the incompressible flow around a NACA 0012 wing." *J. Fluid Mech.*, **496**:63–72, 2003.

[HGP17] W. He, R. S. Gioria, J. M. Pérez, and Vassilis V. Theofilis. "Linear instability of low Reynolds number massively separated flow around three NACA airfoils." *J. Fluid Mech.*, **811**:701–741, 2017.

[HGV22] P. R. Hammer, D. J. Garmann, and M. R. Visbal. "Effect of Aspect Ratio on Finite-Wing Dynamic Stall." *AIAA J.*, pp. 1–13, 2022.

[HH85] M. Gad el Hak and C.-M. Ho. "The pitching delta wing." *AIAA J.*, **23**(11):1660–1665, 1985.

[HH86] M. Gad el Hak and C.M. Ho. "Unsteady vortical flow around three-dimensional lifting surfaces." *AIAA J.*, **24**(5):713–721, 1986.

[HI04] F. Ham and G. Iaccarino. "Energy conservation in collocated discretization schemes on unstructured meshes." *Annual Research Briefs, Center for Turbulence Research*, pp. 3–14, 2004.

[Hil92] D. Hill. "A theoretical approach for analyzing the restabilization of wakes." AIAA Paper 1992-67, 1992.

[HLB12] P. Holmes, J. L. Lumley, G. Berkooz, and C. W. Rowley. *Turbulence, coherent structures, dynamical systems and symmetry.* Cambridge Univ. Press, 2nd edition, 2012.

[HM64] C. W. Harper and R. L. Maki. "A review of the stall characteristics of swept wings." Technical Report NASA/TN D-2373, NASA, Washington, DC, 1964.

[HMI06] F. Ham, K. Mattsson, and G. Iaccarino. "Accurate and stable finite volume operators for unstructured flow solvers." *Annual Research Briefs, Center for Turbulence Research*, pp. 243–261, 2006.

[HMT11a] N. Halko, P.-G. Martinsson, and J. A. Tropp. "Finding structure with randomness: Probabilistic algorithms for constructing approximate matrix decompositions." *SIAM R.*, **53**(2):217–288, 2011.

[HMT11b] N. Halko, P.-G. Martinsson, and J. A. Tropp. "Finding structure with randomness: Probabilistic algorithms for constructing approximate matrix decompositions." *SIAM review*, **53**(2):217–288, 2011.

[HON22] S. Hayostek, J. Ottinger, J. Neal, and M. Amitay. "Experimental Investigation on the Effect of Sweep and Taper on Low Reynolds Number Finite Wings." In *AIAA Paper 2022-0467*, 2022.

[Hor68] H. P. Horton. *Laminar separation bubbles in two and three dimensional incompressible flow.* PhD thesis, Queen Mary University of London, 1968.

[HP84] H. G. Hornung and A. E. Perry. "Some aspects of three-dimensional separation. Part I. Streamsurface bifurcations." *Z. Flugwiss. Weltraumforsch*, **8**:77–87, 1984.

[HSR22] D. C. House, C. S. Skene, J. H. M. Ribeiro, C.-A. Yeh, and K. Taira. "Sketch-Based Resolvent Analysis." AIAA Paper 2022-3335, 2022.

[HT21] W. He and S. Timme. "Triglobal infinite-wing shock-buffet study." *J. Fluid Mech.*, **925**:A27, 2021.

[HTP17] W. He, J. A. Tendero, P. Paredes, and V. Theofilis. "Linear instability in the wake of an elliptic wing." *Theor. Comput. Fluid Dyn.*, **31**:483–504, 2017.

[HTS22] J. Houtman, S. Timme, and A. Sharma. "Resolvent Analysis of Large Aircraft Wings in Edge-of-the-Envelope Transonic Flow." In *AIAA Paper 2022-1329*, 2022.

[HTS23] J. Houtman, S. Timme, and A. Sharma. "Resolvent analysis of a finite wing in transonic flow." *Flow*, **3**:E14, 2023.

[HVT15] Y. Huang, J. Venning, M. C. Thompson, and J. Sheridan. "Vortex separation and interaction in the wake of inclined trapezoidal plates." *J. Fluid Mech.*, **771**:341–369, 2015.

[HWJ01] R. F. Huang, J. Y. Wu, J. H. Jeng, and R. C. Chen. "Surface flow and vortex shedding of an impulsively started wing." *J. Fluid Mech.*, **441**:265–292, 2001.

[Irv37] H. B. Irving. "Some Notes on Tapered Wings: The Effects of Brake Flaps, Taper and "Sweep" on Stalling." *Aircraft Eng. Aero. Tech.*, **9**(2):31–36, 1937.

[JB05] M. R. Jovanović and B. Bamieh. "Componentwise energy amplification in channel flows." *J. Fluid Mech.*, **534**:145–183, 2005.

[JH95] J. Jeong and F. Hussain. "On the identification of a vortex." *J. Fluid Mech.*, **285**:69–94, 1995.

[JMS16] A. R. Jones, A. Medina, H. Spooner, and K. Mulleners. "Characterizing a burst leading-edge vortex on a rotating flat plate wing." *Exp. Fluids*, **57**(4):1–16, 2016.

[JNJ16] J. Jeun, J. W. Nichols, and M. R. Jovanović. "Input-output analysis of high-speed axisymmetric isothermal jet noise." *Phys. Fluids*, **28**(4):047101, 2016.

[Jov04a] M. R. Jovanović. *Modeling, analysis, and control of spatially distributed systems.* PhD thesis, University of California at Santa Barbara, Dept. of Mechanical Engineering, 2004.

[Jov04b] M. R. Jovanović. *Modeling, analysis, and control of spatially distributed systems*. University of California at Santa Barbara, Dept. of Mechanical Engineering, 2004.

[JS37] E. Jacobs and A. Sherman. "Airfoil section characteristics as affected by variations of the." Technical Report NACA-TR-586, NASA, 1937.

[JSS10] L. E. Jones, N. D. Sandham, and R. D. Sandberg. "Acoustic source identification for transitional airfoil flows using cross correlations." *AIAA J.*, **48**(10):2299–2312, 2010.

[KFB16] J. N. Kutz, X. Fu, and S. L. Brunton. "Multiresolution dynamic mode decomposition." *SIAM J. App. Dyn. Sys.*, **15**(2):713–735, 2016.

[KG89] J. Katz and J. B. Galdo. "Effect of roughness on rollup of tip vortices on a rectangular hydrofoil." *J. Aircraft*, **26**(3):247–253, 1989.

[KHN11] Y. Khalighi, F. Ham, J. Nichols, S. K. Lele, and P. Moin. "Unstructured large eddy simulation for prediction of noise issued from turbulent jets in various configurations." In *AIAA Paper 2011–2886*, 2011.

[KT17] T. Kajishima and K. Taira. *Computational fluid dynamics: incompressible turbulent flows*. Springer, 2017.

[KYT20] Y. Kojima, C.-A. Yeh, K. Taira, and M. Kameda. "Resolvent analysis on the origin of two-dimensional transonic buffet." *J. Fluid Mech.*, **885**:R1, 2020.

[Lai01] E. V. Laitone. *Wind tunnel tests of wings and rings at low Reynolds numbers*, volume 195, pp. 83–90. 2001.

[LD09] D. Lentink and M. H. Dickinson. "Rotational accelerations stabilize leading edge vortices on revolving fly wings." *J. Exp. Biol.*, **212**(16):2705–2719, 2009.

[Leg56] R. Legendre. "Separation de l'ecoulement laminaire tridimensionell." *La Rech. Aéro.*, (54):3–8, 1956.

[LHC12] J.-J. Lee, C.-T. Hsieh, C.-C. Chang, and C.-C. Chu. "Vorticity forces on an impulsively started finite plate." *J. Fluid Mech.*, **694**:464–492, 2012.

[Lig63] M. J. Lighthill. "Attachment and separation in three-Dimensional flows." *Laminar bound. layer theory*, pp. 72–82, 1963.

[Lis83] P. B. S. Lissaman. "Low-Reynolds-number airfoils." *Annu. Rev. Fluid Mech.*, **15**(1):223–239, 1983.

[LMS07] D. Lentink, U. K. Müller, E. J. Stamhuis, R. De Kat, W. Van Gestel, L. L. M. Veldhuis, P. Henningsson, A. Hedenström, J. J. Videler, and J. L. Van Leeuwen. "How swifts control their glide performance with morphing wings." *Nature*, **446**(7139):1082–1085, 2007.

[LP96] J. C. M. Lin and L. L. Pauley. "Low-Reynolds-number separation on an airfoil." *AIAA J.*, **34**(8):1570–1577, 1996.

[LRW22] H. F. S. Lui, T. R. Ricciardi, W. R. Wolf, J. Braun, I. Rahbari, and G. Paniagua. "Unsteadiness of shock-boundary layer interactions in a Mach 2.0 supersonic turbine cascade." *Phys. Rev. Fluids*, **7**(9):094602, 2022.

[LSY21] Q. Liu, Y. Sun, C.-A. Yeh, L. S. Ukeiley, L. N. Cattafesta, and K. Taira. "Unsteady control of supersonic turbulent cavity flow based on resolvent analysis." *J. Fluid Mech.*, **925**:A5, 2021.

[Lum67] J. L. Lumley. "The structure of inhomogeneous turbulent flows." *Atmospheric turbulence and radio wave propagation*, 1967.

[Lum70] J. L. Lumley. *Stochastic tools in turbulence*. Courier Corporation, 1970.

[LW18] J. Li and Z.-N. Wu. "Vortex force map method for viscous flows of general airfoils." *J. Fluid Mech.*, **836**:145–166, 2018.

[LW19] H. F. S. Lui and W. R. Wolf. "Construction of reduced-order models for fluid flows using deep feedforward neural networks." *J. Fluid Mech.*, **872**:963–994, 2019.

[LZG20] J. Li, X. Zhao, and M. Graham. "Vortex force maps for three-dimensional unsteady flows with application to a delta wing." *J. Fluid Mech.*, **900**:A36, 2020.

[MAB10] A. Monokrousos, E. Åkervik, L. Brandt, and D. S. Henningson. "Global three-dimensional optimal disturbances in the Blasius boundary-layer flow using time-steppers." *J. Fluid Mech.*, **650**:181–214, 2010.

[Mag11] J. Magnaudet. "A reciprocal theorem for the prediction of loads on a body moving in an inhomogeneous flow at arbitrary Reynolds number." *J. Fluid Mech.*, **689**:564–604, 2011.

[Mar87] J. F. Marchman. "Aerodynamic testing at low Reynolds numbers." *J. Aircraft*, **24**(2):107–114, 1987.

[McC95] B. W. McCormick. *Aerodynamics, aeronautics, and flight mechanics*. John Wiley & Sons, 1995.

[Mil36] C. B. Millikan. "On the Stalling of Highly Tapered Wings." *J. Aero. Sci.*, **3**(5):145–150, 1936.

[MM21a] K. Menon and R. Mittal. "Quantitative analysis of the kinematics and induced aerodynamic loading of individual vortices in vortex-dominated flows: a computation and data-driven approach." *J. Comput. Phys.*, **443**:110515, 2021.

[MM21b] K. Menon and R. Mittal. "Significance of the strain-dominated region around a vortex on induced aerodynamic loads." *J. Fluid Mech.*, **918**:R3, 2021.

[MMG15] P. Mancini, F. Manar, K. Granlund, M. V. Ol, and A. R. Jones. "Unsteady aerodynamic characteristics of a translating rigid wing at low Reynolds number." *Physics of Fluids*, **27**(12):123102, 2015.

[MPH21] S. Mittal, J. S. S. Pandi, and M. Hore. "Cellular vortex shedding from a cylinder at low Reynolds number." *J. Fluid Mech.*, **915**:A74, 2021.

[MRT11] P.-G. Martinsson, V. Rokhlin, and M. Tygert. "A randomized algorithm for the decomposition of matrices." *Appl. Comput. Harmon. Anal.*, **30**(1):47–68, 2011.

[MRT21] E. Martini, D. Rodríguez, A. Towne, and A. V. G. Cavalieri. "Efficient computation of global resolvent modes." *J. Fluid Mech.*, **919**:A3, 2021.

[MS10] B. J. McKeon and A. S. Sharma. "A critical-layer framework for turbulent pipe flow." *J. Fluid Mech.*, **658**:336–382, 2010.

[MS14] S. Mittal and G.S. Sidharth. "Steady forces on a cylinder with oblique vortex shedding." *J. Fluids Struct.*, **44**:310–315, 2014.

[MST13a] R. Moarref, A. S. Sharma, J. A. Tropp, and B. J. McKeon. "Model-based scaling of the streamwise energy density in high-Reynolds-number turbulent channels." *J. Fluid Mech.*, **734**:275–316, 2013.

[MST13b] R. Moarref, A. S. Sharma, Joel A Tropp, and Beverley J McKeon. "Model-based scaling of the streamwise energy density in high-Reynolds-number turbulent channels." *J. Fluid Mech.*, **734**:275–316, 2013.

[MTP20] L. Masini, S. Timme, and A. J. Peace. "Analysis of a civil aircraft wing transonic shock buffet experiment." *J. Fluid Mech.*, **884**:A1, 2020.

[MTS68] B. W. McCormick, J. L. Tangler, and H. E. Sherrieb. "Structure of trailing vortices." *J. Aircraft*, **5**(3):260–267, 1968.

[Mue01] T. J. Mueller. *Fixed and flapping wing aerodynamics for micro air vehicle applications*. American Institute of Aeronautics and Astronautics, Inc. Reston, VA, 2001.

[MWG22a] R. F. Miotto, W. R. Wolf, D. Gaitonde, and M. Visbal. "Analysis of the onset and evolution of a dynamic stall vortex on a periodic plunging aerofoil." *J. Fluid Mech.*, **938**:A24, 2022.

[MWG22b] R. F. Miotto, W. R. Wolf, D. Gaitonde, and M. Visbal. "Pitch–Plunge Equivalence in Dynamic Stall of Ramp Motion Airfoils." *AIAA J.*, pp. 1–15, 2022.

[MZ06] R. B. Morgan and M. Zeng. "A harmonic restarted Arnoldi algorithm for calculating eigenvalues and determining multiplicity." *Lin. Alg. Appl.*, **415**(1):96–113, 2006.

[NA23] J. M. Neal and M. Amitay. "Three-dimensional separation over unswept cantilevered wings at a moderate Reynolds number." *Phys. Rev. Fluids*, **8**:014703, 2023.

[NAP08] V. D. Narasimhamurthy, H. I. Andersson, and B. Pettersen. "Cellular vortex shedding in the wake of a tapered plate." *J. Fluid Mech.*, **617**:355–379, 2008.

[NBJ19] Navrose, V. Brion, and L. Jacquin. "Transient growth in the near wake region of the flow past a finite span wing." *J. Fluid Mech.*, **866**:399–430, 2019.

[NFL17] S. Nakashima, K. Fukagata, and M. Luhar. "Assessment of suboptimal control for turbulent skin friction reduction via resolvent analysis." *J. Fluid Mech.*, **828**:496–526, 2017.

[NGA23] J. M. Neal, B. Gares, M. Amitay, A. Burtsev, V. Theofilis, J. H. M. Ribeiro, and K. Taira. "Wake dynamics of tapered wings. Part II: an experimental study." In *AIAA Paper 2023-2298*, 2023.

[NRL23] G. Nastro, J.-C. Robinet, J.-C. Loiseau, P.-Y. Passaggia, and N. Mazellier. "Global stability, sensitivity and passive control of low-Reynolds-number flows around NACA 4412 swept wings." *J. Fluid Mech.*, **957**:A5, 2023.

[PB06] D. J. Pines and F. Bohorquez. "Challenges facing future micro-air-vehicle development." *J. Aircraft*, **43**(2):290–305, 2006.

[PBD19] E. Paladini, S. Beneddine, J. Dandois, D. Sipp, and J.-C. Robinet. "Transonic buffet instability: From two-dimensional airfoils to three-dimensional swept wings." *Phys. Rev. Fluids*, **4**(10):103906, 2019.

[PBK16] J. L. Proctor, S. L. Brunton, and J. N. Kutz. "Dynamic mode decomposition with control." *SIAM J. App. Dyn. Sys.*, **15**(1):142–161, 2016.

[PDB21] F. Plante, J. Dandois, S. Beneddine, É. Laurendeau, and D. Sipp. "Link between subsonic stall and transonic buffet on swept and unswept wings: from global stability analysis to nonlinear dynamics." *J. Fluid Mech.*, **908**:A16, 2021.

[PDD06] C. Poelma, W. B. Dickson, and M. H. Dickinson. "Time-resolved reconstruction of the full velocity field around a dynamically-scaled flapping wing." *Experiments in Fluids*, **41**(2):213–225, 2006.

[PDL20] F. Plante, J. Dandois, and É. Laurendeau. "Similarities between cellular patterns occurring in transonic buffet and subsonic stall." *AIAA J.*, **58**(1):71–84, 2020.

[PH84] A. E. Perry and H. G. Hornung. "Some aspects of three-dimensional separation. Part II. Vortex skeletons." *Z. Flugwiss. Weltraumforsch*, **8**:155–160, 1984.

[PM00] A. Pelletier and T. J. Mueller. "Low Reynolds number aerodynamics of low-aspect-ratio, thin/flat/cambered-plate wings." *J. Aircraft*, **37**(5):825–832, 2000.

[PM19] J. S. S. Pandi and S. Mittal. "Wake transitions and laminar separation bubble in the flow past an Eppler 61 airfoil." *Phys. Fluids*, **31**(11):114102, 2019.

[PMR90] L. L. Pauley, P. Moin, and W. C. Reynolds. "The structure of two-dimensional separation." *J. Fluid Mech.*, **220**:397–411, 1990.

[Poi82] H. Poincaré. "Les points singuliers des équations différentielles." *C. R. Acad. Sci. Paris*, **94**:416–418, 1882.

[Pra20] L. Prandtl. "Theory of lifting surfaces." Technical Report NACA/TN-9, NASA, Washington, DC, 1920.

[PRA72] D. J. Peake, W. J. Rainbird, and E. G. Atraghji. "Three-dimensional flow separations on aircraft and missiles." *AIAA J.*, **10**(5):567–580, 1972.

[PSN00] B. Protas, A. Styczek, and A. Nowakowski. "An effective approach to computation of forces in viscous incompressible flows." *J. Comput. Phys.*, **159**(2):231–245, 2000.

[PT80] D. J. Peake and M. Tobak. "Three-dimensional interactions and vortical flows with emphasis on high speeds." (252), 1980.

[PV93] P. S. Piccirillo and C. W. Van Atta. "An experimental study of vortex shedding behind linearly tapered cylinders at low Reynolds number." *J. Fluid Mech.*, **246**:163–195, 1993.

[QN83] L. Quartapelle and M. Napolitano. "Force and moment in incompressible flows." *AIAA J.*, **21**(6):911–913, 1983.

[QS17] U. A. Qadri and P. J. Schmid. "Frequency selection mechanisms in the flow of a laminar boundary layer over a shallow cavity." *Phys. Rev. Fluids*, **2**:043902, 2017.

[RCO18] E. Rossi, A. Colagrossi, G. Oger, and D. Le Touzé. "Multiple bifurcations of the flow over stalled airfoils when changing the Reynolds number." *J. Fluid Mech.*, **846**:356–391, 2018.

[Rib17] J. H. M. Ribeiro. *"Analysis of coherent structures in wall-bounded turbulent flows using proper orthogonal decomposition."*. Master's thesis, UNICAMP, Campinas, SP, Brazil, 2017.

[RJF22] L. V. Rolandi, T. Jardin, J. Fontane, J. Gressier, and L. Joly. "Stability of the low Reynolds number compressible flow past a NACA0012 airfoil." *AIAA J.*, **60**(2):1052–1066, 2022.

[RMB09] C. W. Rowley, I. Mezić, S. Bagheri, and D. S. Henningson. "Spectral analysis of nonlinear flows." *J. Fluid Mech.*, **641**:115–127, 2009.

[Roc93] D. Rockwell. "Three-dimensional flow structure on delta wings at high angle-of-attack-Experimental concepts and issues." In *AIAA Paper 1993-0550*, 1993.

[Row02] C. W. Rowley. *Modeling, simulation, and control of cavity flow oscillations*. PhD thesis, California Institute of Technology, 2002.

[Row05] C. W. Rowley. "Model reduction for fluids, using balanced proper orthogonal decomposition." *Int. J. Bif. Chaos*, **15**(3):997–1013, 2005.

[RST09] V. Rokhlin, A. Szlam, and M. Tygert. "A randomized algorithm for principal component analysis." *SIAM J. Matrix Anal. Appl.*, **31**(3):1100–1124, 2009.

[RTN23] J. H. M. Ribeiro, K. Taira, J. M. Neal, M. Amitay, A. Burtsev, and V. Theofilis. "Wake dynamics of tapered wings. Part I: a computational study." In *AIAA Paper 2023-2297*, 2023.

[RW17] J. H. M. Ribeiro and W. R. Wolf. "Identification of coherent structures in the flow past a NACA0012 airfoil via proper orthogonal decomposition." *Phys. Fluids*, **29**(8):085104, 2017.

[RWS18] T. R. Ricciardi, W. R. Wolf, and R. Speth. "Acoustic prediction of lagoon landing gear: Cavity noise and coherent structures." *AIAA J.*, **56**(11):4379–4399, 2018.

[RWT22] T. R. Ricciardi, W. R. Wolf, and K. Taira. "Transition, intermittency and phase interference effects in airfoil secondary tones and acoustic feedback loop." *J. Fluid Mech.*, **937**, 2022.

[RWY19] B. L. O. Ramos, W. R. Wolf, C.-A. Yeh, and K. Taira. "Active flow control for drag reduction of a plunging airfoil under deep dynamic stall." *Phys. Rev. Fluids*, **4**(7):074603, 2019.

[RYT20] J. H. M. Ribeiro, C.-A. Yeh, and K. Taira. "Randomized resolvent analysis." *Phys. Rev. Fluids*, **5**(3):033902, 2020.

[RYT23] J. H. M. Ribeiro, C.-A. Yeh, and K. Taira. "Triglobal resolvent analysis of swept-wing wakes." *J. Fluid Mech.*, **954**:A42, 2023.

[RYZ22a] J. H. M. Ribeiro, C.-A. Yeh, K. Zhang, and K. Taira. "From biglobal to triglobal resolvent analysis: laminar separated flows over swept wings." AIAA Paper 2022-2428, 2022.

[RYZ22b] J. H. M. Ribeiro, C.-A. Yeh, K. Zhang, and K. Taira. "Wing sweep effects on laminar separated flows." *J. Fluid Mech.*, **950**:A23, 2022.

[SA40] H. A. Soule and R. F. Anderson. "Design charts relating to the stalling of tapered wings." Technical Report NACA-TR-703, NASA, 1940.

[SB14] P. J. Schmid and L. Brandt. "Analysis of fluid systems: Stability, receptivity, sensitivity." *Applied Mechanics Reviews*, **66**(2), 2014. 024803.

[SBH19] T. Shoji, A. Besnard, E. W. Harris, R. T. M'Closkey, and A. R. Karagozian. "Effects of Axisymmetric Square-Wave Excitation on Transverse Jet Structure and Mixing." *AIAA J.*, **57**(5):1862–1876, 2019.

[Sch41] F. W. Schmitz. *Aerodynamics of the model airplane*. Redstone arsenal translation, 1941.

[Sch01] G. Schewe. "Reynolds-number effects in flow around more-or-less bluff bodies." *J. Wind Eng. Ind. Aerodyn.*, **8**:1267–1289, 2001.

[Sch07] P. J. Schmid. "Nonmodal stability theory." *Annu. Rev. Fluid Mech.*, **39**:129–162, 2007.

[Sch10] P. J. Schmid. "Dynamic mode decomposition of numerical and experimental data." *J. Fluid Mech.*, **656**:5–28, 2010.

[SH01] P. J. Schmid and D. S. Henningson. *Stability and transition in shear flows*. Springer, 2001.

[SK16] J. Serpieri and M. Kotsonis. "Three-dimensional organisation of primary and secondary crossflow instability." *J. Fluid Mech.*, **799**:200–245, 2016.

[Spa98] P. S. Spalart. "Airplane trailing vortices." *Annu. Rev. Fluid Mech.*, **30**:107, 1998.

[SPO16] M. Sieber, C. O. Paschereit, and K. Oberleithner. "Spectral proper orthogonal decomposition." *J. Fluid Mech.*, **792**:798–828, 2016.

[SRT22] C. S. Skene, J. H. M. Ribeiro, and K. Taira. "csskene/linear-analysis-tools: Initial release." https://doi.org/10.5281/zenodo.6550726, May 2022.

[SS90] P. J. Strykowski and K. R. Sreenivasan. "On the formation and suppression of vortex 'shedding'at low Reynolds numbers." *J. Fluid Mech.*, **218**:71–107, 1990.

[SS19] C. S. Skene and P. J. Schmid. "Adjoint-based parametric sensitivity analysis for swirling M-flames." *J. Fluid Mech.*, **859**:516–542, 2019.

[STC17] Y. Sun, K. Taira, L. N. Cattafesta III, and L. S. Ukeiley. "Biglobal instabilities of compressible open-cavity flows." *J. Fluid Mech.*, **826**:270–301, 2017.

[Ste02] G. W. Stewart. "A Krylov–Schur algorithm for large eigenproblems." *SIAM J. Mat. Anal. App.*, **23**(3):601–614, 2002.

[STR18] O. T. Schmidt, A. Towne, G. Rigas, T. Colonius, and G. A. Brès. "Spectral analysis of jet turbulence." *J. Fluid Mech.*, **855**:953–982, 2018.

[SYS22] C. S. Skene, C.-A. Yeh, P. J. Schmid, and K. Taira. "Sparsifying the resolvent forcing mode via gradient-based optimisation." *J. Fluid Mech.*, **944**:A52, 2022.

[TAT22] Y. Tamaki, H. Asada, R. Takaki, and S. Kawai. "Wall-modeled LES around the CRM-HL using fully-automated Cartesian-grid-based flow solver FFVHC-ACE." In *AIAA Paper 2022-3435*, 2022.

[TBD17] K. Taira, S. L. Brunton, S. T. M. Dawson, C. W. Rowley, T. Colonius, B. J. McKeon, O. T. Schmidt, S. Gordeyev, V. Theofilis, and L. S. Ukeiley. "Modal analysis of fluid flows: An overview." *AIAA J.*, **55**(12):4013–4041, 2017.

[TBW15] L. W. Traub, E. Botero, R. Waghela, R. Callahan, and A. Watson. "Effect of taper ratio at low reynolds number." *J. Aircraft*, **52**(3):734–747, 2015.

[TC09] K. Taira and T. Colonius. "Three-dimensional flows around low-aspect-ratio flat-plate wings at low Reynolds numbers." *J. Fluid Mech.*, **623**:187–207, 2009.

[TE05] L. N. Trefethen and M. Embree. *Spectra and pseudospectra*. Princeton Univ. Press, 2005.

[THB20] K. Taira, M. S. Hemati, S. L. Brunton, Y. Sun, K. Duraisamy, S. Bagheri, S. T. M. Dawson, and C.-A. Yeh. "Modal analysis of fluid flows: Applications and outlook." *AIAA J.*, **58**(3):998–1022, 2020.

[THD00] V. Theofilis, S. Hein, and U.Ch. Dallmann. "On the origins of unsteadiness and three-dimensionality in a laminar separation bubble." *Phil. Trans. Roy. Soc. London (A)*, **358**:3229–324, 2000.

[The03] V. Theofilis. "Advances in global linear instability analysis of nonparallel and three-dimensional flows." *Prog. Aero. Sci.*, **39**:249–315, 2003.

[The11] V. Theofilis. "Global linear instability." *Annu. Rev. Fluid Mech.*, **43**:319–352, 2011.

[THT98] A. H. Techet, F. S. Hover, and M. S. Triantafyllou. "Vortical patterns behind a tapered cylinder oscillating transversely to a uniform flow." *J. Fluid Mech.*, **363**:79–96, 1998.

[Tim20] S. Timme. "Global instability of wing shock-buffet onset." *J. Fluid Mech.*, **885**:A37, 2020.

[TM04] G. E. Torres and T. J. Mueller. "Low-aspect-ratio aerodynamics at low Reynolds numbers." *AIAA J.*, **42**(5):865–873, 2004.

[TP79] M. Tobak and D. J. Peake. "Topology of two-dimensional and three-dimensional separated flows." AIAA Paper 79-1480, 1979.

[TP82] M. Tobak and D. J. Peake. "Topology of three-dimensional separated flows." *Annu. Rev. Fluid Mech.*, **14**(1):61–85, 1982.

[TP18] N. Thomareis and G. Papadakis. "Resolvent analysis of separated and attached flows around an airfoil at transitional Reynolds number." *Phys. Rev. Fluids*, **3**(7):073901, 2018.

[Tra13] L. W. Traub. "Aerodynamic impact of aspect ratio at low Reynolds number." *J. Aircraft*, **50**(2):626–634, 2013.

[TRL14] J. H. Tu, C. W. Rowley, D. M. Luchtenburg, S. L. Brunton, and J. N. Kutz. "On Dynamic Mode Decomposition: Theory and Applications." *J. Comput. Dyn.*, **1**(2):391–421, 2014.

[TSC18] A. Towne, O. T. Schmidt, and T. Colonius. "Spectral proper orthogonal decomposition and its relationship to dynamic mode decomposition and resolvent analysis." *J. Fluid Mech.*, **847**:821–867, 2018.

[TTR93a] L. N. Trefethen, A. E. Trefethen, S. C. Reddy, and T. A. Driscoll. "Hydrodynamic stability without eigenvalues." *Science*, **261**(5121):578–584, 1993.

[TTR93b] L. N. Trefethen, A. E. Trefethen, S. C. Reddy, and T. A. Driscoll. "Hydrodynamic stability without eigenvalues." *Science*, **261**(5121):578–584, 1993.

[TY21] C. E. Toppings and S. Yarusevych. "Structure and dynamics of a laminar separation bubble near a wingtip." *J. Fluid Mech.*, **929**:A39, 2021.

[TY22] C. E. Toppings and S. Yarusevych. "Structure and dynamics of a laminar separation bubble near a wing root: towards reconstructing the complete LSB topology on a finite wing." *J. Fluid Mech.*, **944**:A14, 2022.

[TYU17] J. A. Tropp, A. Yurtsever, M. Udell, and V. Cevher. "Practical sketching algorithms for low-rank matrix approximation." *SIAM J. Matrix Anal. Appl.*, **38**(4):1454–1485, 2017.

[VAJ02] B. Valles, H. I. Andersson, and C. B. Jenssen. "Oblique vortex shedding behind tapered cylinders." *J. Fluids Struct.*, **16**(4):453–463, 2002.

[Van82] M. Van Dyke. *An album of fluid motion*, volume 176. Parabolic Press Stanford, 1982.

[VG19] M. R. Visbal and D. J. Garmann. "Effect of sweep on dynamic stall of a pitching finite-aspect-ratio wing." *AIAA J.*, **57**(8):3274–3289, 2019.

[Vis12] M. R. Visbal. "Flow Structure and Unsteady Loading over a Pitching Low-Aspect-Ratio Wing." AIAA 2012-3279, 2012.

[Vre04] A. W. Vreman. "An eddy-viscosity subgrid-scale model for turbulent shear flow: algebraic theory and applications." *Phys. Fluids*, **16**(10):3670–3681, 2004.

[VSP04] J. J. Videler, E. J. Stamhuis, and G. D. E. Povel. "Leading-edge vortex lifts swifts." *Science*, **306**(5703):1960–1962, 2004.

[WAL12] W. R. Wolf, J. L. F. Azevedo, and S. K. Lele. "Convective effects and the role of quadrupole sources for aerofoil aeroacoustics." *J. Fluid Mech.*, **708**:502–538, 2012.

[WB80a] A. E. Winkelman and J. B. Barlow. "Flowfield model for a rectangular planform wing beyond stall." *AIAA J.*, **18**(8):1006–1008, 1980.

[WB80b] A. E. Winkelmann and J. B. Barlow. "Flowfield model for a rectangular planform wing beyond stall." *AIAA J.*, **18**(8):1006–1007, 1980.

[WBS80] A. Winkelmann, J. Barlow, J. Saini, E. J. Anderson Jr., and Jones. "The effects of leading edge modifications on the post-stall characteristics of wings." AIAA Paper 1980-0199, 1980.

[Wer56] H. Werlé. "Sur l'eclatement des turbillons d'apex d'une aile delta aux faibles vitesses." *La Rech. Aéro.*, (74):25–30, 1956.

[Wer71] H. Werlé. "Visualization hydrodynamique d'ecoulements instationnaire." Technical Report ONERA Note Technique 180, ONERA, 1971.

[Wer86] H. Werlé. "Structures des decollements sur les ailes cylindriques." *Recherche Aerospatiale*, **3**:221–242, 1986.

[Whi91] F. M. White. *Viscous fluid flow.* McGraw-Hill, 1991.

[WLR08] F. Woolfe, E. Liberty, V. Rokhlin, and M. Tygert. "A fast randomized algorithm for the approximation of matrices." *Appl. Comput. Harmon. Anal.*, **25**:335–366, 2008.

[WM00] M. Wang and P. Moin. "Computation of trailing-edge flow and noise using large-eddy simulation." *AIAA J.*, **38**(12):2201–2209, 2000.

[WNC18] Z. Wei, T. H. New, and Y. D. Cui. "Aerodynamic performance and surface flow structures of leading-edge tubercled tapered swept-back wings." *AIAA J.*, **56**(1):423–431, 2018.

[WR56] H. Werlé and M. Roy. "Partage et rencontre d'ecoulement fluids." *La Rech. Aéro.*, (79):9–26, 1956.

[WR88] C. H. K. Williamson and A. Roshko. "Vortex formation in the wake of an oscillating cylinder." *J. Fluids Struct.*, **2**(4):355–381, 1988.

[WTK11] I. Wygnanski, P. Tewes, H. Kurz, L. Taubert, and C. Chen. "The application of boundary layer independence principle to three-dimensional turbulent mixing layers." *J. Fluid Mech.*, **675**:336–346, 2011.

[WTT14] I. Wygnanski, P. Tewes, and L. Taubert. "Applying the boundary-layer independence principle to turbulent flows." *J. Aircraft*, **51**(1):175–182, 2014.

[YBT20] C.-A. Yeh, S. I. Benton, K. Taira, and D. J. Garmann. "Resolvent analysis of an airfoil laminar separation bubble at Re = 500 000." *Phys. Rev. Fluids*, **5**(8):083906, 2020.

[YH07] S.-C. Yen and C. M. Hsu. "Flow patterns and wake structure of a swept-back wing." *AIAA J.*, **45**(1):228–236, 2007.

[YH09] S.-C. Yen and L.-C. Huang. "Flow patterns and aerodynamic performance of unswept and swept-back wings." *J. Fluids Eng.*, **131**(11), 2009.

[YR12] T. O. Yilmaz and D. Rockwell. "Flow structure on finite-span wings due to pitch-up motion." *J. Fluid Mech.*, **691**:518–545, 2012.

[YSK09] S. Yarusevych, P. E. Sullivan, and J. G. Kawall. "On vortex shedding from an airfoil in low-Reynolds-number flows." *J. Fluid Mech.*, **632**:245–271, 2009.

[YT19] C.-A. Yeh and K. Taira. "Resolvent-analysis-based design of airfoil separation control." *J. Fluid Mech.*, **867**:572–610, 2019.

[ZBH23] K. Zhang, Y. Bao, Z. Han, and D. Zhou. "End boundary effects on wakes dynamics of inclined circular cylinders." *Ocean Eng.*, **269**:113543, 2023.

[ZHA20a] K. Zhang, S. Hayostek, M. Amitay, A. Burstev, V. Theofilis, and K. Taira. "Laminar separated flows over finite-aspect-ratio swept wings." *J. Fluid Mech.*, **905**:R1, 2020.

[ZHA20b] K. Zhang, S. Hayostek, M. Amitay, W. He, V. Theofilis, and K. Taira. "On the formation of three-dimensional separated flows over wings under tip effects." *J. Fluid Mech.*, **895**:A9, 2020.

[ZSB22] K. Zhang, B. Shah, and O. Bilgen. "Low-Reynolds-Number Aerodynamic Characteristics of Airfoils with Piezocomposite Trailing Surfaces." *AIAA J.*, **60**(4):2701–2706, 2022.

[ZT22] K. Zhang and K. Taira. "Laminar vortex dynamics around forward-swept wings." *Phys. Rev. Fluids*, **7**(2):024704, 2022.